

---

# Ion-conducting Nanopores in Polymer Membranes for (Bio)Molecular Sensory Applications

---

Ionenleitende Nanoporen in Polymer-Membranen für (bio)molekulare Sensor-Anwendungen

---

Zur Erlangung des akademischen Grades Doktor der Ingenieurwissenschaften (Dr.-Ing.)  
genehmigte Dissertation von  
Diplom-Chemikerin Ivana Duznovic ; geb. in Sarajevo (Bosnien und Herzegowina)

---

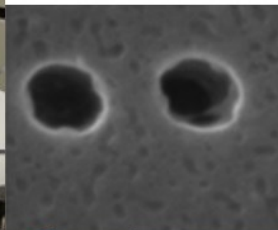
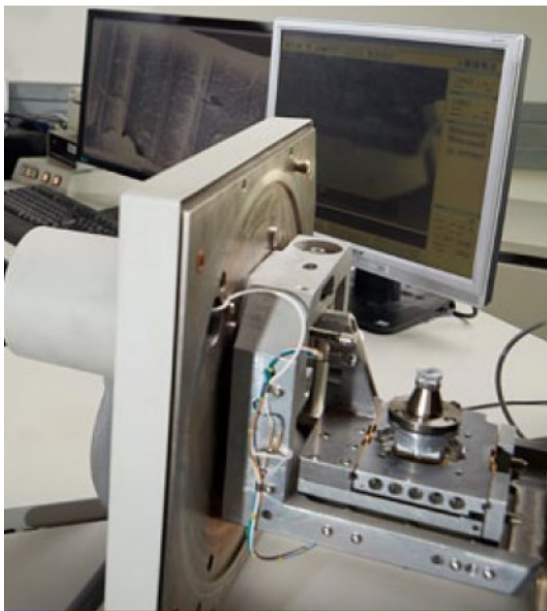
**Gutachten: Prof. Dr. Wolfgang Ensinger**

**Gutachten: Prof. Dr. Viktor Stein**

---

Tag der Einreichung: 2. Oktober 2020; Tag der mündlichen Prüfung: 6. November 2020  
DARMSTADT 2021

---

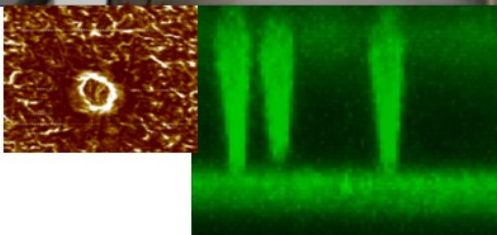


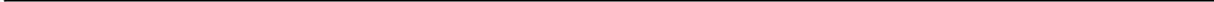
  
**INAPO**

  
**MATERIAL  
ANALYTIK**



**TECHNISCHE  
UNIVERSITÄT  
DARMSTADT**





---

# Ion-conducting Nanopores in Polymer Membranes for (Bio)Molecular Sensory Applications

- Ionenleitende Nanoporen in Polymer-Membranen für (bio)molekulare Sensor-Anwendungen

Genehmigte Dissertation von Dipl.-Chem. Ivana Duznovic aus Sarajevo (Bosnien und Herzegowina)

1. Gutachten: Prof. Dr. Wolfgang Ensinger
2. Gutachten: Prof. Dr. Viktor Stein

Tag der Einreichung: 2. Oktober 2020

Tag der Prüfung: 6. November 2020

DARMSTADT 2021

Bitte zitieren Sie dieses Dokument als:

URN: urn:nbn:de:tuda-tuprints-140701

URL: <https://tuprints.ulb.tu-darmstadt.de/id/eprint/14070>

Dieses Dokument wird bereitgestellt von tuprints,  
E-Publishing-Service der TU Darmstadt

<http://tuprints.ulb.tu-darmstadt.de>  
[tuprints@ulb.tu-darmstadt.de](mailto:tuprints@ulb.tu-darmstadt.de)



Die Veröffentlichung steht unter folgender Creative Commons Lizenz:

Namensnennung – Keine kommerzielle Nutzung – Keine Bearbeitung 4.0 International

<https://creativecommons.org/licenses/by-nc-nd/4.0/deed.de>



---

---

## **Erklärung zur Dissertation**

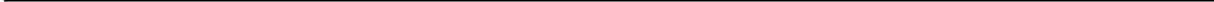
---

Hiermit versichere ich, die vorliegende Dissertation ohne Hilfe Dritter nur mit den angegebenen Quellen und Hilfsmitteln angefertigt zu haben. Alle Stellen, die aus Quellen entnommen wurden, sind als solche kenntlich gemacht. Diese Arbeit hat in gleicher oder ähnlicher Form noch keiner Prüfungsbehörde vorgelegen.

Darmstadt, den 2. Oktober 2020

---

(Ivana Duznovic)





*“Curiosity is not a sin. But we should exercise caution with our curiosity.”*

*– ALBUS PERCIVAL WULFRIC BRIAN DUMBLEDORE*



---

---

## ABSTRACT

---

In the recent years, track-etched nanopores became the major impulse in the development of nanofluidic biosensing devices. The fabrication is processed first by bombarding polymeric films with swift heavy ions. Subsequently, damaged zones within the polymer membrane are created, which are transformed into nanopores via chemical etching technique. Here, pore geometry and diameter are controlled by selecting a suitable chemical etchant and track-etching conditions. As-prepared nanopores are cation selective due to the presence of the ionized carboxylic acid moieties under physiological conditions, which are generated as a consequence of the ion-track etching process. The fixed surface charge polarity and concomitant ion-selectivity of nanopores is tuneable by the modification of native carboxylic acid groups. Moreover, these groups are used to attach desired receptors for biorecognition purpose through specific ligand-receptor interactions. Surface modification and biorecognition processes are monitored by measuring the changes in the electric response of the nanopore via current-voltage (*IV*) experiments. Regarding the design and miniaturization of nanopore-based biosensing devices, this thesis focusses on the three major challenges, which must be taken into account to enable applications in real systems: i) investigating the application of commercially available nanopore membranes and biodegradable membranes as alternative substrates for nanofluidic sensors. ii) Examining innovative receptor-analyte moieties towards their sensitive, selective and reproducible sensing performance. Here, a variety of receptors and analytes are investigated regarding the detection of metal cations, small molecules (histamine) and biomacromolecules (proteins) as well as polyelectrolytes. In case of metal cations, the selective recognition of potassium ion is achieved by immobilizing pseudo-crown ether-moieties on the pore surface. Moreover, ultrasensitive subnanomolar Cu(II)-detection is obtained by decorating nanopores with an *amino-terminated copper and nickel* (ATCUN) motif. Both metal cations play crucial roles within neuronal systems of living organisms. Hence, monitoring of ion level is beneficial regarding diagnostic applications. Further inflammatory indicators like histamine are also successfully detected by the use of nanopore membranes functionalized with Ni(II)-nitrilotriacetic acid (NTA)-complexes. In Addition, LBL-deposition is achieved inside nanopores through the electrostatic attraction between poly(allylamine hydrochloride) and poly(acrylic acid) with poly(4-vinylpyridine) (PVP) as a hydrogen-bond compound. After the cross-linking of stacked polyelectrolytes, the exposure to basic pH-conditions triggered the PVP-release, leading to the formation of porous networks in the nanopores as observed by changes in the electrical readout and an increased mass transport across the membrane. This represents the proof of concept for the stimulated release of drugs. Moreover, the highly selective and sensitive performance of pore-bounded camellia nanobody-protein is successfully investigated, which are single domain antibodies and, therefore, considered as highly efficient detectors within immune systems. The used nanobodies exhibit high affinity towards fluorescent proteins (GFP and mCherry) as evidenced by *IV*-changes of modified pore membranes and by CLSM-imaging methods. This study demonstrates novel analyte detection using nanobody as receptors on nanopore surfaces and to date receptor-analyte interactions were performed in macro-sized setup, whose implantation in real system is quite challenging due to their sampling volumes of about 7 mL. Therefore, nanoporous membranes were integrated in miniaturized *Lab-on-Chips* to investigate the modification and sensing performance. Further, the standard aqueous electrolyte used for *IV*-measurements is exchanged by human serum to investigate the *IV*-impact of a more complex medium on receptor-analyte interactions across nanopore membranes.

---

---

## Kurzbeschreibung

---

Im Zuge der Entwicklung und des Designs nanofluidischer Biosensoren nimmt die Verwendung ionenspur-geätzter Nanoporen eine essentielle Bedeutung ein. Deren Herstellung erfolgt in zwei Stufen, wobei zunächst Polymerfilme mit Schwerionen beschossen werden. Anschließend werden die hieraus resultierenden beschädigten Zonen innerhalb der Polymermembran, auch Spuren genannt, durch chemisches Ätzen in Nanoporen umgewandelt. Durch die Wahl der chemischer Ätzmittel und -bedingungen während des Spurätzverfahrens lässt sich die Porengeometrie sowie der Durchmesser steuern. Solch hergestellte Nanoporen enthalten freigelegte Carboxylgruppen an den Porenwänden sowie an der Membranoberfläche. Dabei bewirkt die negative Ladung ionisierter Carbonsäureeinheiten unter physiologischen Bedingungen die Generierung kationenselektiver Membranen. Diese stabile oberflächliche Porenpolarität und die damit einhergehende Ionenselektivität der Nanopore ist durch Modifikation dieser nativen Carbonsäuregruppen manipulierbar. Darüber hinaus werden über diese Gruppen auch Rezeptoren angebracht, die in der Lage sind spezifische Ligand-Rezeptor-Wechselwirkungen innerhalb der Nanopore einzugehen. Die Oberflächenmodifikation sowie die Biokonjugation innerhalb der Pore werden überwacht, indem die Änderungen des elektrischen Widerstands der Nanopore mittels Strom-Spannungs-Messungen (*IV*) analysiert werden. Der Rahmen dieser Doktorarbeit befasst sich mit dem Design von nanoporen-basierten Biosensoren sowie deren Miniaturisierung und konzentriert sich hierbei auf drei Herausforderungen, deren Berücksichtigung essenziell sind um eine spätere Anwendung in realen Systemen zu ermöglichen: i) Untersuchung von kommerziellen Nanoporenmembranen sowie deren biologisch abbaubare Pendants als mögliche alternative Substrate; ii) Ausarbeitung innovativer Rezeptor-Funktionalisierungen der Nanopore in Bezug auf ihre Empfindlichkeit, Selektivität sowie Reproduzierbarkeit gegenüber möglichen Biomarkern. Hierbei wird eine Vielzahl von Rezeptoren und Analyten zum Nachweis von Metallkationen, Molekülen (Histamin) und Biomakromolekülen (Proteinen) sowie Polyelektrolyten untersucht. Im Fall der Metallkationen wurde die selektive Erkennung von Kaliumionen über eine Immobilisierung von Pseudokronenether-Einheiten auf der Nanoporenoberfläche erreicht. Des Weiteren wurde der ultrasensitive Nachweis von Kupferionen in subnanomolaren Bereichen erzielt mittels molekularer Anbringung des aminoterminierten Kupfer- und Nickelmotifs (ATCUN). Beide Metallkationen spielen eine entscheidende Rolle im neuronalen System lebender Organismen, wobei die Überwachung des Ionen-Gehalts für diagnostische Anwendungen eingesetzt werden kann. Weitere Entzündungsindikatoren wie Histamin sind erfolgreich durch die Verwendung von Nanoporen nachgewiesen worden, welche zuvor mit Nickel-Nitrilotriessigsäure (NTA)-Komplexen modifiziert wurden. Ferner wurde die LBL-Schichtung durch die elektrostatische Anziehung zwischen Poly(allylaminhydrochlorid) und Poly(acrylsäure) mit Poly(4-vinylpyridin) (PVP) über Wasserstoffbrücken erzielt. Nach der erfolgreichen Vernetzung dieser Polyelektrolyten innerhalb dieser Schichtstruktur, löst die Exposition in basischem pH-Milieu die PVP-Komponente heraus, was zur Bildung poröser Netzwerke innerhalb der Nanoporen führt, bewiesen durch Änderungen der elektrischen Flusses sowie Zunahme des Massentransports durch die Membran. Weiterhin fungiert dieses Experiment als Machbarkeitsnachweis für eine stimulierte Freisetzung von Arzneimitteln. Darüber hinaus konnte die hochselektive und sensitive Leistung von porengelassenen kameliden Nanokörper-Proteinen erfolgreich untersucht werden. Diese Nanokörper zählen zu den Einzeldomänen-Antikörpern und sind hochselektive Detektoren für Biomarker innerhalb des Immunsystems. Der jeweilige Nanokörper zeigte eine hohe Affinität zu fluoreszierenden Proteinen (GFP und

---

mCherry), wie aus den Änderungen der *IV*-Messung der modifizierten Nanopore und aus CLSM-Bildgebungsverfahren hervorgeht. Diese Studie demonstriert somit den erfolgreichen Nachweis von Analyten mit Nanoporen, welche mit Nanokörper-Einheiten funktionalisiert wurden. Bisher wurden die Messungen der Rezeptor-Analyt-Wechselwirkungen in praktikablen Labor-Aufbau durchgeführt, welche Probenvolumina von 7 mL benötigen und somit weniger für reale Systeme geeignet sind. Daher beschäftigt sich der letzte Abschnitt dieser Doktorarbeit mit der Integration nanoporöser Membranen in miniaturisierte Lab-on-Chips. Hierbei wurde die Modifikations- und Sensorleistung untersucht und mit der des Labor-Aufbaus verglichen. Ferner wurde der wasserbasierte Standard-Elektrolyt, welcher für die *IV*-Messungen verwendet wird gegen humanes Serum getauscht, um den Einfluss eines komplexeren Mediums auf die Rezeptor-Analyt-Wechselwirkungen und die Nanopore selbst zu studieren.

---

---

## Acknowledgements

---

---

## Scientific Contributions

---

Diese Arbeit wurde unter der Leitung von Herrn Prof. Dr. Wolfgang Ensinger im Fachgebiet Materialanalytik des Fachbereichs Material- und Geowissenschaften der Technischen Universität Darmstadt in der Zeit von März 2016 bis September 2020 angefertigt. Die Ergebnisse, die in dieser Zeit erzielt wurden, sind in dieser Dissertation sowie in folgenden Publikationen und Patenten veröffentlicht worden.

---

## Patents

---

El Khoury, M.; Ensinger, W.; Göringer, H. U.; Quednau, S.; Schlaak, H. F.; **Duznovic, I.** (2019) „Detektionssystem und Verfahren zu dessen Herstellung“, German Patent DE102017114349

---

## Publications

---

Müller, L. K., **Duznovic, I.**, Tietze, D., Weber, W., Ali, M., Stein, V., Ensinger, W., Tietze, Al. (2020) “*Ultrasensitive and selective copper (II) detection: introducing a bioinspired and robust sensor*”, Chemistry A European Journal, 26 (39): 8511-8517.

**Duznovic, I.**, Diefenbach, M., Ali, M., Stein, T., Biesalski, M., Ensinger, M. (2019) “*Automated measuring of mass transport through synthetic nanochannels functionalized with polyelectrolyte porous networks*”, Journal of Membrane Science 591:117344.

Ali, M., Ahmed, I., Nasir, S., **Duznovic, I.**, Niemeyer, C.F., Ensinger, W. (2018) “Potassium-induced ionic conduction through a single nanofluidic pore modified with acyclic polyether derivative” Analytica Chimica Acta 39: 132-139.

El Khoury, M., **Duznovic, I.**, Ali, M., Ensinger, W., Schlaak, H.F. (2017) „*Integration konischer Nanoporen in Lab-on-Chip-Systeme für die Histamin-Analyse*“, Mikrosystemteknikkongress, München, Unterschleißheim, Deutschland. Proceedings – Mikrosystemtechnik Kongress 2017

Ali, M., Ramirez, P., **Duznovic, I.**, Nasir, S., Mafe, S., Ensinger, W. (2017) „*Label-free histamine detection with nanofluidic diodes through metal ion displacement mechanism*”, Colloids and Surfaces B: Biointerfaces 150: 201-208.

Ali, M., Nasir, S., **Duznovic, I.**, Ensinger, W. (2017) “*Ion conducting nanopores for (bio)molecular sensing: the iNAPO project*”, Department of Materials- and Geo-Sciences, TU Darmstadt, Annual Report 2016, 78-81.

Ensinger, W., Thiel, G., **Duznovic, I.**, Nasir, S., Ali, M. (2016) “*iNAPO – Ion Conducting Nanopores in Polymer Foils Chemically Modified for Biomolecular Sensing*”, ICNNFC 126, 1 – 5, in: Proc. World Congress on Recent Advances in Nanotechnology (RAN’16), Prague, Czech Republic, April 1–2, 2016, International ASET Inc., Ottawa, Canada ISBN: 978-1-927877-19-7.

---

---

## Conference Contributions

---

**MSE Congress: Materials Science and Engineering (2018)**

Darmstadt, Darmstadt (poster)

**Faraday Discussions: Electrochemistry at Nano-Interfaces (2018)**

University of Bath, Bath, United Kingdom (poster)

**9. GMM-Workshop: Energieautonome Sensorsysteme (2018)**

Hilton Hotel, Dresden (poster and oral presentation)

**Medizintechnik Symposium der Rhein-Main-Universitäten (2017)**

Darmstadt, Darmstadt (poster)

**iNAPO Workshop for Sensors: Formation, Characterization and Modelling (2017);** Georg-

Christoph-Lichtenberg-Haus, Darmstadt (poster and oral presentation)

**Wilhelm und Else Heraeus-Seminar (2017)** “Transport Mechanisms in Biological and Synthetic nanopores and –channels”, Jacobs University, Bremen (Poster)

---

## Supervision of Theses

---

### Bachelor theses

„*Sensorische Detektion von GST basierend auf ionenleitenden Nanoporen*“

Niklas Leimeroth, completed October 2017.

„*Impedanzspektroskopische Untersuchung ionenleitender Nanoporen*“

Yasemin Bolat, completed August 2018.

„*Nanobody funktionalisierte ionenleitende Nanopormembranen*“

Christopher Hofferberth, completed September 2019.

### Master theses

“*Tailoring geometrical dimensions and electrical properties of ion conducting nanopores via layer-by-layer self-assembly*”;

Tom Stein; completed May 2018.

“*Development of a Sensory Analysis for Human Serum with Ion Conducting Nanopores*”;

Vanessa Mehlhorn, completed September 2019.

---

---

## Table of Content

---

CHAPTER I: GENERAL INTRODUCTION	1
1. Origin of the Nanopores	1
1.1. Biological Model	1
1.2. Biomimetic Approach towards Solid-State Nanopores	3
2. Track-Etched Membranes	5
2.1. Fabrication of Polymeric Nanopores	5
2.1.1. Latent-Track Formation	5
2.1.2. Etching-Process	9
2.1.3. Physical Properties of Charged Surfaces	10
2.1.4. Surface Modification	11
2.2. Sensing Concept	13
2.2.1. Electrostatic and Electrodynamical Insights	14
2.2.2. Sorption-promoted Analyte Detection	16
3. Road to Medical Devices	19
3.1. Biosensors	19
3.2. <i>In-vitro</i> diagnostic and Point-of-Care-Testing (POCT)	21
3.3. Lab-on-a-Chip (LOC) and Micro-Total-Analysis System ( $\mu$ TAS)	22
CHAPTER II: EXPERIMENTAL	24
1. Fabrication of Polymeric Nanopores	24
1.1. Symmetrical Etching	25
1.2. Asymmetrical Etching	25
2. Functionalization of Nanopore Surface	26
2.1. Covalent Functionalization	27
2.1.1. EDC-Coupling Chemistry	28
2.1.2. HATU-Coupling Chemistry	29
2.2. Click-Chemistry	30
2.2.1. Strain-Promoted Azide-Alkyne Cycloaddition (SPAAC)	30
2.2.2. Tag-Catcher System	31
2.3. Electrostatic Interactions	33
2.3.1. Layer-by-Layer Technique (2 compounds)	34
2.3.2. Combined LBL-Modification (3 compounds)	34
2.4. Metal Complexation	36
2.4.1. Nickel-NTA-Complexes	36
2.4.2. Electroless metal deposition	37
3. Characterization of Polymeric Nanopores	39
3.1. Physicochemical Properties	39
3.1.1. Current-Voltage Characteristics	39

3.1.2. Mass Transport Measurement	41
3.2. Optical Investigations/imaging Procedures	42
3.2.1. Scanning Electron Microscopy	42
3.2.2. Confocal Laser Scanning Microscopy	44
3.2.3. Atomic Force Microscopy (AFM)	45
CHAPTER III: MOTIVATION AND AIM	46
CHAPTER IV: NANOPORE MATERIALS	47
1. Nanopore Fabrication in Commercial Poly(ethylene terephthalate)-Membranes	47
1.1. Introduction	47
1.2. Results and Discussion	48
1.2.1. <i>In-situ</i> Control over Nanopore Dimensions	49
1.2.2. <i>Ex-situ</i> Control of Nanopore Dimensions	52
1.3. Conclusion	57
2. Nanopores inside Biodegradable Poly(lactic acid)-Membranes	59
2.1. Introduction	59
2.2. Results and Discussion	60
2.2.1. Temperature-Dependence of PLA-Track-Etching	61
2.2.2. Concentration-Dependence of PLA-Track-Etching	63
2.3. Conclusion	68
CHAPTER V: Nanopore Modification and Sensing Properties	69
1. Label-free Histamine Detection with Nanofluidic Diodes through Metal Ion Displacement Mechanism*	69
1.1. Introduction	69
1.2. Results and Discussion	70
1.2.1. Sensitive Detection of Histamine	71
1.2.2. Selective Detection of Histamine	72
1.2.3. Reversible Detection of Histamine	74
1.3. Conclusion	74
2. Potassium-Induced Ionic Conduction through a Single Nanofluidic Pore modified with Acyclic Polyether Derivative*	75
2.1. Introduction	75
2.2. Results and Discussion	76
2.2.1. Qualitative Estimation of Ionic Transport	77
2.2.2. Quantitative Estimation of Ionic Transport	78
2.2.3. Modification in Absence/Presence of Potassium Ions	79
2.3. Conclusion	80
3. Automated Measuring of Mass Transport through Synthetic Nanochannels Functionalized with Polyelectrolyte Porous Networks*	82
3.1. Introduction	82

3.2. Results and Discussion	83
3.2.1. Investigations on Classical LBL-Modification (2-Compound System)	84
3.2.2. Investigations on Hybrid LBL-Modification (3-Compound System)	90
3.3. Conclusion	98
4. Ultrasensitive and Selective Copper (II) Detection: Introducing a Bioinspired and Robust Sensor*	99
4.1. Introduction	99
4.2. Results and Discussion	100
4.2.1. <i>IV</i> -Characterization of ATCUN-Cu <sup>2+</sup> -Interface	102
4.2.2. Optical Investigations of the ATCUN-Cu <sup>2+</sup> -Interface	104
4.3. Conclusion	107
5. Ultrasensitive, Electrical Biosensing of Protein Analytes by means of Nanobodies immobilised inside Track-Etched Nanopores*	109
5.1. Introduction	109
5.2. Results and Discussion	110
5.2.1. Pore-Modification and Sensing Performance of Nanobodies	111
5.2.2. Nanobody-selectivity towards Cognate Protein-Epitopes	114
5.2.3. Negative Control Experiment	118
5.3. Conclusion	121
CHAPTER VI: NANOPORE MEASUREMENTS IN REAL SYSTEMS	122
1. Nanopore-Sensing within <i>Lab-on-Chip</i> -Systems	122
1.1. Introduction	122
1.2. Results and Discussion	122
1.2.1. Laboratory Set-up vs. LOC-System	123
1.2.2. 1 <sup>st</sup> Generation of LOC-devices	125
1.2.3. 2 <sup>nd</sup> Generation of LOC-devices	127
1.3. Conclusion	130
2. Nanopore-Sensing in Human Body Fluids	131
2.1. Introduction	131
2.2. Results and Discussions	132
2.2.1. Copper (II)-Sensing in Human Serum (HS)	132
2.2.2. Copper (II)-Sensing in Human Albumin Electrolyte	137
2.3. Conclusion	139
CHAPTER VII: SUMMARY AND OUTLOOK	141
References	145
Appendix	159
Supplemental Data of Mass Transport Experiments	159
Supplemental Data of Nanobody-Experiments	165
List of Abbreviations	166

---

List of Figures

168

List of Tables

179

---

---

## CHAPTER I: GENERAL INTRODUCTION

---

Decades of scientific research have focussed on the development of chemical-engineered sensors, whereas ongoing investigations symbolize a cutting edge technology in the nanoconfinement of biology, chemistry, physics and engineering. (1, 2) Potential applications in the field of physiological (medical) and environmental analysis are investigated on polymers and presented in this thesis.

Looking at nature, the communication of cells with each other and with their environment provide an essential platform to respond to external changes. (3) The cell reacts at the molecular level causing a better adaptability towards changed external conditions. Thus, cell communication enables a crucial contribution to the evolutionary optimization of organisms. (4) From a scientific point of view, it is essential to study the processes of cellular communication to get better insights into directed signal and molecular transport across the cell membrane. (5) Moreover, it is important to understand the process of cell membranes promoted by so-called *nanopores* allowing certain particles to pass through the membrane whereas damaging moieties, like toxins, were hindered to permeate into the inner of the cell. (6) The result can be transferred onto applications for the medical detection of diseases, in which the specific and selective molecular recognition is indispensable. (7)

---

### 1. Origin of the Nanopores

---

The lateral translation of the word “nanopores” describes the function of a pore itself. Now, the word stem 'pore' originates from the greek word 'porós' (πόρος) in the mean of 'opening' or 'hole'. (8) The prefix 'nano' defines the dimension of the pore, i. e., less than 100 nm. (9) In fact, the transport of information or material across the nanoconfined system is promoted by this opening from the outside to the inside and *vice versa*.

#### 1.1. Biological Model

Biological pores located in the cell membrane regulate the communication among the cells and with the environment. (10) Hence, the cell pores are not primitive openings. They are more similar to a gate allowing the targeted or controlled translocation of certain ions, molecules or signals. (11–14) Biological nanopores are integral transmembrane proteins located in the external phospholipid layer of the cell membrane that separates the interior of the cell from the external environment (see Figure 1). (15) The membrane proteins are classified, first, by the direction in which the transport takes place, and, second, by the type of molecules being transported. (16, 17)

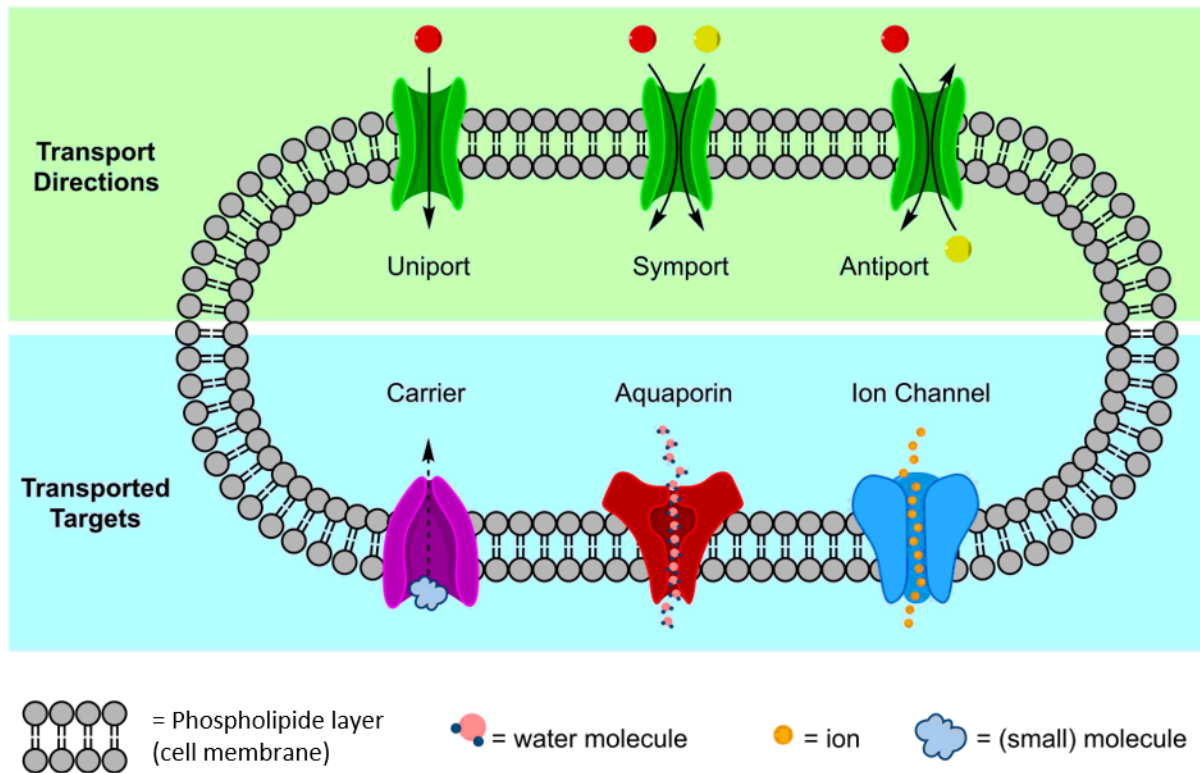


Figure 1: Classification of membrane transport proteins anchored inside the phospholipid layer: Directed membrane transport of targets: 'Uniport', 'Symport' and 'Antiport' (green-highlighted area); Different classes of membrane proteins according to the transport cargo: selective transport of specific molecules by "Carrier proteins"; water permeation throughout 'Aquaporins' and transport of ionic species via 'Ion Channels' (blue-highlighted area). Adapted from Hediger *et al.* (17), copyright (2013) Elsevier.

According to Figure 1, transport proteins differ in the direction the transport takes place. If the permeation occurs in one direction, e. g., from the external into the interior of the cell, the respective transport is defined as 'uniport'. The 'symport' describes the case of a coupled transport of more than one species across one pore. For the case of an 'antiport', one species is transported from the external environment into the cell while another species leaves the cell. Furthermore, the membrane proteins are separated by the nature of the transported species. (18, 19) Here, carrier proteins selectively transport certain molecules, whereas the water transfer occurs especially throughout aquaporin proteins. In addition, ion channels carry both anionic, e. g.  $\text{Cl}^-$  ions, and cationic species, e. g.  $\text{K}^+$ ,  $\text{Na}^+$  or  $\text{Ca}^{2+}$ -ions, across the pore region. (20-22)

The driving force of the transport process across the pore region is either (i) diffusion-controlled (ii), based on a concentration gradient between the cell interior and the environment (23) or (iii) potential-triggered due to electrolytic imbalances between the outside and inside of the cell regions. (24) For the case of (iv) ligand-induced transport, the membrane proteins are usually closed, but they can be opened for certain molecules to pass through the pore region. (25) The transport protein consists of a specific receptor unit located on the pore openings and is able to bind a specific ligand molecule. According to the key-and-lock-principle, the interaction between receptor and the respective ligand (antagonist) undergoes a bioconjugation reaction that induces the opening of the pore and initiate transport processes from the outside to the cell and *vice versa* (see Figure 2). (19)

Regarding the ion channels, the transport of ions is in accordance to a movement of ions. Physically, the transport performance along an ion channel can be determined throughout a conductance measurement using the patch-clamp method (see Figure 2). (26–28)

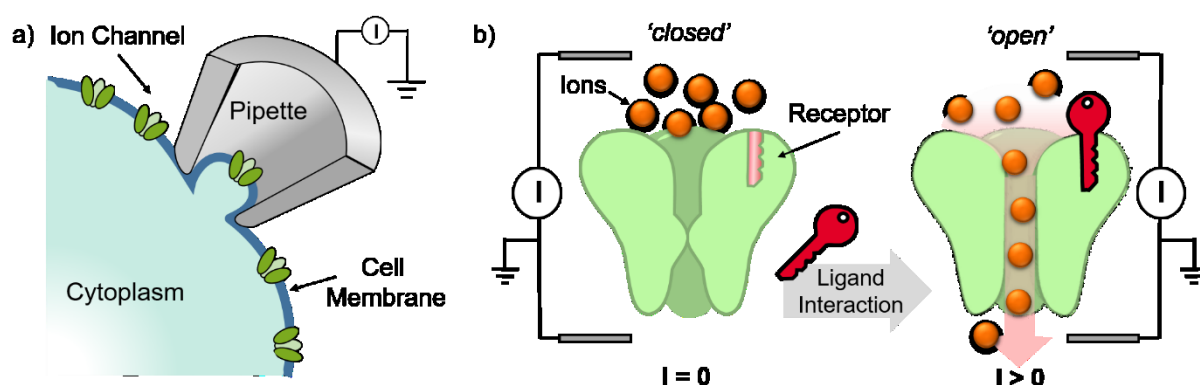


Figure 2: Schematic illustration of the patch-clamp-technique for the gating characterization of biological pore proteins, i. e. ion channels. Here, the cell membrane containing just a few ion channels is sealed by a glass pipette (a). (adapted from Collingridge *et al.* (29), copyright (2009) Elsevier) In the presence of a corresponding ligand, the channel opens and provides a flux of ions, which is detected as current (mostly in the pA range) (b). (adapted from Unwin *et al.* (30), copyright (1993) Cell Press).

Here, the ligand-promoted gating of the pore is studied: In the presence of a respective ligand, the successful bioconjugation reaction opens the pore and induces a measurable ion current. In the absence of the ligand, the pore remains closed and no current is detected. This method provides an explicit base for chemical engineering of stimuli-triggered conductance measurements based on transport proteins. (28, 29)

In addition, investigations of the transport processes are based on a high motivation in the scientific community, because of the potential use in the development of quantitative and qualitative analysis of biological pores. Nonetheless, there are two main challenges that has to be avoided: Firstly, the stability of membrane proteins vanishes without being embedded inside the phospholipid layer. (31) Because of incipient denaturation processes, the pore geometry collapses and no transport phenomena can occur. Therefore, analyses are just possible as long as the pore proteins are embedded in an intact cell. (32) Secondly, as part of the development of pore-based sensors, the variety of recognition units (receptors) located at the pore openings must be expanded. This is carried out synthetically, whereby it must be ensured that the attachment of new binding sites does not affect the pore formation and the subsequent transport performance. Hence, fundamental studies of the modified pore proteins are required before the sensor performance can be tested itself. (33, 34)

Overall, the mechanical instability limits the applicability of pore-based analysis, whereas the sensitive fusion between innovative receptor units and the sensitive pore region decelerates the development of possible sensors. (35, 36) This underlines the need for a new substrate system without the cellular matrix to enhance the research towards sensor applications. (37, 38)

## 1.2. Biomimetic Approach towards Solid-State Nanopores

Non-biological substrates pervaded by artificial nanopores established themselves as a material with adjustable porosity. (39) These so-called 'solid-state nanopores' attract huge interest of the scientific community and became candidates for the detection of analysis by means of artificial pores.(40) Hence, the receptor-ligand interactions located in the pore-openings (see Figure 2)

are used as a model system to introduce specific recognition units onto the inner surface of artificial pores (see Figure 3). (41, 42)

Their high robustness and integrability into engineered devices initiated numerous research studies and developed new classes of materials, accompanied by innovative fabrication methods. (1, 2, 43–45) Here, the nanopore fabrication is carried using (i) high-energetic beam techniques, (ii) the controlled break-down (CBD) method or (iii) throughout the use of pipette pullers and (iv) the track-etching procedures. (39, 46, 47) The fabrication of nanopores inside suitable materials are listed in Table 1.

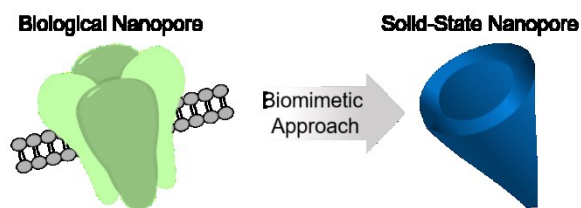


Figure 3: Biomimetic approach towards solid-state nanopores (blue) to overcome the fragility of biological nanopores (green) out of the integral cellular membrane.

Table 1: Overview of the developed methods for the fabrication of nanopores. (CBD = controlled break-down)

Beam Technique	CBD -Method	Pipette Pullers	Track-Etching
Si(48), Al(49), SiC(50), SiO <sub>2</sub> (51)	MoS <sub>2</sub> (52)	Glass(53) Quartz(54)	Polymers(55)
Si <sub>3</sub> N <sub>4</sub> (56), Graphene(57)			

Here, the fabrication of nanopores can be carried out in various materials ranging from inorganics, like silica (50) and silica derivatives (50, 51, 56), aluminium (49), to amorphous glass (53) or graphene (57) as well as semi-crystalline polymers (55).

---

## 2. Track-Etched Membranes

---

The nanoscale control over shape and size of the nanopore plays a crucial role for the detection of analytes inside the nanopore-confinement. If the analyte and the pore are of the same order of magnitude, the interaction of only one analyte molecule (ligand) is sufficient to provide a significant blockade of the pore. (58–60)

Siwy *et al.* showed the crucial role of the spatial dimensions of the pore region for the detection of analytes. By using a gold-coated asymmetrical nanotube, the ionic transport across the pore mimics a voltage-gated ion channel able to detect various proteins, like streptavidin, immunoglobulin and ricin. (61) Numerous scientific publications underlined the importance of nanoscale control over the geometry of the nanopores for the use as sensing elements for the precise detection of molecules like small molecules (62–64), DNA (65) and DNA-fragments (66) or ions (67, 68).

### 2.1. Fabrication of Polymeric Nanopores

The control over the pore diameter can be obtained throughout the selected fabrication method. The so-called ‘track-etching technique’ for particles was introduced by Fleischer *et al.* (69), whereas the adaptation for polymeric substrates was initiated by Apel *et al.* (70) Here, the use of step-growth polymers, like polyethylene terephthalate, polycarbonate (71) or polyimide foils (72), have become the major material for the production of nanopores. Their heteroatomic backbone allows the etchant to penetrate easier into the track zone to create the nanopores. (70) For this reason, chain-growth polymers in which C-C bonds prevail in the interior of the polymer are not fully suitable for alkali-promoted pore generation and harsher etching conditions are needed. (73) In addition, the track-etching method states that every pore is originated from the respective track. (74) Therefore, low frequency radiation results in less pore density. (75) The higher the beam intensity is, i. e. ions per unit area, the higher the track density and the resulting pore density is. (76) It turned out that, polyesters, like polyethylene terephthalate (PET), polycarbonate (PC) and also polyimide (PI) (see Figure 4), are suitable candidates for substrate materials of nanopores. (77)

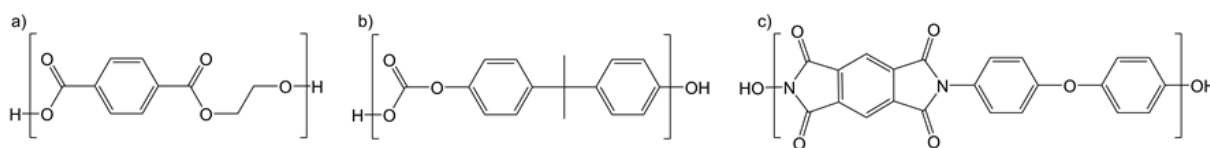


Figure 4: Scheme of step growth polymers with their respective repeating units: a) poly(ethylene terephthalate) (Hostaphan® obtained by Mitsubishi Polyester Films GmbH); (b) poly(carbonate) (Macrofol® obtained by Bayer AG); (c) poly(imide) (Kapton® obtained by Dupont). (77)

#### 2.1.1. Latent-Track Formation

Nanopores are generated through a two-step process: Firstly, latent tracks are formed by treating the foils with swift heavy-ions (SHI). The high energetic irradiation is performed inside the universal linear accelerator (UNILAC) at the GSI-Helmholtz-Centre for Heavy Ion Research located in Wixhausen-Darmstadt, Germany (see Figure 5).

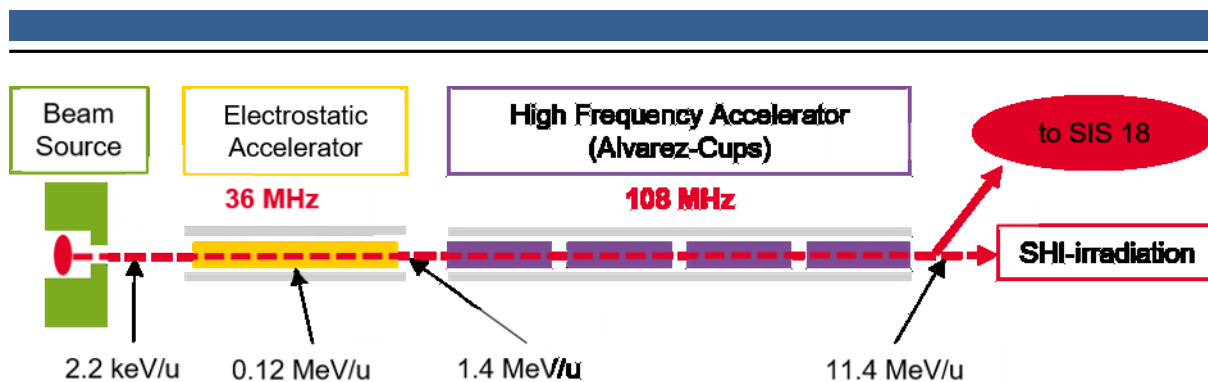


Figure 5: Schematic set-up of the universal linear accelerator (UNILAC) at Wixhausen, Darmstadt. Acceleration pathway is illustrated and divided in three parts: the ion beam source at the beginning (green). The exit-energy amounts to 2.2 keV/u. After the handling in the electrostatic deflector (yellow), the specific energy is increased to 1,4 MeV/u. An additional flight through the high frequency accelerator (purple) speeds up the ion energy to 11.4 MeV/u. (74) (adapted from Toimil-Molares *et al.* (79), copyright (2012) Beilstein-Institute.)

The polymeric foils (target material) are irradiated with swift heavy ions having a kinetic energy of 11.4 MeV per nucleon ( $\sim 15\%$  compared to the speed of light). The binding energy of esters fits with the energy transfer of the swift heavy ions to the polymer and causes a rupture of the bond between the carboxylic C-atom and the O-atom. In the next step, the latent tracks, which are now located within the bombarded substrate can be transformed into nanochannels/-pores using an alkaline etching method along the trajectory of the track, which will be described briefly in the next sections. (78) Throughout the entire thesis the term nanopores and -channels is used equivalently. To provide smoother and more precise pores, the irradiated foils were treated with soft UV-light in order to sensitize the surface of the substrate (see Figure 5). (74, 79)

The SHI-penetration of the polymeric target induces an energy loss of the projectile and transfers its kinetic energy into the substrate resulting the formation of a latent track along with the trajectory of the SHI (see Figure 6). (80)

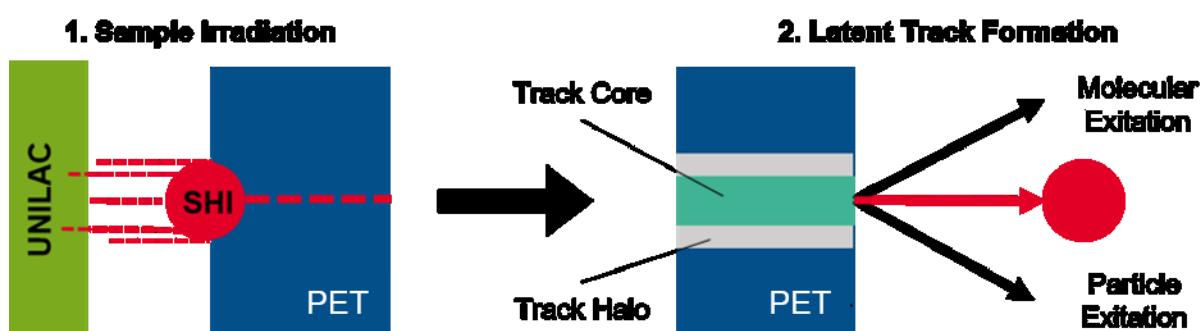


Figure 6: SHI-irradiation throughout the polymeric sample: First, the sample irradiation generates an energy loss and the kinetic energy of the SHI is transformed into an electrostatic and then a nuclear energy loss. Second, due to the energy transfer, covalent bonds inside the polymeric target are broken along the trajectory of the SHI-pathway. Hence, a latent track formation is observable, including the track core as well as the track halo region. In addition, the process of the SHI provides molecules, such as hydrogen, oxygen, carbon dioxide, as well as particle formation and excitation of neutrons, protons and electrons. (77, 80)

From the molecular point of view, the track formation is based on the rupture of the covalent bonds inside the polymer chains: Once the projectile ion passes the material, excited and ionized states inside the target are generated (energy loss). However, there are also elastic interactions between the accelerated ion and the target material atoms referred as nuclear energy loss. Moreover, free electrons as a part of the particle excitation are released inducing a subsequent

collision cascade of the surrounding material. The interaction of these electrons with the polymeric chains lead to the formation of radicals and, therefore, the homolysis of the molecular bonds occurs. Hence, oligomers as well as hydrogen atoms are generated leading to a decreased density of the track zone when comparing it with the untreated substrate. The track consists of a central track core region and a surrounding halo region. Typically, the track halo has a range of  $0.1 \mu\text{m}$  to  $1 \mu\text{m}$ , whereas the track core ranged of up to  $10 \text{ nm}$  relative to the original pathway of the SHI. Fragmented polymer chains are located inside the core region due to the induced radiolysis after the SHI-irradiation. The core region is primarily etched to generate pores within the polymeric substrate. The halo region is dominated by cross-linked polymer chains of the substrate induced by the radicals formed after the SHI-irradiation. It can be assumed, that the etching rate of the halo region is lower than the core etching rate. (70, 75)

From the theoretical point of view, the energy loss of the SHI-projectile is determined as  $dE/dx$  and is composed of the electronic energy loss  $(dE/dx)_{Elec.}$ , caused by the inelastic excitations inside the target sample, and the nuclear energy loss  $(dE/dx)_{Nuc.}$  promoted by the elastic collision of projectile ions and substrate. (81)

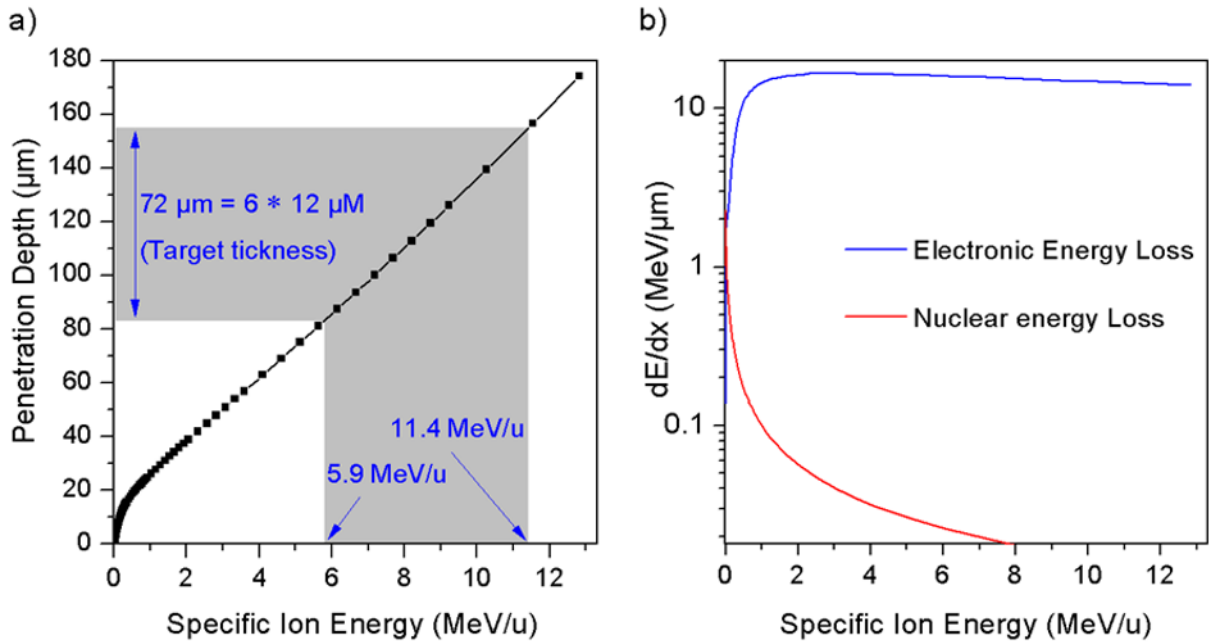


Figure 7: Penetration depth as a function of specific projectile energy and energy loss  $dE/dx$  in dependence on specific ion energy. Calculated by SRIM 2008. (87)

According to Figure 7, the nuclear energy loss is predominant at low energies ( $< 0.01 \text{ GeV}$ ). For higher values ( $> 2.6 \text{ MeV}$ ), most of the energy loss is caused by the electronic energy loss and the inelastic interactions (excitation and ionization) with the target material are creating damage trails inside the penetrated target.

The penetration depth  $R$  is equal to the projectile range and determined according to the equation below:

$$R = \int_0^{E_0} \left( \frac{dE}{dx} \right)^{-1} dE \quad (\text{Eq. 1})$$

Here, the energy loss can be calculated using the BETHE-BLOCH-equation (82):

$$\frac{dE}{dx} = 4\pi \frac{Z_{eff}^2 n_e e^4}{m_e c^2 \beta^2} \left( \ln \left( \frac{2m_e c^2 \beta^2}{I (1 - \beta^2)} \right) - \beta^2 \right) \quad (Eq. 2)$$

with:

$Z_{eff}$  = effective charge of the projectile ion

$n_e$  = electron density of target material:  $n_e = Z_t \cdot n_t$

$Z_t$  = atomic number of target atoms

$n_t$  = number density of target atoms

$m_e$  = free electron mass

$e$  = elementary charge

$\beta$  =  $v/c$ ;  $v$  is the velocity of the projectile;  $c$  is the value for the speed of light

$I$  = ionization energy

According to Eq. 2, the projectile interaction with the target is mainly influenced by the effective charge  $Z_{eff}$ . In turn,  $Z_{eff}$  can be calculated using the BERKA's-equation. (see Eq. 3):

$$Z_{eff} = Z_t \left( 1 - \exp \left( - \frac{130\beta}{Z_t^{\frac{2}{3}}} \right) \right) \quad (Eq. 3)$$

Here,  $Z_{eff}$  depends on the velocity of the accelerated ions. In sum, if both the energy and the effective charge of the accelerated ions is sufficiently high, a sufficient penetration of the target material can occur leading to a formation of the latent track. (77)

Once the beam is calibrated, the expose to longer irradiation times lead to even higher fluences inside the bombarded substrate. This results in an adjustable accelerated fluence inside the substrate, ranging from  $10^3$  to  $10^9$  ions per  $\text{cm}^2$ . Moreover, if the beam is defocused by the use of magnetic lanses, and reduced to a low frequency of only few ions per second a single-ion penetration of the polymeric foils can be achieved. For this purpose, an additional metal mask (copper plate), which contains one single hole with an opening of  $300 \mu\text{m}$ , is placed in front of the sample stack, to keep the contact area between sample and SHI as small as possible. Moreover, a detector is placed right behind the polymeric sample. After a SHI has passed the polymeric sample, the SHI reaches the detector area and the detector identifies this hit as a signal. Subsequently, the shutter stops the beam that is placed in between the beam and the polymeric foil. (83)

For a better overview, in this thesis the SHI-irradiated polymeric foils are classified in three different groups, depending on the track density per  $\text{cm}^2$  and the pore density, respectively (see Figure 8): i) single pore membranes; (ii) oligoporous membranes and (iii) multiporous membranes.

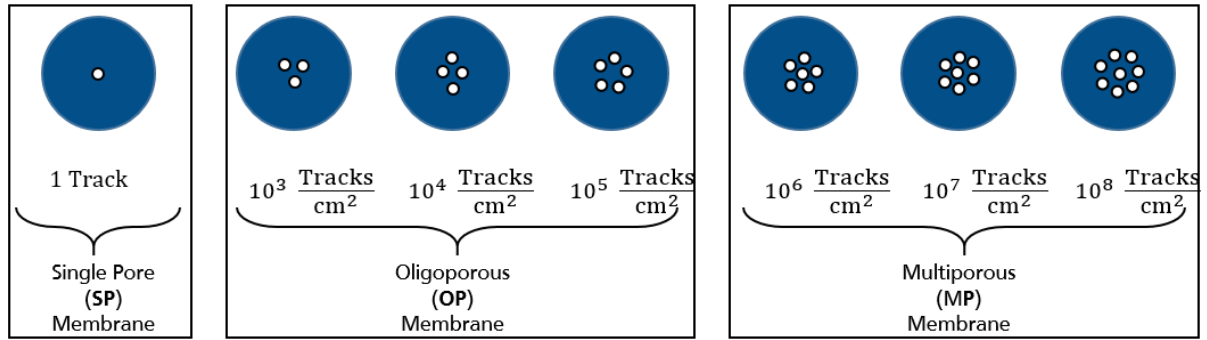


Figure 8: Scheme of various pore densities used in this thesis and fabricated by the UNILAC-accelerator. It can be assumed that every track is transformed into a pore. Consequently, the unit [pore/cm<sup>2</sup>] is used equally to the unit [tracks/cm<sup>2</sup>]. (83, 84)

After the SHI-irradiation, the latent ion tracks are transformed into nanopores having a certain geometry by the use of the track-etching technique, described in the next chapter.

### 2.1.2. Etching-Process

After the polymer irradiation, damage zones, i. e. the tracks, appear inside the polymeric substrate that are converted into pores upon immersing the bombarded polymer foil into an etching solution. (78) Prior to the alkaline treatment, the polymeric foils are sensitized with soft UV light (320 nm). (85) The aforementioned decrease of density after the SHI-irradiation is caused by the presence of oligomers after the homolysis of the polymer chains inside the core track zone. The less dense area provides a higher activity of the etchant is enhanced, where the access to the substrate is more suitable and a selective formation of pores can occur. The pathway of the etchant throughout the track per time increment, is described as the track etch rate  $v_t$ , whereas the etching rate of the substrate material is referred as the bulk etch rate  $v_b$  (see Figure 9).

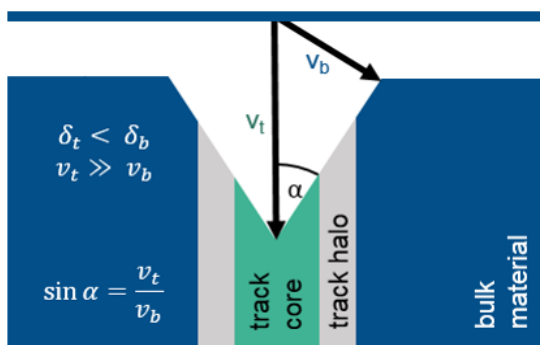


Figure 9: Scheme of the etching-profile and the calculation of the etching-rate of the track zone and the bulk region. (adapted from Toimil-Molares *et al.* (79), copyright (2012) Beilstein-Insitute).

The opening angle of the etching front  $\alpha$  is declared by the ratio of the track etch rate and the bulk rate and provides information about the symmetry of the etched nanopore: the smaller the value of  $\alpha$ , the more bulk and track etch rate are aligned, indicating a cylindrical pore geometry. Due to the higher reactivity of the etchant inside the track compared to the bulk material, the track etch rate is always higher than the bulk etch rate. (86) As a consequence, further adjustment of the track-etching rate provides various geometries of the resulting nanopore influenced by the etching time, the temperature as well as the used solvent. (87)

The diameter of the nanopore depends on the time in which the polymer film is in contact with the lye. The etching rate is adjustable throughout temperature treatment and etchant concentration, respectively. (88) For example, Nguyen *et al.* calculated an etching rate of 5.4 nm per minute for the case of PET-polymer foils having a thickness of 12  $\mu\text{m}$  by the use of

2M NaOH-solution at 50 °C. (89) Furthermore, the latent track can be sensitized with soft UV-light to enhance the track etch rate. Thus, the solubility is enlarged and the access of the etchant is facilitated. (85)

From the molecular point of view, the etching process is caused by an ester cleavage. The carboxylic group inside the polymeric chains are attacked by the hydroxide ions of the etchant that are acting as nucleophiles. In the next step, the unstable intermediate is rearranged and the former ester group splits into a resonance-stabilized carboxylate group and a free alcoholate group. Throughout an additional storage in pure water, the surface alcoholate and carboxylate groups become reprotonated (see Figure 10). (86)

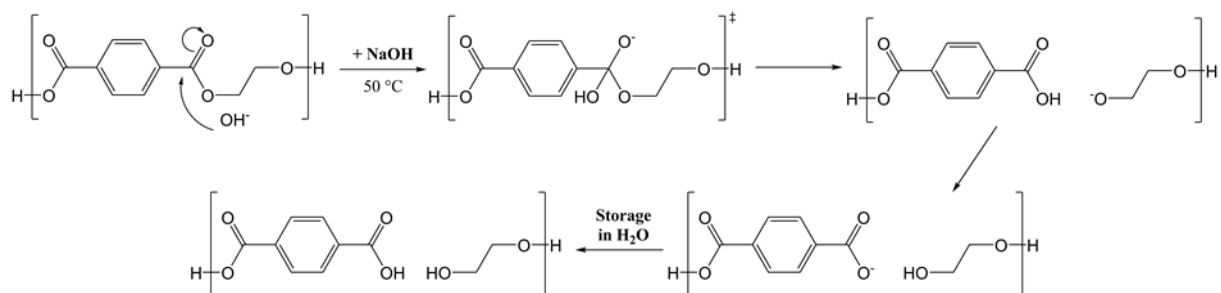


Figure 10: Underlying ester cleavage mechanism during the etching process. Adapted from Spohr *et al.* (90).

Moreover, various etching techniques were established during the last two decades creating different pore-shapes (see Figure 11) depending on whether the etchant has access to both sides (symmetrical etching) of the membrane or only from one side (asymmetrical etching). (91)

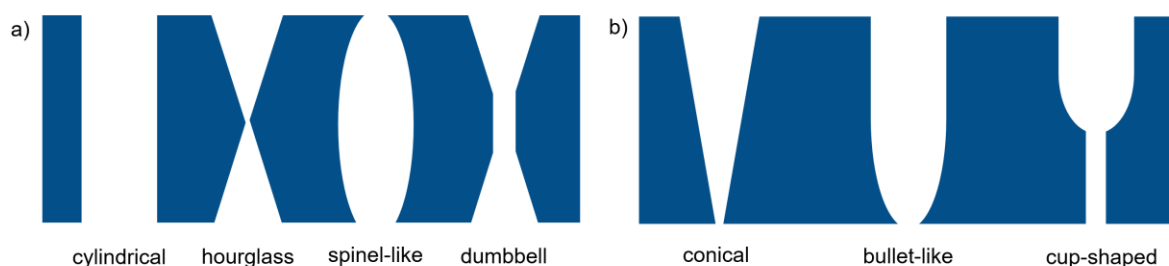


Figure 11: Illustration of symmetrical (a) and asymmetrical (b) shaped nanopores inside polymeric membranes.

Besides the aforementioned cylindrical shapes, spinel-shaped nanopores are generated throughout the addition surface-active reagents like sodium dodecylsulfate (SDS). Further, if the symmetrical etching is stopped right at that point, where both etching fronts are hitting each other, hourglass-formed nanopores are achievable. (92) Throughout asymmetrical etching setups conical pores are generated. Here, only one side of the polymeric foil is in contact with the etching bath, whereas the other side is protected from the lye. Bullet-like shaped pores are created if surfactants are added to the lye. (93) Furthermore, multistep procedures accompanied by the combination of two- and one-sided etching methods to expand the range of feasible pore shapes. (94, 95) Experimental background about the fabrication of nanopores and detailed insights into track-etched polymers are described in the following section.

### 2.1.3. Physical Properties of Charged Surfaces

Despite the formation of nanopores, the alkaline ester cleavage causes the generation of carboxylic groups across the entire nanopore membrane. Depending on the environment, these

moieties can provide surface charges due to their protonated or deprotonated state at certain pH-values (see Figure 12a).

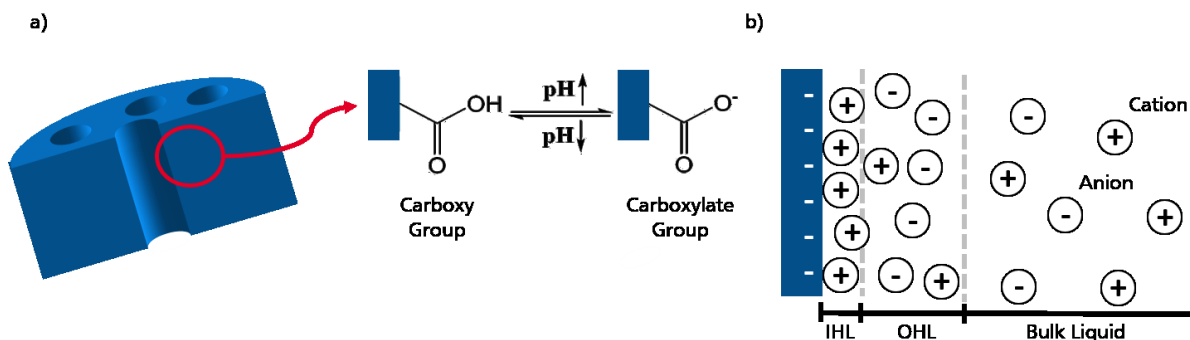


Figure 12: Schematic composition of the nanopore membrane surface. Here, the molecular surface groups created throughout the track-etching procedure are co-existing in a protonated neutral charged state and a negatively deprotonated stage. The  $pK_a$ -value amounts to 4.5 (a). (96) Formation of the EDL of the electrolyte onto charged surfaces. Rigid IHO = inner HELMHOLTZ-Layer; diffuse OHL= outer HELMHOLTZ-Layer (b).

The  $pK_a$ -value of general PET-Polymers is at a pH of 3.0. (97). However, due to the nanoconfined surrounding the  $pK_a$  of the carboxylic groups inside the nanopore region amounts to  $pK_a$  4.5. (96) Above the  $pK_s$  value, the carboxylic groups are deprotonated (carboxylic moieties) bearing a negative net charge. For  $pH < pK_a$  the carboxylic groups remain protonated and thus, the nanopore surface became uncharged.

The existing negatively charged moieties induce the generation of an electrical double layer, (EDL) when the nanopore foil is dipped into an electrolyte solution. Here, the cations are covering the nanopore surface due to the electrostatic attraction forces and the so-called inner Helmholtz-layer (IHL) is formed. To compete electrostatic imbalances, a further layer onto the IHL is formed by the anions of the electrolyte. This layer is denoted as outer Helmholtz-layer (OHL). The rigidity of the aligned IHL and OHL decreases with increasing distance from the nanopore surface until the arrangement of the ions coincide with that of the bulk liquid. (see Figure 12b). In sum, the pore surface in dependence of the pH surrounding is negatively charged or neutral.

Especially polymer-based substrates are particularly suited for the use as sensors: First, nanometer-precise adjustability and, second, the etching process exposing chemical groups on the surface allowing molecular attachment of receptors. Here, the ability of selective analyte recognition is evaluated throughout the record of ions passing the nanopore region. For this purpose, the as-prepared nanopore surface has to be decorated by receptor-moieties able to bind specifically to the respective analyte. The molecular surface functionalization is described in the following section. In this way, the nanopore membrane became sensitive towards analytes. Thus, the characterization of the modified membrane performance can be analysed by performing current-voltage measurements. (101) Here, the record of the analyte-dependant ion passage across the membrane is assessed and briefly described in section 2.2.

#### 2.1.4. Surface Modification

In the wide range of suitable materials, polymeric nanopore membranes stand out regarding their tremendous definability and geometric control over the dimensions, size and shape of the pore region. (102) However, the molecular introduction of receptor units onto the pore walls is suitable to implement sensing properties in presence of the respective analyte. (101, 103,

104) Regarding the surface modification, the formation of carboxylic groups over the entire pore surface (see Figure 10) provides the ability to incorporate new novel molecules with unique properties, which classifies track-etched membranes as ideal candidates for the development of membranes with tailored and tuneable functions. (13)

Here, the attachment of new functional groups is carried out using different approaches by the use of (i) the covalent functionalization (105–107), (ii) the click-chemistry (108–110), (iii) electrostatic interactions (111–113) and (iv) the metallic complexation (114–116), respectively (see Figure 13).

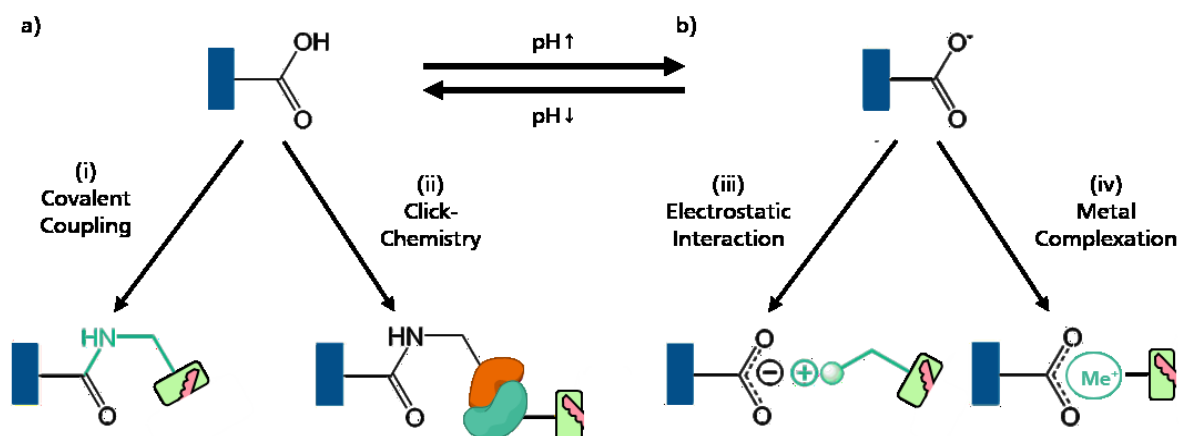


Figure 13: Scheme of possible surface modifications inside track-etched nanopore membranes based on the conversion of the surface (carboxylic) groups to introduce new functional properties (herein symbolized by the lock-compound): i) covalent coupling chemistry, ii) click-chemistry, iii) electrostatic interaction and iv) metal-surface complexation. Further, the modification using coupling chemistry (i) induces a new molecular bond between the lock-compound and the pore surface. Click-chemistry (ii) is illustrated using the reaction of two puzzle pieces inside the molecule. The electrostatic interaction (iii) is determined using common “plus and minus” symbols and the metal complex (iv) is expressed throughout a complexation between metal ion ( $\text{Me}^+$ ) and the surface group. (13, 42, 55, 117)

In case of covalent coupling functionalization, a new molecular bond between the carboxylic carbon and the attached molecule is formed (see Figure 13, i). Moreover, click-chemistry reactions (see Figure 13, ii) between the surface group and its counterpart, represented by the puzzle pieces inside the molecule, can be used to introduce new functionalities onto the nanopore surface. However, the Click-chemistry is referred as a special class of covalent coupling chemistry, as the reacting species show a outstanding affinity towards each other. Therefore, this reaction class is presented as an own method for surface functionalization. Electrostatic interactions (see Figure 13, iii) are determined as turquoise “plus and minus”-symbols) as well as complexations between metal ions (see Figure 13, (iv)). Based on this approaches, the surface of the nanopore is able to undergo selective interactions with analytes that were not possible before.

It should be mentioned that the modification of the nanopore primarily means, of course, the molecular conversion of the superficial carboxyl group (primary surface modification). However, with the carboxyl group, the full range of molecular transformations cannot be exploited. Therefore, further functionalization of the first modification stage has to be carried out (secondary surface modification). In this way, more selective and complex properties can be created throughout the nanopore modification leading to a maximum adaptability and specific applications. For this purpose, experimental aspects about the surface modification are given in CHAPTER II, whereas detailed insights regarding the (primary and secondary)

attachment of surface groups inside track-etched polymers are described in the respective introduction sections in CHAPTER III, i. e. the results and discussion part.

## 2.2. Sensing Concept

The qualitative and quantitative sensing of analytes through nanopores having either biological or solid-state nature is obtained using current-voltage ( $I/V$ ) measurements. Conductive changes, i. e. the signals, are detected in dependence on the presence of certain amounts of analyte, also referred as the dose, and are transferred to a signal-to-dose relation. (118) Here, the voltage-induced ions passing the nanopore region is analysed by an arrangement of electrodes connected to an Amperemeter/Voltage source (see Figure 14).

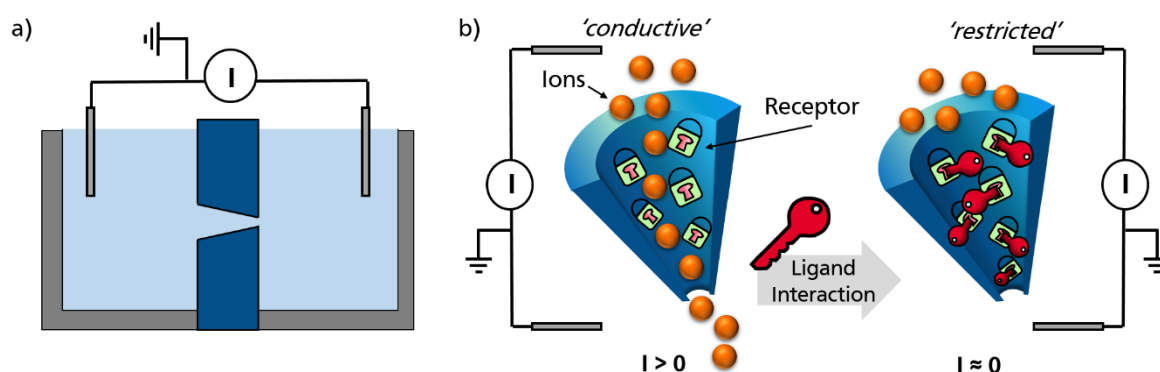


Figure 14: Characterisation of the nanopores throughout  $I/V$ -measurements. The setup consists of two measurement cells separated by the nanopore membrane and filled up with electrolyte solution. A pair of electrodes is inserted into the cells and an Amperemeter/Voltage source (not depicted) (a) Engineered sensing of solid-state nanopores based on a ligand-receptor interaction inside the pore region. Here, the inner surface of the nanopores is covered with receptor-units. In the presence of the respective ligand, the bionconjugation reaction occur causing a blockage of the pore region and leading to a restricted movement of ions.

The porous membrane is fixed in between two measurement cells that are filled with an electrolyte. Figure 14a illustrates the schematic setup of an  $I-V$  measurement. (119) Additional and more detailed setup information is provided in the experimental section in chapter 2. Besides the shape and charge influence of nanopores, the ionic flux can be manipulated and triggered in the presence of respective ligands (analytes). The sorption of analytes (the key) is provided by the molecular decoration of receptor moieties (the lock) onto the nanopore surface. Hence, this biomimetic approach (based on the key-and-lock principle) allows the introduction of sensory properties in a *hitherto* non-selective porous material accompanied by the beneficial intrinsic robustness of the used substrate (see Figure 2b and Figure 14b).

According to the biological model, the analyte recognition is promoted throughout the immobilization of receptor units onto the nanopore surface. The signal-readout of the sensing performance is provided by the comparison of the resulting  $I-V$  curves before and after the addition of the respective analyte (see Figure 15). (42)

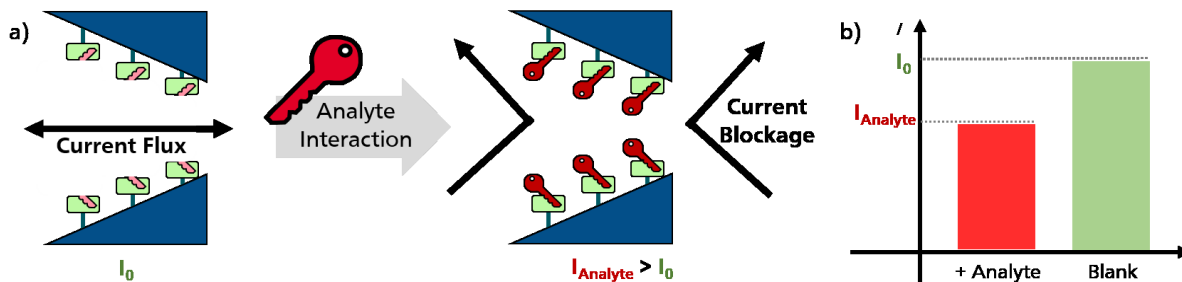


Figure 15: Cross-section of a conical shaped nanopore covered by receptor-units across the entire nanopore surface with and without the analyte interaction (a) and their respective current output (b). In absence of the analyte (blank state), the current flow is unimpeded across the pore region (green bar). In contrast, the presence of the respective analyte (red key), the formation of the analyte-receptor conjugate occurs and leads to a blockage of the transmembrane current (red bar).

Thus, highly specific analyte-receptor conjugation induces more sensitive, selective and stable sensing properties.

### 2.2.1. Electrostatic and Electrodynamic Insights

During *IV*-measurement the transmembrane current is affected by the nanopore shape. For instance, if the used membrane contains only cylindrical nanopores, an applied triangular voltage leads to a measured current originated by the equal flow of anions and cations across the membrane. The resulting OHMIC behaviour is symbolized by a characteristic linear *IV*-curve (see Figure 16).

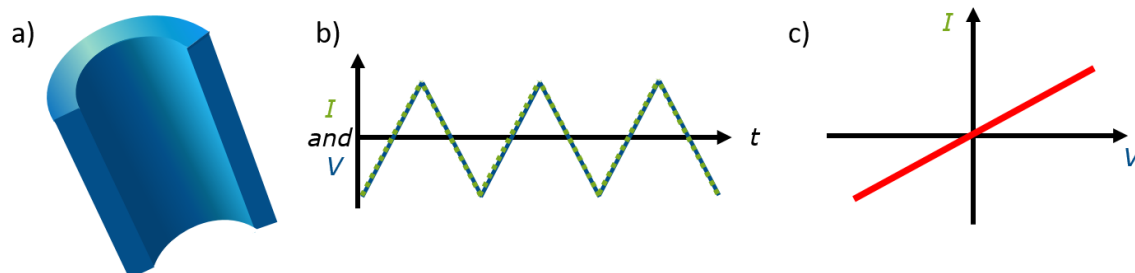


Figure 16: The cylindrical pore profile is presented (a) and the underlying current record versus time (green dotted line) caused by the applied triangular voltage versus time (blue line) (b). The plot of the measured current trace against the applied voltage course results in the current-voltage curve (red curve) (c), which explicitly has a linear course and is denoted as OHMIC behaviour.

However, for the case of conical pores whose tip side is made of a tiny opening of only a few nanometres, the transmembrane current flow deviates from its linear behaviour during an *IV*-measurement (see Figure 17).

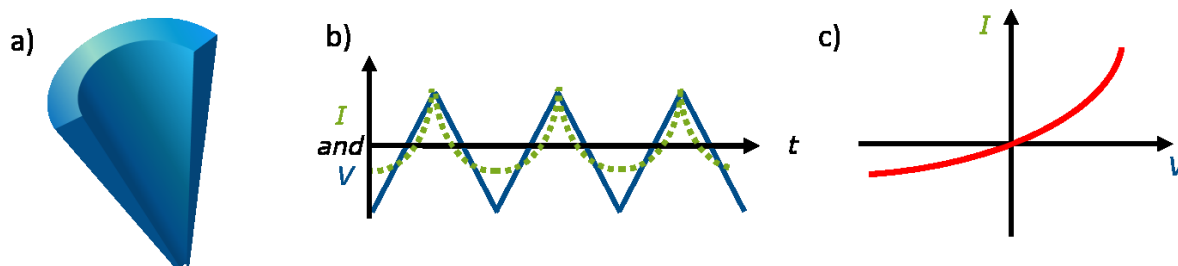


Figure 17: The conical pore profile is presented (a) and the underlying current record versus time (green dotted line) caused by the applied triangular voltage versus time (blue line) (b). The plot of the measured current trace against the applied voltage course results in the current-voltage curve (red curve).

Since the tip opening of a conical nanopore is so small but negatively charged due to surface  $\text{COO}^-$ -groups, the anion passage is hindered near to the narrow tip region for positive bias. (120) By performing an  $IV$ -measurement, the ion conductance of the nanopores depends strongly on the formation of the negatively charged nanopore surface generated after the immersion of the charged nanopore surface into electrolyte solutions (see Figure 18).

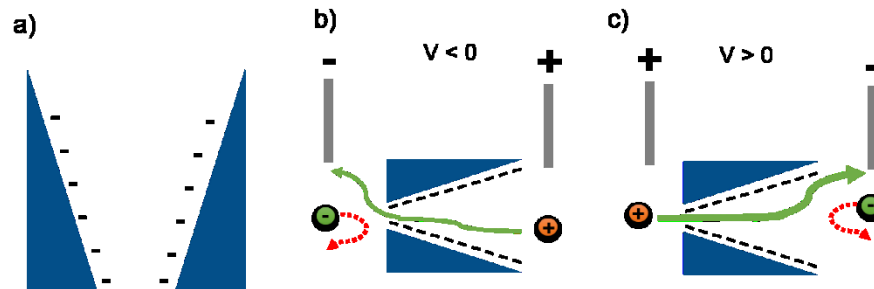


Figure 18: Negatively charged nanopore surface after the immersion of the conical nanopore membrane into the electrolyte (a). For the case of negative bias, the recorded current is mainly caused by the anion movement towards the anode (b). For the case of positive bias, the recorded current is induced by the enlarged cationic movement across the membrane (c).

Here, for the case of positive voltages the measured current is mainly promoted by cationic migration, whereas anionic movements through the nanopores are blocked due to the negatively charged surface (anion discrimination). Consequently, the membrane behaves like a diode and the resulting  $IV$ -curve shows a so-called rectification behaviour.

In cylindrical shaped nanopores, the pore surface is negatively charged as well (see Figure 19a). However, due to the large diameter of the pore, no ion discrimination occurs. As a result, a linear shaped  $IV$ -curve is measured (see Figure 16c). Here, the transmembrane current is caused by the equal movement of cations and anions, regardless to the net charge of the applied potential (see Figure 19).

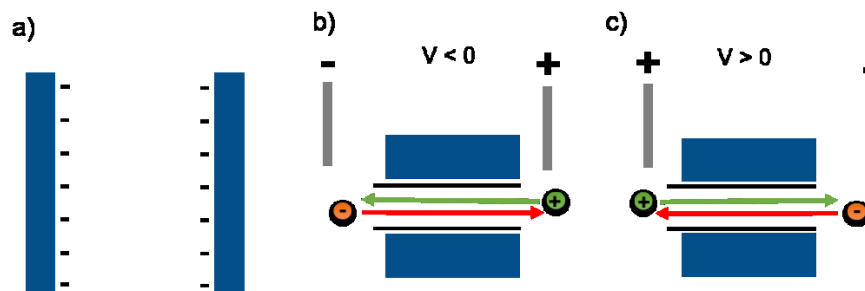


Figure 19: Negatively charged nanopore surface upon immersion of the cylindrical nanopore membrane into electrolyte (a). For the case of negative and positive bias, the current flux remains the same leading to a linear shaped  $IV$ -curve. Here, no discrimination in the movement of cations and anions take place (b; c).

Nevertheless, conical-shaped nanopores can show OHMIC behaviour and provide linear  $IV$ -curves, too. In fact, if the surface carboxylic groups are protonated, i. e. in acidic surroundings, then the surface charge is neutral. Thus, no ion discrimination occurs, and the resulting  $IV$ -curve is linear (see Figure 20).

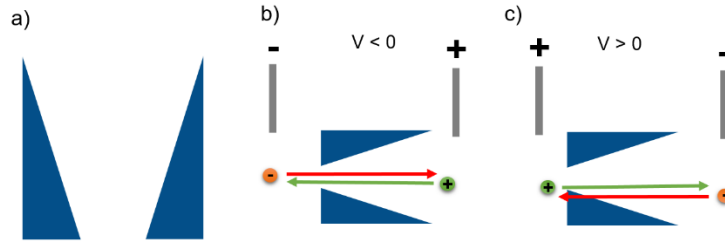


Figure 20: In acidic surroundings, the carboxylic groups located on the pore surface are protonated and, therefore, the nanopore surface remained uncharged, after the immersion of the nanopore membrane into the electrolyte occurs (a). For the case of negative and positive bias, the current flux remains the same leading to a linear shaped  $I/V$ -curve. Here, no discrimination of cations and anions take place (b; c).

The  $I/V$ -measurements are used to indicate a successful modification of the nanopore surface. For example, the attachment of ethylene diamine (EDA), whether covalent or electrostatic, alters the surface chemistry. In alkaline pH-ranges, the amine groups are protonated and therefore, the surface becomes positively charged. Thus, the course of the  $I/V$ -curve is exactly the opposite compared to a negatively charged surface and causes a current flow promoted by a facilitated anion flow (cation discrimination) due to the positively charged overlapped EDL (see Figure 21). (121, 122)

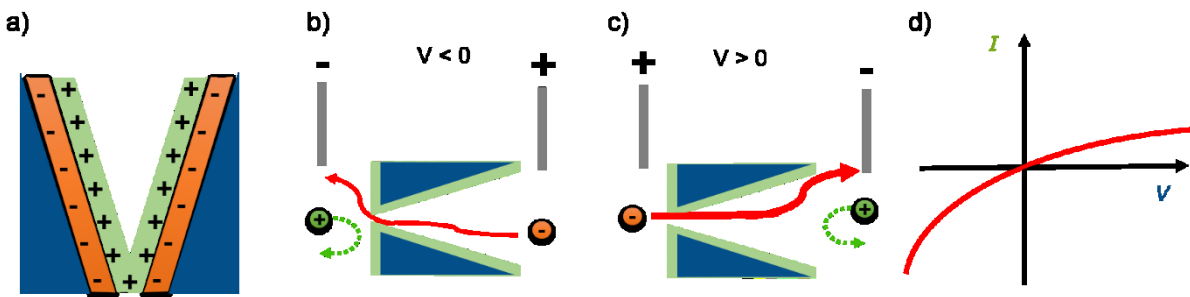


Figure 21: Positively charged nanopore surface upon immersion of the conical nanopore membrane into electrolyte. Here, the nanopore surface is already modified with positively charged moieties causing an inverted EDL-arrangement compared to the EDL formed onto negatively charged surfaces (a). For the case of negative bias, the recorded current is mainly caused by the anion movement towards the cathode (b). For the case of positive bias, the recorded current is promoted by the enlarged movement of anions across the membrane (c).

An indicator for the degree of rectification is given by the rectification factor  $\alpha$ . (123) According to Eq. 18,  $\alpha$  is defined as the relative ratio the maximum (for +1 V) and of the minimum (for -1 V) current:

$$\alpha = f_{rec.} = \frac{|I_{+1V}|}{|I_{-1V}|} \quad (Eq. 18)$$

For  $\alpha > 1$ , anion-discrimination is detected, whereas for  $\alpha < 1$ , cation-discrimination is observed.

### 2.2.2. Sorption-promoted Analyte Detection

Depending on the surface-attached receptors, there are two different approaches to detect the analyte: (i) the direct or *labelled detection* and (ii) the indirect or *label-free detection*. Regarding the signal output, i. e. the conductance, both methods differ in the analyte-receptor interaction causing either a loss or a gain of conductance. (41)

## Labelled Analyte Detection

For the case of a labelled detection, the analyte is adsorbed directly onto the receptor-terminated nanopore wall throughout a selective bioconjugation reaction (see Figure 22). The as-prepared nanopore surface is chemically modified with receptor-moieties to create sensing properties into the membrane. In the next step, the testing solution is added containing the respective analyte. Throughout the formation of a stable analyte-receptor complex, the diameter of the nanopore is decreased. The successful formation of the complex leads to a decreased current during *IV*-measurements.

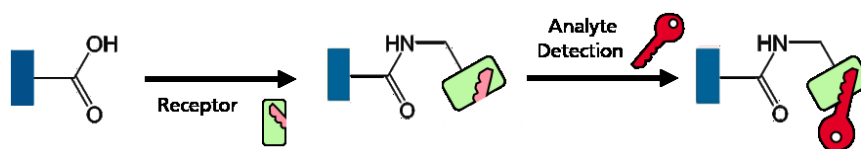


Figure 22: Scheme of labelled analyte detection. Here, the analyte is interacting directly with the receptor-modified pore.

Here, a sufficient interaction between analyte and receptor leads to a decreased diameter of the pore, and, thus, a lower conductance is detected. (55, 101)

## Label-free Analyte Detection

In the opposite way, the nanopore wall is covered with precursor groups able to interact significantly with the receptor-agent by forming a preliminary complex (see Figure 23).

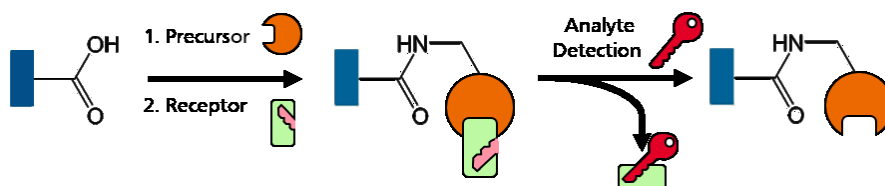


Figure 23: Scheme of label-free analyte detection. Here, the analyte is interacting directly with the receptor, which is attached in a preliminary complex to the pore surface having higher affinity to the respective analyte than to the precursor-moiety.

In the presence of the respective analyte, a more stable analyte-receptor complex is generated and released into the electrolyte solution accompanied by simultaneous recover of the precursor groups. Throughout the formation of a stable analyte-receptor complex accompanied by the regeneration of precursor-moieties onto the nanopore wall, the diameter of the nanopore is now increased. Regarding the *IV*-measurement, the conductance is enhanced due to the loss of the preliminary complex. The remaining precursor-terminated surface provides a higher conductance than an intact surface pervaded by precursor-receptor complexes (see Figure 23). These detection methods require highly efficient complex formation between the analyte-ligand interaction being constantly higher than the one of the ligand-precursor-complex. (64, 132)

In addition, the interaction of analytes onto the nanopore wall can promote changes of net charge inside the nanopore region as well. For example, if the analyte is negatively charged and the surface charge is neutral, the adsorption of the analyte could provides an enhanced conductance. Since the ion flux across charged membrane is more facilitated compared to an uncharged one.

---

In turn, the adsorption of an analyte onto charged receptor-modified membranes could cause charge compensation, if the analyte and receptor-moieties are oppositely charged. Thus, the net current flux is limited because of two effects. First, the physical adsorption of an analyte according to Figure 22, and the charge compensation causing a further reduction of the measured transmembrane current.

In fact, the resulting current is composed of all the internal phenomena happening during the *IV*-measurement. The impact of analyte sorption onto the walls can cause changes in the effective nanopore diameter and affecting concurrently the nanopore net charge, as well. In the nanoconfined transmembrane area, both surface charges and the sorption of analytes highly affects the conductivity of the nanopore and, the interpretation of the analysis during sensing experiments. This underlines the complexity of the ionic flux across the nanopore membrane and offers the potential to evaluate analyte-receptor-interactions qualitatively and quantitatively. Therefore, *IV*-measurements have become a powerful and essential method for the characterization and sensing performances of analytical (including medical) devices.

---

### 3. Road to Medical Devices

---

In 2015, the United Nations (UN) declared the “17 sustainable development goals (SDG)” that summarizes the aim of the current generation without affecting the future generations in terms of economy, technology and science to be reached until 2030. One of these SDG is to ensure a good “health care and well-being” for every human being. (133)

To accomplish this goal, medical tests are essential to detect, diagnose and monitor either the disease or the health level. These tests differ depending on whether the analysis is carried out inside (*in-vivo*) or outside (*in-vitro*) of the human body. (134) Common *in-vivo* diagnostics include imaging procedures throughout X-ray (135), magnetic resonance (136) and sonographic methods. (137) However, many malfunctions originate from misdirected metabolic and molecular processes. Therefore, testing of human tissues, blood, plasma, serum and urine, offers a huge potential for the detection of biomolecules, i. e. DNA, RNA and proteins, or bioentities, like cancer cells, bacteria or viruses analysed throughout *in-vitro* diagnostic methods (IVD). (138) Depending on the detection pathway, the diagnostic procedures is separated in immune, chemical and molecular diagnostics. (139) The main part corresponds to the immune diagnostics. Here, the “Enzyme-linked Immunosorbent Assay” (ELISA) is the most frequent method used to detect a bright spectra of analytes, like proteins (140), antibodies (141), viruses (142) and low molecular species like hormones (143), toxins (144) and biocides (145). Based on the specific antigen-antibody interaction (immune complex), the biomarker inside the testing sample is interacting with its respective antigen. The readout is based on a successful formed complex that promotes a luminescent reaction and dependant on the concentration of the biomarker. (141)

#### 3.1. Biosensors

*Biosensors* have been established to detect and analyse specific substances inside human body fluids. According to the International Union of Pure and Applied Chemistry (IUPAC), biosensors belong to a subcategory of chemical sensors defined as “*devices able to transform chemical information into an analytically useful signal*”. (146) Here, the chemical information ranges from the concentration value of a specific component to an entire analysis of the testing medium. In dependence of the origin of the analysed information, sensors are separated into two classes: (i) physical and (ii) chemical sensors. For the case of physical sensors, no reactions takes place. Here, only physical changes are measured, like temperature, conductivity, absorbance or the refractive index. For the case of chemical sensors, chemical reaction affect the signal output. Regarding the class of “*Biosensors*”, reactions correspond to a biochemical process, such as bioconjugation processes between receptors and specific ligands. (147, 148) For instance, the *immunosensors* like ELISA are referred as biosensors as their initial recognition reaction of the analytes (here: the antibodies) is caused by the formation of the immune complex.

Sensors are typically made of a *receptor* and a *transducer* compound. The sensing information is transformed into an (electrical) signal analysed by the *transducer* (see Figure 24). (149)

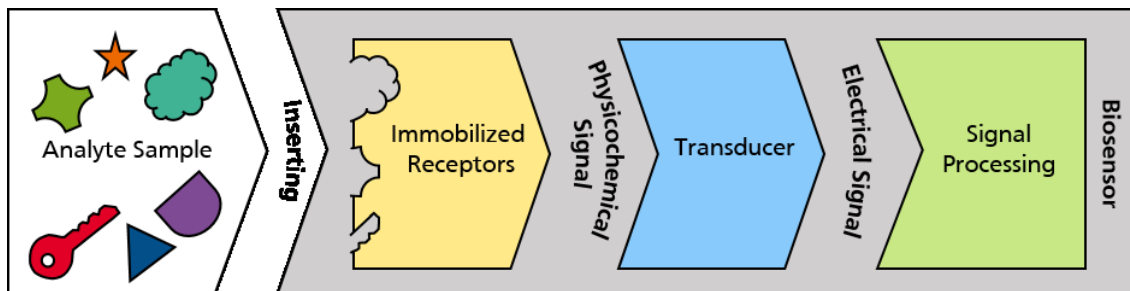


Figure 24: Sensing concept of a Biosensor: The analyte sample contains a mixture of various Bioligands. After the analyte sample is added to the biosensor, physicochemical signal is generated and transformed into an electrical signal throughout the Transducer. Then, the electrical signal is analysed throughout a data processor (computer). Adapted from (149).

After the testing sample is inserted into the biosensor, the respective analytes are recognized, due to the formation of a ligand-receptor-interaction. The formed molecular pair is inducing a physicochemical signal, e. g. enhanced surface charge of the substrate surface. This change is now transformed by the transducer into an electrical signal, e. g. conductance change. In the next step, the relation between signal change and concentration of the respective analyte is examined throughout signal processing (computer). (150) Mostly, there is no clear line between a physical or chemical sensor. In this thesis, receptors were immobilized onto a nanopore membrane. The recognition reaction is mainly promoted throughout bioconjugation reactions. In turn, these reactions are causing resistance changes during a current-voltage measurement. In this case, the signal transducer is represented by a pair of electrodes and the whole setup is referred as a conductimetric biosensor. (149) Throughout the design of biosensing devices, there are some challenges to overcome to obtain precise analysis of the respective testing fluid. The efficiency of a sensor is based on the following criteria (146, 150):

- Sensitivity
- Selectivity
- Stability

Here, sensitivity determines the defined relation between the signal and the analyte concentration similar to classical dose-response curve visualized by a semi-logarithmic sigmoidal fit. Now, the selective analysis is ideal, for the case, that analyte B provides no signal response, but analyte A causes sigmoidal signal-concentration relation. (Figure 25). (151)

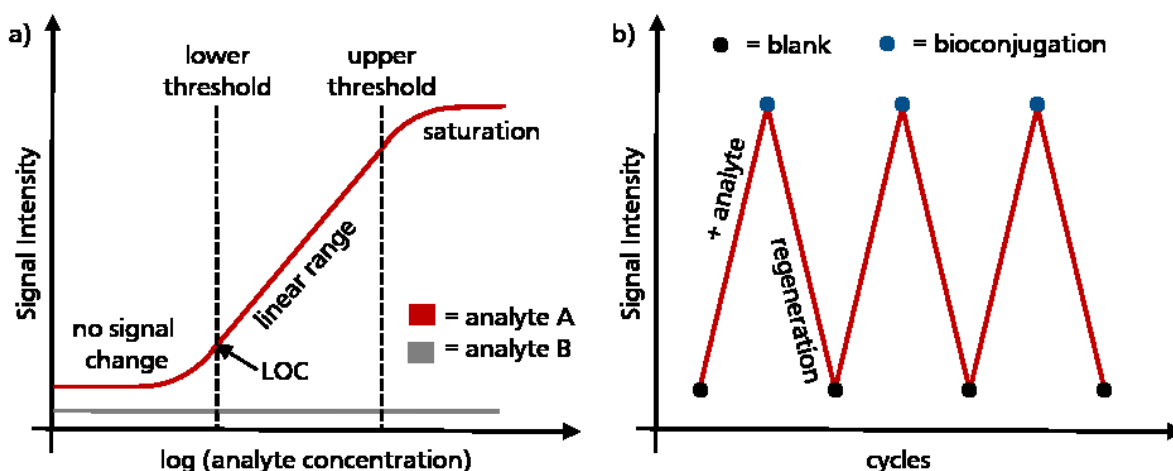


Figure 25: The parameters that characterises a precise biosensor is illustrated: sensitivity and selectivity (a) and the stability (b). (Graphical adaption of (150)).

---

In detail, the sigmoidal course is divided into three parts. At the beginning and for small amounts of analyte, there is an insufficient signal response. Then, at the lowest threshold, the slope of the graph increases generating a linear rise with respect to the higher analyte concentration. After passing the upper threshold area, saturation occurs and a further signal increase is not detectable. In addition, the limit of detection (LOC) is obtainable through the sigmoidal fit, since it is the lowest concentration, where the analyte amount is resolvable. Regarding the stability, a precise sensor should have as little deviation as possible, as long as the analysis is carried out multiple times. If the analyte is in contact with the sensor, the signal should change by a certain amount (see Figure 25b). The sensor can be regenerated by flushing the sensor with the respective solvent to remove the analyte, the input signal should have the same value like prior to the analyte measurement. Now, these signal stability is just obtainable, if the bioconjugation reaction is reversible. Here, the reversible analyte recognition provides the ability to calibrate the system, before a blind sample can be tested. For the development of a nanopore-based sensor, this criteria is crucial although it is a special one. (152)

Therefore, such constructed biosensors are able to detect even small amounts of analytes making them a powerful tool for the early diagnosis of diseases.

### **3.2. *In-vitro* diagnostic and Point-of-Care-Testing (POCT)**

Now, the development of new diagnostics and improving of established ones is crucial for medical care. The sooner a disease is detected, the sooner the appropriate therapy can be started and, thus, maximized chances of healing are achievable. Here, industrial trends manifested on inventions including features like automated and digitalized health care that provides a personalized medical monitoring and treatment. (139)

In 2017, the in-vitro diagnostic (IVD) division within the medical device industry has become the segment with the highest turnover (see Figure 26). With an estimated sales value of approx. \$ 80 billion, the IVD division will continue to be the major contributor to the medical technology industry. With a growth forecast of more than 30%, it will continue to contribute the leading share of sales in medical technology industry in the future. Overall, this underlines the economic benefit of a growing IVD-technology. (153) Thus, personalized medicine, diagnostics and therapy has become the main impulse in the development of new medical devices. (154)

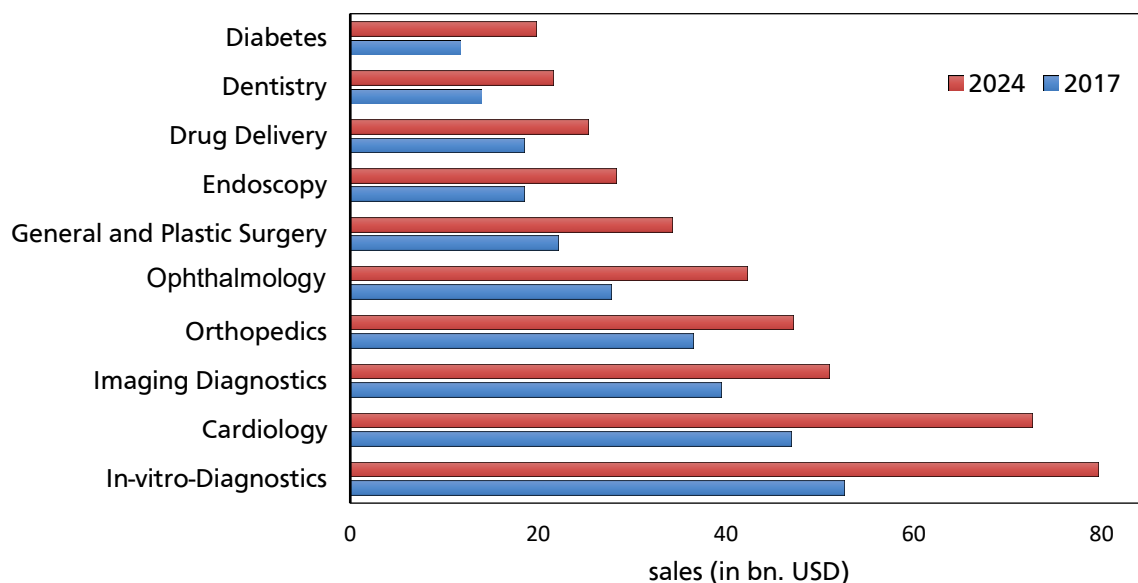


Figure 26: Top 15 of the top-selling segments of the global medical technology industry in 2017 (blue bars) and forecast for the year 2024 (red bars) in billions of US dollars. (graphical application according to the data of survey "EvaluateMedTech - World Preview 2018, Outlook to 2024" adapted from Statista® on 10<sup>th</sup> December 2019).

The individualized medical care is determined as "point of care testing" (POCT) and sets guidelines on medical devices and systems, like: (155)

- easy-to-use
- easy-to-understand
- low-cost
- quick-response
- at the point of need

In sum, the clinical diagnosis is carried out on site without the actual presence of a physician accompanied by a minimized *turnaround time* (TAT). (156) In this case, testing results were analysed and available within a few minutes after the testing volume was added to the device. Hence, the subsequent start of medical treatment is obtained. Moreover, POCT-devices enables more time spend on the analyses of the clinical results, whereas transport and preparation of testing samples is omitted. (154) Common POCT-devices are for example pregnancy tests or glucometers. Both examples are part of lateral flow assays. Here, the test strip is made paper- or cellulose-based. The testing medium is transported throughout capillary forces into the device. The wetted area is covered by labelled biomarkers, in most cases antibodies or aptamers. In presence of the respective ligand inside the testing medium, the immune complex is generated and, the signal is visualized by a colour change of the test strip. (157) Collectively, lateral flow tests provide all qualitative information about the appropriate diagnosis, although there are some approaches to realize a quantitative analysis, with the help of the cell phone camera. Here, the intensity of the colour change could be analysed and transformed into a concentration value. (155, 158–160)

### 3.3. Lab-on-a-Chip (LOC) and Micro-Total-Analysis System ( $\mu$ TAS)

Nowadays, so-called *Lab-on-a-Chip* (LOC) systems provide incentives for the development of new IVD-devices to expand the quantitative analysis in the frame of the POCT-systems. (161) Here, LOC are seen as a downscaled laboratory, where the sample analysis is carried out

---

immediately on the chip. They are embedded within a *microelectromechanical system* (MEMS), where the device is made of microfluidic channels, valves and pumps. To simplify operations and handling, the LOC-system is always incorporated into an automated device carrying the entire processing of the measurement. On one hand, LOC-systems can be integrated as subsets of laboratory assays baring functions, like miniature gas chromatography or electrophoresis. But on the other hand, they can also act as stand-alone devices, like the blood sugar tests, or for the determination of blood coagulation factors. These analyses are carried out within few minutes to seconds, but there are always one-time measurements. Current developments in the LOC-segment are geared towards multiple measurements. With minimized timeframes, the over-all monitoring of health status is achievable. (162–165) A special case of microfluidic LOC-devices are the “micro total analysis systems”, so-called  $\mu$ TAS-assays, replacing entire analysing processes that are usual provided by an external laboratories. (166, 167) Regarding the final application, a nanopore membrane pervaded by receptor-units is embedded in a biosensing device able to specifically, i. e. sensitively and selectively, measure even small amounts of the respective ligands. Hence, the biosensor is miniaturized in a Lab-on-Chip setup to achieve an on-site monitoring of disease level and health status, respectively.

---

---

## CHAPTER II: EXPERIMENTAL

---

The biomimetic approach and application of solid-state nanopores obtained great interest in the scientific society, where one of the most important substrates are polymeric membranes pervaded by damaged zones generated throughout the ion track technology. (47, 55) In this thesis, the transformation of these ion tracks into nanopores through chemical etching is presented. As a result, chemical moieties, i. e. carboxyl groups, were generated by means of the alkaline treatment. (42) By modifying the pore surface, the chemical surface nature and, therefore, the pore net charge is changed and offers the opportunity for incorporation of recognition units on to the pores surface. This surface tailoring enables nanopores to serve as devices for the qualitative and quantitative detection of (bio) molecules. (45) Finally, the obtained nanopores were characterized and their biosensing potential was monitored by using various optical and physicochemical methods. (168)

---

### 1. Fabrication of Polymeric Nanopores

---

Nanopore membranes used in this thesis were either provided by the GSI-HELMHOLTZ Centre for Heavy Ion Research in Darmstadt or commercially available membranes purchased by *it4ip* – *ion track technology* from Louvain-la-Neuve in Belgium.

For a better overview, all track-etched nanopore membranes used in this thesis are listed in the table below.

Table 2: list of the used nanopore membranes including they thickness and track fluences.

Site	SHI	Material	Thickness	Ion fluence	
GSI	Au <sup>25+</sup>	Poly(ethylene terephthalate)/ <i>PET</i>	12 $\mu\text{m}$	1	track/foil
				10 <sup>3</sup>	tracks/cm <sup>2</sup>
				10 <sup>4</sup>	tracks/cm <sup>2</sup>
				10 <sup>7</sup>	tracks/cm <sup>2</sup>
		Poly(lactic acid)/ <i>PLA</i>	50 $\mu\text{m}$	1	track/foil
				10 <sup>3</sup>	tracks/cm <sup>2</sup>
10 <sup>6</sup>	tracks/cm <sup>2</sup>				
it4ip	Ar <sup>9+</sup>	<i>PET</i>	12 $\mu\text{m}$	10 <sup>4</sup>	tracks/cm <sup>2</sup>
				10 <sup>7</sup>	tracks/cm <sup>2</sup>

PET-foils (Hostaphan RN12® by Hoechst-Company, Germany) with a thickness of 12  $\mu\text{m}$  and PLA-foils (Gs PLA® by Mitsubishi Chemical Corp., Japan) with a thickness of 50  $\mu\text{m}$  were used as a substrate. The generation of nanopores throughout the polymeric foil is carried out by a two-step process already introduced in section 2.1 (CHAPTER I). The track-formation was carried out by bombarding the polymeric foils with swift heavy ions at the UNILAC in the GSI-Helmholtz-centre (Darmstadt, Wixhausen). The irradiations took place during beam times in June 2016, May 2018, March 2019 and were kindly provided by Prof. Dr. Christina Trautmann and Dr. Eugenia Toimil-Molares (RG Trautmann, GSI). After irradiation, the foils were stored

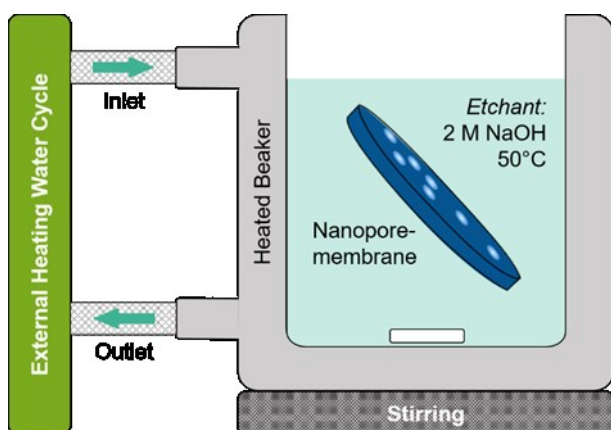
---

several weeks to months until the internal nuclear activity was no longer detectable. Regarding the commercially available PET- and PLA-Foils, membranes having a thickness of 12  $\mu\text{m}$  and an accelerated fluence of  $10^4$  and  $10^7$  tracks/ $\text{cm}^2$  were purchased by *it4ip* – ion track technology, respectively.

The transformation of tracks into pores was carried out by exposing the polymeric foil pervaded by latent-tracks into alkaline solution. The shape control is provided by using different techniques to generate either cylindrical or conical pore geometries. In this thesis only cylindrical and conical shaped were fabricated and modified with specific recognition units to evaluate the sensing ability towards specific analytes. In addition, *it4ip*-membranes were purchased having already nanopores of 100 nm diameter. Moreover, an exposure to UV-light (Vilber Lourmat GmbH; VL-230.E, Lamp: T-30.M, 312 nm) for one hour per side induces photo-oxidation processes inside the tracks generating more polar groups on the broken chain ends.

### 1.1. Symmetrical Etching

Upon immersing the irradiated polymeric foil into an etching bath, symmetrical pore formation occur from both sides and provides cylindrically shaped nanopores. For this purpose, the foils were suspended in a heated beaker that is connected to an external water cycle and filled with the etching solution (see Figure 27). (89)



For the case of PET-membranes, the etching process is performed in a 2 M NaOH-solution at 50 °C for a fixed period of time having an etching rate of 5.4 nm/min reported by Nguyen *et al.*(89) Afterwards, the foil is removed from the etching bath and washed numerous times with pure water. Then, the etched membranes are stored in fresh distilled water overnight to dispose the residues of alkaline solution inside the pores.

Figure 27: Set-up for the symmetrical etching of nanopores to establish cylindrically shaped nanopore within the polymeric membrane.

### 1.2. Asymmetrical Etching

Because the ongoing etching process is mainly dominated by a conical progress, a one-sided etching of irradiated polymeric foils leads to conical nanopores. (74) The asymmetrical etching was performed in a custom-made conductivity cell (see Figure 28). The following protocol is based on the pioneering work of Apel *et al.* (169) and Siwy *et al.* (170, 171)

The irradiated PET-foil is mounted between the two half-chambers filled with the etchant (9 M NaOH-solution) and a stopping-solution (1 M KCl and 1 M formic acid) (see Figure 28). Note that for the fabrication of conical nanopores it is used to etch a foil with multiple ion tracks and one with a single ion track simultaneously. The etching was carried out at 30 °C and monitored by applying a transmembrane potential (of -1 V) between the etching chamber and the stopping chamber of the single-track foil.

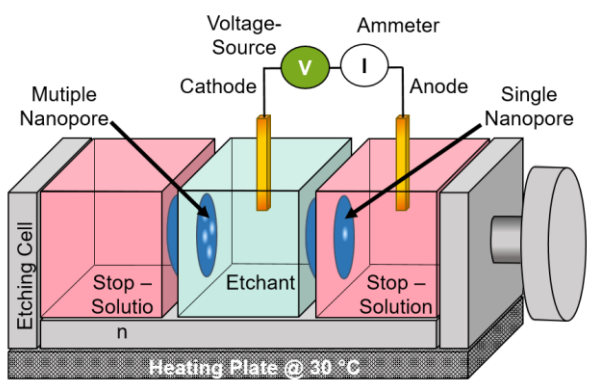


Figure 28: Asymmetrical etching set-up. For conical etching, single pore membranes and multipore membranes are treated simultaneously with the etchant and the identical etching conditions.

As soon as the etchant breaks through the pore, a transmembrane current is measurable. After the break-through current is reached, the etching process is still ongoing leading to a widened cone angle. To counteract the persistent etching, the formic acid neutralizes entering lye and the negative applied voltage helps to keep the hydroxide ions of the etchant away from the pore tip region. In this way, the pore tip is kept as small as possible. The etching is aborted as after a certain current value ( $\sim 1$  nA) is reached. Then, the etching and stopping solution are removed and the foil is washed numerous times with pure water and stored overnight in water.

## 2. Functionalization of Nanopore Surface

After etching, the surface of the as-prepared nanopore membrane is terminated with carboxyl-groups that can be functionalized with certain ligands. In this way, sensing properties can be introduced to the former non-selective nanopore membrane. For this purpose, the nanopore membrane is fixed into the two-chambered measurement cell, already introduced in section 2.2 (CHAPTER I).

The two-chamber setup of the same conductivity cell as displayed above is illustrated in Figure 29 and acts as both an aperture to functionalize the nanopore surface as well as a vessel for the measurement of transmembrane current to track the modification process. In order to evaluate the sensor performance of the nanopore membrane, the transmembrane area must be characterised by *IV*-measurements before and after the modification as well as before and after the contact with the respective analyte. The half-cells vary in their volumes (3.5 mL, 0.65 mL and 0.15 mL) and side openings with diameters ranging from 28 mm, 8 mm, and 3.5 mm facing the pore membrane.

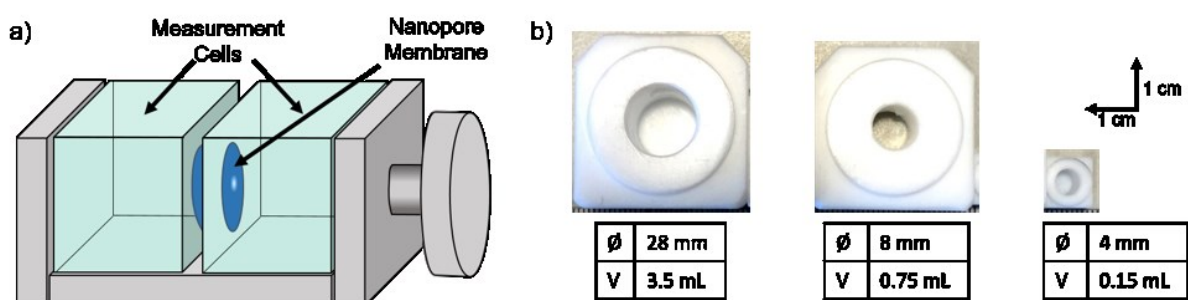


Figure 29: Scheme of the two-chamber setup filled with modification solution or electrolyte. (a); Picture and geometrical parameters of the half-cells used (b).

The chronological process to evaluate sufficient pore modifications is presented in Figure 30.

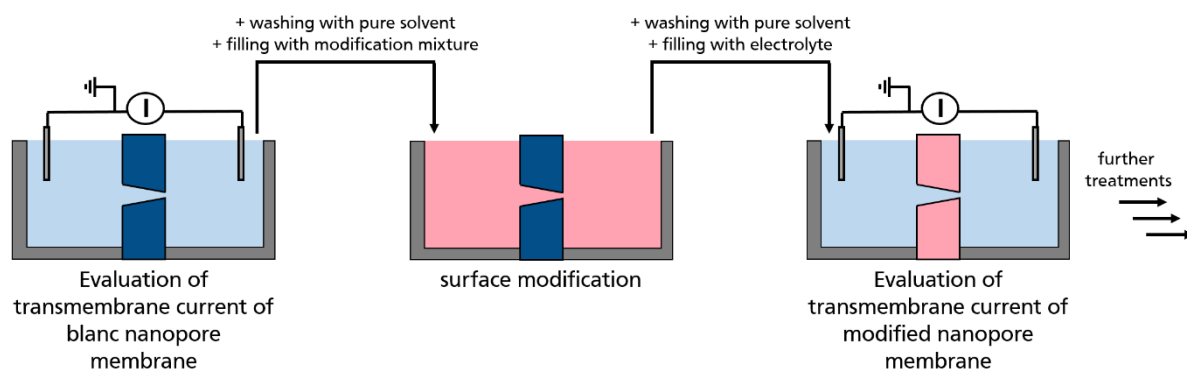


Figure 30: Scheme of experimental setup for the entire record of the modification procedure. Note that for  $I/V$  measurements, the cell is grounded and placed into a FARADAY-cage. Moreover, a pair of Ag/AgCl-electrodes is immersed into half-cells.

Besides the record of transmembrane changes induced throughout the nanopore modification, the same setup is used to assess the sensing performance as well. For this purpose, both half-cells are filled with the same electrolyte already used for the modification-evaluation that contains now certain amounts of the respective analyte. Throughout the entire modification and sensing process, the position of the fixed nanopore membrane remains unchanged to enable the evaluation of the exactly the same transmembrane area and to guarantee the comparability of the different stages of the nanopore surface (see Figure 30) during the sensing measurement.

Regarding the surface modification numerous routes to modify the nanopore walls has been established and rely on the (bio)molecular modification of the carboxyl groups on the nanopore surface that serve as anchor for the attachment of new molecular moieties. The functionalization used in this thesis can be summarized into four groups depending on the chemical functionalization method used for the surface modification:

- i. Covalent functionalization
- ii. Click-chemistry
- iii. Electrostatic interactions
- iv. Metallic complexation

The modification routes are used to attach ligands onto the nanopore surface. In the following, the experimental procedures will be briefly described in the following chapters. The sensing performance of the attached ligands in presence of the analyte is described and discussed in the respective section in chapter III.

## 2.1. Covalent Functionalization

The aforementioned incorporation of new functionalities inside the pore can be carried out by the use of common coupling chemistry. Considering the application of nanopores as potential sensors, surface modification of the nanopore may contribute to the possible detection of the analyte. In this case, the attachment of the detection unit or receptor (the lock) to the surface of the nanopore occurs throughout the formation of a new covalent bond.

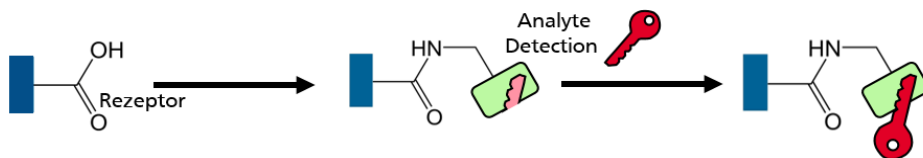


Figure 31: reprint of Figure 22; Incorporation of the recognition unit (the lock) for the analyte (the key) detection using the covalent modification method.

Here, the molecular pathway has to be selective and high yielding. Typically, the surface carboxyl group is transferred into a stable amide group carrying a new functional group in turn. For this purpose, the carbodiimide coupling chemistry has become a standard method in case of nanopore-functionalization and will be described in the following chapters.

### 2.1.1. EDC-Coupling Chemistry

The conversion of the surface carboxyl groups into stable amide bonds is carried out using a two-step reaction, since the carboxyl group tends to deprotonate easily in presence of amine agents. Deprotonation generates a resonance-stabilized carboxylate group, which in fact represents a dead end for any further covalent surface treatment. Therefore, the carboxylic groups have to be activated with a good leaving group for a successful amidization of the carboxyl groups. The experimental procedure was carried out using the protocol of Ali *et al.* (172)

For this purpose, track etched membranes were first immersed in a freshly prepared solution containing 1-ethyl-3-(3-dimethylaminopropyl)carbodiimide (EDC) (100 mM) and the nucleophilic agent (200 mM), e.g. pentafluorophenol (PFP) or *N*-hydroxysulfosuccinimide (*sulfo*-NHS) (see Figure 32). For the case of PFP, absolute ethanol serves as the solvent, whereas for case of *sulfo*-NHS an aqueous solution was prepared. After one hour and numerous washing steps with either ethanol or pure water, the foil is exposed to 200 mM of the amine compound, herein referred as  $R_4$ -NH<sub>2</sub>, for at least eight hours at room temperature.

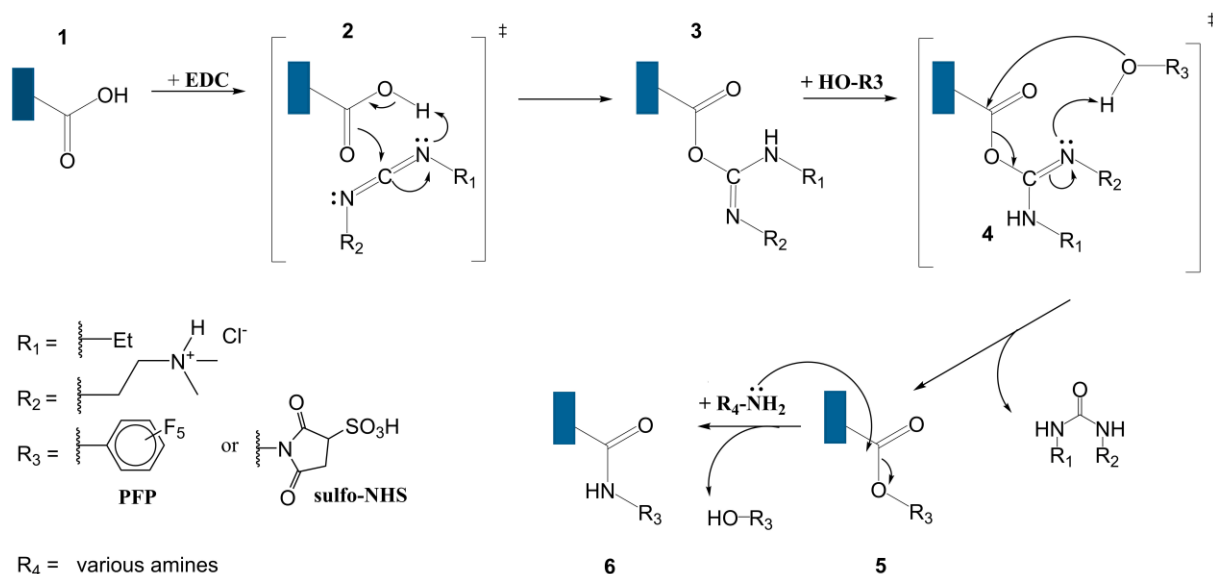


Figure 32: Molecular pathway for the modification of track-etched PET-nanopore membranes using carbodiimide-coupling chemistry. Note that in case  $R_3 =$  PFP, the reaction is carried out in absolute ethanol, whereas in case of  $R_3 =$  *sulfo*-NHS, an aqueous solution was used instead.

Regarding the mechanism in Figure 32, the surface carboxyl groups attack the carbodiimide carbon of EDC. The following rearrangement of the resulting six-centered transitional state **2** causes the formation of the activated EDC-ester intermediate (*O*-Acylisourea) **3**. In the next step, **3** is reacting with the nucleophilic agent, e. g. PFP or *sulfo*-NHS, in a tetrahedral transition state **4**. The subsequent elimination of the urea compound transforms the former carboxyl group into an activated ester **5** bearing an excellent leaving group. In the next step, the treatment with the amino agent takes place. The strong nucleophilic nature of the amino group ensures the desired formation of the amide bond **6**. In this thesis, various amines were utilized for the EDC-coupling route, such as: ethylene diamine (EDA) (CHAPTER IV.1, V.4, VI.2), dibenzocyclooctyne-amine (DBCO) (CHAPTER V.5), *N*<sub>ω</sub>,*N*<sub>α</sub>-bis(carboxymethyl)-*L*-lysine (BMCL) (CHAPTER V.1 and VI.1), *bis*-podand-NH<sub>2</sub> (CHAPTER V.2).

### 2.1.2. HATU-Coupling Chemistry

The described coupling chemistry using EDC and good leaving groups can only be carried out in protic-polar solvents such as ethanol or water. In order to expand the attachable functional groups onto the nanopore walls using coupling chemistry, a new route was developed using 1-[bis(Dimethylamin)methylen]-1H-1,2,3-triazol[4,5-b]pyridinium-3-oxid-hexafluorophosphate (HATU) as the coupling reagent instead of EDC.

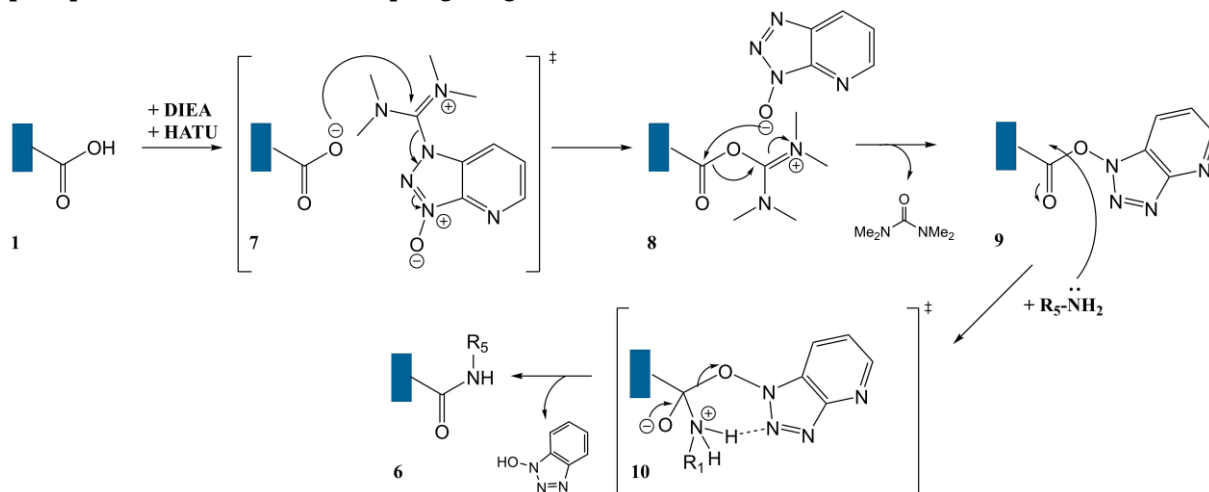


Figure 33: Molecular pathway for the modification of track-etched PET-nanopore membranes using carbodiimide-coupling chemistry with 1-[bis(Dimethylamin)methylen]-1H-1,2,3-triazol[4,5-b]pyridinium-3-oxid-hexafluorophosphate (HATU). Note, that R<sub>5</sub> symbolizes the residual molecular structure of the amine agents used in the HATU-coupling chemistry.

According to Figure 33, the coupling reaction with HATU can be considered as a one-step *N*-acylation compared to the aforementioned EDC-PFP-route. In the presence of HÜNIG's base diisopropylethylamin (DIEA), the carboxyl groups are deprotonated. Now, the iminium isomer of HATU **7** (*N*-species) gets attacked by the anionic carboxylate groups and produces an unstable *O*-acyl(tetramethyl)isouronium salt **8**. This species is consisting of the reactive 1-hydroxyl-7-azabenzotriazole anion. A subsequent reattack of **8** leads to the formation of the activated ester **9**, whereby the stoichiometrical elimination of tetramethylurea occurs. Finally, the nucleophilic amino compound (R<sub>5</sub>-NH<sub>2</sub>) is added and a seven-centered transition state **10** is traversed resulting in the derivation of the desired amide **6**.

Moreover, the described HATU coupling works as well, when combining an amino-terminated nanopore membrane with molecules carrying carboxyl groups. Hence, the membrane surface must be first covered with amino groups using the protocol described in section 2.1.1. and

ethylene diamine as amine agent. In this thesis, the HATU-coupling reaction was used for the case of the ATCUN-modification in CHAPTER V.4 and VI.2 as well as for the DMF-promoted EDA-functionalization in CHAPTER IV.1. To this end, a solution containing HATU (50 mM) and DIEA (1 vol.-%) as well as the carboxylic compound (0.5 mM), namely a peptide, was freshly prepared using pure DMF as solvent. The amine terminated membrane was exposed to the reaction mixture and left to react for at least eight hours at room temperature. The peptide used for the HATU-coupling was custom-made by Dr. Lena Müller (RG Tietze), whose structure is presented and briefly discussed in CHAPTER V.4 and VI.2.

## 2.2. Click-Chemistry

The immobilization of receptors onto the nanopore surface is limited since attachable molecules required at least one structural group that is linkable with the carboxylic surface, and one receptor unit for the later analyte detection. Structural similarities between both parts within the molecule can cause competitive reactions and a directed surface attachment is questionable. In addition, some analytes are detectable only throughout highly specific conjugations. However, this limits the range of possible couplings to carboxylate groups. To detect especially complex classes of molecules such as enzymes or proteins, click-chemistry is a beneficial modification strategy. Here, the receptor moiety is attached to the nanopore surface through a specific interaction of two “puzzle pieces” (see Figure 34).

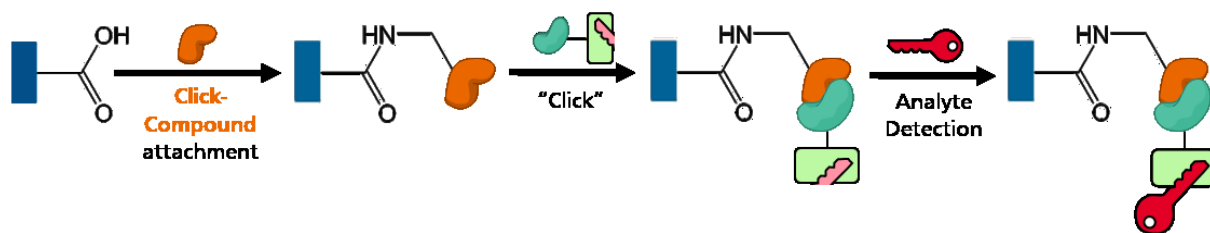


Figure 34: Incorporation of the receptor units (the lock) onto the nanopore surface for the later analyte (the key) detection using the modification method based on click-chemistry.

Prior to the click-reaction, the nanopore surface has to be functionalized in order to link one part of the click-component onto the membrane. There is a wide range of feasible moieties that can be used for the click-reactions. (173) In this thesis, all surface-click reactions will be discussed briefly with respect to the used “puzzle interactions” in the chapters below.

### 2.2.1. Strain-Promoted Azide-Alkyne Cycloaddition (SPAAC)

One of the most famous click-reactions is a [3+2]-cycloaddition, in which a terminated C-C triple bond reacts with a 1,3-dipolar species to form a triazole. (174) The cycloaddition can be catalysed in the presence of copper-(I)-ions and is referred as copper-catalysed azide-alkyne cycloaddition (CuAAC). (175) Here, the removal of copper ions afterwards can be difficult and depends on the used system. However, the replacement of a terminal triple bond by a spread triple bond can be carried out under copper-free conditions. (176) The steric hindrance of the triple bond enables the pericyclic formation of the pentagonal ring in the presence of a 1,3-dipole. Here, the increased strain inside the molecule increases the reactivity and the transition state is more accessible even without the need of a catalyst. (177, 178) By means of the use of a cyclooctyne derivative and an azide-labelled reactant a strain-promoted azide-alkyne cycloaddition, e. g. SPAAC-reaction, can be carried out to immobilize recognition elements onto a nanopore-surface in a simple way under physiological conditions. The reported mechanism

adaption onto the nanopore environment is illustrated in Figure 35 and adapted from the protocol described by Shea *et al.* (179)

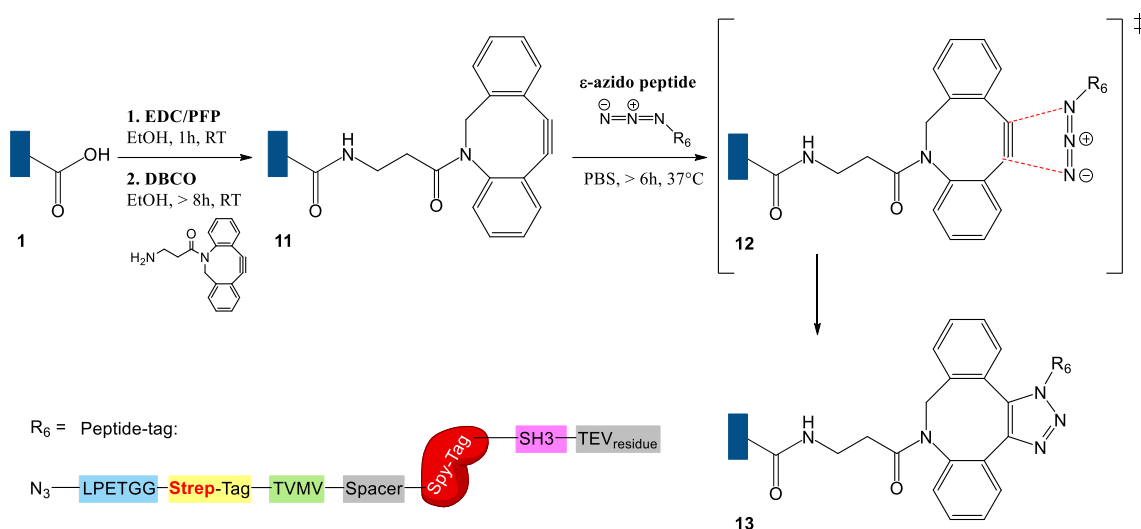


Figure 35: Illustrated mechanism of the strain-promoted azide-alkyne cycloaddition (SPAAC) onto the nanopore walls. The detailed sequence of the peptide is presented in the appendix section in Figure 150.

Regarding the SPAAC-mechanism, the cycloaddition takes place through a pericyclic electron transfer between a triple bond compound and an azido-labeled compound. For this purpose, in the first step the cyclooctyne derivate, i. e. dibenzocyclooctyne-amine (DBCO) was attached to the pore walls **11** using an unmodified nanopore foil mounted between two-cells in a measurement setup. The attachment of DBCO onto the nanopore surface was carried out according to the already described protocol in section 2.1.1. Then, the  $\epsilon$ -labelled azido-peptide (0.1 mM) resolved in PBS-buffer (pH 7) was added to the measurement cells. Next, the pentagonal transition state **12** was generated leading to the formation of the triazole **13**. Accompanied by the successful linkage of the peptide onto the pore walls. The protocol was adapted from Feringa *et al.* (180), whose research group performed the reaction in solution only.

Figure 35 shows only abbreviated peptide sequences of the used  $\epsilon$ -labelled azido-peptides **12**. Detailed amino acid sequences of the illustrated peptide can be found in the three-letter code in the appendix section (see Figure 150). In addition, the peptide was fabricated by Alexander Gräwe, M. Sc. (RG Stein), and kindly provided for the nanopore attachment.

### 2.2.2. Tag-Catcher System

To further attach molecular receptors, a new strategy based on the click chemistry of proteins was used, the so-called ‘Tag/Catcher-System’. For this purpose, one reactant, i. e. the ‘Tag’, has first to be linked to the nanopore wall, while the corresponding counterpart, i. e. the ‘Catcher’, is part of the receptor molecule. The principle is analogous to the one of molecular click chemistry and can be seen as a special version of the key-lock principle. (181–183) Regarding the structure of **12** and **13**, a ‘SpyTag’-sequence is displayed. After the successful Spy-Tag immobilization onto the nanopore walls, further modification can occur as long as the molecule to be attached consists of the respective counterpart of ‘SpyTag’, namely a ‘SpyCatcher’ sequence (see Figure 36). In addition, these molecules are carrying the receptor-moieties. In this thesis, the receptor is made of a single-domain antibody, the so-called nanobody symbolized

by the purple protein structure in Figure 36. This nanobody-structure is able to undergo a sensitive linkage with a highly specific analyte, which makes the nanobody a selective ligand to detect biomolecules and, thus, a suitable candidate for a medical sensor.

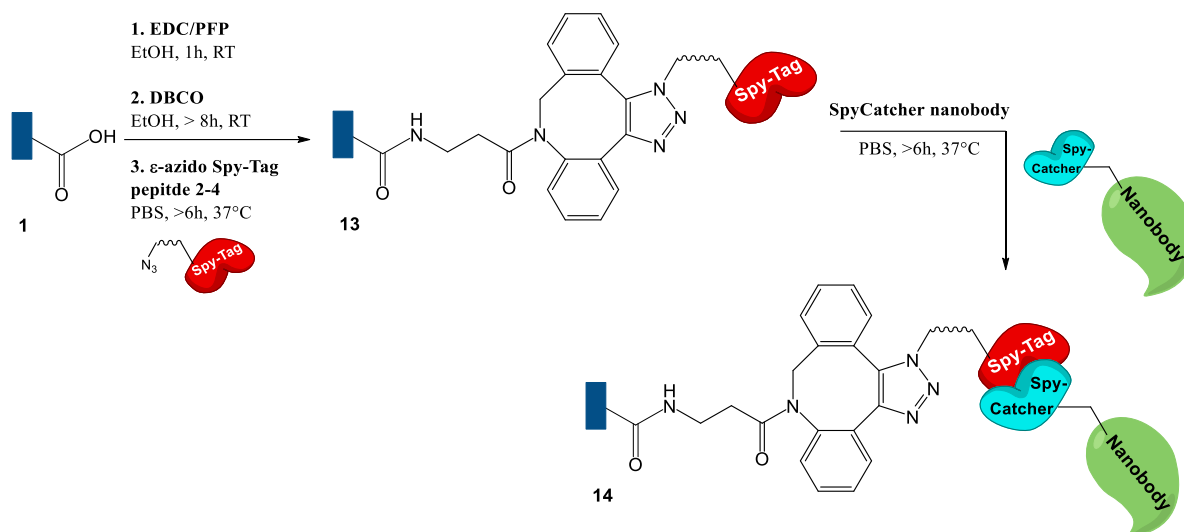


Figure 36: SpyTag/Catcher reaction for a successful immobilization of nanobodies onto the nanopore walls.

For this purpose, the ‘SpyCatcher’-nanobody (30  $\mu$ M) synthesized by Alexander Gräwe, M. Sc. (RG Stein), was dissolved in PBS buffer solution. The blank nanopore membrane was fixed between two half-cells of the measurement cell and the ‘SpyTag’-modification of the nanopore membrane was achieved throughout the protocol already introduced in section 2.2.1. Then, the freshly prepared nanobody-solution was filled into both chambers and the mixture was allowed to react for at least 6 hours at 37°C. Afterwards, the reaction mixture was taken out of the cells and the membrane was washed numerous times with PBS-buffer solution for a complete washout of all the unreacted compounds. The entire modification and characterization using the Tag/Catcher-system is presented in CHAPTER V.5.

The fusion between ‘SpyTag’- and ‘SpyCatcher’-moieties is based on the formation of a covalent isopeptide bond between the amino group of the lysine (Lys31) located in the ‘SpyTag’ side-chain and the carboxyl side group of aspartic acid (Asp117) in the ‘SpyCatcher’-sequence (see Figure 37). (183)

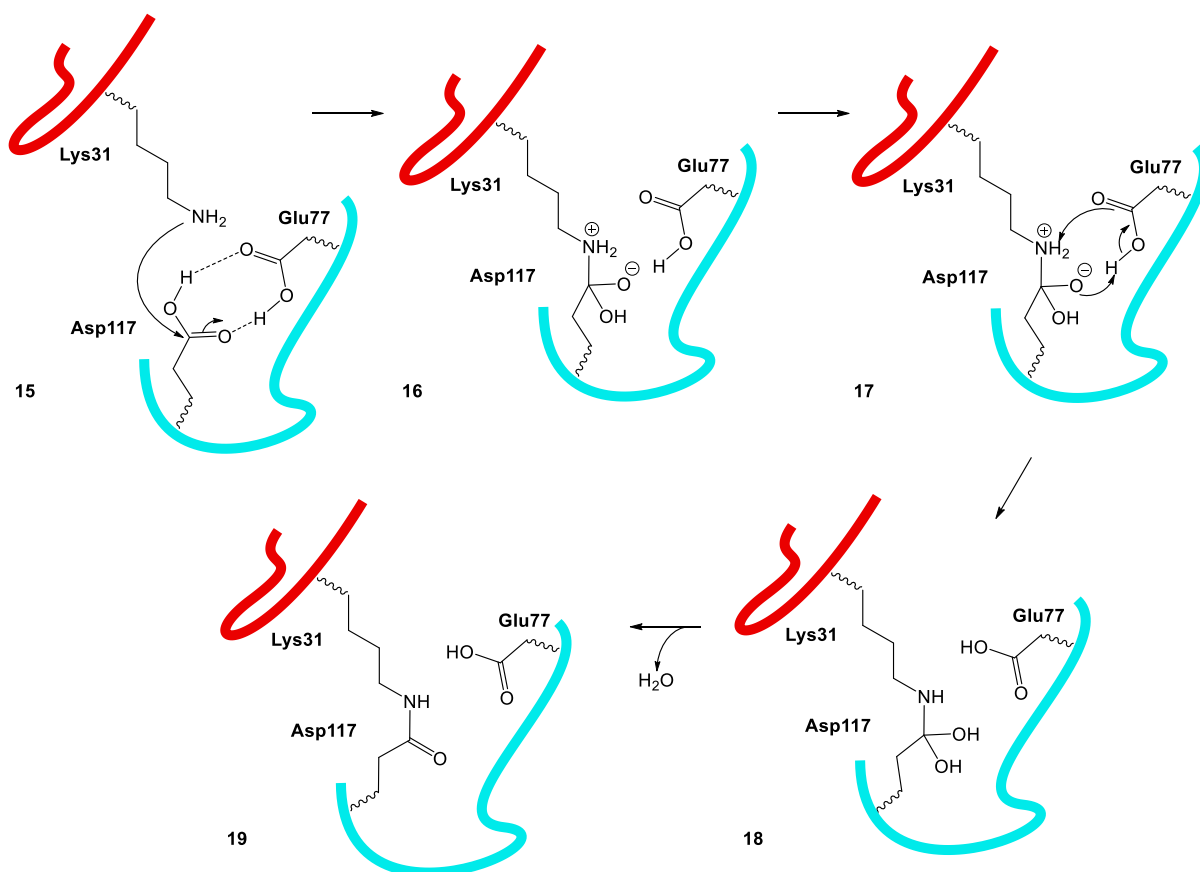


Figure 37: Mechanistic pathway of the covalent formation of the isopeptide bond between the amino acids lysine (Lys 31) of the 'SpyTag'-sequence and aspartic acid (Asp117) of the 'SpyCatcher'-sequence **15** with glutamic acid acting as proton shuttle **16** and facilitator of the reaction. Firstly, amino group of Lys31 is nucleophilic attacking the carboxyl-carbon of ASP117 and forms a zwitterionic intermediate **17**. The proton rearrangement reveals the hydrate structure **18** of the former Asp117. Finally, the amide group **19** is generated upon the release of water.

In regard to the reported mechanism of Reddington *et al.* the formation of the isopeptide bond is promoted by the carboxylic group of glutamic acid (Glu77). (184) Asp117 and Glu77 are connected via hydrogen bonds **15** facilitating a nucleophilic attack of the amino side chain of lysine located in the 'SpyTag'-sequence. The resulting zwitterionic intermediate **16** is rearranged by the help of Glu77 acting as a proton shuttle **17** and generating its hydrate derivate **18**. According to ERLLENMEYER's rule, the hydrate form is converted into the carbonyl structure, revealing the new created amide bond (isopeptide bond) **19** and water as by-product. (185)

The use of the protein click-chemistry can help to further extend the repertoire of substances that are attachable to the nanopore surface and, therefore, more complex molecules can be attached and detected. Accompanied by their simple experimental feasibility, the reaction between 'Tags' and 'Catchers' is targeted, directed and takes place without the need of difficult purifications.

### 2.3. Electrostatic Interactions

In the already described functionalization methods, the carboxyl group serves as a covalent binding partner. For alkaline pH-ranges, these groups are deprotonated forming the resonance stabilized carboxylic anion (see Figure 38). The negative charge acts as an anchor for the adsorption of positively charged molecules to form an electrical double layer (EDL). With regard

to the application of the nanopore membrane as a sensor, molecules with recognition units can now be brought to the wall via electrostatic interactions in addition to the already described covalent bond.

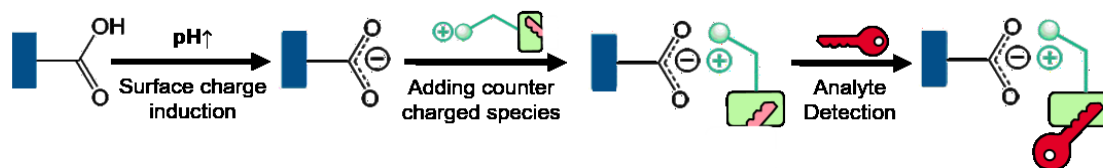


Figure 38: Incorporation of the recognition unit (the lock) for the later analyte (the key) detection using the modification method based on electrostatic interactions. For this purpose, the surface carboxylic groups has to be deprotonated (alkaline pH-range) to generate negatively charged surface groups acting as the core for the electrostatic attachment of positively charged molecules bearing a recognition unit for the later analyte detection.

### 2.3.1. Layer-by-Layer Technique (2 compounds)

The treatment of a charged nanopore surface with polycations provides the adsorption of a self-assembled monolayer (SAM) onto the membrane's surface causing a positive net charge. The further treatment of the positively charged SAM with polyanions lead to the generation of a layer-by-layer structure with an alternating electrostatic interaction.

Numerous combinations of negatively and positively charged polyelectrolytes were established in the past years. (188, 189) Here, poly(allyl amine hydrochloride) and poly(acrylic acid) were deposited in an alternating order and are herein referred as [PAA] and [PAH] (see Figure 39) .

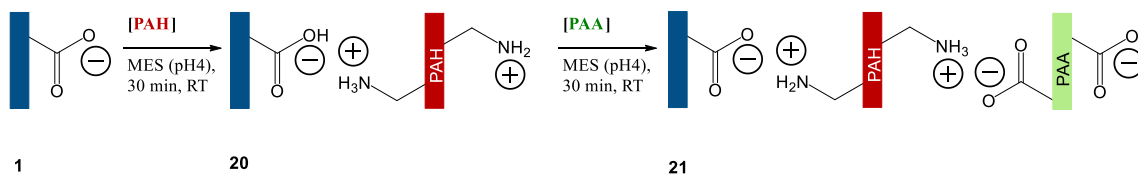


Figure 39: Alternating deposition of the cationic Poly(allyl amine hydrochloride) [PAH] **20** and the anionic Poly(acrylic acid) [PAA] **21** onto the negatively charged nanopore surface covered with deprotonated carboxylic groups. Note that the deprotonation of carboxylic group occurs above pH 3 according to the  $pK_a$  value.

For this purpose, the membrane was fixed between two compartment-cells of the measurement-cell. Prior to the polyelectrolyte deposition, both half-cells were filled with an alkaline solution (1 vol.-% NaOH-solution) for few minutes to enable the sufficient generation of negatively charged carboxyl groups. Then, the membrane was treated with a freshly prepared solution (50 mM) [PAH] to form the cationic SAM **20**. A brief washing with MES buffer (pH4) removed unbound polycationic moieties. A subsequent exposure of the membrane to a fresh (50 mM) PAH solution (MES buffer; pH4) led to the formation of a bilayer [PAH|PAA] **21**. After an additional washing step, this layer-by-layer (LBL) structure can be further constructed through an alternating treatment with the polyelectrolyte solutions. The experimental condition was adapted from Tsuge *et al.* (190)

### 2.3.2. Combined LBL-Modification (3 compounds)

The formation of LBL-structures based on electrostatic interactions between polyelectrolytes are extendable by the addition of a hydrogen donor compound. For this case, the LBL-build-up is promoted throughout electrostatic-interactions and hydrogen bonding forces that lead to a formation of a hybrid multilayer film on the nanopore surface. This allows more structural

control during the surface functionalization. (191) Here, the first deposited layer on the nanopore is composed of a polycation [PAH] and the *H*-donor component, i. e., Poly(4-vinylpyridine) [PVP], whereas the polyanion deposition with [PAA] is carried out as already described in the previous section (see Figure 40).

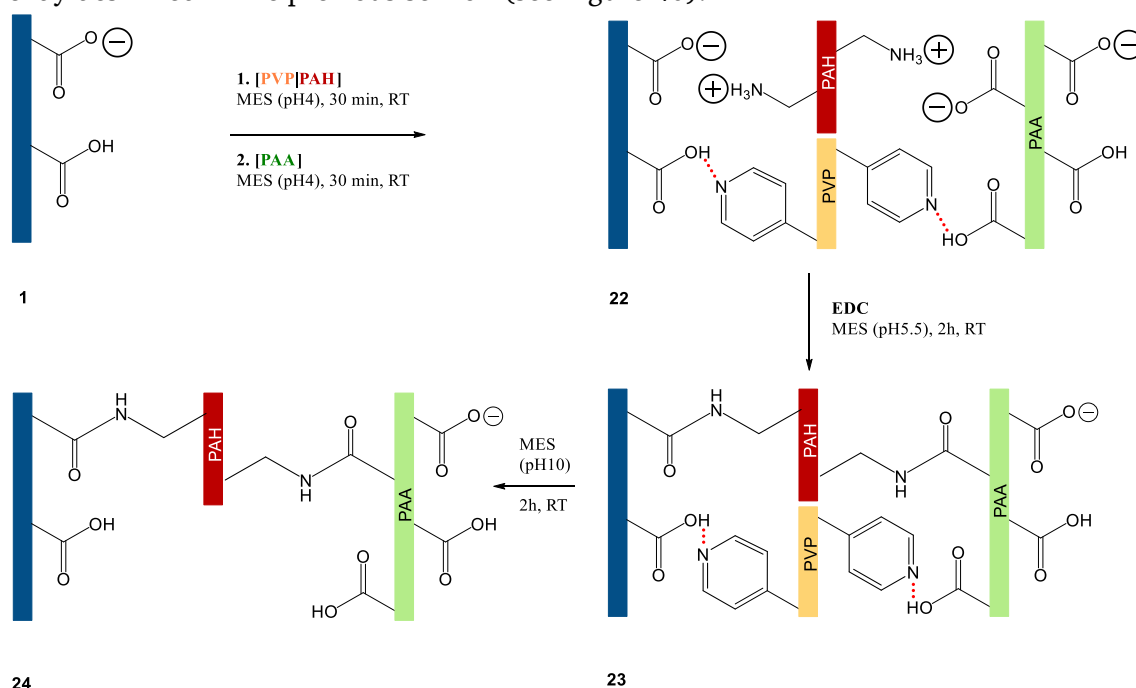


Figure 40: Illustration of the alternating deposition of a polycationic blend, made of Poly(allylamine hydrochloride) [PAH] and poly(4-vinylpyridine), and the polyanionic Poly(acrylic acid) [PAA]. Consequently, a bilayer made of three components is formed onto the nanopore surface.

The simultaneous adsorption of PAH and PVP on the nanopore surface is sufficient, only if carboxyl groups are insufficiently charged. Thus, the protonated moieties enter a *H*-bridge with the [PVP]-component, while deprotonated moieties are bound to [PAH] throughout electrostatic attractions (22).

For this purpose, the nanopore membrane was fixed in between the two-compartment measurement cell, and treated with MES-buffer solution (pH4) to generate a semi-deprotonated pore surface. Then, the cells were filled with the MES-buffered polycationic blend [PVP|PAH] at pH 4. After 30 min, the excess of unbounded blend was removed through numerous washing steps with pure MES-buffer solution (pH 4). Afterwards, the polyanion diluted in MES-buffer, was filled into the cells. Within 30 min the formation of first bilayer 23 onto the nanopore surface occurs. These layering steps are repeated four to ten times and multilayer films are formed all-over the substrate. Then the electrostatic interactions were transformed into covalent amide bonds by the treatment with freshly prepared solution (100 mM) of EDC leading to a contraction of the multilayers 24. The further treatment of the membrane with an alkaline solution (1 vol.-% NaOH solution) for 1 hour led to the dissolution of the H-bridges, leading to removal of the PVP-compound causing porous but covalently linked multilayers. The experimental conditions are adapted using the protocol by Li *et al.* with slight modifications. (191)

## 2.4. Metal Complexation

Specific categories of electrostatic interactions are coordinative metallic complexes where metals play a main role regarding the COULOMB-attraction. Here, the deprotonated carboxyl group acts as a chelate ligand and forms a carboxyl complex with the central metal atom.

Referring to the sensory application of the nanopores, chelation is useful to bring metal ions onto the surface (see Figure 41).

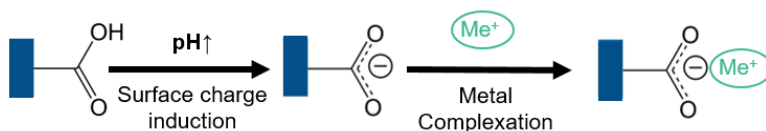


Figure 41: Illustrated pathway of metallic surface complexation onto the nanopore walls.

The carboxyl group is able to bind various divalent metal ions in a stable chelate complex. (192) However, the covalent modification method allows other complexing ligands to be placed on the wall. (193) In turn, these groups are able to bind selectively ions of certain metals or specific analytes (see section 2.4.1). In this case, the metal ion itself is the detected analyte. Moreover, pore surfaces covered with metal ions offers the possibility of galvanic depositions upon redox-conditions (see section 2.4.2).

### 2.4.1. Nickel-NTA-Complexes

In order to anchor metal ions selectively to the nanopore wall, a complexing agent must first be covalently attached to the surface. Here, the pore surface is modified with nitrilotriacetic acid (NTA) moieties as this group is able to form an octahedral complex with  $\text{Ni}^{2+}$ -ions, leaving residual sites linked with water molecules (see Figure 42).

For this purpose, *N,N*-bis(carboxymethyl)-*L*-lysine hydrate (BMCL) was coupled to the nanopore wall (29) throughout EDC/PFP-coupling. In a second step,  $\text{Ni}^{2+}$ -ions were adsorbed selectively on the nanopore wall to form the stable Ni-NTA-complex 26.

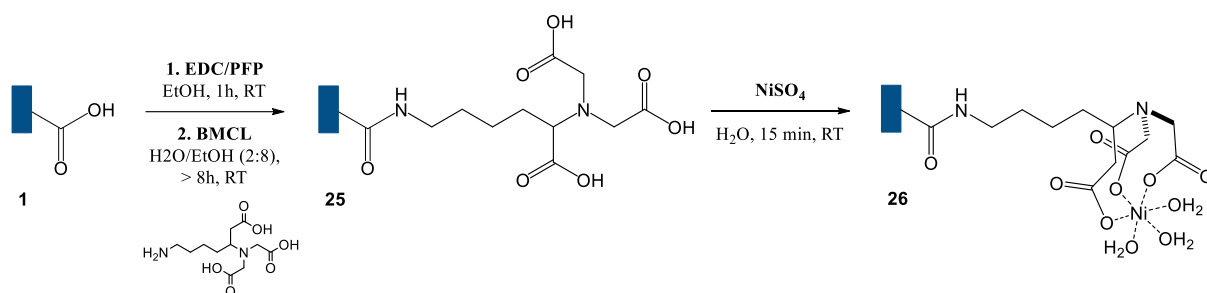


Figure 42: Two-step modification pathway for the generation of Ni-NTA-complexes onto the nanopore membrane. Therefore, the carboxylic surface groups are transformed into NTA-moieties throughout the successful EDC/PFP-coupling of BMCL 25. In the presence of  $\text{Ni}^{2+}$  the formation of the stable Ni-NTA-complex 26 occurs.

The nanoporous membrane was mounted between the two halves of the measuring cell. The covalent linkage of BMCL was carried out analogously to the protocol from section 2.1.1. BMCL (25 mM) was dissolved in an ethanol/water mixture (8:2) and neutralized with few drops of triethylamine (TEA). After numerous washing steps with pure ethanol and water, the BMCL-terminated nanopore membrane was treated with water (pH 10) to generate fully deprotonated carboxyl moieties. Then, the half-cells were filled with an aqueous solution of 100 mM  $\text{NiSO}_4$

(pH 10). Within four hours, the Ni-NTA complex is formed on the surface. Then, the membrane was washed again with pure water to remove excess of Ni<sup>2+</sup>-ions.

## 2.4.2. Electroless metal deposition

The surface carboxyl groups are capable to undergo coordinative interactions with metal ions, especially bivalent species. By the appropriate choice of redox conditions, the electroless deposition of an entire metal film along the nanopore wall can be achieved. (194)

According to Figure 43, the nanopore membrane is immersed into a freshly prepared solution (water: ethanol = 1:1) of tin sulfate for at least 30 minutes to generate a pore surface covered with Sn<sup>2+</sup>-ions **31**. The activation step is followed by a washing with pure water/ethanol (1:1) mixture to remove excess of Sn<sup>2+</sup>-ions. Then, the membrane was dipped into a fresh prepared palladium(II)solution to achieve the reduction of Pd<sup>2+</sup> to elementary Pd<sup>0</sup>, while Sn<sup>2+</sup> is oxidized to Sn<sup>4+</sup>. (195)

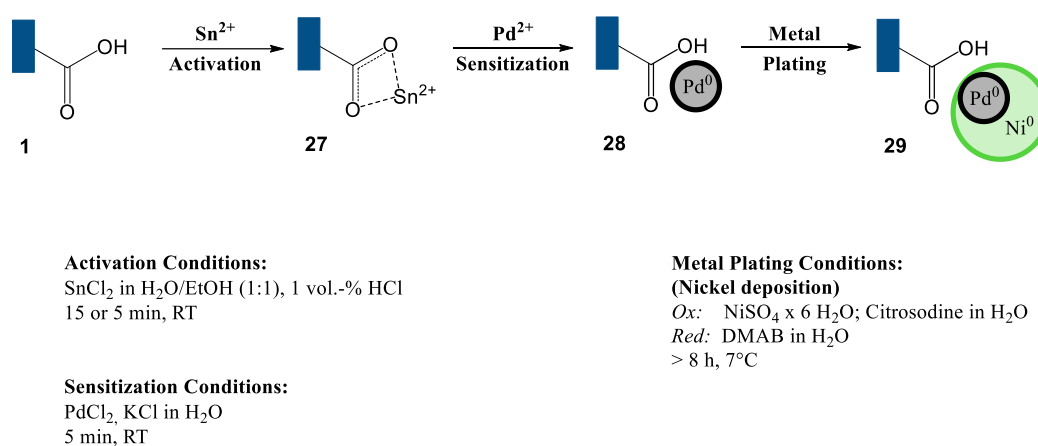


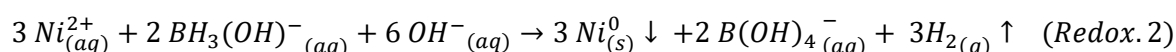
Figure 43: Scheme of the metallic deposition onto the nanopore surface throughout a controlled redox-reaction.

The underlying redox-reaction is presented in the following *Redox. 1* and provides the formation of metallic nanoparticles onto the membrane surface **29** (sensitization step).



An additional washing step with pure water prepares the membrane for the second sensitization and activation step accompanied by all washing steps. Note, that the first activation step takes about 15 minutes, whereas all further activation steps are reduced to 5 minutes of exposure time. The sensitization time period is kept for 4 minutes throughout the entire metal deposition.

Moreover, a less noble metallic film, i. e. a nickel film, can be deposited instead of a gold film, especially if only the morphological properties are assessed via the microscope. Here, the underlying redox reaction *Redox.2* takes place as soon as the sensitized and activated membrane is immersed into the nickel deposition bath consisting of an oxidizing and a reducing compartment according to the protocol of Muench *et al.* (199).



For this purpose, a separate oxidizing aqueous solution containing the metal source was freshly prepared. Therefore, 0.1 M nickel sulfate hexahydrate (NiSO<sub>4</sub> × 6 H<sub>2</sub>O) was dissolved and the nickel ions were masked with 0.1 M citric acid. The reducing solution was made of 0.1 M

---

dimethylamine borane (DMAB). For the case of alkaline solutions, DMAB exists in the form of the hydroxytrihydroborane ion, i. e.  $\text{BH}_3(\text{OH})^-$  (see CR. 3). (200) Here, the previously formed Palladium-germs act as a catalyst. The formation of the metallic nickel film at room temperature was stopped after 20 minutes and the metallized membrane was washed numerous times with pure water to remove excess of the deposition bath.

The metalized structures are released by the entire removal of the polymeric substrate. In this thesis, the metallic deposition was performed on PLA-membranes (CHAPTER IV.2). To remove the polymeric substrate the metallized PLA-foil was easily dissolved upon immersion into 5 M NaOH-solution at 50°C for 8 h.

### 3. Characterization of Polymeric Nanopores

Starting from a nonselective nanoporous material, the introduction of sensing properties is characterized by the ability to influence the flow through surface bioconjugation reactions. For this purpose, ligands are immobilized on the surface of nanopores, which are able to bind biomarkers (bioconjugation) causing a change of the pore geometry or net charge. The bioconjugation performance of the membrane was analysed with the help of optical and physicochemical methods (see Table 3).

Table 3: Overview and classification of used membrane characterizations.

Evaluation	Investigation	Method	Validity
Physico-chemical changes	Conductance	Current-Voltage-Measurement ( <i>IV</i> )	SP, OP
	Diffusion	Mass Transport Measurement ( <i>TM</i> )	MP*
Optical studies	Geometry	Scanning Electron Microscopy ( <i>SEM</i> )	MP
	Morphology	Confocal Laser Scanning Microscopy ( <i>CLSM</i> )	OP, MP
	Surface	Atomic Force Microscopy ( <i>AFM</i> )	MP

\* Due to slow diffusion rates of the ultra-small pore openings of conical shaped nanopores, the diffusion behaviour of these asymmetrical pores could not be investigated in realistic periods, i. e. from minutes to hours. Therefore, *TM* measurements of conical shaped nanopore membranes were not performed. For the case of all other listed characterizations, there are no limitations in terms of the nanopore shapes.

The physicochemical flux change is tested throughout mass transport experiments (*TM*). Successful modifications and bioconjugation reactions onto the nanopore are evaluated by running current-voltage measurements (*IV*). Moreover, the material itself and its ongoing morphological changes throughout the modification steps are determined using optical imaging methods such as scanning electron microscopy (*SEM*), confocal laser scanning microscopy (*CLSM*) and atomic force microscopy (*AFM*), respectively.

#### 3.1. Physicochemical Properties

Nanoporous polymeric membranes can be tailored on demand due to their ability to tune the functionality of the inner pore walls throughout surface chemistry according to the intended purpose. To evaluate the membrane performance, the transmembrane surface is tested for its ability to detect certain species, such as ions or analytes passing along the membrane. The investigation of the ion flux is recorded throughout current-voltage measurements (section 3.2.1). The diffusion of dye molecules across the pore region can be induced by concentration gradient and was performed via mass transport experiments (section 3.2.2).

##### 3.1.1. Current-Voltage Characteristics

Successful surface modification of the nanoporous membrane was investigated using current-voltage measurements (*IV*). The attachment of molecules to the pore walls causes a physical surface change on both the pore diameter as well as on the pore charge density. Moreover, a sufficient, selective and sensitive analyte detection is monitored through *IV*-measurements. (202) At  $\text{pH} > 3$  (corresponding to the  $\text{pK}_a$  value), the carboxyl groups of the nanopore membrane are deprotonated. This generates a negatively charged pore surface, whose charge

density rises with increasing pH value. In addition, these charges are influencing the transmembrane current during *IV*-measurements. (203) *IV*-measurements became one of the standard methods as the experiments gave detailed insights about changes within the transmembrane area with respect to performed modifications or further sensing experiments with respective analytes. Consistently all nanopore membranes presented in this thesis were analysed at least by *IV*-measurements.

Here, the porous membrane is clamped between two chambers of a measuring cell and both cells are filled with electrolyte solution (unless otherwise stated, the electrolyte solution contains of 100 mM KCl in pure water) and Ag/AgCl electrodes connected to a picoamperemeter/potentiostat Keithley 6487 (Keithley instruments, OH) are mounted in each chamber (see Figure 44).

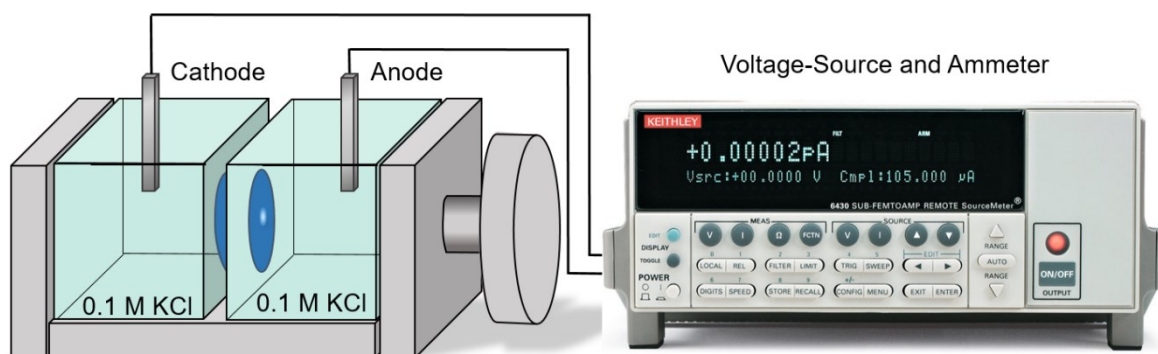


Figure 44: *IV*-measurement setup for the conductance record across a nanoporous membrane. Here, the exemplary measurement of a single nanopore membrane is presented. The membrane is fixed in-between the two measurement cells filled with electrolyte solution (0.1 M KCl in pure water). A pair of Ag/AgCl-electrodes that is already connected to a grounded voltage source (Keithley 6487), is placed inside each half-cell. By applying a triangular voltage sweep from -1 V to 1 V, the current flux is monitored.

The as-prepared measurement cell is placed in a FARADAY-cage and additionally connected to the ground. For the case of asymmetrical nanopore membranes, the positive pole is located on the tip side of the foil and the negative one is placed on the bulk side. The same software-program (LabView 2013) already introduced in the CHAPTER II.1 is used for the *IV*-measurements as well. The table below displays the software settings used for the record of *IV*-curves.

Table 4: Parameters and settings for the *IV*-measurements.

Parameters	No. of periods	Points per period	Off-set	Amplitude	Time/points	Range
Settings	3	80	0 V	$\pm 1$ V	1150 ms	SP: $10^{-6}$ to $10^{-7}$ MP: $10^{-4}$ to $10^{-2}$

The presented method was used especially for conductance characterization of single pore membranes and was adapted from the protocol already described by Ali *et al.* (172) The current flux is depending on the nature of the respective single pore inside the whole membrane. If the number of pores per membrane is enlarged, a current is recorded, which is composed of the sum of all pores located within the consideration transmembrane area, i. e. the part of the membrane located between the two chambers of the measurement cell. *IV*-measurements of highly porous membranes ( $> 10^7$  pores/cm<sup>2</sup>) show a diffuse capacitive behaviour due to the

higher charge density inside the material that is causing a superposition of the signals and a complex *IV*-characteristic. (204) Therefore, highly porous membranes are not suitable for *IV*-characterizations. Only single pore membranes and those with pore arrays of  $10^3$ - $10^4$  pores/cm<sup>2</sup> provide adequate *IV*-curves that can be used for further interpretations of the pore modification state and sensing performance.

### 3.1.2. Mass Transport Measurement

Previous studies underlined the beneficial use of track-etched nanopores having high pore densities, i. e.  $> 10^7$  pores/cm<sup>2</sup>, in terms of filtration applications. Moreover, the easier fabrication of multiple tracks inside one membrane compared to the single pore fabrication process favours the research and application. So-called mass transport experiments can be carried out to evaluate the transmembrane performance as common *IV*-methods are not suitable. Here, the diffusion of positively or negatively charged organic salts across the membrane is investigated according to the different modification states of the membrane's surface. However, only cylindrical shaped nanopore membranes having a pore density of more than  $10^6$  pores/cm<sup>2</sup> are feasible (in contrast to *IV*-measurements). The diffusion through a conical shaped nanopore having a tip opening of just few nanometers, causes low rates and, thus, the mass transport can become time-consuming. Moreover, high pore densities are required to ensure a facile and sustainable record of transported analyte.

For this purpose, membranes having pore densities of at least  $10^6$  pores/cm<sup>2</sup>, were fixed inside the same measurement cell already introduced in section 2 (see Figure 29). For mass transport measurements, the half-cells were filled on one side with feed solution having a set concentration of analyte, and on the other side, pure buffer was added, in order to generate a high concentration gradient across the transmembrane area (Figure 45). The diffusion rates of various charged analytes were evaluated using an automated sample collection and analysis.

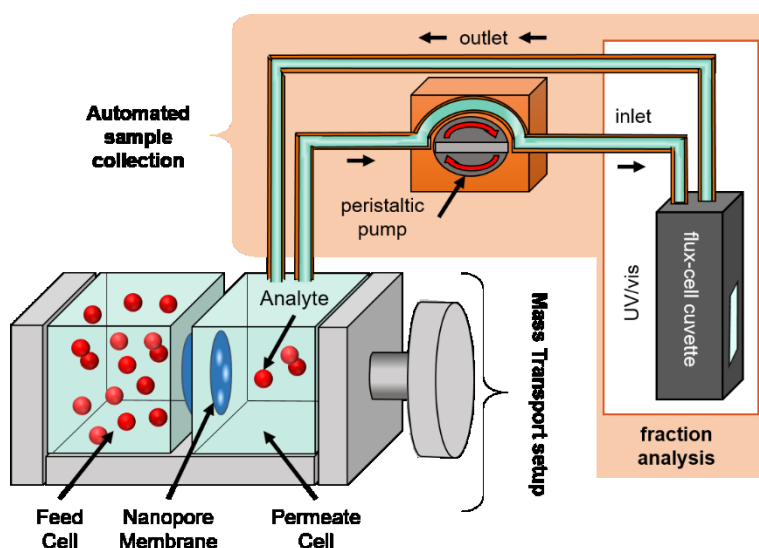


Figure 45: Mass transport experiment for the evaluation of analyte permeation across multiporous membranes. The membrane is clamped between two chambers, that are filled with feed solution (known amount of analyte) and pure buffer solution inside the permeate cell. Analyte permeation is recorded either using the manual or the automated setup.

Experimental conditions were adapted from Nguyen et al. (206) , whose sample collection was performed manually. Both half-cells have a volume of each 3.5 mL and a permeation area of 50 mm<sup>2</sup>. One of the chambers was filled with pure buffer solution (PBS-buffer, 10 mM). Hence, the record of UV/vis-spectra has to be active before the analyte solution (50 mM) was added to the remaining chamber as mass transport immediately starts. This experiment was performed with the negatively charged 1,5-naphthalene disulfonate (NDS) and the positively charged

---

methylviologen (MV). After the permeation of one type of analyte, the cells were washed numerous times with pure water or buffer solution to remove any residues of former analytes, and the mass transport was performed with the remaining analyte. The mass transport was evaluated before and after a modification step of the nanopore membrane. Moreover, the membrane was clamped once inside the mass transport setup. Now, the permeation experiment as well as the later modification steps were obtained without membrane removal to guarantee that the permeation area (for mass transport) is exactly the modified area of the membrane.

For the automated record of analyte permeation, the sample collection and characterization via UV/vis-spectroscopy is performed simultaneously (see Figure 45). Here, the nanopore membrane is placed between two chambers having a volume of just 650  $\mu\text{L}$  and a permeation area of 50  $\text{mm}^2$ . The filling with feed and buffer solution is performed like the manual mass transport. However, the setup is directly connected to an all-quartz flow-through cuvette (Suprasil®; Starna scientific; Volume: 450  $\mu\text{L}$ ) located inside the UV/visible-spectrophotometer (Agilent Cary 60) by a pair of tubes (inlet and outlet, Volume: 61  $\mu\text{L}$ , Diameter: 3.17 mm, Length: 40 cm; Material: poly(vinyl chloride), SPETEC GmbH). In total, the volume of the feed-cell amounts to 1222  $\mu\text{L}$ . The mass transport starts immediately as soon as the feed solution is added to the feed cell. The inlet tube is placed in a peristaltic pump (REGLO DIG MS-CA4/12®, ColeParmer GmbH) to generate a continuous flow from the permeation cell into the cuvette and to ensure constant monitoring of analyte permeation accompanied by a direct record of UV/vis absorbance using the “CaryWin UV”-software in the “scanning Kinetics” mode in adjustable time intervals. Moreover, the half-cells were stirred during the whole experiment. The automated mass transport experiment was performed as long as the recorded absorption reached a value of 1.0 a. u.. Afterwards, the record and the experiment was stopped. The cells, tubes as well as the cuvette were rinsed with pure water or appropriate buffer solution and prepared for the following diffusion experiment or modification step. Note that prior to the evaluation of UV/vis-absorbance, a calibration of the respective analyte was performed through a dilution series. The maximum transmission dates are plotted and the extinction coefficient is obtained through the linear fit, which in turn serves for the conversion of transmission value into the exact analyte amount according to the BEER-LAMBERT-equation. The add-on for the automated record of analyte diffusion was kindly provided by Dr. Mathias Diefenbach (RG Biesalski).

### **3.2. Optical Investigations/imaging Procedures**

Imaging procedures such as scanning electron microscopy (SEM) are used for the evaluation of geometrical factors. (208) Moreover, to test the biosensing abilities inside the nanopore region, confocal laser scanning microscopy (CLSM) was used, which is a well-established method for the case of fluorescent analytes. (209)

#### **3.2.1. Scanning Electron Microscopy**

Morphological studies, such as the estimation of the pore diameters and the roughness can be performed using field-emission scanning electron microscopy (FESEM-JEOL JMS 7401F, Japan) having a spatial resolution of up to 1.5 nm. For successful imaging of the polymeric nanopores by SEM, the substrate material, i. e. the nanopores membranes, has to be electrically conductive. Otherwise, the scanning beam is deflected and charging effects become visible resulting in a useless picture image. Therefore, the polymeric membranes are covered by a thin gold layer having just few nanometer thickness. For this purpose, the samples were treated with a sputter

---

coater (Quorum Technologies, Q300TD Sample Preparation System) bearing a gold target (99.9% purity, Baltic Präparation e. K.).

Figure 46 shows a representative top-view and a cross-section image of a cylindrical PET-nanopore membrane with fluence of  $10^7$  pores/cm<sup>2</sup>.

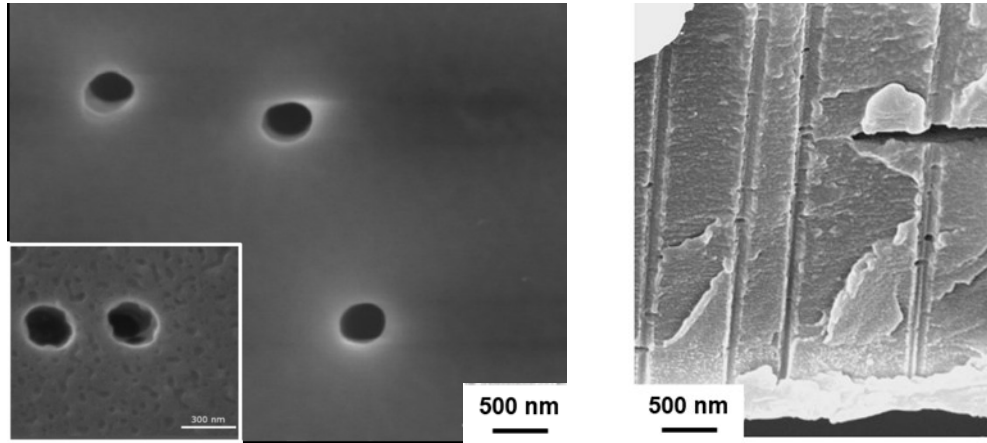


Figure 46: Representative top-view (a) and cross-section (b) image of etched nanopores using scanning-electron microscope at different magnifications (2M NaOH @ 50°C, etching time 37mins). In addition, a thin sputtered gold-layer is covering the scanning samples to avoid charging effects.

For the lateral image, the nanopore membranes have to be irradiated additionally with UV-light for about 90 hours. This treatment causes internal fragility inside the membrane and by pulling the membrane in two pieces, the nanopores serve as breaking points. These membrane pieces are now placed in an upright position between two pieces of silica plates on the SEM holder and sputtered with a thin conductive cold layer. For the case of top-view images, small membrane pieces are glued directly on the SEM holder by using carbon glue leaflets. (210)

The SEM is used for the determination of the pore diameter, but for only multipore membranes having at least a pore density of  $>10^4$  channels/cm<sup>2</sup>. Otherwise, the location of a low number of pores is a time-consuming procedure. For the case of symmetrical nanopore shapes, i. e. cylindrical forms, the analysis of the top-view images are used to calculate the diameter of the pores. For the case of asymmetrical pore geometries, such as cone-shaped pores, consisting of two separate diameters, i. e. the base diameter  $D$  and tip-opening  $d$ , only  $D$  is provided by SEM-images, because the dimensions of the small tip-openings is in the lower nanometre range and the location of such small structures is time-consuming.

However, the tip-opening value is crucial for the later applications of nanopores membranes. Therefore, the tip-opening is calculated by the help of  $IV$ -measurements of the single pore membrane, that is etched simultaneously with the multipore. Now, an  $IV$ -measurement is performed with the single pore and the transmembrane current  $I$  is obtained. By using the following Eq. 4 reported by Apel *et al.* and the already provided  $D$  value (from SEM-image of the respective multipore membrane), the determination of the tip-opening is achievable and was used to calculate all conical pore diameters in this thesis. (169)

$$d = \frac{4LI}{\pi\kappa UD} \quad (\text{Eq. 4})$$

Here,  $L$  = length of the conical pore  
 $d$  = tip-opening

$D$	= base opening (estimated by SEM)
$k$	= specific conductance of the electrolyte (for 0.1 M KCl, 100 mS/m at 24 °C)
$I$	= transmembrane current
$U$	= applied voltage

### 3.2.2. Confocal Laser Scanning Microscopy

Bioconjugation reactions inside the nanopore membranes were investigated by means of the use of the confocal laser scanning microscopy (CLSM). (211) However, the incorporation of fluorescent moieties to the pore membranes are crucial for a successful visualisation of the substrate and ongoing reactions, respectively. (209)

The substrate material, i. e. PET polymer, is intrinsically not fluorescent. Therefore, the membrane has to be modified or to be exposed to a fluorophore. Moreover, qualitative studies about the biosensing performance can be evaluated, if either the membrane is modified with a ligand, that binds fluorophores, or the membrane is already functionalized with a fluorescent ligand. In this way, the internal fluorescence is quenched after a treatment with the concerned analyte (see Figure 47).

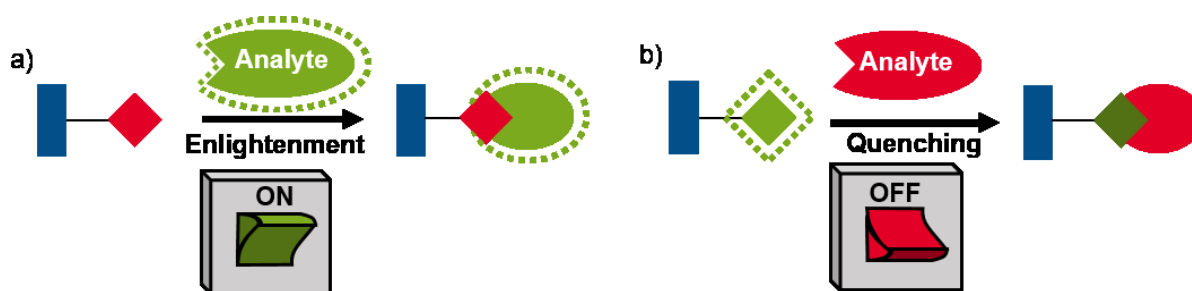


Figure 47: Scheme of bioconjugation reactions inside pore membranes. (a) The ligand terminated nanopore membrane is non fluorescent. The treatment with fluorescent analyte leads to a glowing nanopore region (ON-reaction); (b) The nanopore is functionalized with a fluorescent ligand. The addition of analyte causes a quenching reaction of the former fluorophore (OFF-reaction).

Fluorescent dyes used in this thesis are the carboxy-fluorescein (212) or the green and red fluorescent proteins, i. e. GFP and mCherry. (213) These qualitative conclusions are achievable even on pores with a low pore density ( $10^3$ -  $10^7$  pores/cm<sup>2</sup>) and offers the opportunity to characterize the less used oligopore membranes.

For this purpose, the membrane is placed onto the CLSM holder (see Figure 48) The bottom of lower piece consists of a thin cover glass. The upper piece has an open ring shape. Prior to the placement of the nanopore membrane, one 10  $\mu$ L-drop of aqueous agarose-gel (0.5 wt.-%) is placed onto the cover glass to ensure a proper fixation of the pore.

Then the respective buffer solution is added into the holder that is already placed in the CLSM setup. The lateral scan of the membrane was performed. The measurements were performed with the help of Wadim Weber, M. Sc. (RG Stein) and Dr. Tobias Meckel (RG Biesalski). This method offers the opportunity to evaluate the optical switching properties in an aqueous environment. Moreover, the use of monochromatic light minimizes the chromatic aberration for the laser light focus and



Figure 48: CLSM holder for the nanopore membranes.

---

there is no need for the use of a monochromator. CLSM-studies are a beneficial addition to the IV-measurements for the determination of binding phenomena inside the nanoconfined membranes in the presence of the respective analyte.

Measurements performed in this thesis are presented in CHAPTER V.4 and V.5. All measurements were carried out in 100 mM MES-buffer (pH 6.5) or PBS-buffer (pH 7). In both cases, the fluorophores enable the detection of the analyte. In CHAPTER V.4, the fluorescent ATCUN-modified multipore was analysed in presence or absence of Cu(II)-ions. In CHAPTER V.5, the Nanobody-functionalized multipore was treated with their respective analytes, i. e. GFP and mCherry. Upon successful interaction between the nanobody with the respective analyte fluorescence was induced and evaluated using the CLSM-method. For further details please refer to the respective section in CHAPTER V.5.

### **3.2.3. Atomic Force Microscopy (AFM)**

Imaging was proceeded in the tapping mode at room temperature on air using an atomic force microscope (Asylum Research, Oxford Instruments, Santa Barbara, CA). Here, a 1.5 V amplitude was applied onto the silicon cantilever (PPP-Zeihl AFM Tip, Nanosensors™, Switzerland) with force constant of 27 N/m and the phase and topography pictures were imaged simultaneously. AFM was carried out to evaluate the surface morphology changes upon peptide modification. Therefore, blank unmodified multipore PET-membranes ( $10^7$  pores/cm<sup>2</sup>, cylindrical-shaped pores with 150 nm diameter) and ATCUN-modified membranes were investigated (CHAPTER V.4). For this purpose, the membranes were fixed into plane silica plates (2 x 2 cm<sup>2</sup>) using standard superglue.

---

## CHAPTER III: MOTIVATION AND AIM

---

Biosensors are of special interest as they play an essential role in medical diagnosis but contribute also to enabling the sufficient monitoring of the health level. Nowadays, clinical diagnostic is obtained by screening the presence and amount of biomarkers inside human body fluids such as saliva, blood or urine. In order to improve the detection limit of biomarkers inside the diagnostic medium, the development of innovative and highly precise sensing devices are crucial to save and prolong life of human beings.

Over the last 20 years, track-etched nanopores came into the focus as novel material to miniaturize highly specific and selective sensory devices because of the following features: First, the polymeric substrate is highly mechanically robust for long-lasting research and potential applications. Second, several modification methods are already well-established to tailor the pore surface on demand. Numerous reports demonstrate the successful attachment of a broad range of receptor-moieties onto the pore walls and surface. Hence, the chemical moieties on the pore walls serve as a chemical trigger to control the transmembrane passage of ions, ensuring the direct and quantitative correlation of ionic transport with the respective analyte concentration. Finally, the track-etching procedure of nanopore fabrication provides control over geometrical shape and size in the nanometre range. Hence, lower detection limits are achievable as the fabricated pores are of the same size as that of analyte molecule. Overall, polymeric nanopores would have to be considered as powerful candidates in the miniaturization of diagnostic tools.

However, the nanopore-based biosensing devices are still in initial research stage. Aiming the application of nanopores in clinical environment is still challenging (Figure 49).

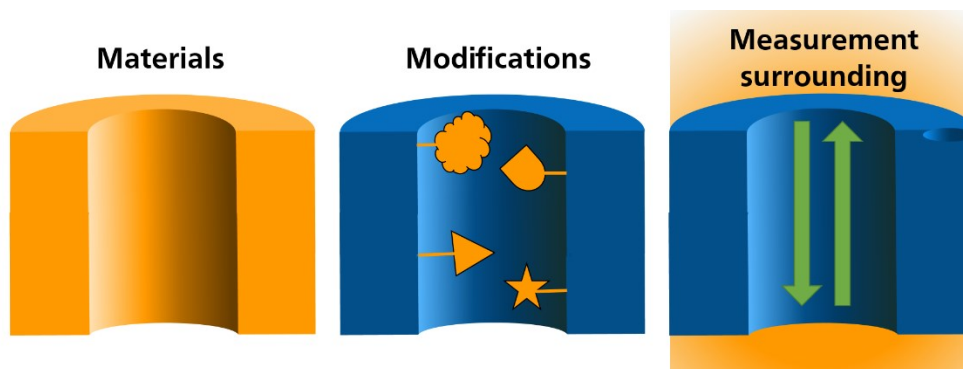


Figure 49: Scientific approach of track-etched nanopores towards nanopore-based biosensing applications. The investigated parameter is highlighted with the orange colouring. Here, the focus lies on the used pore materials, the successful attachment of (novel) receptors as well as the right choice of the measurement surrounding.

Figure 49 shows the mechanism of a possible nanopore-based sensing device. Moreover, CHAPTER IV is dedicated on establishing further polymeric materials as possible substrate for track-etched nanopores. CHAPTER V presents suitable pore modifications for the successful incorporation of specific receptor units along with a brief examination of respective analyte detection. In CHAPTER VI, the analyte recognition of modified nanopore membranes is tested inside LOC-devices as well as in human serum as an electrolyte solution to step further towards real measurement systems.

---

---

## CHAPTER IV: NANOPORE MATERIALS

---

Regarding the design of nanopore based sensors, one of the core challenges is the nanopore material itself, i. e. the polymeric films. During the past decades, polyesters became one of the most frequently used nanopore substrates, especially the PET-films.

To meet the commercial requirements for potential applications, nanopore substrate would require irradiation and polymeric production at large scale. Therefore, the first part of this chapter focuses on, whether commercially available membranes are suitable to produce pores. In the second part, the investigation of alternative routes is examined in order to counteract investigated for the fabrication of nanopores by track-etching technique.

---

### 1. Nanopore Fabrication in Commercial Poly(ethylene terephthalate)-Membranes

---

#### 1.1. Introduction

Regarding the commercial use of nanopore based biosensors, it is important to ensure that the source for nanopore membranes is not exhaustive. Because, the production of nanopores in polymeric membranes requires ion irradiation steps inside an ion accelerator, whose running is energy- and cost-intensive and mainly used within the surrounding for fundamental studies (214). In particular, the use of a heavy ion accelerator, like the universal linear accelerator (UNILAC), located in Darmstadt (Germany), enables the generation of new elements by bombarding substrate materials with accelerated swift heavy ions. The irradiation of polymeric substrates results in the generation of latent tracks which can be selectively removed with a suitable chemical etchant for producing nanopores. (70)

However, the irradiation of polymeric film using accelerator facilities is limited because of the versatile use of the ion beam. To satisfy the high request of nanopore membranes, commercially available nanopore membranes are investigated with respect to their:

- initial track nature
- geometrical nanopore dimensions
- behaviour during the track-etching process
- the *IV*-characteristics
- adequate surface functionalization

To this end, commercially available membranes were examined and compared with the already used GSI-membranes. The membranes are purchased by the company *it4ip S. A.*, located in Belgium. According to Figure 50, the ion beam irradiation is carried out perpendicular to the polymeric substrate like the SHI-treatment at the UNILAC accelerator (GSI, Darmstadt). Here, accelerated  $\text{Ag}^{9+}$  ions are penetrating the polymeric film located in a roll-up line. Using this automated assembly line, the irradiation step provides a maximum output in contrast to the production of irradiated polymer films at the GSI-centre, where only one stack of up to six membranes (50 mm<sup>2</sup> area) is obtained in one slot during the irradiation step.

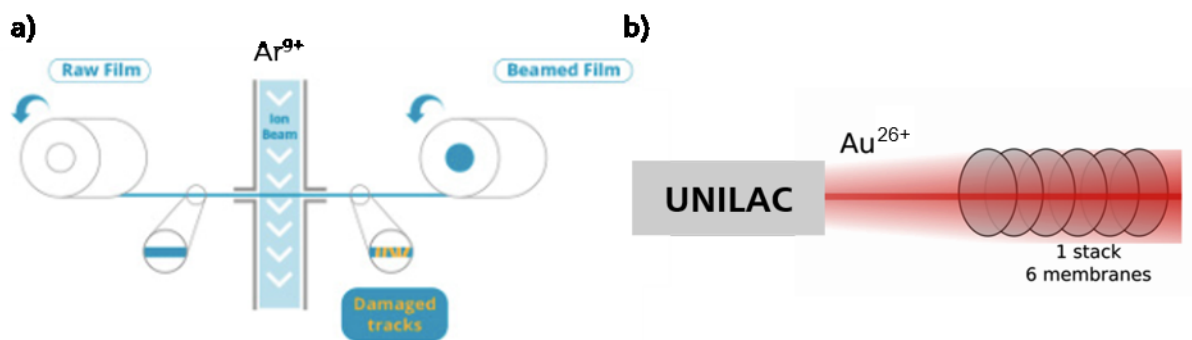


Figure 50: (a) Beam treatment for the irradiation of polymeric films at: (a) the company *it4ip* S.A (Adapted from *it4ip*-webpage (215), copyright (2020) *it4ip-iontracktechnology S. A.*) and (b) at the GSI-HELMHOLTZ-Centre for Heavy Ion Research.

Further, the company offers membranes having already etched nanopore inside the material, whose production is similar to the irradiation alignment, where the irradiated polymer role is immersed into etching baths for a pre-set time period. (215)

## 1.2. Results and Discussion

Among the broad range of achievable nanopore shapes, the fabrication of cylindrical and conical nanopores inside commercial membranes is preferred for the following reasons. Conical shapes are of interest due to their ability of sensing performances based on receptor-analyte-interactions within the pore region. In addition, the cylindrical pores offer the possibility to control the pore diameter by tuning the track-etching time, which is essential for the development of reproducible and adjustable pore dimensions. In general, the purchased membranes investigated in this study consist of PET-substrates having a thickness of  $12\ \mu\text{m}$  to ensure a better comparability with the GSI-membranes. Moreover, the membranes contain either already nanopores, that have been etched by the company itself, or only contain the latent tracks (irradiated membranes, i. e., where the nanopore fabrication is still pending). To this end, membranes having an array of  $10^4$  or  $10^7$  pores/ $\text{cm}^2$  and ion track/ $\text{cm}^2$  are examined, respectively.

To this end, the nanopore shape control is reached either by using the *in-situ* or *ex-situ* strategy (see Figure 51). Herein, the *in-situ* approach displays the classical route of transforming tracks into pores. Depending on etching conditions, the pore shape results in symmetrical or asymmetrical forms. Here, *in-situ* study uses the track-etching method and are carried out on the irradiated membranes by adapting rout A (see section 2.2.1). On the contrary, the *ex-situ* technique demonstrates the approach to create conical shapes from cylindrical pores using post-treatment method using route B (see section 2.2.2). For *ex-situ* studies, membranes already containing cylindrical nanopores (100 nm diameter) are used.

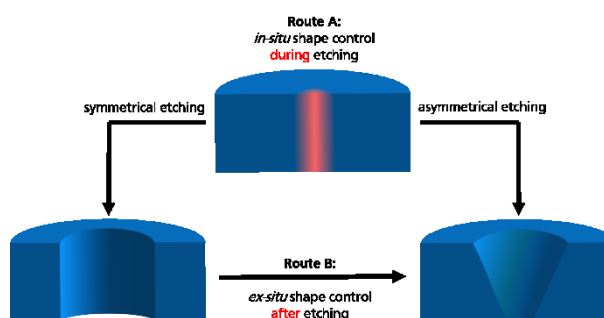


Figure 51: *In-situ* and *ex-situ* shape control of nanopores.

### 1.2.1. *In-situ* Control over Nanopore Dimensions

To investigate the etching behaviour, irradiated *it4ip*-membranes are etched according to the etching protocols for conical and cylindrical shapes already used for GSI-membranes (see CHAPTER II, section 1.1 and 1.2). Afterwards, the etched membranes are characterized by *IV*-measurements as well as by SEM-imaging.

Here, the cylindrical pore fabrication is carried out by immersing the membranes in 2 M NaOH-solution at 50°C for a pre-set time period. In order to estimate the etching rate of *it4ip*-foils, the etching process is terminated after 10 min, 20 min, 30 min and 60 min. Then, the pore formation of the as-prepared membranes is evaluated by SEM-images (see Figure 52).

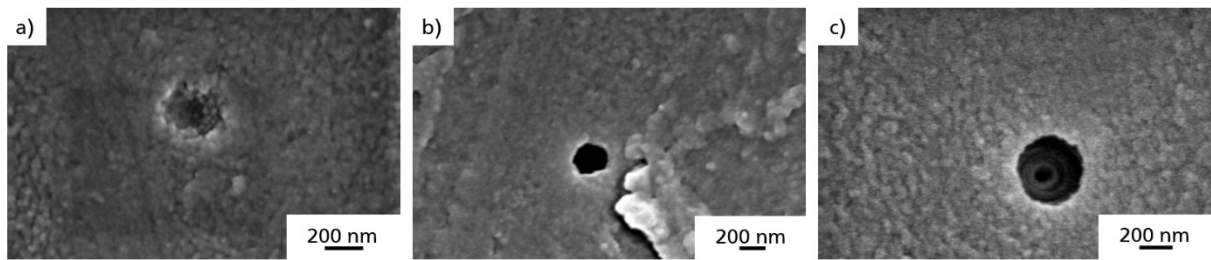


Figure 52: *SEM*-images of commercial membranes ( $10^4$  ion tracks/cm<sup>2</sup>) after immersing the membranes in 2 M NaOH-solution at 50 °C for 20 min (a), 30 min (b) and 60 min (c).

After 10 min of etching time, no pore formation is observed at all, whereas for 20 min of etching, the formation of pores is resolved along with insufficient depth indicating the start of the pore generation (see Figure 52a). By increasing the etching time to 30 min (Figure 52b), the pore formation is more significant and provides an estimated nanopore opening of 262 nm. After 60 min of etching time, the pore formation progress revealed a base opening of about 437 nm. Moreover, the images provide sufficient pore depths.

Membranes having only  $10^4$  tracks/cm<sup>2</sup> are difficult to investigate under the SEM. Due to the low pore density the localization of pores can be time-consuming. Moreover, the estimated nanopore diameter could not be averaged due to large inter pore distance. Therefore, the etchings series is repeated on nanopore membranes having  $10^7$  tracks/cm<sup>2</sup> and imaged again by SEM.

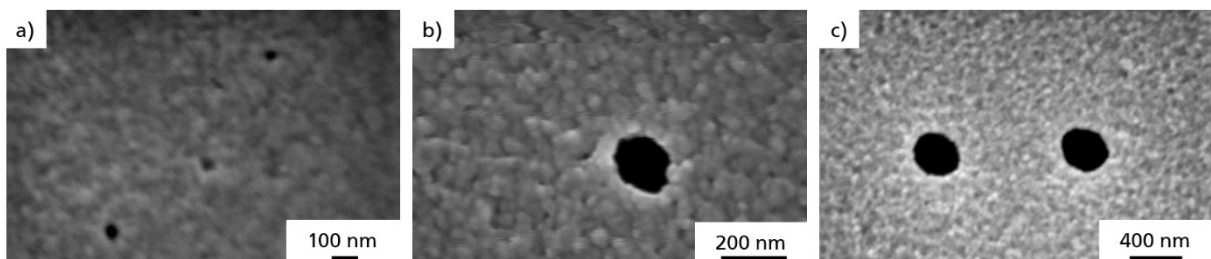


Figure 53: *SEM*-images of commercial membranes ( $10^7$  tracks/cm<sup>2</sup>) after immersing the membranes in 2 M NaOH-solution at 50 °C for 10 min (a), 30 min (b) and 60 min (c).

The pore diameter calculations of the higher fluence membranes are much more practicable. The estimated pore diameter after 10 min of etching time amounts to  $57 \text{ nm} \pm 12.3 \text{ nm}$  (see Figure 53a) accompanied by insufficient resolved images. Upon increasing the etching time to 30 minutes, the pores are resolvable with good quality and the calculated diameter is  $161 \text{ nm} \pm 5.6 \text{ nm}$  as an average over 10 pores (Figure 53b). After 60 min, the pore diameter is more than two times higher ( $356 \text{ nm} \pm 4.5 \text{ nm}$ ), indicating linear increase in pore diameter.

For a better comparability, GSI-membranes having the same track fluence are etched under the same conditions and presented in Figure 54.

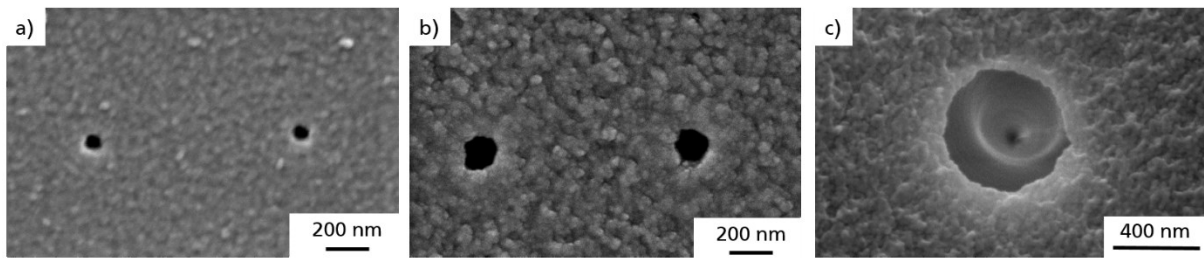


Figure 54: SEM-images of GSI-membranes ( $10^7$  tracks/cm<sup>2</sup>) after immersing the membranes in 2 M NaOH-solution at 50 °C for 20 min (a), 30 min (b) and 60 min (c).

In contrast, GSI-membranes reveals pore sizes of  $97 \text{ nm} \pm 4.6 \text{ nm}$  after 10 min,  $198 \text{ nm} \pm 3.2 \text{ nm}$  after 20 min and  $526 \text{ nm} \pm 1.9 \text{ nm}$  for 60 min calculated on an average of 10 pores.

For a better overview, the estimated pore diameters are correlated with the etching times and presented in Figure 55a.

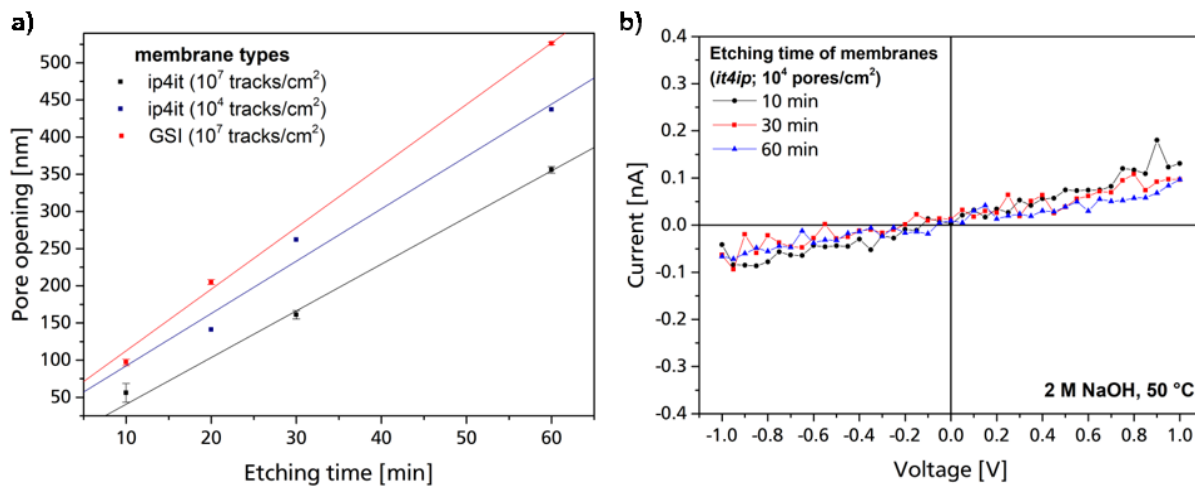


Figure 55: Nanopore opening as a function of etching time (a). *IV*-measurements of commercial membranes ( $10^4$  tracks/cm<sup>2</sup>) after immersing the membranes in 2 M NaOH-solution at 50 °C for certain etching times (b).

Hence, the etching rate per minute is derived from the numerical value of the slope. Here, the highest etching rate is found for GSI-membranes ( $8.2 \text{ nm/min} \pm 0.3 \text{ nm}$ ). In contrast, the linear fit of the commercial membranes with  $10^7$  tracks/cm<sup>2</sup> provides an etching rate of  $6.2 \text{ nm} \pm 0.3 \text{ nm}$  being 25% lower compared to the membranes irradiated at GSI accelerator. Additionally, the data obtained from  $10^4$  tracks/cm<sup>2</sup> are also presented with their estimated etching rate of  $\sim 7.0 \text{ nm} \pm 1.3 \text{ nm}$ . However, the last-mentioned rate must be treated with caution because the estimated pore diameters are not represented by average values.

Further, the as-prepared membranes were characterized by *IV*-measurements according to the protocol introduced in section 3.2.1 (CHAPTER II). Here, only the membranes having  $10^4$  tracks/cm<sup>2</sup> were examined, because proceeding *IV*-measurements with highly porous membranes is not feasible. (204) According to Figure 55b, the current flow is recorded in pA-range regardless of the etching times. In contrast, single pore membranes provide at least ionic transports in the nanoampere range assuming that the measured current flow is not originated by the ionic transport across nanopores but across the latent tracks of insufficiently etched membranes. TEM-studies of Trautmann *et al.* demonstrated the track formation in the

range of several nanometres in polymeric substrates emphasizing the assumptions of track-promoted current record. (216)

In order to demonstrate this assumption, the pore depth is estimated by imaging the cross-sections of the commercial membranes after 30 min and 60 min of etching time (Figure 56) by following the protocol in section 3.3.1 (experimental part).

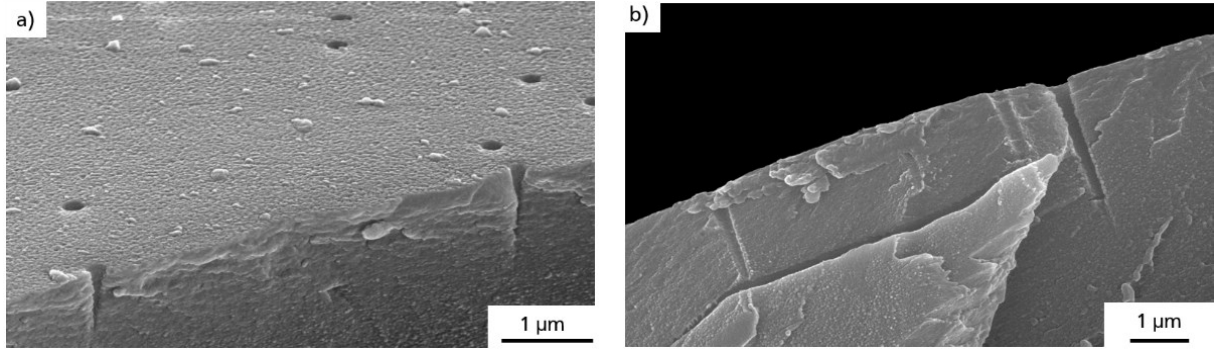


Figure 56: SEM-images of cross-sections of commercial membranes ( $10^7$  track/cm<sup>2</sup>) after 30 min (a) and 60 min (b) of etching time.

In contrast to the top-view SEM-images, the cross-section reveals discontinuous pore-profiles across the membrane.

Because successful pore formation is only achievable, if the track etching rate  $v_t$  is significantly higher than the bulk etch rate  $v_b$ , appropriate pore generation is obtained for  $v_b/v_t > 1000:1$ , particularly for cylindrical pores. (217) Based on the cross-sections, the real pore depth  $d_{pore}$  is calculated to  $0.85 \mu\text{m} \pm 0.36 \mu\text{m}$  (after 30 min) and to  $2.94 \mu\text{m} \pm 0.48 \mu\text{m}$  (after 60 min) as an average over 10 pore profiles. It can be assumed that the bulk etching rate  $v_b$  of PET for commercial and GSI membranes is the same, since it only depends on the etching solution, the temperature and the etching concentration being identical for both membranes. (218) The bulk etch rate  $v_b$  found in the literature amounts to 2 nm/min. (74) Considering the etching time of 30 min and 60 min,  $d_{bulk}$  should be 60 nm and 120 nm, respectively. Figure 57 displays, that the real pore depth  $d'_{pore}$  in dependence of the distance to the original membrane surface and can be calculated using  $d'_{pore} = d_{pore} + d_{bulk}$ . Therefore,  $d_{pore}$  should be  $0.91 \mu\text{m}$  (30 min) and  $3.06 \mu\text{m}$  (60 min), respectively. Now, the track-etching rate  $v_t$  is defined as:

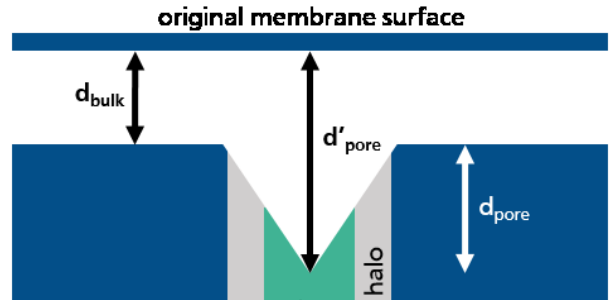


Figure 57: Schematic track-etching process and the respective distances  $d$ .

(218) The bulk etch rate  $v_b$  found in the literature amounts to 2 nm/min. (74) Considering the etching time of 30 min and 60 min,  $d_{bulk}$  should be 60 nm and 120 nm, respectively. Figure 57 displays, that the real pore depth  $d'_{pore}$  in dependence of the distance to the original membrane surface and can be calculated using  $d'_{pore} = d_{pore} + d_{bulk}$ . Therefore,  $d_{pore}$  should be  $0.91 \mu\text{m}$  (30 min) and  $3.06 \mu\text{m}$  (60 min), respectively. Now, the track-etching rate  $v_t$  is defined as:

$$v_t = \frac{d'_{pore}}{t} \quad (\text{Eq. 5})$$

Based on the estimated  $d'_{pore}$ , the track etching rate is around 30 nm/min (30 min) and 51 nm/min (60 min), respectively. Zhu and co-workers already showed the changes of track etching rates upon increasing the distance from the surface. This is due to limitations regarding the degree of freedom for the ionic and molecular movement.

---

Finally, the estimated  $v_t/v_b$ -ratio is between 15:1 and 25:1. In contrast, the already reported  $v_t/v_b$ -ratio of GSI-membranes is about 1000:1 being 100-times higher than the  $v_t/v_b$ -ratio of commercial membranes. (217) To enable a continuous pore formation across the entire substrate length, an etching time of about 2 hours is required in contrast to the formation of GSI-pores revealed after 10 min of etching. This impedes an *in-situ*-etching of commercial membranes being additionally impracticable for research fields and applications.

Adequate track etching is influenced by the ion track nature. Regarding the GSI-membranes, the track formation is performed by bombarding the PET-substrate with accelerated gold-ions ( $\text{Au}^{26+}$ ). In contrast, the beam irradiation of the commercial membranes is carried out using accelerated argon ions ( $\text{Ar}^{9+}$ ). A successful track formation is caused by sufficient energy loss of the accelerated ions within the polymer. The penetration depth of the projectile is mathematically described by the BETHE-BLOCH-equation (section 2. 1. 1, CHAPTER I). Here, the track formation is obtained only, if the charge state and kinetic energy of the projectile is sufficiently high. (77) At GSI-facility, the highly charged gold ions are interacting with the substrate material having an energy of 11.4 MeV/u. (68) In contrast, the  $\text{Ar}^{9+}$ -irradiation is carried out with 5.5 MeV/u.(208) Thus, the track formation is less stable upon the use of low energy and lighter ions enhancing the chance of annealing process within the irradiated material. (219) Consequently, the problematic etching behaviour of the commercial membranes is due to the less reactive tracks after argon-irradiation.

Therefore, following studies are focussing on post-shaping of commercial membranes that have already been bought with cylindrical pores.

### 1.2.2. *Ex-situ* Control of Nanopore Dimensions

Because the track-to-pore transformation of commercially available membranes is questionable, further studies are investigated to prepare conical shape nanopores in commercial membranes. For this purpose, membranes are purchased from *it4ip* having already  $10^4$  and  $10^7$  pores/cm<sup>2</sup> having a diameter of 100 nm and a cylindrical shape.

In the beginning, the actual pore conditions in terms of fluence and diameter are characterized using SEM-imaging and compared with GSI-membranes. Then, the *ex-situ* shaping is carried out by exposing both the commercial and GSI membranes to DMF solution from one side. The formation of asymmetrical pores is expected and monitored by *IV*-measurements prior and after the solvent treatment. Further, the re-shaped DMF-treated membranes are modified with EDA and investigated by *IV*-measurements to evaluate the surface functionalization reaction. Note that for the SEM-imaging highly porous membranes ( $10^7$  pores/cm<sup>2</sup>) are used, while *IV*-measurement were performed with membranes with a pore density of  $10^4$  pores/cm<sup>2</sup>.

## Pretest: porous GSI-membranes vs. porous commercial membranes

In order to examine the actual pore density of both membranes, overview-images (Figure 58), and cross sections (Figure 59) are obtained by SEM-imaging.

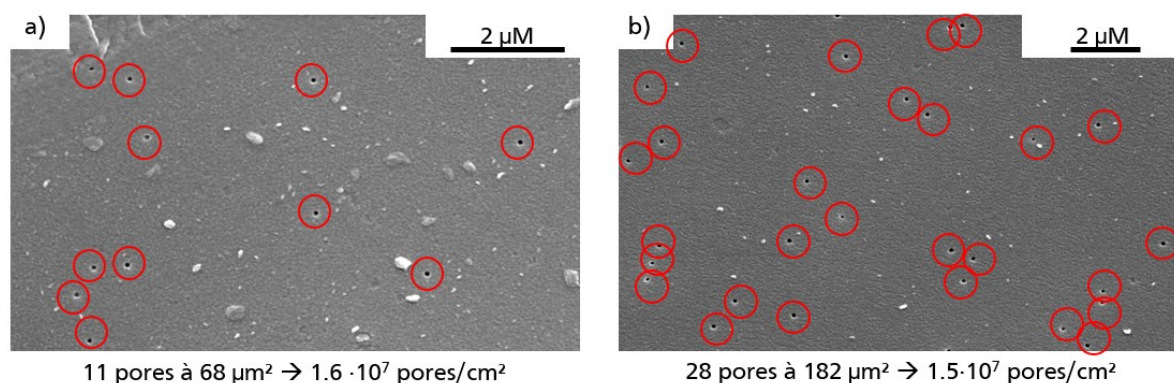


Figure 58: Surface SEM-images of GSI-membranes containing 100 nm pore diameter (a) and commercial membranes containing nanopores with 100 nm diameter (b). In both cases, the specification of the supplier determines pore densities of  $10^7$  pores/ $\text{cm}^2$ . Red circles simplify the pore localization.

Based on surface images of membrane shown in Figure 58, the pore number is estimated (red circles) and correlated to the microscopic area. For the case of GSI-membranes (Figure 58a), 11 pores are located on an area of  $68 \mu\text{m}^2$  revealing an effective pore density of  $1.6 \cdot 10^7$  pores/ $\text{cm}^2$ . Regarding Figure 58b, the estimated pore number amounts to 28 pores distributed on a  $182 \mu\text{m}^2$ -area. The underlying pore density is  $1.5 \cdot 10^7$  pores/ $\text{cm}^2$ .

Because the *in-situ* studies of the commercial nanopores revealed a high number of insufficiently etched pores, cross-section of the membranes are prepared to investigate the pore depth (Figure 59).

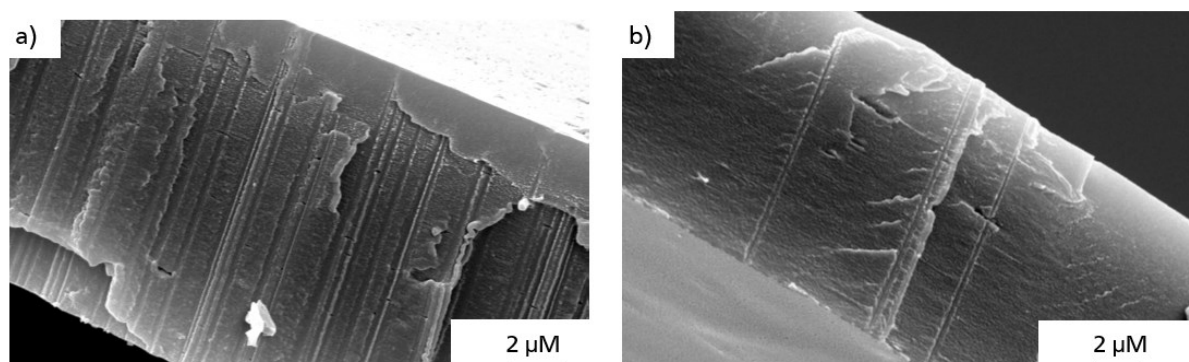


Figure 59: SEM-images showing the cross-section of nanopores (100 nm) of GSI-membranes (a) and commercial membranes (b). In both cases, the specification of the supplier determines pore densities of  $10^7$  pores/ $\text{cm}^2$ .

The cross-section shows the consistent pore profile across the entire membrane thickness. However, the GSI-membranes (Figure 59a) obtain a higher pore number located on the breaking edge compared to the commercial pores (Figure 59b) suggesting a lower pore density of the commercial membranes than the specified pore density specified by the supplier. On the one hand, the lower pore number could be due to annealing effects of the polymeric substrate as already discussed during the *in-situ*-study. On the other hand, the irradiation step of the GSI-

---

foils is different than that of the commercial ones. At GSI-facility, the irradiated area amounts to  $\sim 5 \text{ cm}^2$ , equal to the area of the polymeric foils. The irradiation area of the commercial membranes has the size of a DIN-A4-sheet, namely  $623.7 \text{ cm}^2$  suggesting a more defocused ion beam and, therefore, highly scattered track density was obtained.

To estimate the effective pore diameter, higher resolved top-view SEM-images were prepared and are presented in Figure 60.

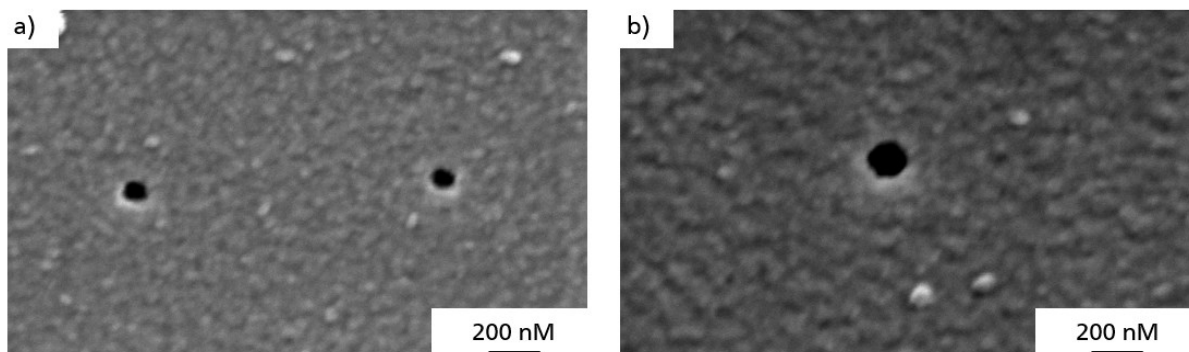


Figure 60: SEM-images showing the top-view of GSI-membranes containing 100 nm pore diameter (a) and commercial membranes containing already etched nanopores with 100 nm diameter (b). In both cases, the specification of the supplier determines pore densities of  $10^7$  pores/ $\text{cm}^2$ .

Here, the estimated pore size amounts to  $97 \text{ nm} \pm 3.1 \text{ nm}$  (GSI-membranes). The pore diameter of commercial membranes is 14% larger than GSI-pores accompanied by a higher deviation, namely  $109 \text{ nm} \pm 9.6 \text{ nm}$ , suggesting that inconsistent track nature during the fabrication process and the irradiation with lighter ions. Here, the diameter calculation was performed on the average of 10 pores.

Overall, the comparison of GSI and commercial membranes gave adequate results. Although, the pore deviation is higher and the pore density of commercial membranes is slightly smaller, the estimated pore sizes are in the same range. Moreover, the low pore density of commercial membranes could be beneficial aiming the development of commercial nanopores to be used in sensing applications. Because single pore membranes are not commercially available, the pore density should be as small as possible.

### DMF-Promoted Asymmetrical Nanopores

Fink *et al.* described that the swelling effect is originated by incorporation of the solvent molecules leading to a phase transition from a solid state to a viscous gel accompanied by a volume expansion. (220) For this purpose, the post-treatment is performed in the measurement cell used for *IV*-measurements upon exposing the membranes to pure DMF on one side. The confined shaping of cylindrical nanopores is monitored by *IV*-measurements prior and after the DMF-treatment using membranes with pore densities of  $10^4$  pores/ $\text{cm}^2$ . Especially, the highly hydrophobic PET-membranes show favoured interactions with organic solvents.

For this purpose, the membranes are clamped into the measurement-cell and a reference *IV*-curve was recorded using 0.1 M KCl-electrolyte (PBS buffer, pH 7). Then, the electrolyte is removed and on one side pure water and on the other side pure DMF was filled. After 8 hours, the half-cells were emptied, washed with pure buffer solution and refilled with electrolyte. Here, the *IV*-curves are displayed in Figure 61 measured at differed pH values (pH 3, 7, 10).

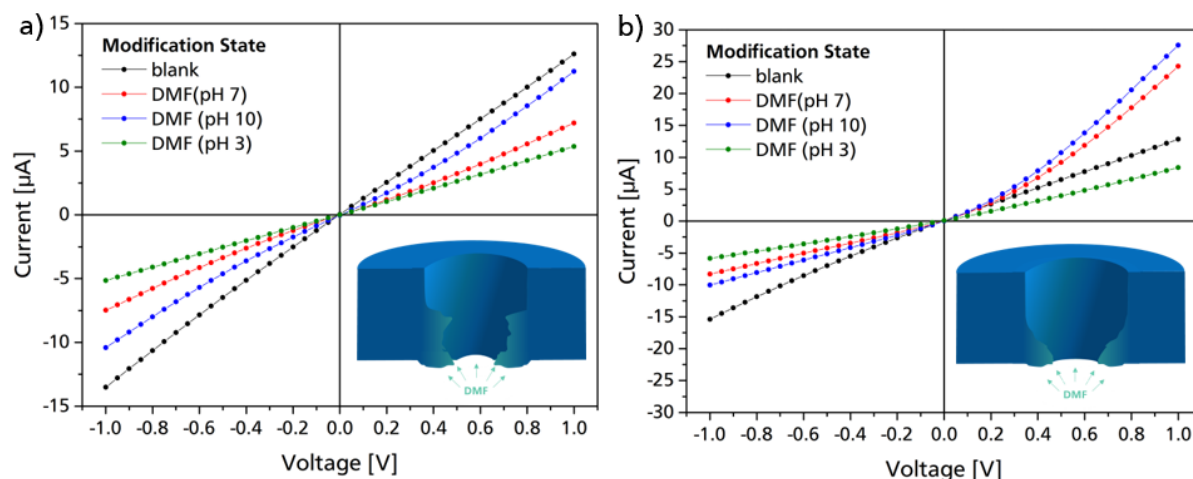


Figure 61:  $I/V$ -curves of GSI-membranes containing nanopores (100 nm)(a) and commercial membranes containing already etched nanopores of 100 nm diameter (b) before and after DMF-treatment over 12 h, measured at different pH values. In both cases, the specification of the supplier pore densities of  $10^4$  pores/cm<sup>2</sup>.

As expected, the  $I/V$ -curves of the blank membranes showed an expected linear behaviour, due to the equal transport of anions and cationic across the membrane. Upon the one-sided DMF-treatment, the asymmetrical swelling of the membrane is evidenced by the generation of an asymmetrical  $I/V$ -curve exhibiting current rectification behaviour. Note that the ionic transport is enhanced for cations due to the negatively charged pore surface of unmodified pores and therefore conical pore shapes reveal positive rectification behaviour. Regarding Figure 61, the commercial membranes behave exactly as expected. Moreover, at pH 10, the ionic transport is even more enhanced due to the higher degree of deprotonated surface groups. In contrast, in acidic surrounding the surface groups are protonated and provides an uncharged/ neutral pore surface. Therefore, the  $I/V$ -curves at pH 3 reveal a loss of rectification due to the movement of both cations and anions across the uncharged membrane. On the contrary, GSI-membranes show no rectification behaviour after DMF-treatment. The  $I/V$ -curves are still symmetrical but the  $I/V$ -behaviour is changed from linear to slightly S-shaped curve, which can be observed for nanopores with cigar-like shapes (92). Stating the higher wettability of the GSI-pores compared to the commercial pores, the enhanced hydrophilicity of GSI-nanopores causes a profound penetration of DMF-molecules within the deeper pore regions leading to more symmetrically swelled pores. Industrial pore membranes are known to be covered with a layer of poly(vinylpyrrolidone) to enhance the hydrophilicity. Therefore, enhanced hydrophilicity reduces the depth of penetration of organic solvents providing the favoured swell of pores near the membrane surface.

Overall, the *ex-situ* control of nanopore shapes on commercial nanopores was successfully adapted by converting cylindrical pores into asymmetrical pores. In order to modify commercial nanopores, the DMF-treated membranes are functionalized with EDA units. Here, the EDA-modification was used due to a simple proceeding and, if successful, significant changes in  $I/V$ -behaviour can be expected.

### DMF-Promoted Modification of Nanopores

Upon the covalent attachment of EDA-moieties onto the nanopores, the pore surface is decorated with amino groups, whose protonation state depends highly on the pH-value. The experimental procedures were performed in DMF-solution using the HATU-promoted covalent attachment of EDA according to the protocol described in experimental section 2.1.2

(CHAPTER II). *IV*-measurements were performed before and after the EDA-treatment to monitor the functionalization progress (see Figure 62).

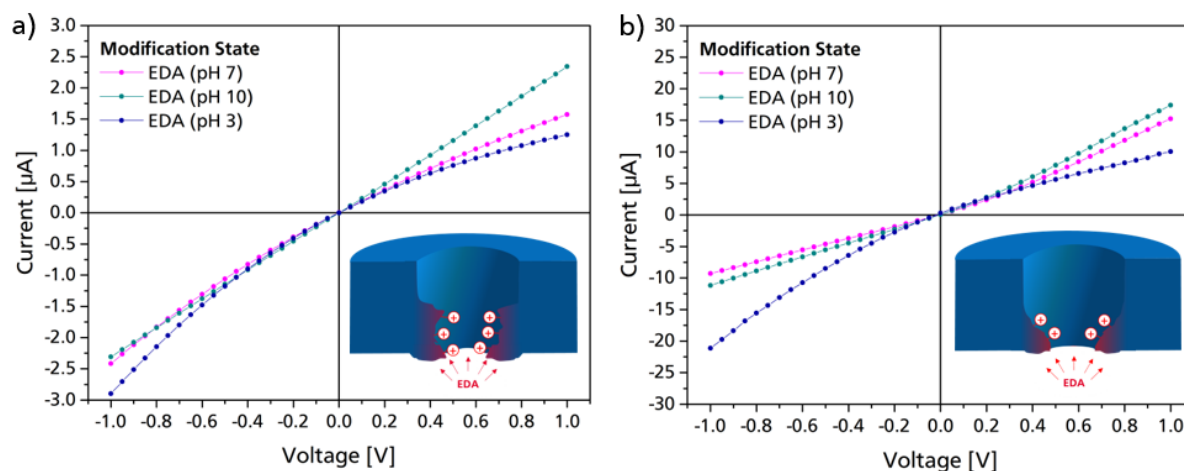


Figure 62: *IV*-curves of GSI-membranes containing 100 nm pore diameter (a) and commercial membranes containing already etched nanopores with 100 nm diameter (b) after EDA-Modification, measured at different pH values. In both cases, the specification of the supplier provides pore densities of  $10^4$  pores/cm<sup>2</sup>.

In general, the modification provides an expected reduction of current flow that ranges from  $\sim 1 \mu A$  to  $2.5 \mu A$ . Because the modification is carried out in DMF, the modification mixture causes not only EDA-terminated pore surfaces but also an on-going swelling. Regarding the commercial membranes in Figure 62a, *IV*-curves obtained at pH 3 show negative rectification (inversion of rectification) behaviour suggesting the presence of positively charged groups on pore walls. In fact, the EDA-modification creates amino-terminated pore surfaces being positively charged in acidic solutions. Consequently, negative rectification behaviour is observed during *IV*-measurement indicating the successful EDA-modification.

Upon increasing the pH-value to basic conditions, an inversion of rectification is observed, indicating the presence of negatively charged groups on the pore surface. Because the modification is carried out only from one side, one part of the nanopore remains unmodified and contains still COOH-groups, whereas the other part is covered by amino-groups (see Figure 63).

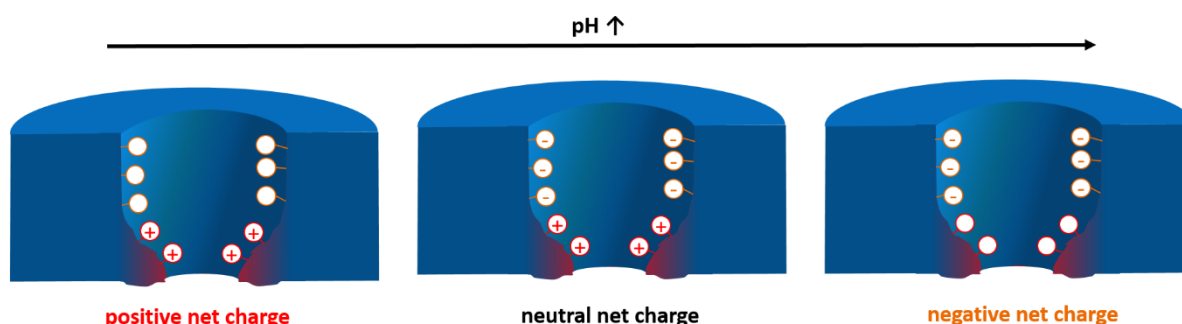


Figure 63: pH-dependant surface charge densities inside commercial membranes upon one-sided EDA-modification.

During *IV*-measurements, the ionic transport is mainly influenced by the charge state of the nanopore. In acidic surroundings, the COOH-groups are uncharged, whereas the protonation of the NH<sub>2</sub>-groups causes the formation of positively charged NH<sub>3</sub><sup>+</sup>-moieties. Thus, the cation

---

movement is hindered, and respective *IV*-curves show negative rectifications. At neutral pH, the deprotonation of the COOH-groups and NH<sub>3</sub><sup>+</sup>-groups occurs generating uncharged NH<sub>2</sub>-groups along with negatively charged COO<sup>-</sup>-groups. Further pH-increase causes the ongoing growth of negative charge density due to a higher degree of deprotonated COO<sup>-</sup>-moieties, while NH<sub>2</sub>-groups remained uncharged. Thus, the anionic movement is discriminated along with an enhanced cationic movement providing a significant of positive rectification behaviour.

A similar *IV*-behaviour is also observed for GSI-membranes upon EDA-modification. According to Figure 62b, the *IV*-curves show negative rectification at pH 3, due to positively charged amino-moieties inside the pore region. In contrast to the commercial membranes, the increase of pH provides linear *IV*-curves indicating uncharged pore regions. Thus, it can be suggested that the pore surface is almost completely covered by EDA-moieties, which are uncharged at higher pH values. Based on the swelling experiments, an enhanced penetration depth of DMF into GSI-membranes was observed. Hence, the modification is carried out in DMF leading to not only a significant swelling effect but also a higher degree of EDA-moieties inside the pore occurs. Thus, the increasing pH-values causes only to the deprotonation of the amino-groups and a respective neutral net charge as evidenced from the linear *IV*-curves.

Finally, the EDA-modification was successfully obtained on both GSI and commercial membranes. *IV*-measurements were used to monitor the functionalization process, which was carried out only from one side using DMF as solvent. Consequently, significant current rectification is obtained, indicating a confined asymmetric pore shape.

### 1.3. Conclusion

The ability of commercial PET-membranes (from *it4ip S. A.*, Belgium) to serve as substrate for the nanopores was tested in two studies.

In the first part, only the irradiated PET-membranes having a track density of 10<sup>4</sup> and 10<sup>7</sup> tracks/cm<sup>2</sup>, were etched from both sides with 2 M NaOH at 50 °C in order to obtain cylindrical nanopores. The etched membranes were analysed by SEM-imaging and *IV*-measurements. Based on the membranes having 10<sup>7</sup> track/cm<sup>2</sup>, the respective etching rate was estimated around 7.0 nm/min. Moreover, the same etching series using standard membranes irradiated at the GSI-facility revealed an etching rate of 8.2 nm/min indicating only minor differences of etching rates. In contrast, *IV*-measurements of the commercial membrane did not provide measurable ionic currents. In fact, the recorded *IV*-curves remain in the pA-range suggesting that pore-like structures do not extend across the entire length of the membrane. SEM-Investigation of the cross-section of the respective membranes confirmed the presence of insufficiently etched pore structure assuming still unetched track-zones inside the membranes. In addition, the highest track-to-bulk ratio was calculated to about 25:1 suggesting less reactive track nature of the commercial pores than the GSI-membranes. The reduced track etching is caused by the use of lighter accelerated ions (Ar<sup>9+</sup>-ions with 5.5 MeV/u) compared to the heavier and highly charged Au<sup>26+</sup>-ions with 11.4 MeV/u used at the GSI-facility.

In the second part, commercial membranes were purchased having already cylindrical nanopores (100 nm diameter; 10<sup>4</sup> pores/cm<sup>2</sup>). The formation of conical shapes inside the cylindrical pores was investigated by treating the membranes with DMF. The post-shaping was monitored using *IV*-measurements in comparison with cylindrical shaped GSI-membranes having the same pore density and diameter. As expected, upon DMF-promoted swelling from

---

one side, current rectification behaviour was observed for commercial membranes. On the contrary, slightly *S*-shaped *IV*-curves were obtained by GSI-membranes presumably due to their higher hydrophilic surface that amplifies the diffusion of the molecules inside deeper pore regions. Uniform swelling of the entire pore region is evidenced by the almost linear *IV*-curves. Finally, the DMF-membranes were modified with EDA-molecules to compare surface functionalization on both membrane types. The experimental results showed an expected negative rectification behaviour due to the enhanced anion passage across the positively charged nanoporous membrane.

Overall, the commercial membranes appear as an alternative and promising substrate for nanopore based biosensors. Surface modification was carried out by attaching EDA-molecules inside the pore area. The *IV*-characterization obtained sufficiently modified pores. Hence, conical structures require an additional post-treatment step that could restrain the application of commercial membranes.

---

## 2. Nanopores inside Biodegradable Poly(lactic acid)-Membranes

---

### 2.1. Introduction

Over the recent years, the track-etching technique have been established as the main fabrication method of polymeric nanopores offering the ability to adjust pore size and shape. Along with the increased scientific interest of nanopore based molecular detection systems, the commercial use of highly polymerized films and membranes became questionable due to the ecological and environmental difficulties.

Among the variety of polymeric substrates, poly(*L*-lactic acid), herein referred as PLA, is considered as a sustainable, biodegradable and biocompatible polymer.(221) The monomeric lactic acid occurs naturally but their commercial manufacturing is based on the anaerobic fermentation of various sugars into lactic acid promoted by specific lactic acid bacteria. (222) Hence, the PLA degrades within two years and, therefore, it is frequently used in clinical surroundings as a semi-permanent prosthesis material. (223) Overall, its environment-friendly production in combination with the biocompatibility and reliable degradability emphasizes the investigation of PLA films as promising novel nanopore substrates.

During the past twenty years, many routs of PLA-etching methods were established by the selective removal of PLA from block copolymer substrates. The sacrificial role of PLA compounds within multiblock substrates lead to the generation of mesoporous materials. Moreover, pore dimensions offered adequate control simply by varying the PLA-ratio. For instance, Olayo-Valles and co-workers obtained highly defined cylindrical pore structures of 69 nm diameter within poly(styrene)-*b*-poly(*L*-lactic acid) (PS-*b*-PLA) films. Here, they exposed the block polymer in 50 mM NaOH solutions prepared with 60:40 water-methanol-ratio. (224) Rzayev *et al.* also achieved porous structures using PLA in triblock polymers with the same etching conditions. Furthermore, they demonstrated the ability to regulate the etching rate by varying the temperature or the methanol-ratio inside the etching solution. (225) In addition, Cummins *et al.* used etchants like NaOH, NH<sub>4</sub>OH and the enzyme proteinase K and established several selective PLA-etching methods on poly(styrol)-poly(*L*-lactic acid)-blockpolymer (PS-*b*-PLA) substrates. The etching methods revealed different etching rates, where the lowest etching rate was obtained using proteinase K, and the highest etching rate was achieved in NaOH-solutions. (226) However, the specific generation of nanopores inside homopolymeric membranes consisting only of PLA-chains is not yet reported.

In this study, the track-etching of PLA-substrates is evaluated inspired from the selective PLA-degradation of multiblock polymers. The PLA-foils were irradiated at the UNILAC at the GSI-facility using accelerated gold ions (Au<sup>26+</sup> with 11.4 MeV/u). The heavy ion irradiated foils were treated with various etchants and different experimental conditions to obtain reproducible porous structures inside the novel PLA substrate. In addition, the track-to-bulk-etching rate was examined, whose numerical ratio gives insights about the successful formation of nanopores during the track-etching process.

## 2.2. Results and Discussion

The sufficient track-etching was evaluated using SHI-irradiated PLA-membranes having a thickness of 50  $\mu\text{m}$  and various pore densities (single pores to  $10^7$  pores/ $\text{cm}^2$ ). To receive a reproducible etching protocol, the etching process was systematically investigated by varying the following parameters:

- *Etchant*: NaOH,  $\text{NH}_4\text{OH}$
- *Solvent*:  $\text{H}_2\text{O}$ ,  $\text{H}_2\text{O}/\text{MeOH}$
- *Temperature*: 30-50°C
- *Etching time*: 10-120 min

During track-etching process, etchant concentrations, exposure time and temperature were varied. Etching was proceeded either in pure water or in water-methanol-mixtures. Afterwards, the membranes were characterized by SEM-images. In order to evaluate the etched structures more precisely, the etched PLA-membranes were electrolessly coated with metallic films. After sufficient PLA-removal, three-dimensional negative replica were obtained which is highly resolvable by SEM-imaging to provide pore profiles and depths (see Figure 64).

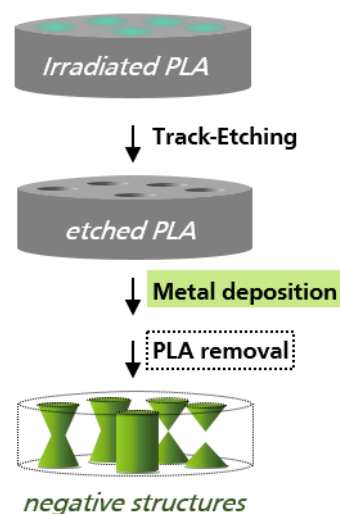


Figure 64: shape characterization approach towards PLA-nanopores. First, the irradiated PLA membranes are pre-treated by organic solvents or UV-sensitization. Etched membranes are analysed by SEM-imaging. Additionally, replica were obtained by metal deposition and PLA-removal.

In general, *IV*-measurements are well-established to analyse nanopore membranes. Their respective ionic transport gives insight about the surface charge density and pore diameter, respectively. Therefore, prior to all etching studies, the unetched membranes were investigated by *IV*-measurement following the protocol in as described in section 3.2.1 (CHAPTER II).

The recorded current values of more than  $\pm 500$  nA are displayed in the Figure 65. Recorded currents cannot be originated by ionic passages through the pore regions. An insufficient packed material inside PLA-membranes is expected accompanied by a higher degree of amorphous regions. Hence, the molecular structure is composed of an aliphatic back bone with repetitive methyl groups, which amplifies the formation of randomly distributed polymeric chains (Figure 65). On the contrary, PET-chains are constructed of terephthalate-units. During the PET-film production, the aromatic moieties aligned in parallel orientation by  $\pi$ -stacking, that provides higher degrees of crystallinity. (227)

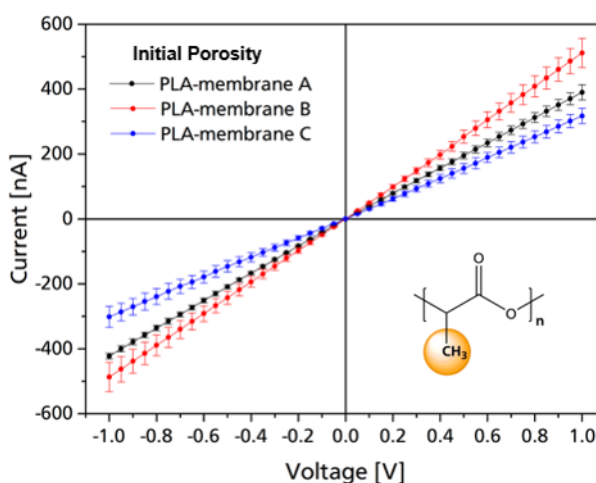


Figure 65: *IV*-curve of three exemplary PLA-membranes prior to the etching step measured in 0.1M KCl solution.

---

As a consequence, this internal insufficiently dense structure of PLA-membranes impede the membrane characterization throughout *IV*-measurements and will be excluded from the discussion.

In this study, the PLA-etching is only focused on cylindrical nanopores. Here, adequate etching times are expected due to the symmetric etching setup carried out on both sides simultaneously.

### 2.2.1. Temperature-Dependence of PLA-Track-Etching

To this end, the etching procedure was examined separately either in NaOH or NH<sub>4</sub>OH solution. Further, both etching series were carried out in presence or absence of methanol. Here, the etchant concentration was fixed at 50 mM according to the etching condition in the aforementioned literature. (224–226) The etching was carried out for 1 hour at different temperatures, namely 30°C, 40°C and 50°C and characterized by scanning electron microscopy.

Upon SEM-imaging, the electron beam interacts with the PLA-samples very intensively, that even the lowest beam energy at 5 keV caused huge deformations on the PLA-surface along with enormous degassing and bloating effects. Although, a conductive film of sputtered gold (10 nm) was coated onto the PLA-membranes. Even a thicker gold layer coated onto the pore surface (80 nm) could not prevent deformations. Therefore, the SEM-images could not be obtained at high resolutions and display only an overview image of the etched PLA-surfaces.

Figure 66 demonstrates the PLA-surface obtained after aqueous NaOH-etching (50 mM, pure water) for 1 hr at different temperatures.

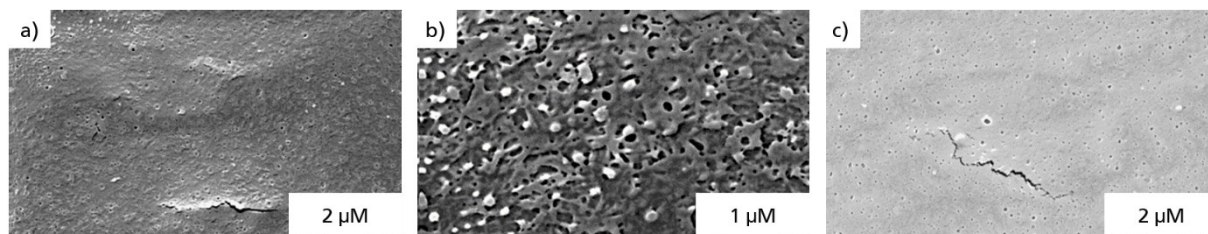


Figure 66: Top-view SEM-images of PLA membrane ( $10^7$  tracks/cm<sup>2</sup>) after 1 h of immersion into aqueous NaOH-solution (50 mM) at 30 °C (a), 40°C (b) and 50°C (c).

By comparing the images of PLA etched at 30°C, 40°C and 40°C, no significant pore formation is observed. However, the exposure to etching solutions caused some roughness on the surface (Figure 66a and c). Unfortunately, high focus could not be achieved due to the deformations under the SEM-beam as evidenced by the bulged and cracked sample surfaces. Figure 66b obtained at higher resolution provides a more detailed look of the surface. Here, an extreme peeling of the sample surface occurred. The picture is reminiscent of an entire removal of the surface layer by assuming the different etching behaviour, that may occur when the top surface of the sample exhibits a slightly different degree of crystallinity compared to inner membrane areas. Overall, Figure 66b shows a sort of circular damaged zones at the sample surface, which could presumably indicate pore-like structures.

The reported etching studies of PLA-block polymers were also employed in etching solutions for 60:40-ratio of water and methanol. Therefore, NaOH-etching of the irradiated PLA-membranes was repeated using the same water-methanol-mixture (see Figure 67).

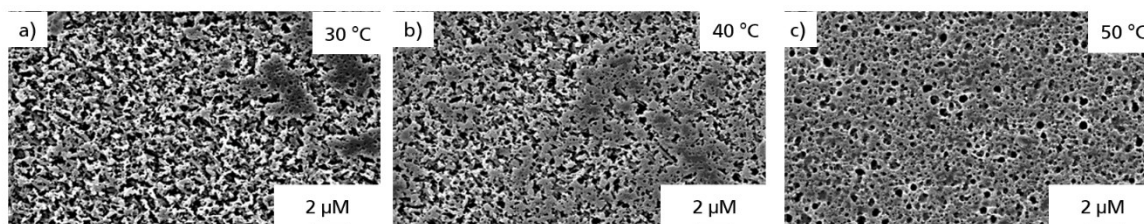


Figure 67: Top-view SEM-images of PLA membranes ( $10^7$  tracks/cm<sup>2</sup>) after 1 h of immersion in 50mM NaOH-solution prepared in water-methanol mixture (60:40) at 30°C (a), 40°C (b) and 50°C (c).

As seen from the SEM-images, the use of methanol in etching solutions leads to a highly porous surface, regardless the temperature. Moreover, in the presence of methanol the comprehensive peel-off of the surface layer appeared, indicating an amplified etching progress. However, deformation processes were less distinct during the SEM-imaging. It can be assumed that the entire membrane is pervaded by highly porous structures, ensuring an elastic reaction without crack formation during the degassing process. However, the spongy structure is obtained at all temperatures and more significant circular zones are obtained at higher temperatures due to harsher etching conditions.

The peel-off effect could be due to the presence of methanol acting as a surfactant to increase the wetting of the PLA-membranes. Methanol molecules penetrate into the tightly packed polymer structure, which increases the distance between two certain polymer chains, causing an enlarged effective contact area of the etchant (see Figure 68).

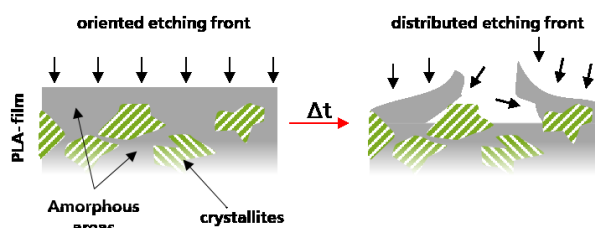


Figure 68: schematic explanation of the peel-off effect observed on PLA-membranes during the etching process.

Spohr *et al.* already reported that the penetration of methanol is enhanced for amorphous regions compared to highly orientated crystalline regions. (219) The distribution of amorphous and crystalline areas inside polymeric sheets is highly complex, but it can be stated, that during the fabrication of polymeric films, crystalline regions are formed deeper inside the polymeric film, whereas amorphous regions are located on the outer surface of the polymer film. Consequently, the methanol-induced swelling is located more at the top of the membrane surface, and therefore, the etching of the membrane surface is more facilitated. This results in a continuous peeling of the membrane surface. In addition, Menges *et al.* showed the significant impact of amorphous areas inside biodegradable polymeric films being one of the major reasons to achieve degradation in short-time frames. (228) Therefore, a huge amorphous degree is expected inside the PLA-membranes, used in this study.

To sum up, the investigation of the original membrane surface was not accessible for etching due to the peel-off effect. Hence, circular zones at 50 °C were observed that could be ascribed to pore-like structures. The etching series are repeated using the NH<sub>4</sub>OH-solutions with and without methanol in order to investigate the PLA-etching process more precisely, where NH<sub>4</sub>OH serves as a smoother etchant than the aggressive NaOH-solution.

Figure 69 shows the etching series carried out in 50 mM  $\text{NH}_4\text{OH}$ -solution at 30°C, 40°C and 50°C, respectively after 1 h of etching time in aqueous surrounding.

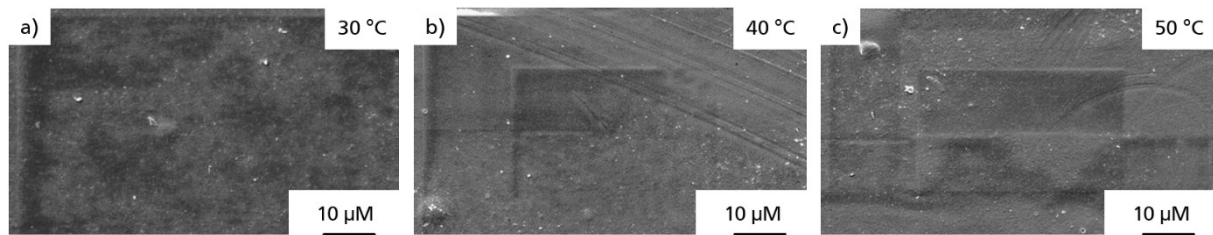


Figure 69: Top-view SEM-images of PLA membranes ( $10^7$  tracks/cm<sup>2</sup>) after 1 h of immersion into aqueous 50 mM  $\text{NH}_4\text{OH}$ -solution at 30 °C (a), 40°C (b) and 50°C (c).

The SEM-imaging was tricky, because an increase in magnification caused again uncontrollable deformation and destructive effects onto the membrane surface. Therefore, only images at low magnification states (3.5 K) were obtained. Unfortunately, no porous and no pore-like structures are obtained as evidenced from the SEM-images in Figure 69. However, the images exhibit smooth surfaces with respect to temperatures compared to the images received for NaOH as etchant. Because  $\text{NH}_4\text{OH}$  is classified as a weak base, the etching power of  $\text{NH}_4\text{OH}$  is insufficient to generate porous surface changes of the PLA-homopolymer films. For the sake of confirmation, the etching procedure was repeated in the presence of methanol, but it could not lead to significant surface changes as demonstrated by the following SEM-images (Figure 70).

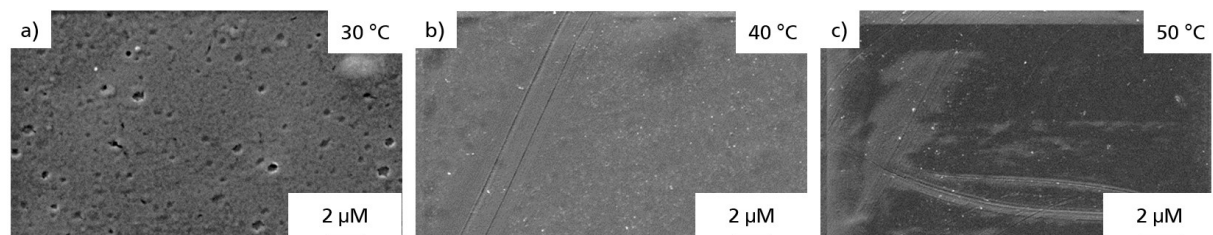


Figure 70: Top-view SEM-images of PLA membranes ( $10^7$  tracks/cm<sup>2</sup>) after 1 h of immersion into 50 mM  $\text{NH}_4\text{OH}$ -solution prepared in water-methanol mixture (60:40) at 30 °C (a), 40°C (b) and 50°C (c).

In summary, the etching of PLA-membranes was performed in NaOH- and  $\text{NH}_4\text{-OH}$ -solutions. Because peel-off effect occurred during the NaOH-etching (with/without MeOH), it was assumed that NaOH is too strong for track-etching, where methanol amplifies the peeling of the surface. Since the etching series using the weak base  $\text{NH}_4\text{OH}$  showed no pore-like transitions at all, regardless the presence of methanol, it is concluded that  $\text{NH}_4\text{OH}$ -solutions were not suitable for track-etching of PLA-membranes.

Based on the first results, further etching was carried out in NaOH-solution without MeOH at 50°C. In the next section, the concentration as well as the etching time was varied in order to examine the etching process in detail.

### 2.2.2. Concentration-Dependence of PLA-Track-Etching

To this end, the etching procedure was performed separately either in 2 M NaOH or 3 M NaOH-solution at 50°C at different etching times.

The characterization is carried out by SEM-imaging of the membrane surface as well as of the respective metallized 3D-replica image. The fabrication of the metallic negative replica is carried out using the electroless plating by adapting the protocol described in experimental

section 2.4.2 (CHAPTER II) by depositing nickel-films onto the membrane surface. Then, the metallic structures are obtained by the dissolution of the PLA-substrate using 5M NaOH-solution at 50 °C for about 8 hours. Now, no distinctive effects are noticed during SEM-beam penetration upon investigating the metallic negatives.

Figure 71 displays the top-view of the PLA-membranes after exposure in 2 M NaOH solution for different times.

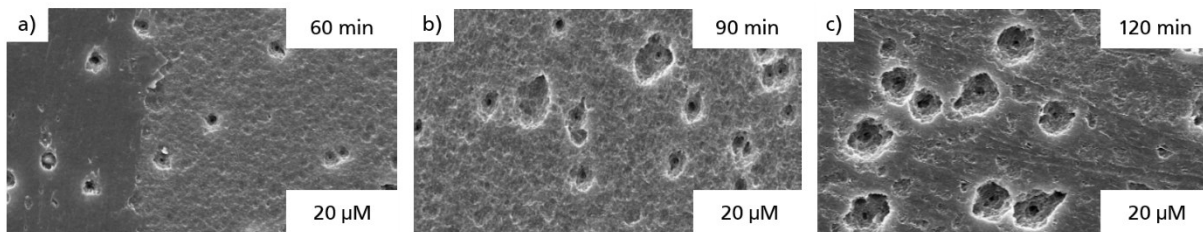


Figure 71: Top-view SEM-images of PLA membranes ( $10^7$  tracks/cm<sup>2</sup>) after immersion into 2 M NaOH-solution for different etching times: 60 min (a), 90 min (b) and 120 min (c).

First, the PLA-surface shows significant circular damaged zones. Moreover, it can be observed, that the depth of these craters is very low suggesting that the etching process did not fully proceed across the whole length of the membrane. Herein, these structures are pronounced as *pits*. The estimated values for the diameters are averaged over 20 values and amounts to  $4.5 \mu\text{m} \pm 0.7 \mu\text{m}$  (60 min),  $8.7 \mu\text{m} \pm 0.7 \mu\text{m}$  (90 min) and  $12.5 \mu\text{m} \pm 0.7 \mu\text{m}$  (120 min), calculated as an average of 5 pores. An increase of etching time by a factor of 2, results in an about three times increase of the *pit* diameter.

However, the etching condition is suggested to be insufficient to proceed the pore etching into deeper membrane areas. Therefore, the etching was repeated at 50 °C using 3 M NaOH.

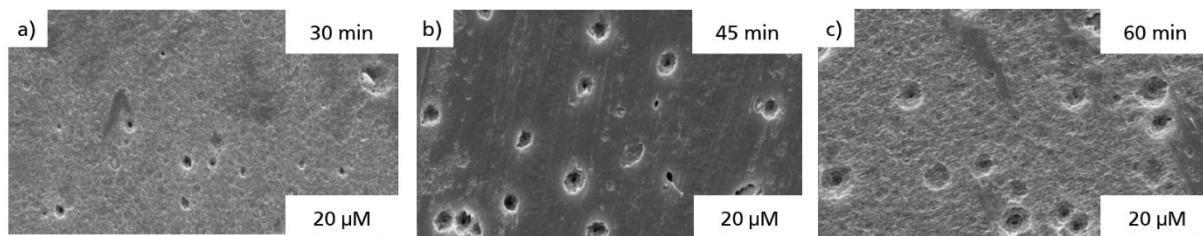


Figure 72: Top-view SEM-images of PLA membranes ( $10^7$  tracks/cm<sup>2</sup>) after immersion into 3 M NaOH-solution for different etching times: 30 min (a), 45 min (b) and 60 min (c).

According to Figure 72, the circular damaged zones were successfully produced onto the PLA-membrane surface. Here, porous structures were observed even after 15 min of etching time, providing *pit*-diameters of about  $2.86 \mu\text{m} \pm 0.9 \mu\text{m}$  (Figure 72a). Moreover, after 45 min the *pit*-diameter is almost 50% increased ( $5.89 \mu\text{m} \pm 0.41 \mu\text{m}$ ) and further etching lead to the *pit*-sizes of about  $8.6 \mu\text{m} \pm 0.5 \mu\text{m}$  after 1 h (Figure 72c). The higher concentrated etching series provides larger diameters and, thus, faster etching rates compared to the 2 M NaOH-etching series are assumed. In order to obtain the etching rate, the estimated *pit*-diameters were correlated with the etching time (Figure 73).

From the slope of the linear regression, the respective etching rate can be assessed. For the case of 2 M NaOH, the etching rate is about  $133.4 \text{ nm/min} \pm 5.8 \text{ nm}$ , whereas for the case of 3 M NaOH, we have observed 30%-faster etching rate, i. e.,  $186.6 \text{ nm/min} \pm 8.3 \text{ nm}$ . These results clearly demonstrated the huge affect of etchant concentration on the etching rate that is owed by the higher degree of amorphous regions inside PLA-substrates used for pore fabrication compered to common membranes made of step growth polymers like PET, PC or PI.

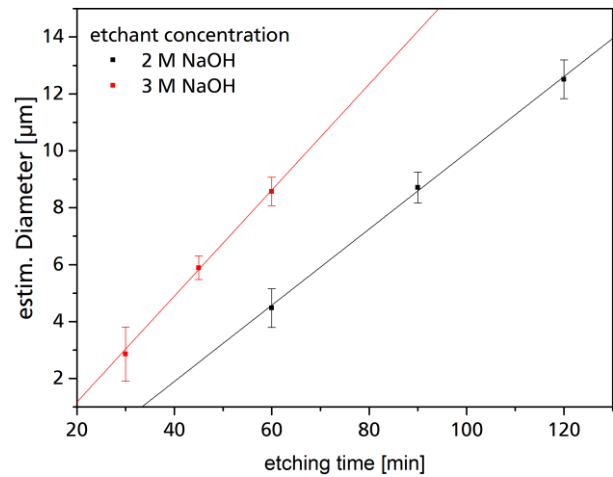


Figure 73: graphical correlation and linear fit of estimated *pit* diameters with the etching time.

In order to gain more detailed insights of the *pit*-structure, the 3D-replica image was prepared using metal deposition. With the metallic deposition, compact nickel films are filling the *pit*-like structures. After sufficient dissolution of PLA-substrate, the disclosed replicas of the PLA-surface are obtained. In the following, the nickel-filled *pits* are pronounced as *tips* and presented in the following Figure 74.

Figure 74 demonstrated the negative image of the PLA-membrane upon exposure to 2M NaOH at different etching times at 50 °C.

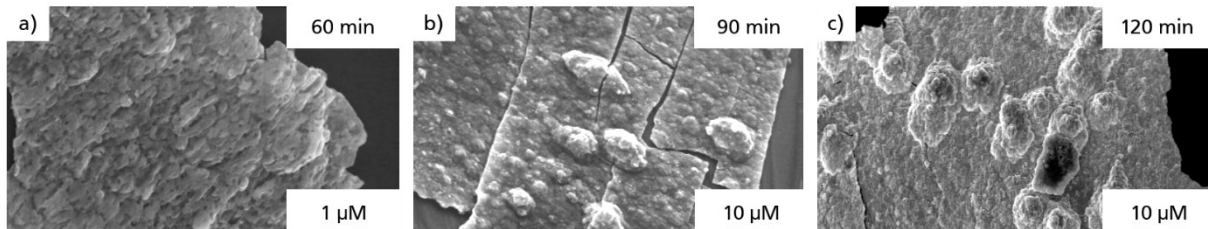


Figure 74: Top-view SEM-images of the 3D-replica of PLA membranes ( $10^7 \text{ tracks/cm}^2$ ) upon nickel film deposition and dissolving of the PLA-membrane. Here, the negative structures are presented after the membrane was exposed to 2M NaOH-solution at 50°C for different etching times: 60 min (a), 90 min (b) and 120 min (c).

Based on the received tip-images, a proportional relation between etching time and tip-diameter is noticed. When the etching time is increased, the tips became larger revealing a cone-like structure. However, the tips do not differ significantly from the background, which indicates short tip heights. The primary penetration of the etchant is highly located at the membrane surface. After 30 min of etching, no tips are resolvable. However, after 45 min and 60 min of etching, the tip-diameter is averaged from 20 values is  $11.5 \mu\text{m} \pm 1.1 \mu\text{m}$  and  $13.9 \mu\text{m} \pm 0.9 \mu\text{m}$ , respectively. The tip-size deviates from the respective *pit*-values. However, the boundary of the tip edge from its background was only determined visually and is therefore highly prone to errors. Nevertheless, qualitatively a correlation of etching time and structural changes is evidenced by the SEM-images. Consequently, the respective top-view images of the 3M etchant series are evaluated as well (Figure 75).

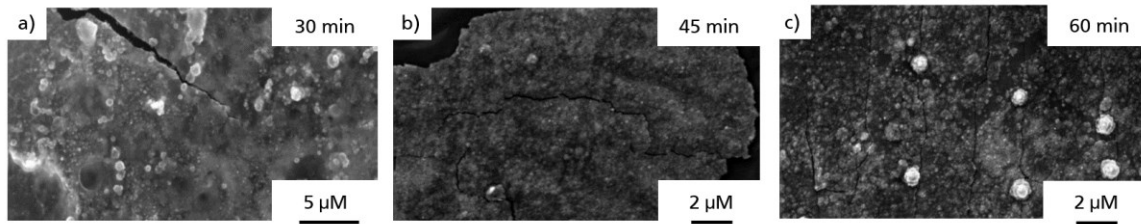


Figure 75: Top-view SEM-images of the 3D-replica of PLA membranes ( $10^7$  tracks/cm<sup>2</sup>) after nickel film deposition and dissolution of the PLA-membrane. Here, structures are presented after the membrane was exposed to 3 M NaOH-solution at 50°C for different etching times: 30 min (a), 45 min (b) and 60 min (c).

For the case of 30 min and 45 min of etching, significant tip-structures were not resolvable. Hence, Figure 75c reveals clear circular structures indicating the presence of tips. Their averaged diameter amounts to  $7.0 \mu\text{m} \pm 0.4 \mu\text{m}$ , which is slightly smaller than the diameters calculated from the surface images ( $8.6 \mu\text{m} \pm 0.5 \mu\text{m}$ ) as an average of 5 pores. In addition, the clear demarcation between tip-structures and background was carried out only visually, which hindered the validation of the diameter.

In order to investigate the etching process more efficiently and to have a brief look on the etching progress, the tip-structures are examined laterally upon 90°-tilting of the SEM-holder (Figure 76). Now, the side-view of the tips can convey further information about the real tip height  $H$  regardless the pore-diameter. Further, the cone-angle  $\alpha$  is estimated based on the lateral images. According to Figure 9 in CHAPTER I, bulk-to-track-etch ratio  $v_b/v_t$  is directly obtained calculating  $\sin(\alpha)$ . In the following, the lateral views of the tips are presenting the lateral images of both etching series using 2M NaOH and 3M NaOH at 50 °C.

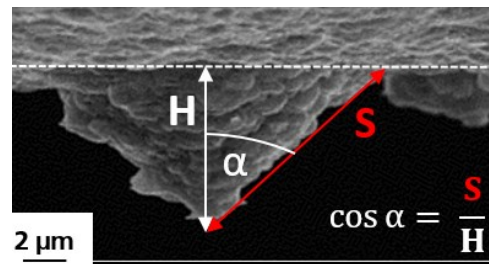


Figure 76: estimation of tip-height  $H$  and cone-angle  $\alpha$  based on SEM-images.

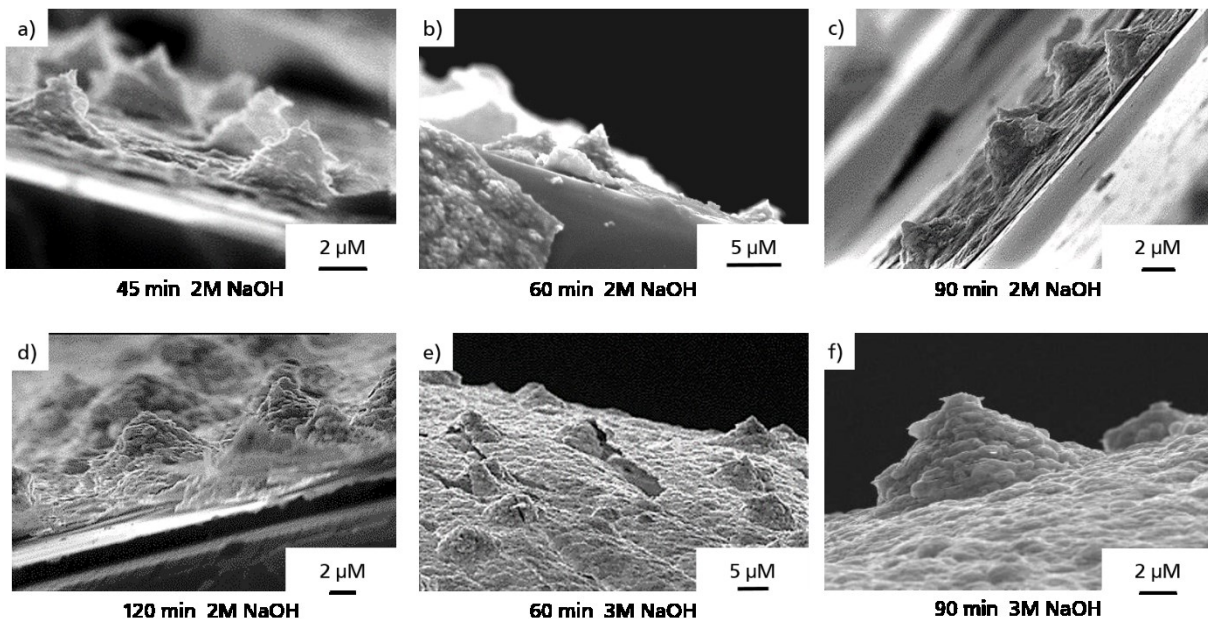


Figure 77: Lateral SEM-images of the 3D-replica of PLA membranes ( $10^7$  tracks/cm<sup>2</sup>) after nickel film deposition and dissolution of the PLA-membrane. Here, the structures are presented after the membrane was exposed to 2 M NaOH-

solution at 50 °C for 45 min (a), 60 min (b), 90 min (c) as well as 120 min (d) and into 3M NaOH-solution for 60 min (e) as well as 90 min (d), respectively.

The lateral faces of the tips reveal a higher degree of roughness for higher etching times. The tip height and tip side length were adapted from the lateral images to calculate the cone-angle and the respective track-to-bulk etch-ratio.

Table 5: Based on the lateral tip-images the listed values were archived for the calculation of the bulk-to-track ratio.

	2 M NaOH				3 M NaOH	
	45 min	60 min	90 min	120 min	60 min	90 min
<i>height H</i> [ $\mu\text{m}$ ]	2.82 ( $\pm 0.33$ )	2.66 ( $\pm 0.03$ )	3.09 ( $\pm 0.91$ )	3.65 ( $\pm 1.96$ )	3.74 ( $\pm 0.18$ )	4.83 ( $\pm 0.64$ )
<i>side S</i> [ $\mu\text{m}$ ]	3.38 ( $\pm 0.34$ )	3.33 ( $\pm 0.31$ )	4.02 ( $\pm 0.26$ )	2.67 ( $\pm 1.25$ )	4.42 ( $\pm 0.21$ )	3.83 ( $\pm 0.78$ )
<i>tip <math>\alpha</math></i>	33.42° ( $\pm 2.43^\circ$ )	36.86° ( $\pm 0.79^\circ$ )	39.71° ( $\pm 2.61^\circ$ )	54.78° ( $\pm 6.54^\circ$ )	37.92° ( $\pm 1.24^\circ$ )	54.56° ( $\pm 3.42^\circ$ )
$v_t/v_b$	1.09	1.01	1.09	1.02	1.13	1.08

By comparing both etching series, the estimated height values are  $\sim 30\%$  larger for the 3M NaOH. For 2M NaOH, after every 30 min, the tip height increases by about  $0.5 \mu\text{m}$ . In contrast, 30 min etching provides a tip height increase for about  $1 \mu\text{m}$  assuming a two-time faster track-etching rate. However, the calculation of the real track-etching rate is only obtained by knowing the bulk-etching rate. Now,  $v_b$  is estimated by the membrane thickness measured before and after etching either throughout SEM-images of cross-sections or by determining the length of the respective metal film negatives as long as the etching pervades the entire membrane. Regarding the PLA-membranes, the estimation of the thickness was not achievable. First, because there was the massive degradation effect of the membranes upon SEM-treatment. Second, the metal replica shows a maximum height of  $\sim 4 \mu\text{m}$ , that obviously do not imbue the entire membrane. Therefore, the actual track etch rate was not reachable. The cone-angle value can be used to calculate at least the track-to-bulk ratio. Since the cone-angle deviates around  $40^\circ$  regardless the etching time and concentration, the averaged etching ratio deviates around 1.05 indicating almost no difference between track-etching and bulk-etching.

It can be assumed that the track-etching is not favoured inside the PLA-membranes as for the case of standard PET-membranes. However, the use of same accelerated ions to irradiate PLA and PET-membranes, the track-formation provide significantly higher structural changes inside PET membranes than in PLA-membranes. Now, track-formation is caused by numerous cleavages of polymeric chains along with the trajectory of the accelerated ions. After degassing and reorganization mechanisms, the track region offers more amorphous regions. Regarding the PLA-membranes, the amorphous areas are conspicuous to enable fast biodegradability. Therefore, the SHI-treatment creates only less damage in the PLA-substrate as evidenced by the track-to-bulk ratio, fluctuating around the value of  $v_t/v_b=1$ , which indicates similar etching velocity of the bulk and track direction.

---

### 2.3. Conclusion

In summary, the pore generation of PLA-membranes having a thickness of 50  $\mu\text{m}$  was investigated. The irradiation occurred at the UNILAC in the GSI-facility by using  $\text{Au}^{26+}$ -nuclei (11.4 MeV/u). Here, the track etching behaviour was examined using NaOH and  $\text{NH}_4\text{OH}$  as potential etchants. In order to obtain the optimum etching conditions, the trials were systematically screened by varying the etchant concentration, temperature and time. Membrane characterization was carried out primarily by using SEM-imaging. It was found, that *IV*-measurements were not suitable to monitor the etching process, because even unetched membranes provided massive creepage currents. The microscopic images revealed no pore-like structures inside the substrate material. Hence, for the use of 2M and 3 M NaOH at 50 °C *pit*-like structures were resolved indicating the start of the track-etching process.

During the SEM imaging, enormous demolition on the PLA-sample occurred, even though a protective gold-layer was coated over the sample. In order to avoid destructive effects of the original membrane surface, the examination was carried out upon electroless deposition of metallic dense films onto the sample. After generating a dense nickel film followed by subsequent dissolution of PLA-substrate, the negative replica of the substrate was disclosed and enabled a more precise investigation of the etching behaviour. The filled *pit*-structures are now represented as *tip*-structures. The calculated *tip*-angles amounted to 40°, whereas the estimated *tip* sizes did not go beyond 4  $\mu\text{m}$ , indicating an inefficient track-etching inside the membrane. It was found that the respective track-to-bulk etch-ratio fluctuated around 1, representing almost no difference between the bulk and the track-etching. On the contrary, the successful formation of pores requires a high track-to bulk-etch rate preferably around 1000:1. To this end, the use of NaOH and  $\text{NH}_4\text{OH}$  as track-etchant is not suitable.

This study showed that the use of biodegradable polymeric substrates is challenging to produce nanopores due to their high amount of amorphous regions. Moreover, the *IV*-measurements provided insights about the packing density of the PLA-substrate. Here, *IV*-experiments were carried out in PLA-membranes prior to the etching. Surprisingly, ionic current was recorded in microampere ranges assuming that the PLA-membranes are insufficiently packed. However, the inability to create pore structures inside the material is suggested to be caused by the huge degree of less-dense packed substrates with a high degree of amorphous regions. As a result, PLA-membranes are not suited to produce nanopores using the track-etching technique. Additionally, the creepage currents of unetched membranes would not favour the use of PLA membranes, even if nanopore generation becomes potentially conceivable upon using optimizing track-reactivity and etching conditions.

---

## CHAPTER V: Nanopore Modification and Sensing Properties

---

The sensing performance of nanopores is based on the specific bioconjugation between pore-bounded receptor and respective analyte molecule. Here, track-etched nanopores are characterized based on the changes in ionic transport passing through the nanopore. Among numerous other analytical techniques, only the *IV*-measurements offer beneficial response due to a simple and low-cost experimental set-up. Recently, track-etched nanopore membranes were used to detect various analytes, such as biomolecules (61, 229–232), metal cations (67, 168), organic anions (233–235), and differentiate between enantiomers (236–238) as well as phosphate moieties (239, 240).

In this thesis, the sensing capability of functionalized nanopores is tested through *IV*-measurements and supported by other analysing methods in terms of analyte sensitivity and selectivity towards specific analyte molecules.

---

### 1. Label-free Histamine Detection with Nanofluidic Diodes through Metal Ion Displacement Mechanism\*

---

#### 1.1. Introduction

A number of the most important of diseases are based on disturbances within metabolic or physicochemical pathways. Regarding neurological diseases, there is a misbalance in the signal transduction between the axons of neuronal cells by bridging the synaptic cleft. (3) These chemical messengers carry neurological information and provide electrical intracellular communication. (241) Neurotransmitters are referred as semiochemicals and are subdivided into four different groups according to their molecular nature:

- *Gases*: nitric oxide or carbon monoxide
- *Monoamines*: dopamine, (nor-) adrenaline, 5-hydroxytryptamine, histamine (Hm), etc.
- *Amino acids*: glutamate,  $\gamma$ -aminobutyric acid, glycine
- *Peptides*: enkephalins, endorphins, cholecystokinin, etc.
- *Purines*: adenosine, adenosine triphosphate

The exact monitoring of the neurotransmitter level within the human body can provide crucial information about the health state. In this way, the neurotransmitter amount can act as an indicator to evaluate transmission processes and offers the possibility to diagnose depressions and psychoses, drug addictions or degenerative diseases. (242) Histamine, herein referred as Hm, is located in the brain areas being responsible for the intact communication of neuronal brain cells. (243) Even small changes in the Hm-level symbolizes inflammations that can affect human body systems leading to sleep disorders, dysfunctional memory storages and thermoregulations. Moreover, an enhanced Hm-level can cause disorder in hormone functioning which lead to allergic reactions within the gastrointestinal and cardiovascular tract. (244–248)

During the last years, a broad range of methods have been established to efficiently detect histamine through gas chromatography (249) and immunoassays (250). Niwa *et al.* developed a method for the continuous measurement of histamine inside rat cells using an electrochemical online sensor. (251) Later on, the efficient sensing of histamine was achieved through the interaction of histamine with metal ion complexes leading to ligand exchange reaction.

---

\* Ali, M., Ramirez, P., Duznovic, I., Nasir, S., Mafe, S., Ensinger, W. (2017) „Label-free histamine detection with nanofluidic diodes through metal ion displacement mechanism”, *Colloids and Surfaces B: Biointerfaces* 150: 201-208.

Oshikawa and co-workers used a fluorescent complex between cobalt(II) ions and cyan dye. In presence of histamine, the coordination displacement process causes a quenched signal. (252) Moreover, Seto *et al.* demonstrated the selective histamine detection using a seminal mechanism. Here, a stable non-fluorescent nickel(II)-iminodiacetic-complex became fluorescent in the presence of histamine. (253)

There is no doubt about the use of the above mentioned methods to detect histamine, but these procedures take a lot of time and need expensive instruments. However, nanopore based sensors have become powerful tools to selectively and sensitively detect specific analyte molecules. With respect to the already mentioned broad range of successfully detectable analytes, the specific recognition of histamine using nanopores is demonstrated.

## 1.2. Results and Discussion

To detect histamine throughout track-etched nanopores, the pore walls are functionalized with NTA-moieties. First, a conical single pore membrane was fabricated using the protocol described in the experimental section 1.2 (CHAPTER II). Then, *N,N*-bis(carboxymethyl)-*L*-lysine (BMCL) was attached to the nanopore surface using EDC/PFP-coupling method already introduced in experimental part (see Figure 32 in section 2.1.1). In this way, the pore walls were functionalized with Nitrilotriacetic acid-moieties able, herein referred as NTA, to form a stable Ni-NTA-complex, when the nanopore membrane is immersed in a nickel-(II)-solution.

As mentioned, the surface decoration and the sensing performance is evaluated from the recording of the transmembrane current before and after the respective modification and sensing step. Therefore, the membrane was fixed in the measurement cell (see Figure 44) and never taken out until the experiment was completed. The immobilization of NTA-moieties and subsequent formation of the Ni-NTA-complex onto the nanopore, the nanopore surface charge serves as an indicator to track the successful modification pathway. For every modification step, an *IV*-measurement was performed in order to monitor the surface modification. The ground electrode was placed on the base side, whereas the working electrode was placed on the tip side. Using this measurement setup, the working electrode serves as cathode and the counter electrode as anode for positive voltages and *vice versa*.

When performing an *IV*-measurement, the transmembrane current of a blank conical single pore membrane (tip diameter: 35 nm, base diameter: 700 nm) is mainly influenced by the carboxyl groups that are produced during the nanopore etching step. Note, that the diameter calculations were obtained using the protocol described in the experimental section 3.3.1 (CHAPTER II).

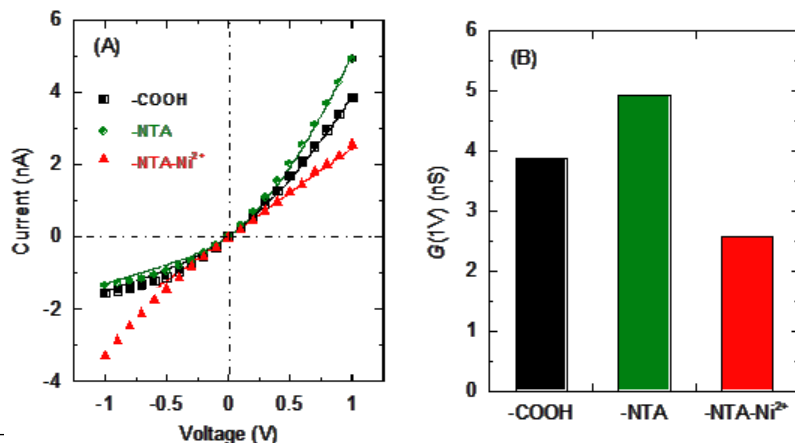


Figure 78: Changes in the *IV*-characteristics (a) and nanopore conductance (b) on the successful surface modification of COOH groups with BMCL and subsequent formation of Ni-NTA-complexes onto the nanopore surface.

Using KCl-solution as an electrolyte, the carboxyl groups are deprotonated leading to a transmembrane current mainly caused by the transport of cations with a maximum current (at 1 V) of 3.9 nA with a positive rectification behaviour in the IV-curve (see Figure 79b). The current is originated mainly by the movement of cations flow from the tip opening towards the base opening across the entire carboxyl-terminated nanopore. (120, 203, 254–256)

Now, the BMCL-attachment leads to an approximately three times higher number of carboxyl groups compared to the blank state. Consequently, a higher transmembrane current, i. e., from 3.9 to 4.9 nA, and an enhanced conductance  $G$  is recorded for positive bias. (232) The formation of the Ni-NTA-complex leads to a charge compensation on the nanopore walls and, therefore, a decreased current (2.7 nA) is detected. Moreover, the shape of the IV-curve shows a quasi-linear character, indicating a high neutralized charge state inside the nanopore promoted by the formation of Ni-NTA-complexes. In the following, the potential of Ni-NTA-complexes for the efficient recognition of histamine is briefly described regarding the sensitivity, the selectivity and the reversibility.

### 1.2.1. Sensitive Detection of Histamine

In presence of Hm, the formation of a more stable Hm-Ni-complex occurs, leading to an regeneration of the NTA-moieties on the nanopore surface (see Figure 79). Here,  $\text{Ni}^{2+}$ -ions are forming a stable chelate complex with the primary amine and the tertiary imidazole nitrogen atom within the Hm-molecule. (257–259)

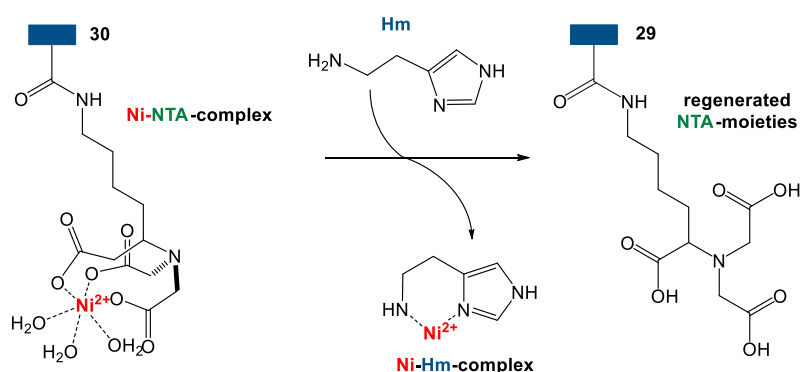


Figure 79: Detection of histamine (Hm) using NTA-modified conical single nanopore. On exposure to Hm, a stable Ni-Hm-complex is generated, which leads to the regeneration of NTA-moieties onto the nanopore.

The successful complexation/decomplexation in the presence of histamine is monitored through current-voltage measurement. By increasing concentration of histamine, more Hm-Ni-complexes are generated, leading to regenerated NTA-moieties on the pore wall. Consequently, the surface charge is enhanced due to negatively charged NTA-groups being exposed on the pore surface. To this end, the transmembrane conductance is strongly correlated to nanopore surface charge. Therefore, the pore conductance  $G$  for the applied voltage of 1 V, herein referred as  $G(1\text{ V})$ , can be quantitatively analysed (for an applied voltage of 1 V) obtained from the corresponding IV-measurements. In Figure 80, the performed IV-experiments for positive bias as well as the obtained  $G$ -values at the applied voltage (1V) are presented.

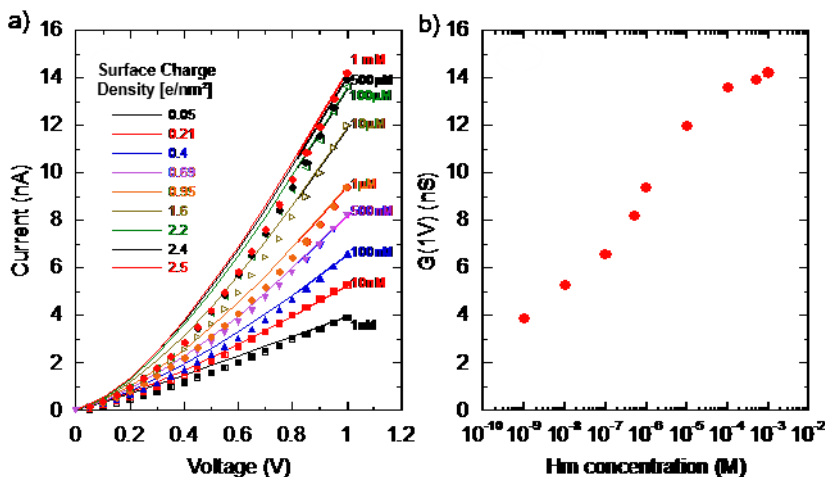


Figure 80:  $I/V$ -characteristics of the Ni-NTA modified conical single nanopore (tip diameter = 35 nm; base diameter = 700 nm) in presence of different Hm-concentrations including the calculated surface charge density (a). Course of the respective conductance  $G$  at 1 V obtained from the corresponding  $I-V$  curve (b).

Here, the Ni-NTA-modified single pore membrane was exposed to electrolyte solution, containing a fixed amount (100 mM) of potassium chloride and various concentrations of Hm, ranging from 1 nM to 1 mM. The selective displacement of Ni(II)-ions from the nanopore walls directly affects the surface charge. The higher the amount of histamine, the more NTA-groups are regenerated, and the pore becomes more conductive. Starting from 3.9 nA for the use of 1 nM Hm, the recorded transmembrane current is roughly 3.5-time higher (14.4 nA), if 1 mM Hm was used (see

Figure 80a). Regarding the entire Hm-concentration series, the overall continuous increase of conductance is given in

Figure 80b. Note that, if the system is given enough time to form the Ni-Hm-complex, even low concentrations of Hm can remove almost all nickel-(II)-ions from the Ni-NTA complexes on pore surface. Therefore, the contact time between pore surface and Hm should be short to achieve sigmoidal correlations between increased Hm amounts and conductance-signal. In this way, the equilibrium of the Hm-Ni-complex formation is according to the LANGMUIR isotherms course calculated by Tagliazucchi *et al.* (260) Quantitatively, the detection ranges over five orders of magnitude. For concentrations higher than 100  $\mu\text{M}$ , the nanopore does not show further increases of conductance and transmembrane current.

### 1.2.2. Selective Detection of Histamine

Amongst the broad range of various chemical messengers, the selective detection of any neurotransmitter with a sensor is crucial for its use in sensing applications. In addition to histamine, the following neurotransmitters were also examined: glycine (Gly), 5-hydroxytryptamine (5-HT),  $\gamma$ -aminobutyric acid (GABA) and dopamine (DA) for the control experiment.

To test the selective detection of Hm, aqueous solutions of 100 mM KCl (pH7) were prepared including a fixed concentration (1 mM) of the mentioned neurotransmitters. The NTA-modified nanopore is fixed in the measurement cell (see Figure 44) and the half-cells are filled with the respective electrolyte, separately. Figure 81 shows the resulting  $I/V$ -curves as well as the respective  $G(1V)$ -values, on positive applied voltages.

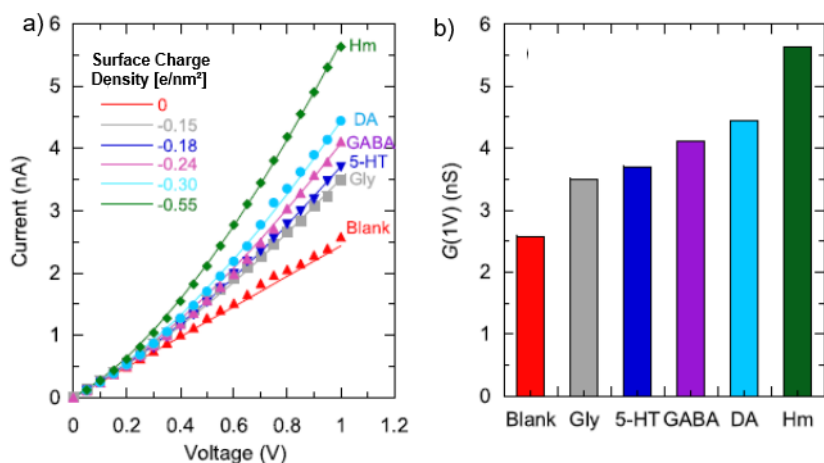


Figure 81:  $I/V$ -characteristics (a) and conductance (b) for the selective Hm-measurement within a conical single pore membrane (tip diameter: 35 nm; base diameter: 700 nm).  $I/V$ -curve of the blank pore (red graph) is presented Ni-NTA complexes onto the pore surface as well as the  $I/V$ -curves in presence of various neurotransmitters (1mM) in the electrolyte solution: glycine (Gly), 5-hydroxytryptamine (5-HT),  $\gamma$ -aminobutyric acid (GABA), dopamine (DA), histamine (Hm).

Treating the nanopore with glycine and 5-hydroxytryptamin causes just changes of  $\sim 25\%$  in the conductance (from 2.7 nS to 3.6 nS and 3.8 nS). The use of GABA and DA leads to an increase of more than 30% (4.1 nS and 4.4 nS), respectively. Only if Hm was used,  $G(1V)$  is significantly enhanced to almost 50%. Furthermore, in presence of Hm,  $G(1V)$  increased to 5.7 nS is similar to the conductance value of 4.9 nS, when the pore surface is only covered by NTA-moieties during the modification steps (see Figure 80). Besides Hm, all other neurotransmitters could not provide such a distinct signal change due to a failed formation of a stable complex with nickel-(II)-ions. Thus, the Ni-NTA-complex still exists on the nanopore surface. The released NTA-moieties cause an enhanced surface net charge indicating that only Hm can displace  $Ni^{2+}$ -ions from the pore surface sufficiently. Comparing the used neurotransmitters only Hm is able to form a six-cantered chelate complex with the nickel-(II)-ions being the thermodynamically stable complex. (252, 253).

To further enhance the selectivity, the geometrical parameter of the nanopore membrane must be adjusted. Since the conductance changes are mostly affected by the release of NTA-moieties and the underlying increase of the surface net charge, a second conical single pore was fabricated having a tip diameter of about 45 nm and a base opening of 700 nm. In this way, the total number of NTA-moieties is enhanced. Note, that the diameter calculations were obtained using the protocol in the experimental part section 3.3.1 (CHAPTER II).

The following figure shoes the  $I/V$ -measurements repeated with the same electrolytes containing the same amount of the mentioned neuro-transmitters.

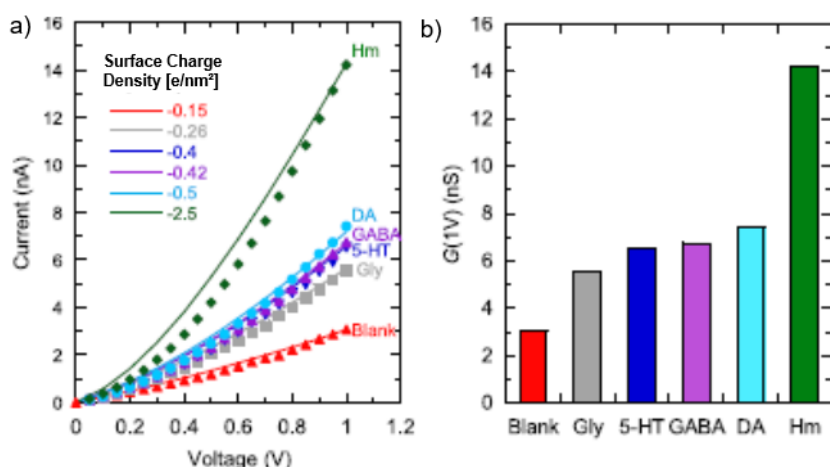


Figure 82:  $I/V$ -characteristics (a) and conductance (b) for selective Hm-measurement within a conical single pore (tip diameter: 45 nm; base diameter; 800 nm).  $I/V$ -curve of blank pore (red graph) is presented indicating Ni-NTA complexes onto the pore surface as well as the  $I/V$ -curves in presence of various neurotransmitters (1mM) in the electrolyte solution: glycine (Gly), 5-hydroxytryptamine (5-HT),

$\gamma$ -aminobutyric acid (GABA), dopamine (DA), histamine (Hm).

As expected, a larger pore provides higher values of conductance. Nonetheless, the exposure to Gly, 5-HT, GABA and DA leads to  $G(1V)$  values ranging from 5.8 nS (Gly) to 7.7 nS (DA). Only the presence of Hm leads to a large increase of conductance of more than 80% as a result of the released NTA-moieties on the pore walls (from 2.9 nS to 14.3 nS). This fact shows the successful displacement of  $Ni^{2+}$ -ions using Hm while other neurotransmitters are unable to displace  $Ni^{2+}$ -ions. In addition, treating the nanopore with only 500 nM of Histamine leads to a conductance change in the same order as the use of 1 mM GABA. This underlines the specific and sensitive correlation between the conductance and Hm-concentrations being one of the key feature to create a good biosensor (see CHAPTER I, section 3.2).

### 1.2.3. Reversible Detection of Histamine

In addition, the reversibility of the proposed system is also important in the development of biosensors (see section 3.2; CHAPTER I). In presence of Hm, the NTA-moieties are regenerated and ready to the reload nickel-(II)-ions. The successful reformation of Ni-NTA leads to a significant reduction of  $G(1V)$ , whereas in presence of Hm, the regenerated NTA-groups causes a huge increase of  $G(1V)$ .

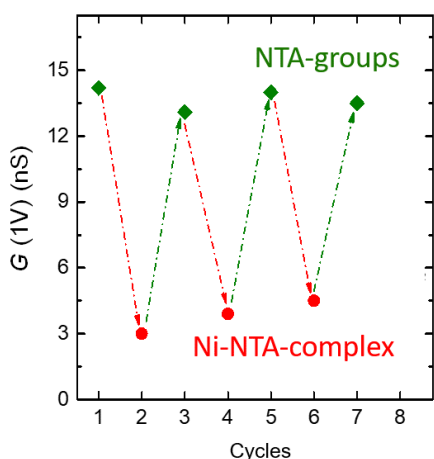


Figure 83: The plots determined the reversibility of the complexation/ decomplexation along the Hm-detection, tested by performing cycles to track the changes obtained in the conductance  $G(1V)$ .

Therefore, the signal stability can be evaluated through  $IV$ -measurements performed at fixed concentrations of Hm (1 mM). The resulting  $G(1V)$ -values according to the performed cycles of regeneration of NTA-moieties and reloading of Ni-NTA-complexes are given in Figure 83. The switchable conductance in the presence/absence of Hm affects the surface charge and subsequently the transport properties of the nanopore.

### 1.3. Conclusion

In summary, the specific detection of histamine was achieved using a conical single pore covalently functionalized with NTA-moieties onto the nanopore wall. In the next step, the metal complex consisting of NTA-groups and  $Ni^{2+}$ -ions is generated and monitored by  $IV$ -measurements, leading to a decreased conductance because of charge compensation between the negatively charged NTA-moieties and the  $Ni^{2+}$ -cations. The  $Ni^{2+}$ -displacement in presence of histamine provides the sensing concept of the histamine. The successful formation of the more stable  $Ni^{2+}$ -histamine complex leads to the regeneration of NTA-moieties on the pore wall and, therefore, an enhanced conductance is recorded by  $IV$ -measurements. These changes are detectable even at nanomolar-concentrations of histamine. Moreover, other neurotransmitters (glycine, 5-hydroxytryptamine,  $\gamma$ -aminobutyric acid, dopamine) were also tested, but failed in their ability to form a stable nickel-complex. Here, only minor changes in conductance and transmembrane current were recorded. The nanopore-based histamine-recognition through the

---

presented complexation/decomplexation mechanism provides sensitive, selective and stable signal outputs. These results showed that such nanofluidic devices would serve as a powerful tool to detect neurotransmitters in a clinical stage.

---

## **2. Potassium-Induced Ionic Conduction through a Single Nanofluidic Pore modified with Acyclic Polyether Derivative\***

---

### **2.1. Introduction**

The control of ionic transport through nanopores is of huge interest for a variety of applications. The specific recognition of a particular metal cation can be achieved by introducing a desired chemical functionality on the pore surface. (261–263) Track-etched nanopores provide an intrinsic transport of metal cations across the conical nanopore. (264) Due to their ability to tailor the geometrical dimensions on-demand, nanopores have become an outstanding candidate to miniaturize sensing devices. The incorporation of receptor units onto the nanopore surface is the strategy of choice to introduce sensing activity towards specific analytes.

Numerous investigations have been made for the specific metal cation recognition by chemical functionalization of track-etched nanopores. However, biological ion pumps show ionic permeability especially towards sodium and potassium ions. These proteins are able to efficiently transport the respective alkali ions due to their extraordinary architecture. (265, 266) A variety of methodologies for the selective detection of alkali metal cations have been developed, because alkali metal cations are involved in numerous neuronal and muscular processes. Jiang *et al.* used nanopores functionalized with DNA-moieties for the specific recognition of potassium ions. (267) A different route for the selective detection of alkali metal cations is reported using so-called polyether moieties immobilized on the nanopore surface. Their ability to form specific complexes with metal cations is caused by their intrinsic chemical structure that was found in antibiotics having ethylene glycol units. (268) The synthetic adaption was successfully achieved by the construction of cyclic polyether assemblies also known as crown ether structures. (269)

The immobilization of cyclic polyether moieties enables the selective transport of specific cations across the membrane- Here, the specificity of transported ions mainly depends on the crown ether size. For instance, Ali *et al.* demonstrated the specific lithium-ion recognition inside track-etched nanopores using amino-terminated 12-crown-4 derivatives, which were covalently attached on the pore surface. Furthermore, Jiang and his co-workers demonstrated the immobilization of 16-crown-5 moieties onto the pore surface, enabling the specific detection of sodium ions. In addition, Perez-Mitta *et al.* reported the generation of a potassium selective ion channel by the covalent attachment of 18-crown-6 moieties onto the pore surface. (270) Furthermore, large caesium ion have also been selectively detected by the incorporation of calix-crown ethers on to the inner pore walls, as reported by Ali *et al.* (271) These studies clearly show that the selective recognition of specific alkali ions can be achieved by the right choice of the polyether moieties. Hence, the host-guest interaction between respective metal cations and the crown-ether derivatives are tuneable simply by varying the number of oligoethylene glycol units within the molecular polyether structure, leading to cavities of different sizes. Moreover, the use of open polyether structures, so-called pseudo-crown ethers have already been reported to specifically bind alkali metal cations. (272, 273). Delbosc *et al.* demonstrated the role of the acyclic crown-ether structure for specific metal cation detection. The open polyether scaffold

enables higher flexibility and, therefore, it became a promising tool to enhance the sufficient generation of alkali metal cation complexes onto the surface. (274)

In this study, the attachment of pseudo-crown ether moieties using *bis*-podand-NH<sub>2</sub> onto the pore walls was performed to evaluate specific bindings of potassium cations. The success of chemical modification of the pore membrane and metal cation complexation is monitored by the examination of changes in the ionic current promoted by alkali cations.

## 2.2. Results and Discussion

Investigations regarding the stimuli-triggered ionic flow were performed using track etched nanopores. The fabrication of the nanopore membrane was carried out using the protocol (section 1.2, CHAPTER II). After the pore generation, the membrane contains carboxylic acid groups on the entire surface. These groups are functionalized with the respective receptors able to bind potassium ions. The modification process was carried out using the already introduced protocol in section 2.1.1 (CHAPTER II) to couple the amino terminated oligoethylene glycol creating *bis*-podand-moieties onto the nanopore surface (see Figure 84). The modification process was monitored through *IV*-measurements, following the protocol of the experimental section 3.2.1 (CHAPTER II). Furthermore, the *bis*-podand attachment onto the nanopore surface was carried out in two different routes: (i) in the presence and (ii) in the absence of potassium ions to get more insights of the ionic transport across the membrane. Note that the synthesis of the *bis*-podand amino-compound was carried out by collaborators (I. Ahmed and C. M. Niemeyer from the Karlsruhe Institute of Technology (KIT)).

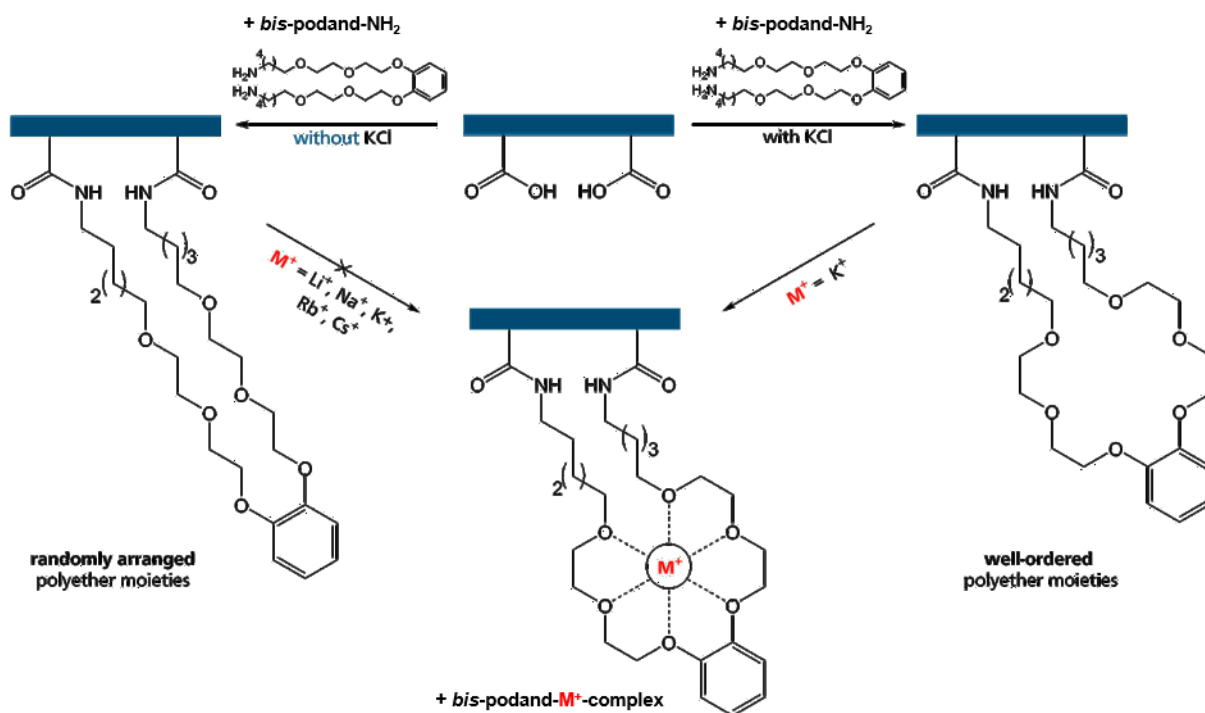


Figure 84: sensing concept of specific potassium detection. Here, the track etched nanopore membrane was modified in the presence or absence of potassium ions with *bis*-podand-NH<sub>2</sub>.

In presence of alkali ions, the formation of a coordinated *bis*-podand-metal ion pair occurs. Here, potassium anions have the highest selectivity towards the *bis*-podand moieties. To track the sufficient interaction between K<sup>+</sup>-ions and oligoethylene glycol units, *IV*-measurements

were carried out using the home-made measurement cell already introduced in the introduction part of CHAPTER I (Figure 44). A single conical nanopore was fabricated according to the protocol in section 1.2 (CHAPTER I) and mounted between the two half-cells that were filled with the respective electrolyte consisting of 100 mM of various alkali salt solutions, such as LiCl, NaCl, KCl, RbCl and CsCl dissolved in 10 mM Tris-buffer (pH 6.5). The cathode was placed on the tip side and the anode was placed on the base side. Using this set-up, large transmembrane currents are achieved when positive voltages are applied. With negative voltages, low currents were recorded. The changes in surface charge were recorded by measuring the transmembrane current and conductance, respectively. The shape of the *IV*-curves gives insights on how the pore inner walls interacts with the respective cations passing through the nanopore.

### 2.2.1. Qualitative Estimation of Ionic Transport

Figure 85a shows the *IV*-characteristics of an unmodified nanopore membrane containing deprotonated COO<sup>-</sup>-groups on the entire nanopore surface at pH 6.5 in dependence of the electrolyte solutions. Their respective *IV*-curve reveals an expected positive rectification behaviour at positive applied voltages (see section 3.2.1, CHAPTER II).

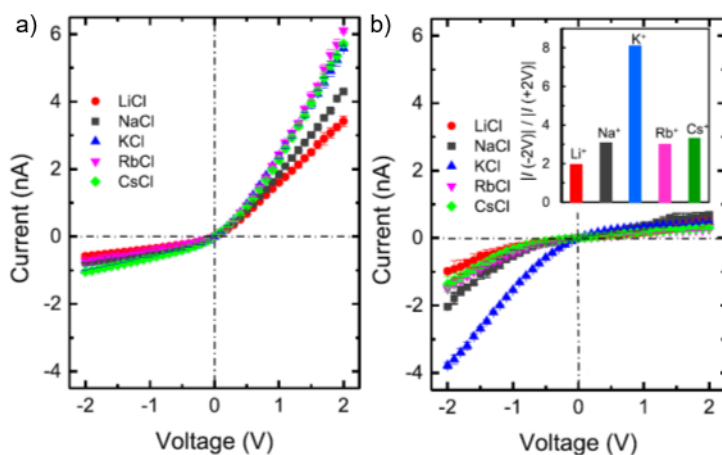


Figure 85: *IV*-curves of unmodified-nanopore (a) and *bis*-podand-modified nanopore (b) upon exposure to various electrolyte solutions having a concentration of 100 mM of the metal chloride (pH 6.5).

The conical pore with negatively charged surface causes an asymmetric movement of electrolyte's cations and anions. (254, 255, 275) In this way, cation-movement is facilitated, while anion passage across pore region is impeded. Hence, the polarity of the nanopore surface can be monitored using *IV*-measurements, whereas the numerical value of the transmembrane current gives insights about the surface charge density, where high surface densities provide a higher rectification behaviour. In the present study, the use of LiCl and NaCl shows slightly lower conductance, i. e., with a current of 3.6 nA and 4.1 nA, for the case of LiCl and NaCl electrolyte solutions, respectively. In comparison, alkali metal electrolytes, like KCl, RbCl and CsCl solution provide higher currents (~6 nA), indicating the presence of high surface charge density.

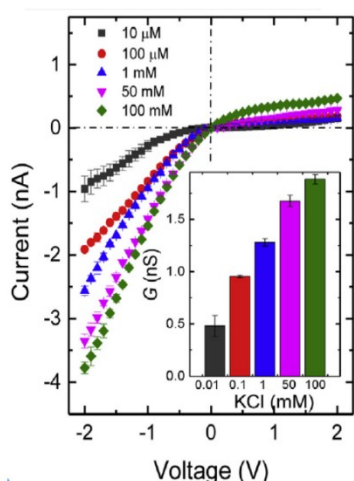
The successful attachment of *bis*-podand to the same nanopore occurs in presence of KCl during the modifications step. Afterwards, the pore was washed carefully to completely remove the prebound potassium ions. Note, that the membrane is still fixed in the same position in the measurement cell. Then, *IV*-curves were recorded using the electrolytes containing various alkali metal species (see Figure 85b). Expecting the measurement in KCl-electrolyte, the absolute current values between the unmodified pore and the *bis*-podand terminated pore revealed a significant loss of current for the case of all electrolytes. The lower conductance is caused by the fact, that the attached *bis*-podand moieties do not carry any charges, leading to

a decreased charge density of the former (negative) pore surface. The resulting *IV*-characteristics show that nearly no interaction between the cations of the electrolytes occur. Hence, the cavity size of the attached *bis*-podand moieties does not coincide with the respective cations. Nonetheless, the trace of the transmembrane current shows an inverted rectification behaviour compared to the *IV*-measurement of the unmodified nanopore. In this case the current flow is mainly carried by anion movements, indicating a positive surface charge density within the pore region. The inversion of rectification is evoked because of remaining potassium-polyether complexes that are not sufficiently removed during washing steps.

In contrast, if KCl-electrolyte was used, the recorded *IV*-curve did not only provide the same inverted rectification behaviour but also a significant higher conductance compared to the remaining electrolytes due to formation of positively charged *bis*-podand-K<sup>+</sup>-cavities. Because KCl was present during the modification process, an optimal binding domain being specific for K<sup>+</sup>-ions was achieved. Treating the pore with further KCl-electrolyte, the surface becomes positively charged (*bis*-podand-K<sup>+</sup>-complexes are formed) covering the pore surface with positively charged moieties. Therefore, an enhanced conductance is obtained which promotes the movement of anions (inverted rectification). Yet, the absolute value of the transmembrane current (3.9 nA) is still lower compared to the one for the measurement of the unmodified pore (5.8 nA) (see Figure 85). This is caused by the fact, that during the modification step, for every attachment of uncharged *bis*-podand molecule substitution of two COOH-groups occur. Now, each *bis*-podand group can carry only one K<sup>+</sup>-ion. In this way, even if all *bis*-podand moieties are loaded with potassium, the maximum charge density can never reach the same range as measured on unmodified pore states.

### 2.2.2. Quantitative Estimation of Ionic Transport

To evaluate the sensitivity of the *bis*-podand-promoted potassium-capture, the same single pore was exposed to electrolyte solution having different KCl concentrations. The respective *IV*-measurements are presented in Figure 86.



showing the sensitivity towards potassium cations using the single pore membrane modified with *bis*-podand moieties in presence of different KCl concentration in electrolyte solution.

Increasing the electrolyte-concentration from 10 μM to 100 mM provides an enhanced transmembrane flow. Moreover, the traces of the *IV*-curve show again an inversion of the rectification behaviour in comparison with the blank nanopore. The experiment clearly shows the ability to control the ionic transport across the pore region. The higher the amount of potassium ions is, the more *bis*-podand complexes are formed, inducing a positively charged nanopore surface. Consequently, the anion transport is facilitated along with a discriminated cation movement during the *IV*-measurement (inversion of rectification). A ten-fold concentrated electrolyte causes a rise of conductance from -1.0 nA (for 10 μM) to -1.9 nA (for 100 μM). The conductance is further enhanced along with the measurement of the concentration series and reaches a current flow of almost -4 nA (for 100 mM) at -2 V. However, the current gain does not follow a linear trend. In fact, with increasing concentrations, a

saturation can be reached. The current value amounts to -3.4 nA for the use of 10 mM electrolyte-solution, whereas the ten-fold higher concentration causes only a further increase to -3.9 nA indicating that all *bis*-podand cavities are loaded with potassium ions and further use of higher concentrations would not affect the pore conductance.

The generated *bis*-podand-K<sup>+</sup>-complexes show high stability during the entire record of the *IV*-curves. To study the stability, each *IV*-curve is obtained by applying a triangular voltage sweep between -2 V and +2 V upon three periods. The plot of the obtained current value at the respective voltage-value provides the demonstrated *IV*-curves. The deviations of each data point being less than 1% do not protrude over the size of the data point, indicating a high signal-stability and, therefore, a sufficient complex-stability across the entire pore region.

Overall, the experiment demonstrates evidently (i) the presence of *bis*-podand-K<sup>+</sup>-complexes on the nanopore wall, when the single pore was exposed to KCl-solution, and (ii) offer the opportunity to further control the transmembrane current flow by varying the potassium concentration in the electrolyte solution.

### 2.2.3. Modification in Absence/Presence of Potassium Ions

So far, the discussion of the experimental results was based on the same single nanopore covalently modified with the polyether-units. Nonetheless, the attachment of the respective molecule was carried out in presence of potassium ions in the modification mixture. The role of potassium chloride during the modification step was further evaluated. The addition of KCl was inspired by previous studies of Echegoyen and co-workers, who already introduced polyether moieties onto gold-surfaces. (273, 272) They showed, if the polyether moieties were attached directly to the surface no complexes could be generated at all. Therefore, they pursued a new strategy. Here, they first generated a complex between metal ion and polyether chains in solution. Thus, a fixation of the previous dangling polyether arms lead to a planar arrangement similar to a crown-ether-structure. (276) Then, these complexes were attached to the surface and the metal ions was washed out. Subsequent examinations indicated that using this route, surface-attached generation of pseudo-crown-ether complexes are possible.

This approach was adopted to the here presented modification procedure. By adding KCl to the modification solutions, former ‘floppy’ polyether units become less dangling and the formation of the preliminary ‘in-plane’ complex occur (see Figure 87). Hence, the surface immobilization is obtained along with the spatial arrangement of the oligoethylene glycol, generating the desired geometrical cavity.

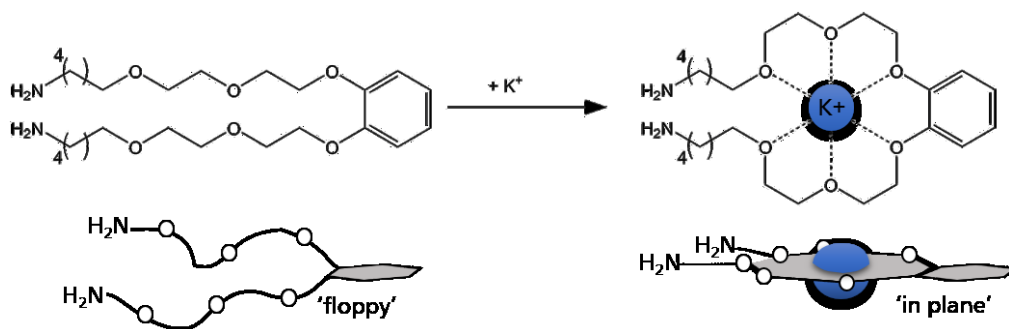


Figure 87: The ‘floppy’ vs ‘in plane’-scaffold of bis-podand-NH<sub>2</sub> in presence and absence of potassium ions.

The *IV*-curves were measured for the nanopore modified without any traces of potassium ions. The respective *IV*-curves recorded before and after the modification are shown in the following figure.

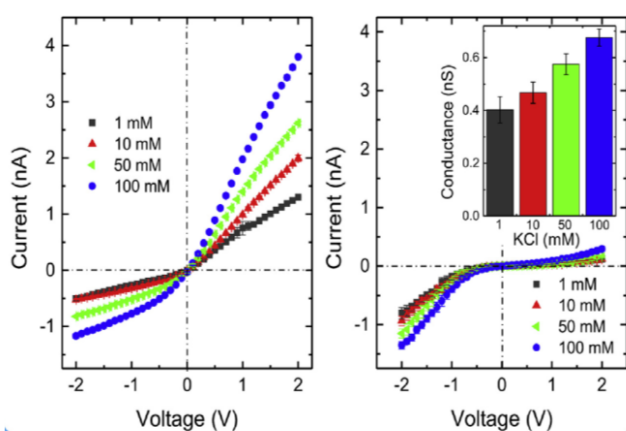


Figure 88: The changes in the ionic transport of the unmodified pore membrane (a) and after the random attachment of *bis*-podand-moieties in absence (b) of

and 0.5 nA for positive applied voltages (2V). In contrast, the recorded current values for negative applied voltages amounts between -0.7 nA and 1.4 nA. The inverted shape of the *IV*-curves indicates a low density of positively charged surfaces caused by capture of potassium ions. These results clearly show the importance of the preliminary formation of the well-ordered *bis*-podand complex to avoid an attachment of ‘floppy’ polyether moieties.

### 2.3. Conclusion

In summary, the functionalization of a conical single nanopore with *bis*-podand moieties offers the possibility to stimulate the ionic transport via potassium-ions. For this purpose, *bis*-podand-NH<sub>2</sub> was attached covalently to the nanopore surface using EDC/PFP-coupling-chemistry. In presence of KCl, the formation of a six-centered pseudo-crown complex occurs which shows the capturing of the potassium ions from the surrounding. The formed cavities led to a positively charged pore surface after modification and upon exposure to KCl solution. The changes in the surface charge were examined through *IV*-measurements, providing an inverted rectification behaviour compared to the *IV*-characteristics of a blank (negatively charged) nanopore. Furthermore, other alkali ions such as Li<sup>+</sup>, Na<sup>+</sup>, Rb<sup>+</sup> and Cs<sup>+</sup> do not show significant changes in the *IV*-characteristics due to their inability to create stable complexes with the immobilized *bis*-podand-units. The experimental results showed significantly the stimulation of ionic transport of nanopores in a qualitative way, i. e., only potassium ions affect the ion transport, and in a quantitative way, i. e., varying the potassium amount influences directly the ionic transport. In addition, if the pore surface is modified with *bis*-podand-moieties in the absence of KCl, the crucial pre-assembly of the well-ordered polyether moieties does not occur. Consequently, a selective detection of alkali ions was not achievable due to an insufficient formation of a binding domain during the modification step.

This study would help to monitor the potassium level in clinical studies because potassium plays a significant role in the neuronal signal transduction. Moreover, the recognition of other ionic

---

types would also be possible by varying the number of oligoethylene glycol-groups. In this way, the cavities can be tuned on-demand to capture the desired cationic species.

---

### 3. Automated Measuring of Mass Transport through Synthetic Nanochannels Functionalized with Polyelectrolyte Porous Networks\*

---

#### 3.1. Introduction

Nanopore membranes can act as sensing devices due to their outstanding ability to incorporate broad ranges of (bio)receptors onto the inner pore surface. (72) However, the modulation of surface charge and, thus, the control over the ionic transport across the membrane can be examined through the immobilization of polyelectrolytes, i. e. highly charged macromolecular chains, onto the nanopore walls. For this purpose, the ‘Layer-by-Layer’ (LBL) method has been established to sufficiently incorporate various polyelectrolyte within the nanoconfinement of the pore region. Numerous reports has demonstrated their easy handling and practical proceeding that don’t require expensive instrumental setups. (112, 188, 189)

Previously, Schmitt and co-workers have introduced LBL-assembly by stacking positively and negatively charged polyelectrolytes onto the solid surfaces. Overtime, the LBL-methods was used to modify the planar surfaces (277, 278) as well as nanoconfined surroundings (279, 280) along with the alternating deposition of oppositely charged polyelectrolytes. The adaption onto track-etched nanopores was firstly presented by Balme *et al.* through the layering of poly(ethyleneimine) and chondroitin-4-sulfate creating a pH-gated single nanopore. (281) Overall, the correlation over surface charge and ionic transport inside track-etched nanopores was demonstrated using LBL-assemblies of poly(acrylic acid) with either poly(*L*-lysine) or poly(ethyleneimine). Exposing LBL-modified nanopores to electrolytes having different concentration gradients they were able to build-up osmotic energy devices that could be used for the production of ‘blue energy’. (282) Ali *et al.* attached biotinylated poly(allyl amine) onto nanopore surfaces and demonstrated the biosensing activity towards streptavidin protein. (58) In addition, Anderson *et al.* enabled the protein-driven transport across the porous membrane by modifying the pore region using cross-linked poly(acrylamide)-moieties onto nanopore surfaces. (283)

Using the LBL-technique, numerous studies showed not only the ability to incorporate sensing properties to well-defined single nanopore membranes but also to act as key-components in (nano)filtrations from the case of multipore membranes. (284)

To enhance already established biomolecular detection pathways through LBL-modified nanopores, innovative combinations of LBL-assemblies have to be figured out. This study focusses on the creation of novel LBL-polyelectrolyte-pairs. In the present case, the negatively charged poly(acrylic acid) is layered onto the nanopore surface in combination with the positively charged poly(allylamine hydrochloride). The experiments are adapted and evaluated not only on single pores but also on oligo and multipore membranes.

### 3.2. Results and Discussion

Surface modification promoted by LBL-technique is a well-established method to coat substrate materials with multilayers. Moreover, the technique enables the possibility to control the film thickness of the coated layer in a nanometre range. (285) Common LBL-procedures are carried out in a cyclical process, where the charged substrate is exposed to a polyelectrolyte solution leading to an electrostatic adsorption of the polyelectrolyte onto the substrate. Then, the exposure to an oppositely charged polyelectrolyte promotes the formation of a bilayer structure in the range of few nanometres. To obtain a multilayer film, the sequential adsorption process has to be repeated. (286)

In detail, the classic procedure for LBL-deposition of polyelectrolytes is based on the periodic immersion of a charged substrate in a polycation and polyanion solution, respectively. In this study, the use of nanopore membranes required a slight distancing from the classical procedure. Generally the LBL-procedure is carried out in cycles by immersing the desired substrate material into the polyelectrolyte solution, then into a washing solution (pure buffer solution) and then into the next polyelectrolyte solution. Since the successful modification needs to be monitored by *IV*-characteristics, the general LBL-method is carried out in the measurement setup as shown in the following figure.

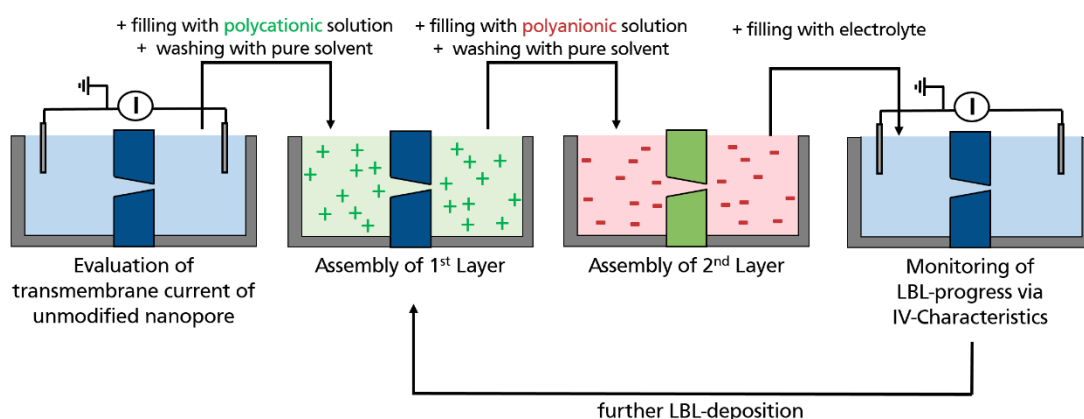


Figure 89: Experimental setup and procedure for the surface modification using LBL-deposition technique onto nanopore membranes. In this case, the experimental pathway for the deposition of two oppositely charged layers is shown by repeating the LBL-assembly the generation of multi-layered films onto the nanopore surface is achieved. After every polyelectrolyte deposition numerous washing steps are carried out, by removing the polyelectrolyte solution and filling the half-cells with pure buffer-solution.

The 'updated' procedure enables the possibility to monitor the progress of the modification via *IV*-measurements. The distribution of the channels on the membrane is statistically arranged due to its production. Therefore, sufficient characterization of the modification on the nanopores (especially for the case of multipore membranes) is only possible if the etched membrane is fixed in the two-cell measurement setup being already introduced in the experimental part (CHAPTER II.2, Figure 29). Then, all subsequent modifications and *IV*-measurements as well as the later in this section described analyte permeation experiments are carried out in this configuration without the membrane being taken out. In this way, the one-time clamping of the membrane guarantees the examination of the same transmembrane area and ensures that not only the equal number of pores, but that exactly the same pores are characterized throughout the whole modification process. Additionally, a comparison of the modification steps is given and performance of the modified membranes is also discussed.

The following experiments were carried out by following two different routes: (i) LBL-modification of 2-compound system and (ii) LBL-modification of 3-compound system (see Figure 90).

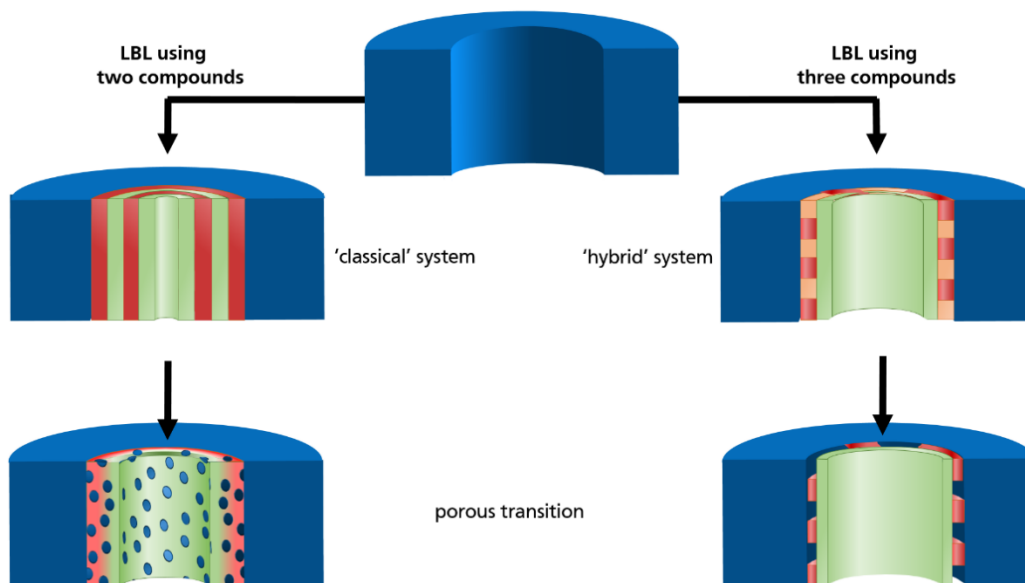


Figure 90: LBL-modification performed through the deposition of two compounds (classical system), presented in section 3.2.1 and three compounds (hybrid system), presented in section 3.2.2., separately.

For both LBL -procedures, the assembled multilayer films are converted into porous structures. Such porous self-assembled polyelectrolytes are composed of high surface areas for the potential use in the field of filtrations/separations, drug delivery or catalysis. (287, 288) Porous transitions are mostly induced by a pH-change or in presence of metal ions causing a reorganization of the stacked layers. For instance, on silica substrates a porous structure of PAH/PAA-films occurs by immersing the LBL-modified substrate into acidic solution. (289) Additionally, Tsuge and co-workers showed a porous transition of the same polyelectrolyte system in the presence of metal ions. (290)

In this study, the layered assembly is obtained at first through the deposition of the polyelectrolyte pair of poly(allylamine hydrochloride), herein referred as [PAH], alternatively stacked with poly(acrylic acid), herein referred as [PAA]. Then, the PAA/PAH-film is converted into porous structures in the presence of silver-ions and the sensitivity towards silver ions has been evaluated. The respective results are briefly described in section 3.2.1.

Secondly, the [PAA|PAH]-modification was extended to a 3-compound system. Here, poly(vinyl-4-pyridine) [PVP] was used to create a hybrid LBL-structure by electrostatic interactions between PAA and PAH moieties, as well as H-donor-activities between PAH- and PVP-units. Here, the porous transformation is induced by wash-out of the PVP-component. The underlying experimental data is presented and discussed in section 3.2.2.

### 3.2.1. Investigations on Classical LBL-Modification (2-Compound System)

In this part, a conical single pore and a multipore membrane, having a pore density of  $10^7$  pores/cm<sup>2</sup>, are coated by the alternating assembly of the cationic PAH and anionic PAA

according to the protocol already described in section 2.3.1 (CHAPTER II). In the next step, the transition of the assembled dense multi-layered films into porous structures is carried out upon exposure to silver-ion solution. An overview about the LBL-deposition and the respective transformation in the presence of silver ions is given in the following figure for the deposition of one bilayer, i. e., one layer of PAH-moieties and one layer of PAA-groups. The experimental data is characterized by *IV*-measurements and SEM-images.

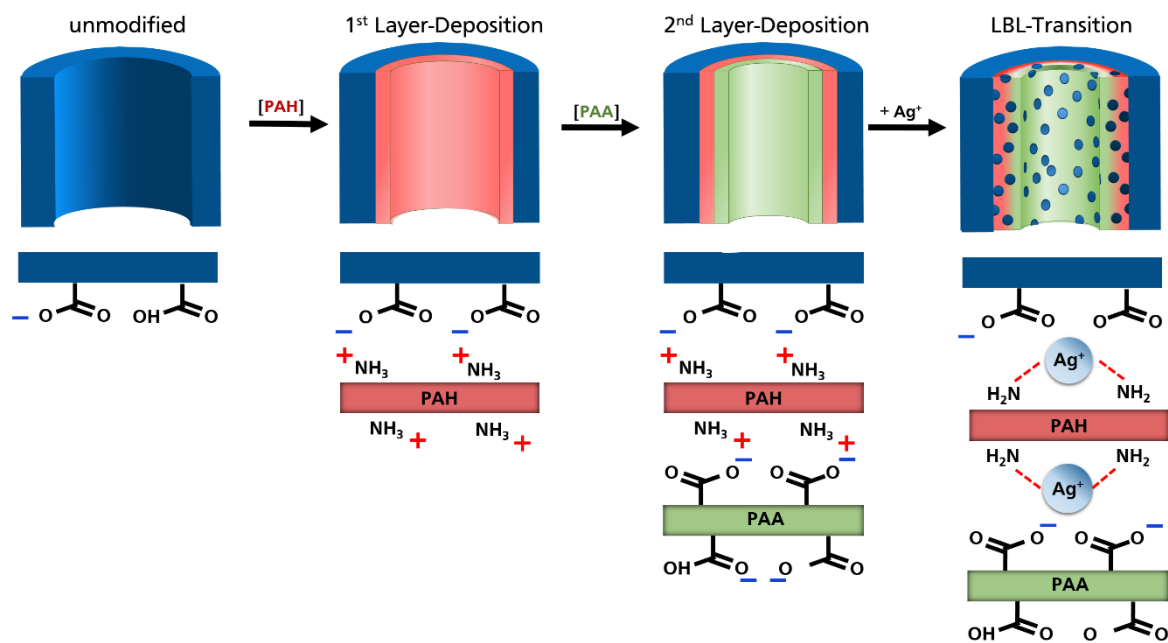


Figure 91: Schematic modification of track-etched nanopores using LBL-method, to deposit polyelectrolytes onto the entire nanopore surface. Here, the deposition of one bilayer  $[\text{PAH}]_1[\text{PAA}]_1$  is presented as well as their transformation into porous networks. Firstly, the unmodified nanopore is coated with a layer of  $[\text{PAH}]$  followed by a layer of  $[\text{PAA}]$ . Coulomb attraction between positive amine groups and negative carboxylic groups are demonstrated leading to the generation of the stacked structures. Afterwards, exposition to silver(I)-ion solutions is carried out leading to a generation of pores within the multilayers.

### Layer-By-Layer Deposition

The modification of track-etched nanopores by LBL-assembly using polycationic PAH and polyanionic PAA was performed according to the protocol as described in section 2.3.1 (CHAPTER II). The modification progress was examined using *IV*-experiments based on the changes in the ionic transport properties during LBL-modification. The resulting *IV*-curves and their corresponding rectifying factor  $f_{\text{rec}}$  for the deposition of two bilayers, i. e., four separate layers, are presented in the following Figure 92a using a conical single pore membrane fabricated according to protocol in section 1.2 (CHAPTER II). The base and tip opening diameters are 307 nm and 28 nm calculated following the protocol described in section 3.3.1 (CHAPTER II), respectively.

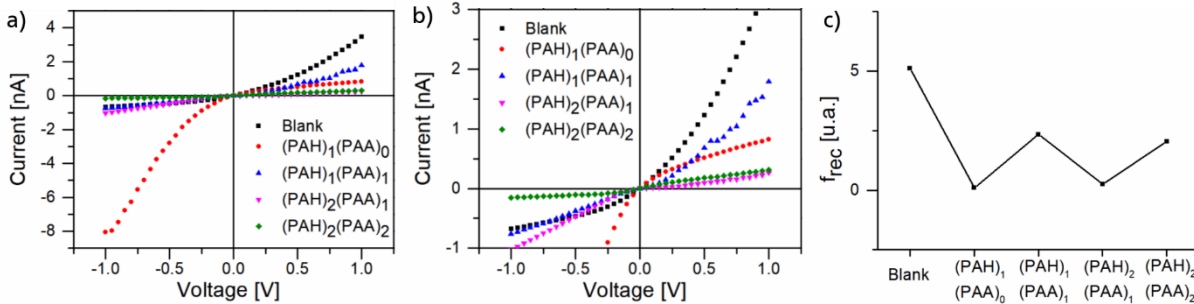


Figure 92: (a) Characteristic  $IV$ -curves before (black line) and after LBL self-assembly of two bilayers of PAH and PAA using a singlepore membrane ( $D=307$  nm and  $d=28$  nm).  $IV$ -curves are measured in 0.1 M KCl-electrolyte. (b) respective zoomed  $IV$ -curves of (a). Illustration of the rectifying factors  $f_{rec}$  calculated by the ratio of the current at +1 V to -1 V, respectively (c).

In order to illustrate the characteristic ion transport properties more clearly, Figure 92b displays the zoomed  $IV$ -curves, whereas the respective rectifying factors are presented in Figure 92c in dependence on the LBL-process. Starting with an unmodified conical nanopore, the measured current provides the expected positive rectification behaviour, indicating a discriminated anionic movement across the membrane. The rectification is induced by the initial negatively charged surface of the pore originated by deprotonated COOH-groups, which are generated during the pore fabrication process.

The assembly of the first layer made of polycationic PAH leads to an inversion of the  $IV$ -curve induced by an oppositely charged inner pore surface compared to the blank state. The formation of the first layer is promoted by COULOMB-attraction between the positively charged amino-groups of PAH-chains and the negatively charged pore surface. Hence, the polarity of the pore surface was inverted and causes a hindrance for the anion movement across the pore region evidenced by the negative rectification behaviour. Regarding the  $IV$ -curves, the maximum current value for positive bias reduced from 3.4 nA (blank state) to about 0.8 nA (1st PAH-layer), whereas at -1 V the current is increased from  $-0.7$  nA to  $-8.1$  nA. The change of selective ion transport is also defined by the rectification factors  $f_{rec}$  with respect to each modification step. Note that for  $f_{rec} > 1$  the ionic transport is mainly induced by cationic movement (positive rectification; negative pore surface), whereas for  $f_{rec} < 1$ , the ionic transport is mainly originated by anionic movements (negative rectification; positive pore surface). In addition, for the case of  $f_{rec} = 1$ , no rectification occurs because of uncharged surface and, thus, the resulting current is carried by the equal movement of anions and cations. Here, after the 1<sup>st</sup>-PAA deposition, the value of  $f_{rec}$  is shifted from  $\sim 10$  to  $\sim 0.4$ . Note that the deposition of the first cationic layer does not promote a charge compensation. Otherwise, a neutral pore surface and a linear  $IV$ -curve would be obtained. In fact, the  $IV$ -curve provides a total current after the 1<sup>st</sup> PAH-layer (8 nA) that is four times higher than the current measured for the blank state (2 nA) indicating charge density of the 1<sup>st</sup>-PAH layer is significantly higher than the pore charge density in the blank state.

The deposition of the 2<sup>nd</sup> layer, i. e.,  $[\text{PAH}]_1[\text{PAA}]_1$ , induces a further inversion of the measured current. Here, the  $IV$ -curve reveals a high cationic selectivity showing a clear rectification behaviour towards cationic movements, indicating a regenerated negative polarity of the pore region. In detail, the current value for the case of 1V changed from 0.8 nA ( $[\text{PAH}]_1[\text{PAA}]_0$ ) to 1.8 nA ( $[\text{PAH}]_1[\text{PAA}]_1$ ) and for the case of -1 V the current shifted from 8.0 nA ( $[\text{PAH}]_1[\text{PAA}]_0$ ) to  $-0.8$  nA ( $[\text{PAH}]_1[\text{PAA}]_1$ ). The total current value of 1.8 nA is only half of the current value

obtained from the unmodified state (3.4 nA). Here, the third layer, i. e., [PAH]<sub>2</sub>[PAA]<sub>1</sub>, provides with  $f_{rec} = 0.3$  with inverted rectification behaviour due to the adsorption of passively charged PAH-chains. Moving on to the assembly of the 4<sup>th</sup> layer, i. e., [PAH]<sub>2</sub>[PAA]<sub>2</sub>, the *IV*-curve overturned ( $f_{rec} = 2.1$ ) and become selective towards cations indicating the generation of the negatively charged layers.

Overall, the decrease of maximum current indicates a decrease in pore diameter upon the on-going LBL-modification. Recently, Ali *et al.* performed the LBL-deposition of PAH with the negatively charged electrolyte poly(styrenesulfonate) (PSS) to modify the ionic transport properties of a polymeric substrate. They reported that the growing bilayer inside the nanopore induces a decrease of surface charge due to formation of bulk ion pairs within the film. (111) Furthermore, Zykwiniska and co-workers emphasized the reports of Ali *et al.*, and demonstrated, that for each layer deposited the tip diameter decreases to about 0.5 nm. (291)

Similar to the LBL-assembly onto the single pore membrane, a conical multipore membrane having a pore density of  $10^7$  ions/cm<sup>2</sup> was modified and characterized by *IV*-measurements. Note that the entire modification process was carried out in the same manner as for the single pore membrane. The resulting *IV*-characteristics show similar rectifying behaviour as that of the single pore. Here, the alternating flipping of rectification behaviour either with the deposition of the respective positive or negative polyelectrolyte is detected but less significant compared to the results obtained by single pore membranes. Although, the *IV*-characteristics are limited to the use of single-nanopore membranes, the LBL-modification was recorded in an adequate quality upon the use of multipore membranes. Due to the high pore density and superposed transport properties, even the unmodified membrane provides only traces of rectification behaviour. Nonetheless, the on-going LBL-deposition provided only marginal but measurable flipping of selective ionic transport. The results can only be analysed qualitatively and, yet, the LBL-deposition of multipores is achievable but cannot be fully examined using *IV*-experiments.

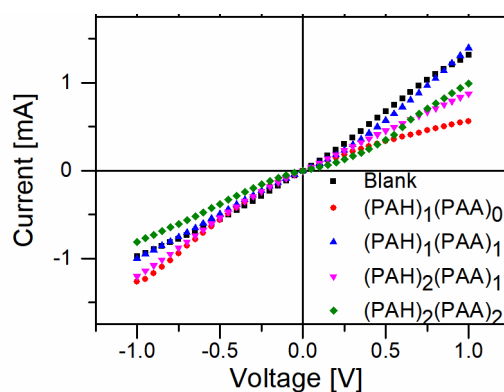


Figure 93: Characteristic *IV*-cures before (black line) and after LBL-assembly of two bilayers of PAH and PAA using a multipore membrane ( $10^7$  pores/cm<sup>2</sup>;  $D=107$  nm;  $d=28$  nm) measured in 0.1 M KCl-electrolyte.

In summary, the on-going layering inside nanopores consequently decreases the transmembrane current as expected due to the formation of ionic bulk pairs (charge compensation) and the decreased pore opening. Moreover, the stepwise reduction of current was accompanied by the alternative inversion of the rectification, indicating the successful formation of oppositely charged multilayers within the nanoconfined geometries.

### Porous Transition

The transition of the polyelectrolyte film [PAH]<sub>2</sub>[PAA]<sub>2</sub> from dense to porous inside the conical single pore is examined through the *IV*-curves after the membrane was exposed to various Ag<sup>+</sup>-solutions having different concentrations of silver ions (see Figure 94a).

Based on the approach of Tsunge *et al.*, a phase transition is achievable upon exposure to  $\text{Ag}^+$ -ions, leading to transformation of dense polyelectrolyte layers to porous one. The phase separation is attributed to the formation of new bonds between the amino groups and metal ions along with ionic bond disruption and reorganization. (290) Therefore, a similar porous transition is expected to occur within the nanopore confinement and, thus, changes in transmembrane current are expected.

Two phenomena were observed during *IV*-measurements upon decreasing the  $\text{Ag}^+$ -concentration in the transition solution from 1 nM to 1  $\mu\text{M}$  (Figure 94a).

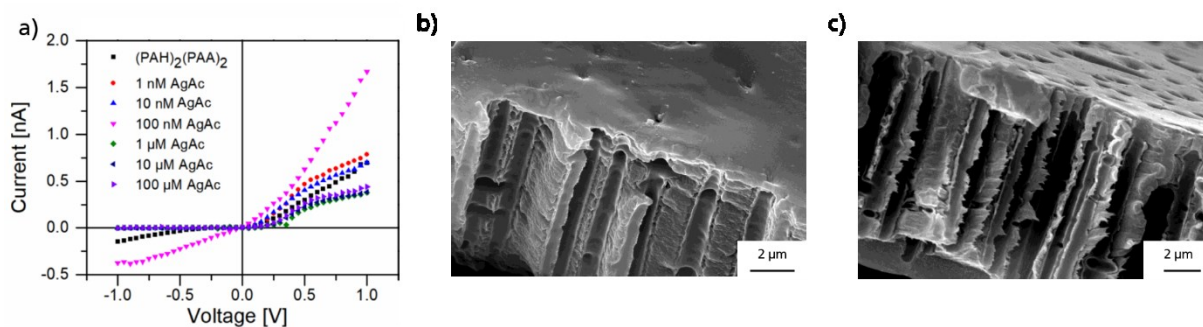


Figure 94: (a) Characteristic *IV*-curves of the single conical nanopore modified with  $[\text{PAH}]_2[\text{PAA}]_2$  (black line) upon exposure to aqueous solutions containing different concentrations of silver(I) ions. (b) Cross-section of multipore membrane having 200 nm cylindrical nanopores ( $d= 200\text{nm}$ ) modified with four bilayers of PAA and PAH and (c) the same multipore membrane after exposure to aqueous  $\text{Ag}^+$ -solution (100 nM).

First, the exposure to 1 nM promoted an increase of current from 0.3 nA (layered state) to 0.5 nA. Moreover, the *IV*-curve shows a change of the rectification behaviour. Prior to the  $\text{Ag}^+$ -exposure, the *IV*-curve shows a positive rectification due to the negatively charged surface of the PAA-moieties. It can be assumed that the  $\text{NH}_2$ -groups of PAH-layers were complexed with silver-ions, leading to the reduction of surface charge density. The  $\text{Ag}^+$ -interaction was performed at neutral pH ranges similar to the LBL-deposition step. According to Ferreira *et al.*, only 20% of the amino groups of PAH are protonated. (292) The remaining uncharged amino-moieties are liable for the formation of silver-amino-complexes within the multifilms. Now, the layers are rearranged in such a way that the bilayers are packed denser due to the more charged PAH-layer. Thus, the current flow is enhanced but less rectifying.

Second, a further increase of  $\text{Ag}^+$ -amount does not lead to an increase in current flow. Contrary to the expectation, the current was decreased from 0.3 nA (10 nM) to 0.2 nA (100 nM), but even higher  $\text{Ag}^+$ -concentrations (10  $\mu\text{M}$ ) provide only marginal changes in transmembrane current (0.19 nA). This could be probably caused by saturation effects. Upon increasing the silver-concentration, more silver-ions are now incorporated into the PAH-layers, leading to a sort of swelling of the PAH layer. The higher amount of silver ions causes a expanding of the PAH-chains, which makes the PAH-layer thicker. The rearrangement of the PAA-chains is limited due to the nanoconfined surrounding and a contraction of the layered structure is not feasible anymore. Consequently, the absolute current value is lower than for the 1 nM silver-amount. A further increase of silver-concentration does not affect the layer growth of PAH-chains within the limited space of the nanopore region, and therefore, the current value remains the same.

Overall, the interaction with silver-ions affects the transmembrane current. The incorporation of  $\text{Ag}^+$ -ions causes not only a decrease in surface charge density but also a rearrangement of

---

the former layered structure. Decher and co-workers have demonstrated that during the LBL-assembly of polyelectrolytes, not only the top layer affects the ionic transport but also the underlying layers. Polyelectrolyte multilayer films are not constituted of precisely stacked separate layers and show interpenetration of up to four layers. (293, 294) The interaction of  $\text{Ag}^+$ -ions with the layers deposited onto the nanopores were significantly noticed but the interpretation is difficult.

Tsuge *et al.* studied the interaction of  $\text{Ag}^+$ -ions with the layered structure onto planar glass-surfaces. (290) By the use of scanning electron microscopy, they were able to show both the successful porous transformation of multilayers prepared by alternatively stacked PAH- and PAA-layers, and the control over the porous transformation in dependence on the silver-ion amount. The adaptation of this study onto the nanopore surrounding is presented in Figure 94b and c. Here, cross-sections of multipore membranes having a pore density of  $10^7$  pores/cm<sup>2</sup> were investigated using SEM-imaging. Tsuge *et al.* have demonstrated the functionalization of the substrate surface with a high number of bilayer ( $> 20$  single layers) to enable a sufficient layer thickness that can be resolved by the SEM. Therefore, the multipore membranes were modified with ten PAH/PAA-bilayers as well. Moreover, the porous transition of the layered structure is of special interest within the pore region and is examined using cross-sections of the respective membranes. Therefore, the production of cylindrical cross sections is more feasible, if cylindrical pores were used.

Prior to the record of the SEM-images, the entire membrane was modified with ten bilayers of PAH/PAA and was cut into two pieces. One half remains the same, the other half was exposed to 1 nM  $\text{Ag}^+$ -solution for about 4 hours. Then the cross-sections of both pieces were prepared and examined under the SEM. Figure 94b shows the profiles of nanopore membranes after the deposition of ten PAA/PAH-bilayers before exposure to silver-ions. The inner pore structure is covered by a smooth film of the PAH/PAA-layers compared to the profile of an unmodified pore already displayed in Figure 46a. Now, Figure 94c demonstrates the pore profile after immersing into the silver-solution. Here, sort of ragged break edges are visible compared to the break profile in absence of silver ions. This ragged profile could be caused due to an enhanced stability of the layers in presence of silver ions. The porous transition observed as reported by Tsuge *et al.* was not resolved using SEM-imaging presumably due to resolution limits or because no porous transition has taken place at all. Nonetheless, it is obvious that the  $\text{Ag}^+$ -contact does affect the assembled layer, otherwise the ragged break edges were not visible.

In sum, the deposition of PAH/PAA-layers using the LBL-technique was successfully performed onto the nanopore membranes as evidenced by *IV*-measurements using not only single pore but also with multipore membranes. Here, the on-going layer-procedure was more significantly monitored by the use of single pores, although multipores provided similar trends of the current change. Moreover, the interaction of silver ions with the layered structure was also investigated. Using both *IV*-experiments and SEM-image, significant morphological changes were observed upon silver-ion interaction, making the LBL-technique a versatile method to control the transmembrane transport of ions. In addition, a linear trend of transport control with respect to the used  $\text{Ag}^+$ -amount was not detected. This could be caused by the fact, that in the presence of  $\text{Ag}^+$ -ions the rearrangement of the PAH/PAA-layers occurred. The first contact to  $\text{Ag}^+$ -ions lead to an increase in the *IV*-current, because incorporation of silver ions occurs into the most closely stacked layers, whereas the further increase of  $\text{Ag}^+$ -amount provides the highest decrease of current due a sort of swelling effects. It is suggested that the enhanced net charge

of PAH-layer leads to highly spreaded PAH-chains. Due to the individual rearrangement of PAH/PAA-layers in presence of silver-ions, the effect of porous transition onto the transmembrane current is not easily controllable.

Overall, the stability of LBL-assembly structures have to be enhanced and the porous transition has to be more controllable in order to regulate more precisely the ionic transport. Therefore, the gain of layer-stability is investigated in the next pages using a LBL-modification method consisting of three compounds.

### 3.2.2. Investigations on Hybrid LBL-Modification (3-Compound System)

The generation of a hybrid multilayer-system inside the nanopore geometry is presented. Here, PET-nanopore membranes containing cylindrical pores with a diameter of 200 nm as well as various pore densities were used. The surface modification was performed according to the protocol in the CHAPTER II, section 2.3.2. Upon exposing the nanopore membranes to a cationic blend [PAH|PVP] followed by treatment with anionic [PAA]-solution, the formation of the layered structure occurs. Note that the ingredient-ratio of the cationic blend was varied along with the experimental course. Next, the membrane is covalently cross-linked in order to stabilize the multilayers. The treatment of the cross-linked membrane with basic solution leads to the wash-out of the PVP-component, leading to the formation of porous networks. To this end, the fabrication of cylindrical nanopores was performed using the protocol already introduced in section 1.1 (CHAPTER II). However, the etching procedure provides not only the formation of pores but also carboxylic acid groups on the entire pore surface, which act as starting points for the following LBL-modification (see Figure 95).

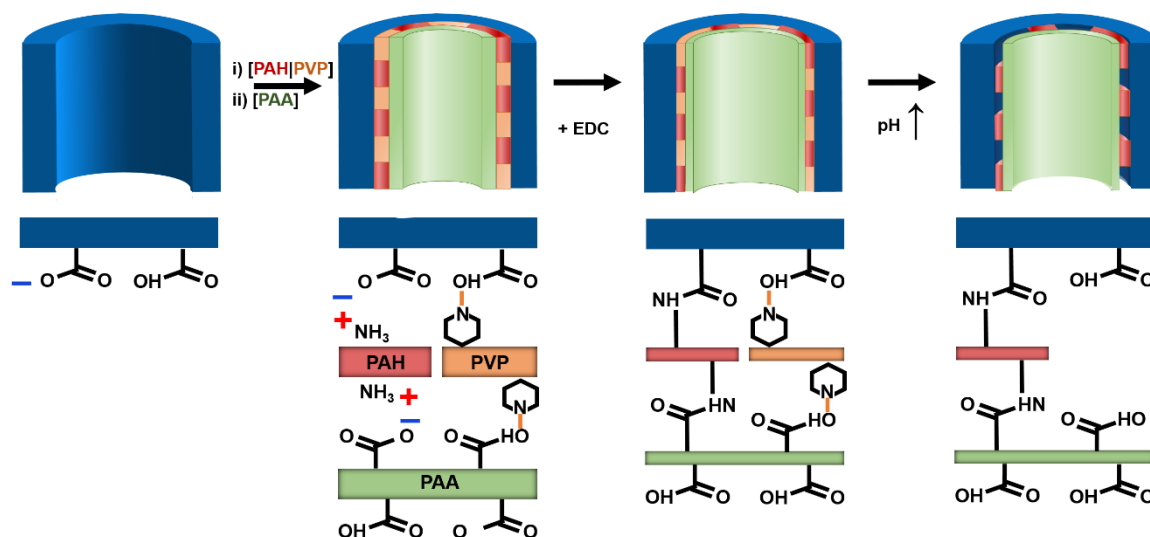


Figure 95: Schematic representation of LBL modification of track-etched nanopores by the deposition of polyelectrolytes onto the entire nanopore surface. Here, the deposition of two bilayers  $[\text{PAH}|\text{PVP}]_2[\text{PAA}]_2$  is presented as well as their transformation into porous networks. Firstly, the unmodified nanopore is coated with a layer of [PAH|PVP] followed by a layer of [PAA]. Coulomb attraction between positive amine groups and negative carboxylic groups as well as hydrogen-bonds of PVP and protonated carboxylic groups are demonstrated, leading to the generation of the stacked structure. Afterwards, cross-linking of the multilayers on the channel surface occurred by a layer contraction. Finally, the pH induced wash-out of hydrogen-bonded PVP is carried out leading to the generation of pores within the multilayers.

The formation of the porous LBL-structure described in Figure 95 was carried out upon exposure of positively charged blend mixture [PAH|PVP] having different ratios and negatively charged [PAA]-solution, in an alternating order. In an acidic surrounding (pH 3.9), the pore surface is composed of both negatively charged COO<sup>-</sup>-groups and uncharged COOH-coups. Hence, the deprotonated state is able to undergo electrostatic interactions with positively charged moieties (PAH), whereas the protonated units are able to form H-bridges with possible *H*-acceptor PVP molecules. (191) For a better overview, the individual modification state is determined by the term [PAH|PVP]<sub>a</sub>[PAA]<sub>b</sub>, where the indices defined the number of assembled polyelectrolyte layers. Here, the deposition of eight layers, i. e., four bilayers [PAH|PVP]<sub>4</sub>[PAA]<sub>4</sub>, was carried out onto the pore surface and treated with EDC-solution to provide a stabilization of the deposited layers through covalent cross-linking. Upon exposure to basic solutions (pH 10), the layered surface is transformed into a porous one because of the rupture of H-bridges, leading to a successful PVP-removal.

In the present case, various pore densities were used to evaluate the LBL-promoted modulation of the transmembrane ionic/molecular transport. For this purpose, single and membranes having 10<sup>3</sup> pores/cm<sup>2</sup> were examined using *IV*-measurements according to the protocol described in section 3.2.1, whereas multipore membranes (10<sup>7</sup> pores/cm<sup>2</sup>) were analysed using mass transport experiments, as described in the next section.

### LBL-modification inside nanopore membranes and their *IV*-characteristics

The process of LBL-treatment was monitored using *IV*-experiments. The respective results are shown in the following figure for a single pore having a diameter of 200 nm. The experiments were performed in MES-buffered KCl-electrolyte at pH 3.9.

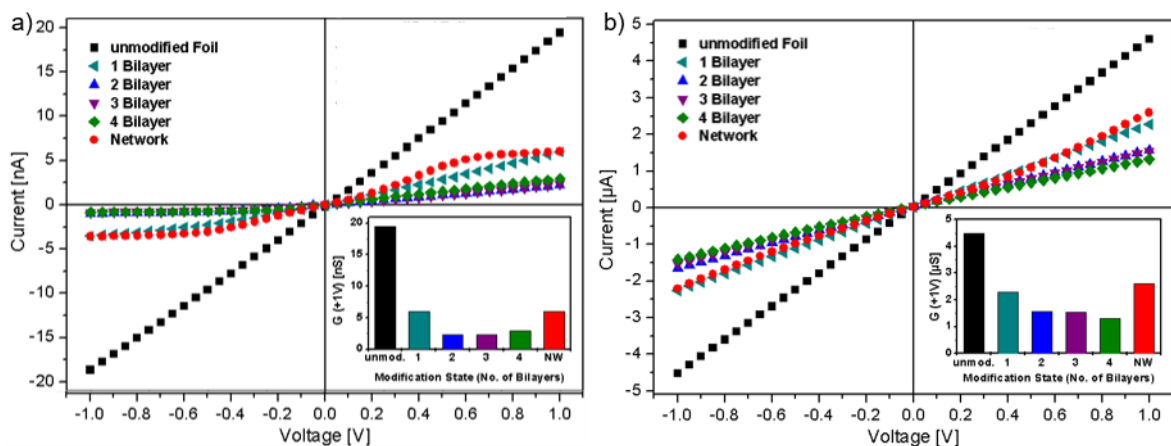


Figure 96: *IV*-measurements using a single pore membrane (a) and an oligopore membrane (b) having a diameter of 200 nm. Note that the measurements were performed using an MES-buffered KCl-electrolyte having a concentration of 100 mM (pH: 3.9). Inlet shows corresponding conductance values at +1 V in dependence on the underlying modification state. Modification state 1 to 4 is referred to one deposited bilayer of polyelectrolytes, e. g. modification state 1 symbolizes [PAH|PVP]<sub>1</sub>[PAA]<sub>1</sub>.

First, the deposition of the first bilayer [PAH|PVP]<sub>1</sub>[PAA]<sub>1</sub> decreases the current (at 1 V) to almost 70% (from ~20 nA to ~6 nA). The assembly of the second bilayer causes a further current reduction to almost 2 nA. Further depositions of bilayers do not affect the current flow (less than 5%) as the deposition of the first two layers indicated the saturation of polyelectrolyte deposition. Adapting the LBL-modification onto oligopore membranes (10<sup>3</sup> pores/cm<sup>2</sup>), the resulted *IV*-characteristics are quite similar (see Figure 95b) to single-pore ones.

---

Overall, the deposition of four bilayers reduce the maximum current up to  $\sim 80\%$  inside single pore membranes, whereas the reduction of  $\sim 70\%$  is noticed for the oligopore membranes.

Recently, Azzaroni *et al.* figured out that the influence of LBL-structures inside track-etched nanopores causes the generation of so-called bulk ion pairs. (111) Upon the further assembly of bilayers, the persistent physical absorption of polyelectrolytes inside the nanopores leads to both a reduction of the pore diameter and the surface charge density as evidenced by the experimental data in Figure 96. Moreover, the huge current decrease is evidenced for the first two bilayers and leads to a more efficient decrease of diameter and higher charge compensation. Two forces promote the deposition of the first layer of the cationic blend: (i) the electrostatic interactions between the positively charged amine groups of PAH and the  $\text{COO}^-$ -groups of the nanopore as well as (ii) *H*-bridges between the  $\text{COOH}$ -groups of the pore surface and the pyridine-units of the PVP-compound. The adsorption of PAA occurs similar to the interactions between pore surface and cationic blend due to the fact, that at pH 3.9 protonated and deprotonated carboxyl groups are coexisting within the PAA-chains. An ongoing LBL-assembly does not further influence the current transport because of the charge compensation is at its maximum level during the deposition the first two bilayers. In addition, *IV*-measurements were performed using the same pH value (pH 3.9) as carried out for the modification steps to avoid the displacement of hydrogen-bonded PVP compound.

Subsequently, the deposited bilayers are interlinked using EDC-solution to decrease the vulnerability towards changes in the experimental surrounding. Recent studies showed the effect of the cross linkage of PAH and PAA to enhance the stability of the layered system. (295) The EDC-treatment leads to the formation of covalent bonds between the carboxylic groups of PAA and the amino groups of the PAH layer.

In the final step, the pore membrane is exposed to a phosphate buffered solution (pH 10). After a specific time period, the rupture of the *H*-bridges between PVP and carboxylic groups occurs, leading to the wash-out of PVP-moieties from the cross-linked layers. The pH-induced wash-out of PVP leads to pore formation within the multilayer-system as evidenced from the increased ionic transport of Figure 96a and Figure 96b, respectively. After the LBL-assembly, the crosslinking and wash-out step increases the transmembrane current from  $\sim 3$  nA to 6 nA (single pore) and from  $-1.3 \mu\text{A}$  to  $2.6 \mu\text{A}$  (oligopore membrane). Overall, the post-modification, i. e., the EDC-treatment and the PVP-washout, leads to a transmembrane current being two-times higher than the current of the LBL-state as shown in Figure 96. In addition, the shape of the *IV*-curve is shifted from almost linear to an *S*-shaped character presumably caused by the different deposition of polyelectrolytes between the pore openings and the inner pore region. In this case, the LBL-treatment leads to cigar-shaped nanopores that are known to provide sigmoidal shaped *IV*-curves. If small voltages are applied, the current flow is increased compared to a linear *IV*-curve. In contrast, higher voltages provide an intrinsic potential located in the interior of the pore causing an ion depletion. This phenomenon is based on the rejection of ion passage due to saturation of ionic transport across the nanopore area being already observed by Ali *et al.* (92) If the LBL-modification is further extended to membranes with higher pore densities, the characterization method has to be adjusted. Experimental data are described in the next section.

---

## Analyte transport using automated mass transport experiments

The membranes having a pore density of  $10^7$  pores/cm<sup>2</sup> or even higher cannot be analysed through *IV*-measurements, because the transmembrane current is a superposition based on the individual ionic transport of every single nanopore within the membrane. Therefore, during *IV*-measurements the electrodes receive only a sum of current provided by the respective flux of all pores located in the transmembrane area. (296) In previous studies, mass transport experiments were established to investigate analyte transport across the pore region of multipore membranes. Here, the diffusion of positively and negatively charged organic molecules instead of the transport of ions across the multipore membranes is examined after fixed time-periods. The molecular concentration in the permeate solution is analysed through UV/vis-spectroscopy. (71, 89, 297–299)

According to the protocols provided in the literature, the analyte diffusion is carried out in the setup described in Figure 6a. Although the experimental method is generally accepted and sufficient, the procedure is quite limited in terms of handling and reproducibility. First, the manual sample collection requires for every sample volume of the permeate solution taken out from the permeate cell. Then the same volume of pure solvent had to be added back to the cell. In this way, on the one hand, disturbances of volume fractions are prevented, and osmotic pressure is also not affected. On the other hand, this strategy causes dilution errors. Secondly, the collected fractions have to be analysed by UV/vis-analysis. Here, every single fraction is evaluated individually, which is time-consuming. At least, the diffusion record could become error-prone, if the analyte transport across the pore region is too high, especially when using highly porous membranes or membranes having large pore diameters. On the contrary, if the analyte diffusion is too low, the effect of permeated analyte cannot be distinguished from the background adsorption. Hence, the low signal-to-noise ratio also limits the accuracy of analyte record.

However, the classical mass transport can be improved with respect to the sample collection, data analysis and experimental procedure. For instance, Baltus *et al.* presented a mass transport method able to automatically record the diffusion of small molecules across the porous alumina membranes. (300) Their revised setup enables the monitoring of changes upon various modifications onto the substrate material. Nonetheless, the adaptation onto the nanopore membranes requires the validation of the nanopores in order to decide the optimum pore density as well as the respective pore diameter. The experimental setup is presented in CHAPTER II (Figure 45) and differs from the classical mass transport setup due to the fact, that the permeate cell is already connected to the UV/vis-device by a flux-cell cuvette located inside the measuring chamber of the spectrophotometer. The automated diffusion record and analysis is achieved through the use of a peristaltic pump to generate an intact circulation between the permeate cell and the cuvette. In this way, the diffusion across the transmembrane area is directly measured. In addition by the appropriate setting for a time scan of two contiguous UV/vis-spectra a time-resolved the detection of the analyte transport is obtained.

To this end, the monitoring of LBL-network formation onto multipore membranes was examined using the automated mass transport to monitor the permeation of either the positively charged methylviologen (MV) or the negatively charged 1,5-naphthalene disulfonate (NDS) across the nanoporous membrane. Contrary to the single and oligopore membranes used for the *IV*-characteristics, cylindrical nanopores of 200 nm diameter were prepared within the multipore membranes having a pore density of  $10^7$  pores/cm<sup>2</sup>. The feasibility of mass transport

for the respective pore density and diameter of blank pore membranes was evidenced through validation experiments performed by Dr. Mathias Diefenbach (RG Biesalski). In this study, various pore densities ( $10^6$ ,  $10^7$ ,  $10^8$  pores/cm<sup>2</sup>) in combination with different pore diameters (35, 90 and 200 nm) were examined and showed the successful record analyte permeation, when unmodified multipore membranes were used having pore densities of  $10^7$  pores/cm<sup>2</sup> and a pore diameter of 200 nm. A detailed description of all validation experiments as well as the respective calibration data can be found in the appendix (see section 5.1 and 5.2).

To evaluate the transformation of unmodified membranes into nanopores covered by cross-linked porous networks, each modification step was monitored by the automated record of analyte permeation across the transmembrane area. For this purpose, the membrane was fixed between the feed cell and the measurement cell and the diffusion of MV and NDS was carried out separately prior to and after the deposition of four bilayers of polyelectrolytes [PAH|PVP]<sub>4</sub>[PAA]<sub>4</sub> as well as after the transformation step, generating porous LBL-networks. The respective UV/vis-absorbance can be found in the appendix section in Figure 147, whereas the diffusion rates in dependence on the respective modifications states is shown in the following Figure.

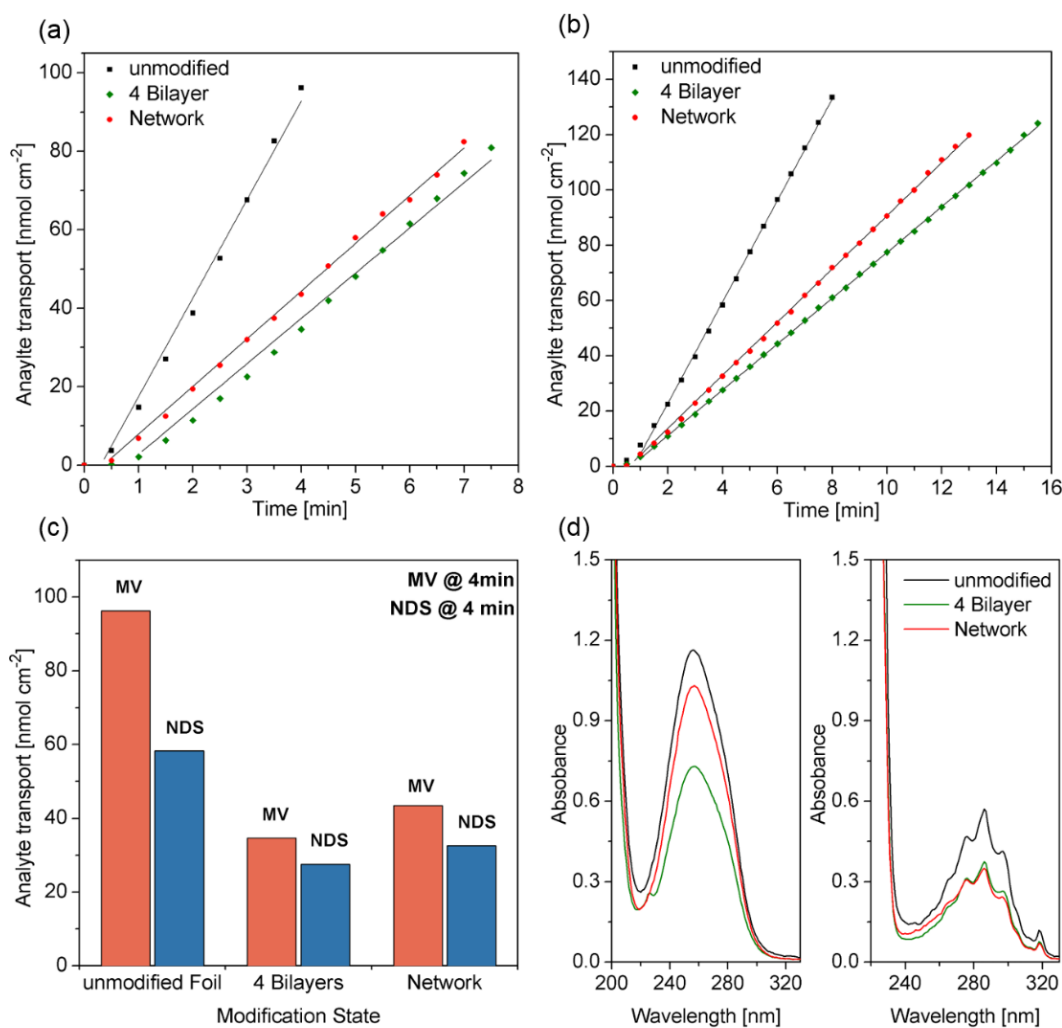


Figure 97: Transport of (a) MV and (b) NDS with respect to the modification state using a 50:50-ratio of [PAH|PVP]. (the corresponding UV/vis-data given in Appendix); (c) comparison of transported amounts and corresponding UV/absorbance spectra of MV (left) and NDS (right) for a fixed diffusion time of 4 min in dependence on the

---

modification state. The results contain the average of three measurements. Note that the error bars are negligible because their value does not protrude beyond the size of the data point.

The analyte transport of MV and NDS across the unmodified membrane is given in Figure 97a and Figure 97b, respectively. According to Figure 97c, the transported amount of NDS ( $\sim 60$  nmol/cm<sup>2</sup>) resulted in an almost two times lower permeation than the amount of transported MV (100 nm/cm<sup>2</sup>), after 4 minutes of diffusion time. Moreover, the influence of LBL-modification progress applied on multipores is evidenced by the experimental data. Here, due to the shrinkage of the effective pore diameter, upon the LBL-assembly of up to four bilayers, the permeation is reduced by up to  $\sim 50\%$  for the NDS-transport and  $\sim 60\%$  of MV-transport compared with the unmodified state. The following cross-linkage and PVP-washout causes an expected increase in permeation to nearly 15% (NDS) and 25% (MV)), respectively. Overall, the total reduction of analyte transport amounts to roughly  $\sim 60\%$  for NDS-transport compared to the unmodified state, whereas a total decrease of about  $\sim 50\%$  was noticed in case of the MV-permeability. In fact, the experimental data underline the significant ability to influence the analyte transport of multipore membranes.

Up to now, the amount of PVP within the cationic blend mixture was fixed using 50:50 ratio of PVP/PAA. Furthermore, to investigate the feasibility to control the transmembrane permeability, the amount of the *H*-bridge building compound PVP is varied. Theoretically, the deposition of cationic blend layers have an increased amount of PVP and should lead to gain of porosity within the cross-linked LBL-assembly. Therefore, a higher permittivity should be achieved. On the contrary, proceeding the LBL-assembly without PVP should not influence the analyte transport significantly. This expectation was examined by performing the LBL-assembly with two additional ratios of the [PAA|PVP]-compound, namely 100:0-blend and 25:75-blend. The automated mass transport experiments were performed by using an unmodified membrane consisting of the same pore density and diameter. The analyte permeation was monitored by the record of UV/vis-absorbance spectra in the same way as already processed in the experiments with the 50:50-blend and can be found in the appendix section (see Figure 148 and Figure 149).

For the case of 100:0-blend ratio, the permeation is changed with respect to the modification state shown in Figure 98. At first, the results showed the reduction of effective analyte transport upon the deposition of four bilayers [PAH|PVP]<sub>4</sub>[PAA]<sub>4</sub>. Here, a decrease of 31% for NDS-transport and 34% is detected compared to the unmodified state. Upon treatment with EDC-solution and exposure to basic solution does not provide any significant change of analyte permeation (see Figure 98a and Figure 98b) were observed. Due to the absence of PVP, the formed LBL-structure is only build-up by electrostatic interactions between PAA- and PAH-compounds. The crosslinking step enables the formation of densely packed multiplayer films. The ongoing exposure to basic solution does not affect the membrane transport because no PVP-compound could be washed-out, and therefore, the porous transition of the interlinked multilayers is not feasible. In particular, no changes in permeation are obtained by LBL-modification without PVP is suggested as a sort of contradictory evidence for the production of porous networks generated upon the presented procedure in presence of PVP.

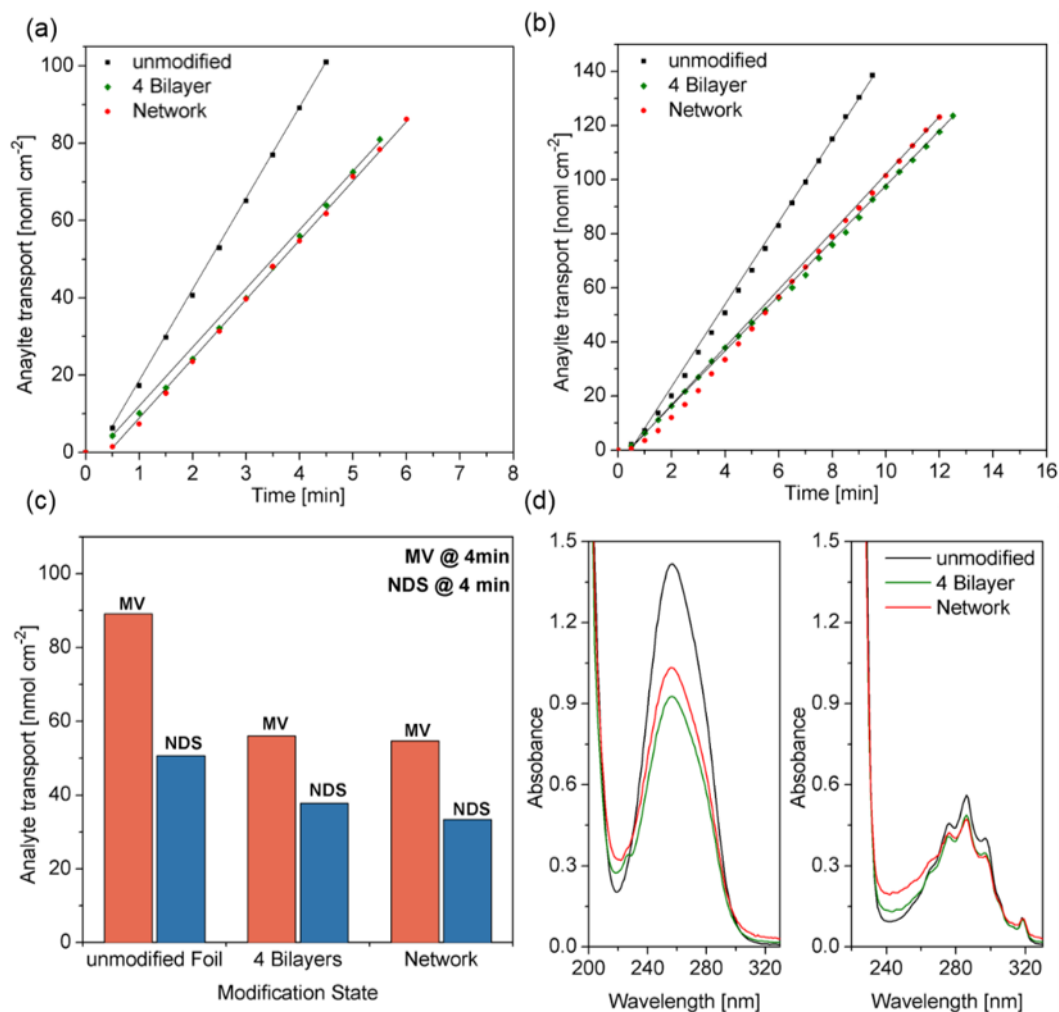


Figure 98: Transport of (a) MV and (b) NDS with respect to the modification state using a 100:0-ratio of [PAH|PVP]. (corresponding UV/vis-data given in Appendix); (c) comparison of transported amounts and corresponding UV/vis-absorbance spectra of MV (left) and NDS (right) for a fixed diffusion time of 4 min in accordance to the modification state. The results contain the average of three measurements. Note that error bars are negligible because their value does not protrude beyond the size of the data point.

Now, the LBL-assembly using the 25:75-blend is presented in the following Figure 100. In contrast to the results using the 50:50-blend, the higher ratio of PVP should affect the permittivity influence more significant change of permittivity than the use of the 50:50-blend.

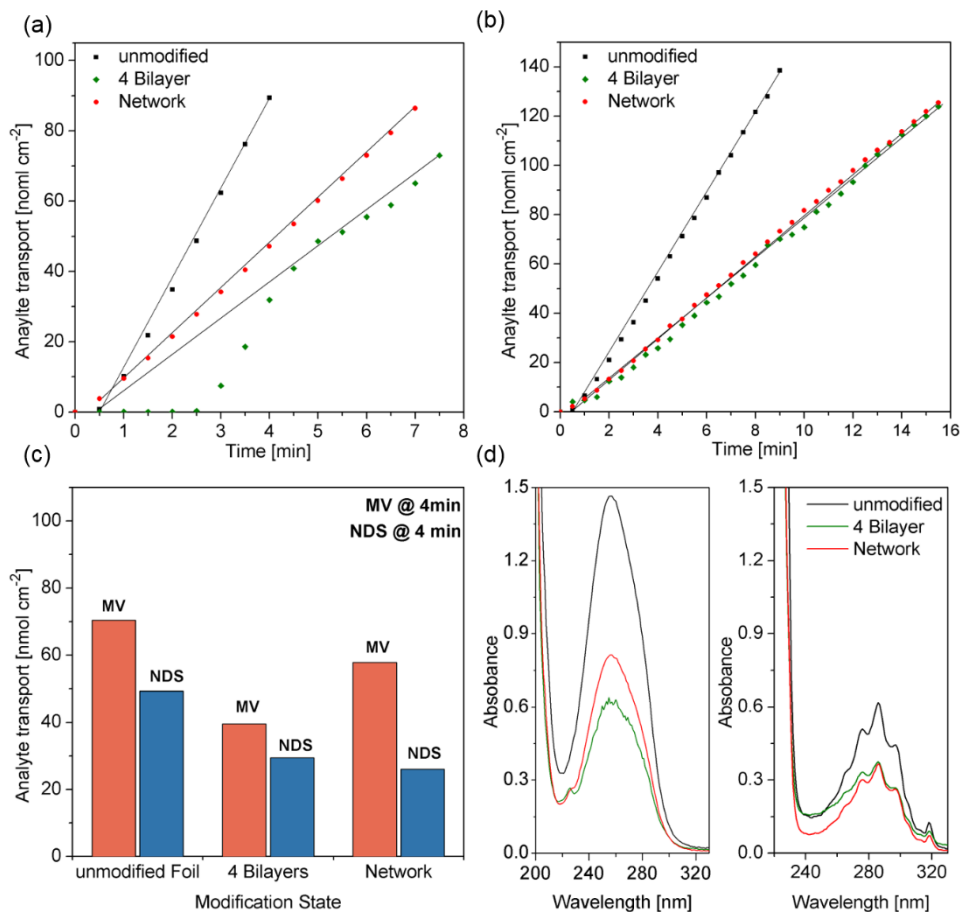


Figure 99: Transport of (a) MV and (b) NDS with respect to the modification state using a 25:75-ratio of [PAH|PVP]. (corresponding UV/vis-data given in Appendix section 5.3); (c) comparison of transported amounts and underlying UV/vis-absorbance spectra of MV (left) and NDS (right) for a fixed diffusion time of 4 min in accordance to the modification state. The results contain the average of three measurements. Note that error bars are negligible because their value does not protrude beyond the size of the data point.

According to the expectation, the analyte permeation is reduced to  $\sim 50\%$  for NDS and  $\sim 60\%$  for MV after the formation of four bilayers on the pore surface with respect to the blank state. The further cross-link and PVP-remove provided an enhanced analyte transport of about  $\sim 8\%$  for the use of NDS, whereas the MV-transport is increased by up to  $\sim 35\%$  (see Figure 99).

In fact, the use of 25:75-blend emphasized the influence of *H*-bonded PVP compound within the LBL-structures, resulting in a total change of analyte flux of  $\sim 8\%$ , if NDS was used, and  $35\%$ , if MV was used compared to the analyte transport across the unmodified membrane. In turn, regarding the LBL-procedure using the 50:50-blend ratio, a total change in analyte permeation of  $16\%$  and  $26\%$  was obtained for the use of NDS and MV, respectively. The higher degree of porosity within the LBL-structures is generated by using higher amount of PVP-compound, as evidenced by a higher influence for the MV-diffusion compared to the 50:50-blend results. In addition, the diffusion of NDS is less affected. Here, the total value of negatively charged PAA-moieties inside the nanopore surrounding is higher because more PVP-chains are removed during the wash-out step compared to the 50:50-blend. Hence, the presence of more negatively charged groups within the layers leads to a gain of electrostatic repulsion between NDS and PAA-moieties that are both negatively charged.

---

### 3.3. Conclusion

In summary, the LBL-modification of the nanopore surface was successfully demonstrated by using either two-component system or the novel three component system.

The experimental results of the classical LBL-method using the two-component system of PAH and PAA clearly showed the successful formation of multi-layered PAH/PAA-film as evidenced by *IV*-characteristics. In presence of silver ions, the former rectification behaviour become linear, indicating a loss of net surface charge induced by the incorporation of silver ions within the PAH-moieties. The further increase of  $\text{Ag}^+$ -amount led to reduction in ionic flux. The phenomena could be originate from the fact, that with an increasing concentration of silver-ions within the PAH-layers, the respective polymeric PAH-chain become more positively charged, leading to highly expanded PAH-chains. Therefore, the multilayer-film thickness is increased leading to a current-reduction. Within the nanoconfinement, the spatial change is limited and therefore, further changes in the ionic transport were not recorded upon increasing the  $\text{Ag}^+$ -amount.

To regulate the transmembrane ionic transport, adjustable porous transition is preferred. Therefore, a new strategy of LBL-deposition and transition was successfully applied onto the nanopores by using a three-component system. In this way, track-etched nanopores were functionalized by the alternating deposition using the cationic blend [PAH|PVP] and the anionic polyelectrolyte [PAA]. In the next step, the multi-layered film was interconnected through amide linkages to enhance the stability between the polymeric layers. Then, the PVP-component was removed on exposure to basic solution, inducing the rupture of the *H*-bridges which in turn lead to porous transition in the former dense multilayer film. The experimental data underline the successive reduction of ionic transport and analyte diffusion across the transmembrane region upon the LBL-deposition, respectively. Moreover, the significant increase of ionic/analyte diffusion occur upon the cross-linking and wash-out step. Furthermore, the importance of PVP during the LBL-deposition was investigated which resulted in an adjustable analyte transport in dependence of the used PAA:PVP-ratio. The concept of the sacrificial use of PVP offered more control about the porous transition of LBL-assembled nanopores and could be adapted for the potential application of triggered drug-release in clinical studies.

In fact, the successful applicability of LBL-networks onto a broad range of nanopore membranes emphasizes the LBL-technique to serve as an excellent candidate to modulate and control the nanoconfinement of porous membranes. Moreover, the analytical results of multipores using automated diffusion record of NDS and MV showed beneficial use of automated mass transport experiments for the efficient evaluation of multipore membranes in terms of molecular transport modulation triggered by surface modification.

---

## 4. Ultrasensitive and Selective Copper (II) Detection: Introducing a Bioinspired and Robust Sensor\*

---

### 4.1. Introduction

Copper ions play a crucial role within biological systems where they act as trace element to regulate enzymatic and other metabolic processes. (301) The oxidation state of copper could be either monovalent (cuprous ion) or divalent. Hence, the divalent cupric ion ( $\text{Cu}^{2+}$ ) is the most common state, since it is mainly found in aqueous surroundings. (302) A broad range of diseases such as WILSON's disease or ALZHEIMER's disease are related to a misbalanced copper level within the human body. (303) Donnelly *et al.* described the crucial influence of copper for the enzyme copper-zinc superoxide dismutase (SOD1), affecting the brain metabolism. They reported about an estimated level of copper ion between 100  $\mu\text{M}$  and 150  $\mu\text{M}$ . (304) Brown and Kozlowski emphasized the effect of imbalances of the  $\text{Cu}^{2+}$ -amount within the human body that play an significant role in the outbreak of ALZHEIMER's disease. (305) The plaque formation inside the human brain is known as the most prominent symptom of ALZHEIMER's disease, herein referred as AD. The formation of these malignant aggregations was found to be triggered by copper ions. Here, the degradation of  $\beta$ -amyloid peptide is triggered by the copper interaction inducing a cleavage from the so-called amyloid precursor protein throughout the generation of  $\text{Cu}^+$ -ions from  $\text{Cu}^{2+}$ -ions, enabling neuron degeneration processes. (305–307)

Recently, Squitti *et al.* highlighted the importance of unbound free-circulating copper level within the body as it could act as a potential diagnostic marker in terms of ALZHEIMER's disease. Moreover, it was found that the copper amount in ALZHEIMER-patients is more than 2.4-times higher compared to the level of healthy probands. Therefore, monitoring the copper level is of special clinical interest to underline the diagnosis of ALZHEIMER's disease. (308) For instance, Hirayama and co-workers demonstrated a sensing device based on a specific fluorescent technique. In the presence of  $\text{Cu}^{2+}$ -species within living cells, they were able to visualize copper through a fluorescent signal that is switched on upon successful interaction with cupric ions. (309)

However, the reported living-cell sensing setup requires complex and high-costly instrumentation. Further research regarding the copper detections are based on the biomimetic strategy to use proteins having already an natural copper binding domain. Here, especially proteins of the albumin class are well-known for their ability to interact with copper due to mandatory sequence of amino acids located within the protein, the so-called *amino-terminated copper(II)- and nickel(II)-binding* motif, herein referred as ATCUN-motif. The structure that enables the copper binding consists of a short peptide having a glycine-glycine-histidine-sequence (Gly-Gly-His) with a *N*-methylated amide form in order to mimic the protein structure more precisely. (310) Lately, the covalent incorporation of a tripeptide containing the ATCUN-motif was successfully attached to a cold-coated polymeric nanopore membrane by Papp *et al.* for copper ion detection in the mM- and  $\mu\text{M}$ -range. (311) The copper detection promoted by surface-bounded sensors was further investigated by Zheng and his co-workers as they combined copper-active fluorescent elements in hydrogels. The presence of cupric ions reduces the fluorescent signal upon exposure of more than 18 hours. (312) The aforementioned studies showed promising methods for the sensitive copper detection. However, expensive instruments, time-consuming procedures and complex analytics are needed. Clinical application requires

---

\* Müller, L. K., Duznovic, I., Tietze, D., Weber, W., Ali, M., Stein, V., Ensinger, W., Tietze, Al. (2020) "Ultrasensitive and selective copper (II) detection: introducing a bioinspired and robust sensor", *Chemistry A European Journal*, 26(39): 8511-8517.

simple and quick-responsive copper-detection strategies accompanied by high sensitive and selective sensing performances within body fluids.

The design of a copper-sensor is presented in this study. For this purpose, ATCUN-moieties were synthesised by Dr. Lena Müller (RG Tietze) and kindly provided for the attachment onto track-etched nanopore membranes. Additionally, the copper-binding motif is labelled with a fluorescent dye providing the ability to monitor the copper-binding performance of the porous membrane not just by *IV*-measurements but also using fluorescence analysing methods such as confocal laser scanning microscopy (CLSM).

## 4.2. Results and Discussion

In this study, the ATCUN-peptide is covalently attached to the nanopore surface. According to Figure 100, the interaction of cupric ions with the ATCUN-motif leads to a fluorescence quenching induced by the formation of the ATCUN-Cu<sup>2+</sup>-complex.

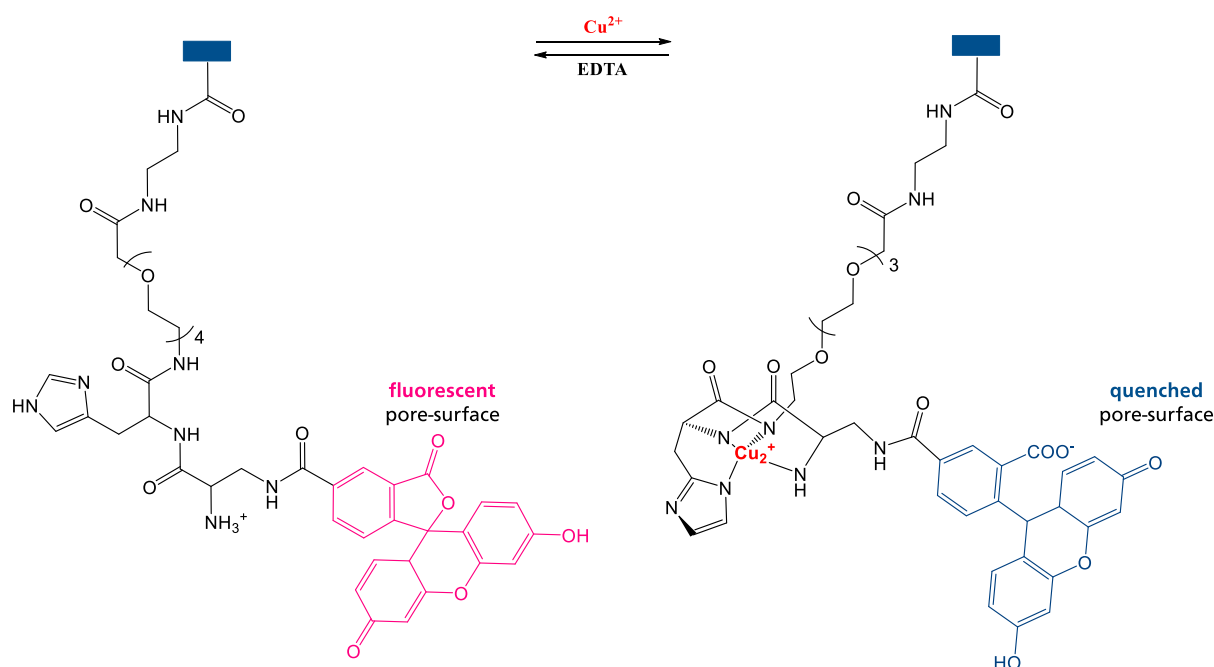


Figure 100: Sensing concept for copper detection using track-etched nanopore membranes modified with fluorophore-marked tripeptide-moieties bearing ATCUN-motif sequence for the specific copper binding. Note that in presence of cupric ions, the formation of the ATCUN-copper-complex occurred, leading to the fluorescent quenching. The addition of EDTA induces the regeneration of the pore surface.

The sensing performance in terms of sensitivity, selectivity as well as reversibility was tested through *IV*-measurements on oligopore membranes (10<sup>4</sup> pores/cm<sup>2</sup>). Moreover, the copper-activity of ATCUN-modified multipore membranes (10<sup>7</sup> pores/cm<sup>2</sup>) was evidenced by using CLSM-imaging methods. As mentioned, the ATCUN-motif peptide that was bounded onto the nanopore, was synthesized by Dr. Lena Karin Müller having the molecular structure of 5(6)-FAM-Dap-βAla-His-PEG<sub>4</sub>. Here, the ACTUN-motif sequence is verified compared to the naturel sequence of Gly-Gly-His. The PEG-linker consist of four ethylene glycol-units terminated with COOH-groups and was used to enable the separation on the solid support during the solid-state synthesis, whereas the term “5(6)-Fam” is denoted as the abbreviation for the carboxyfluorescein moiety.

Prior to the investigations of nanopore-bounded ATCUN, the copper sensing performance was examined briefly in solution by Dr. Lena Müller.

First, Figure 101 represents the metal titration experiments analysed by UV/vis-spectroscopy for the use of copper (II)-ions and nickel (II)-ions in dependence to the pH-value. The BOLTZMANN-fitted curves reveal a clear pH-dependence for the successful formation of the ATCUN-complex. According to Figure 77, the copper-interaction takes place in a neutral pH-range (PH 6-8), whereas the nickel(II)-complexation occurs in a more basic surrounding at pH 7-10. In order to archive a sensitive copper-detection, it is crucial to examine experimental conditions, where only one metal ion is selectively bounded to the ATCUN-motif. At pH 6.5, the experiments proclaim clearly the possibility to detect cupric ions in the presence of Ni<sup>2+</sup>-ions.

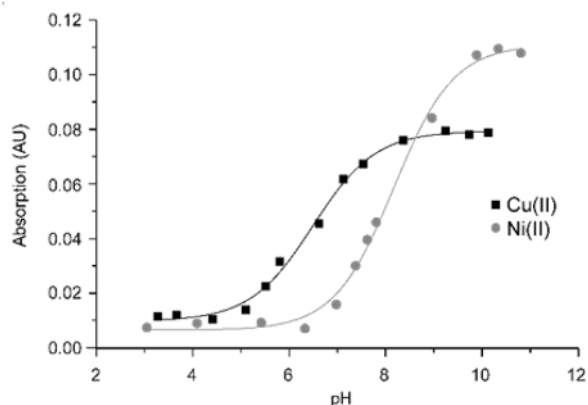


Figure 101: BOLTZMANN-fit (black and grey line) determines the sigmoidal trend of titration curve. The respective absorption values are based on the UV/vis-spectra using 1 mM solution of Cu(II) (black) and Ni(II) (grey) at different the pH conditions. The experimental results were analysed by Dr. Lena Müller.

Moreover, the selectivity towards copper and nickel-ions was examined using fluorescence spectroscopy (see Figure 102). Here, the quenching of the fluorescent signal with respect to the metal ion concentration is monitoring the complex formation.

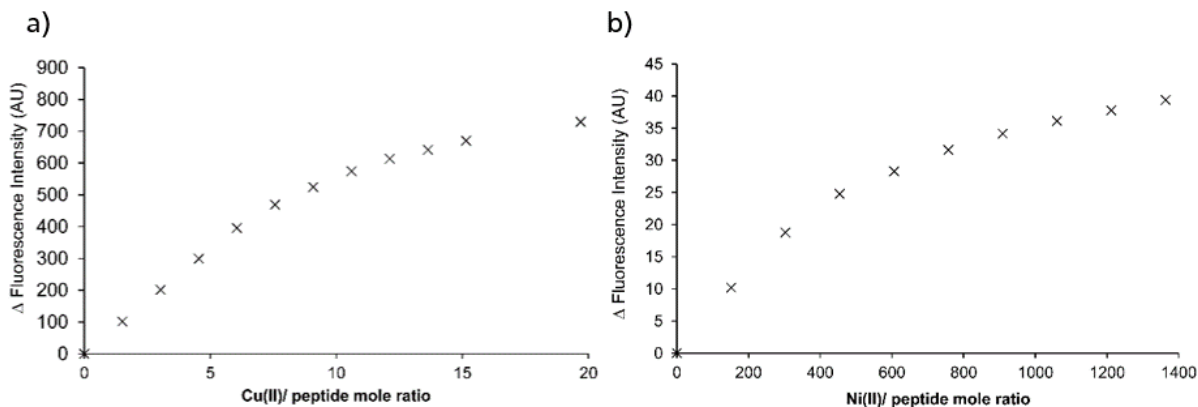


Figure 102: Fluorescence titration curve using the ATCUN-peptide (1  $\mu$ M in 100 mM MES-buffered solution, pH 6.5) at different concentrations of CuSO<sub>4</sub> (a) and NiSO<sub>4</sub> (b). For the case of copper ions, upon increasing the concentration of copper ions (from 0 to 25  $\mu$ M), the significant fluorescence reduction is observed as a function of the molar ratio of copper-(II)-ions to ATCUN-peptide. For the case of nickel ions, upon increasing the concentration of nickel ions (from 0 to 1.3 mM), only marginal fluorescence reduction is observed as a function of the molar ratio of nickel-(II)-ions to ATCUN-peptide. The fluorescence spectra were carried out and analysed by Dr. Lena Müller.

For both metal ions, the fluorescence spectra provide a reduction of fluorescence due to the formation of the ATCUN-complex with the respective metal ions. Nonetheless, the experiments show clearly the strong sensitivity towards copper-ions compared to nickel ions. It was found that the addition of one equivalent of copper causes a decrease of fluorescence of about 90%, while more than 600 equivalents of nickel(II)-ions provide only a  $\sim$ 40%-reduction of the fluorescence. In addition, only one equivalent of nickel, does not affect the fluorescent signal at all.

These preliminary tests show clearly the sensitive and selective ability of track-etched nanopores to detect efficiently copper-ion in solution.

#### 4.2.1. *IV*-Characterization of ATCUN-Cu<sup>2+</sup>-Interface

The characterization of ATCUN-peptide was investigated through ATCUN-modified conical pore membranes having a pore density of 10<sup>4</sup> pores/cm<sup>2</sup>. The nanopore fabrication was carried out using the protocol described in experimental part (CHAPTER II.1) consisting of a nanopore with 30 nm tip diameter and 510 nm base diameter calculated by *IV*-measurements and SEM-imaging (CHAPTER II.3), respectively. Track-etched nanopores within the polymeric substrate material contains carboxylic groups which act as starting points for the covalent attachment of the ATCUN-peptide. For this purpose, the nanopore membrane is fixed in the conductivity cell and in first step the membrane is functionalized with ethylene diamine (EDA) to generate amine groups on the nanopore surface according to the protocol in CHAPTER II, section 2.1.1. In the second step, the incorporation of ATCUN-peptide is carried out using HATU-based coupling chemistry (CHAPTER II.1.2). The ATCUN-modification is promoted by the C-terminus of the PEG-linker bearing a COOH-unit. The successful pore modification as well as the evaluation of the copper sensing ability was monitored using *IV*-measurements. Note that the entire modification process was carried out in the measurement cell without the membranes been taken out of the cell. Moreover, all *IV*-measurements were carried out using 100 mM KCl-electrolyte (in 10 mM MES-buffer, pH 6.5) and the half-cell with the smallest volume (0.68 mL) and opening (4 mm diameter). Therefore, the *IV*-curves are recorded in a one-digit nA-range. The changes in the *IV*-curves on various modification steps on conical pore-membrane is shown in the following figure.

Upon modification with ethylene diamine (EDA), the former positive rectification behaviour was lost compared to blank state (see Figure 103). The linear *IV*-response indicates the loss of surface charge. The amino moieties are almost uncharged at pH 6.5 and, therefore, the ionic transport is mainly carried by the equal movement of cation and anions. Upon ATCUN-modification, significant decrease in the resulted *IV*-curve shows hindered cationic movement. However, the rectification is inverted indicating the presence of positively charged ATCUN-moieties on the surface.

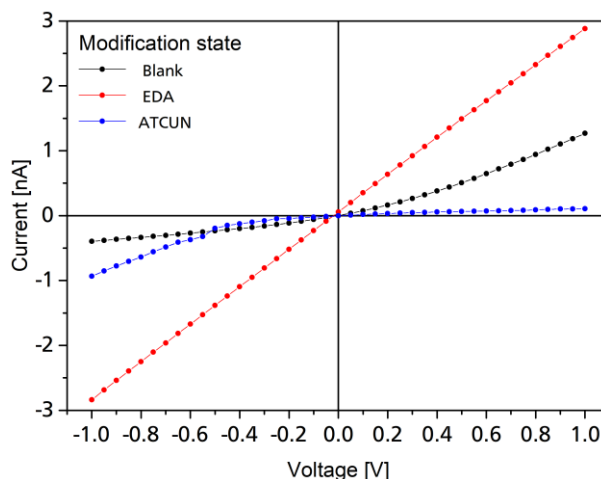


Figure 103: *IV*-curves demonstrating the ATCUN-modification onto a blank conical pore membrane having 10<sup>4</sup> pores/cm<sup>2</sup>.

The ATCUN-terminated pore state is denoted as ‘off-state’. Figure 104 provides insights about the copper sensitivity. Here, the ATCUN-modified membrane was exposed to various copper concentrations ranging from 1 fM to 1 mM.

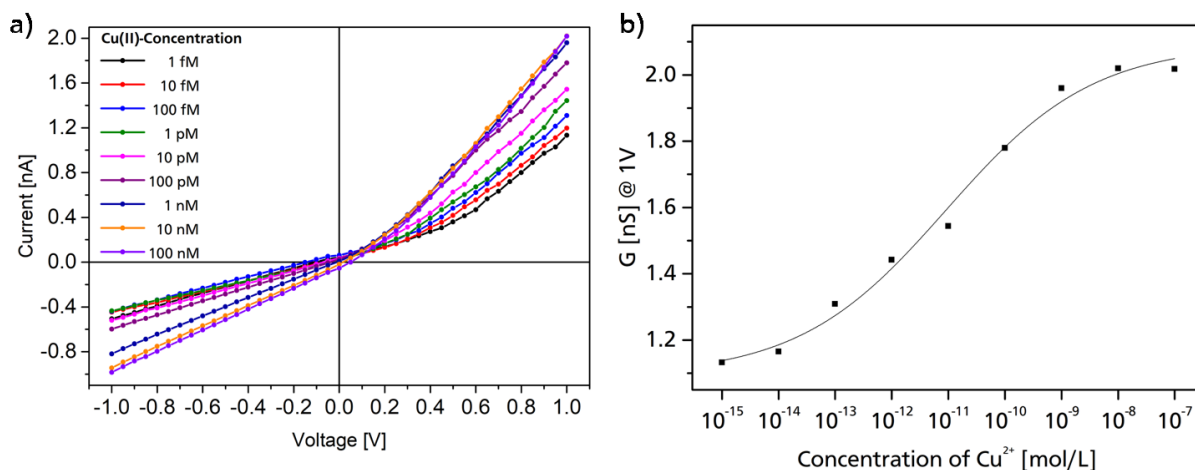


Figure 104: *I/V*-curve of the ATCUN-modified nanopore membrane upon exposure to various  $\text{Cu}^{2+}$ -concentrations in the electrolyte solution (100 mM KCl, MES buffer, pH 6.5) (a). The corresponding conductance values are obtained from the respective *I/V*-data at 1 V that result in a sigmoidal response with respect to the tested  $\text{Cu}^{2+}$ -concentrations (b).

Upon copper ion treatment, the ATCUN-modified pore becomes more and more loaded by copper ions and therefore the former negatively charged pore becomes neutralized as evidenced by a growing linearization of the *I/V*-curve with increasing copper amount. For  $\text{Cu}^{2+}$ -concentrations higher than 100 nM no significant current gain (less than 5%) is noticed, suggesting a nanopore surface fully loaded with ATCUN-Cu-complexes. Overall, the increase of copper amount turns a cation-selective pore region towards a membrane able to permeate cations and anions, as demonstrated by the higher ionic transport at negative applied voltages. Here, the ATCUN- $\text{Cu}^{2+}$ -complex formation is defined as the ‘on-state’. The rectification behaviour and the absolute ionic transport is triggered by the host-guest interactions of cupric ions with the nanopore-bounded ATCUN-peptide and can be served as an evidence for successfully generated ATCUN-Cu-complexes within the pore region. In addition, the copper sensing performance can detect ultra-sensitive amounts of cupric ions in the low picomolar range. The area of detection is estimated between 1 pM to 10 nM  $\text{Cu}^{2+}$ -concentrations.

Subsequently, the selective ionic transport was tested by exposing the ATCUN-modified pore to electrolyte solutions containing 100 pM of different metal ions ( $\text{Ni}^{2+}$ ,  $\text{Zn}^{2+}$ ,  $\text{Cu}^{2+}$ ). The respective *I/V*-curves are presented in Figure 105a. The experimental data shows clearly that only if copper(II)-ions are present in the electrolyte solution, the ionic transport reveals a significant change. The use of nickel(II)- and zinc(II)-solution does almost not affect the ionic current. In fact, the current gain is marginally enlarged ( $\sim 10\%$ ) compared to the *I/V*-curve of the ATCUN-modified pore. On the contrary, the use of 100 pM  $\text{Cu}^{2+}$ -solution causes a two times higher ionic transport compared to the current recorded in absence of any metal ion.

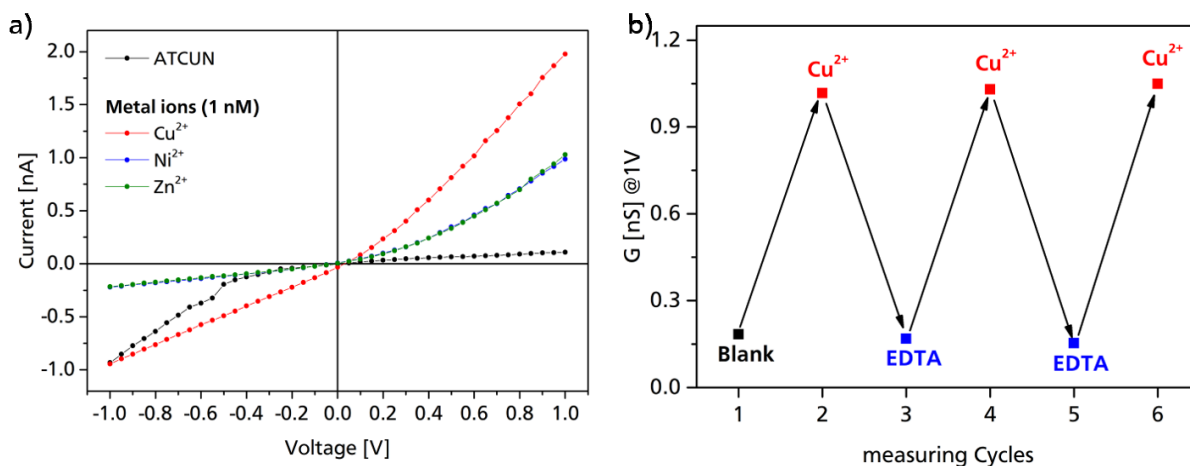


Figure 105: *IV*-curve of the ATCUN-modified pore membrane upon exposure to various divalent metal ions (100pM) in the electrolyte solution (100 mM KCl, MES buffer, pH 6.5) (a) and conductance values at 1 V shows reversible complexation/decomplexation of Cu<sup>2+</sup>-ions (b). Here, the exposure to 1 nM Cu<sup>2+</sup>-amount in the electrolyte solution (100 mM KCl, MES buffer, pH 6.5) leads to the current increase (red dots) due to the enhance surface charge of the pore upon generation of ATCUN-Cu-moieties across the entire pore surface. The on-going treatment with 1 mM EDTA-solution causes the removal of Cu<sup>2+</sup>-ions from the pore surface, inducing a recovery of the pore surface (blue dots).

Finally, the reversibility of the ATCUN-copper interactions was also tested suggesting a reversible binding of Cu<sup>2+</sup>-ions. According to Figure 105b, the pores were regenerated from copper ions upon exposure to 1 mM EDTA-solution. For this purpose, the ATCUN-modified nanopore was exposed to a 1 nM copper solution and the *IV*-curve was recorded. Then, EDTA-solution was filled inside the measurement cell and leaved for about 20 minutes in order to induce ATCUN-Cu<sup>2+</sup>-decomplexation. After numerous washing steps, the electrolyte was filled inside the cells and the *IV*-curve was recorded. Afterwards, the ATCUN-complexation was carried out again with the same copper-concentration. The resulting conductance shows only marginal changes in ionic current compared to the first round of copper treatment. These cycles of copper-complexation and EDTA-promoted copper-decomplexation was repeated three times. The experimental data shows clearly a reversible copper-binding to the nanopore.

Further, to ensure the qualitative copper binding as well as the reversibility tests of nanopore-bounded ATCUN-peptides the optical investigations were carried out using AFM- and CLSM-techniques and are briefly described in the section 4.2.2.

#### 4.2.2. Optical Investigations of the ATCUN-Cu<sup>2+</sup>-Interface

In the following, visualization of the ACTUN-modified nanopore was obtained by atomic force microscopy (*AFM*) to evaluate the structural changes of the pore surface upon successful ATCUN-modification. The *AFM*-experiments were performed in the tapping mode using a silicon-cantilever (free amplitude of 1.5 V). The resulting topography and phase images of the pore surface before and after the ATCUN-functionalization has been recorded by Dr. Christian Dietz (RG Stark) and are presented in the following Figure.

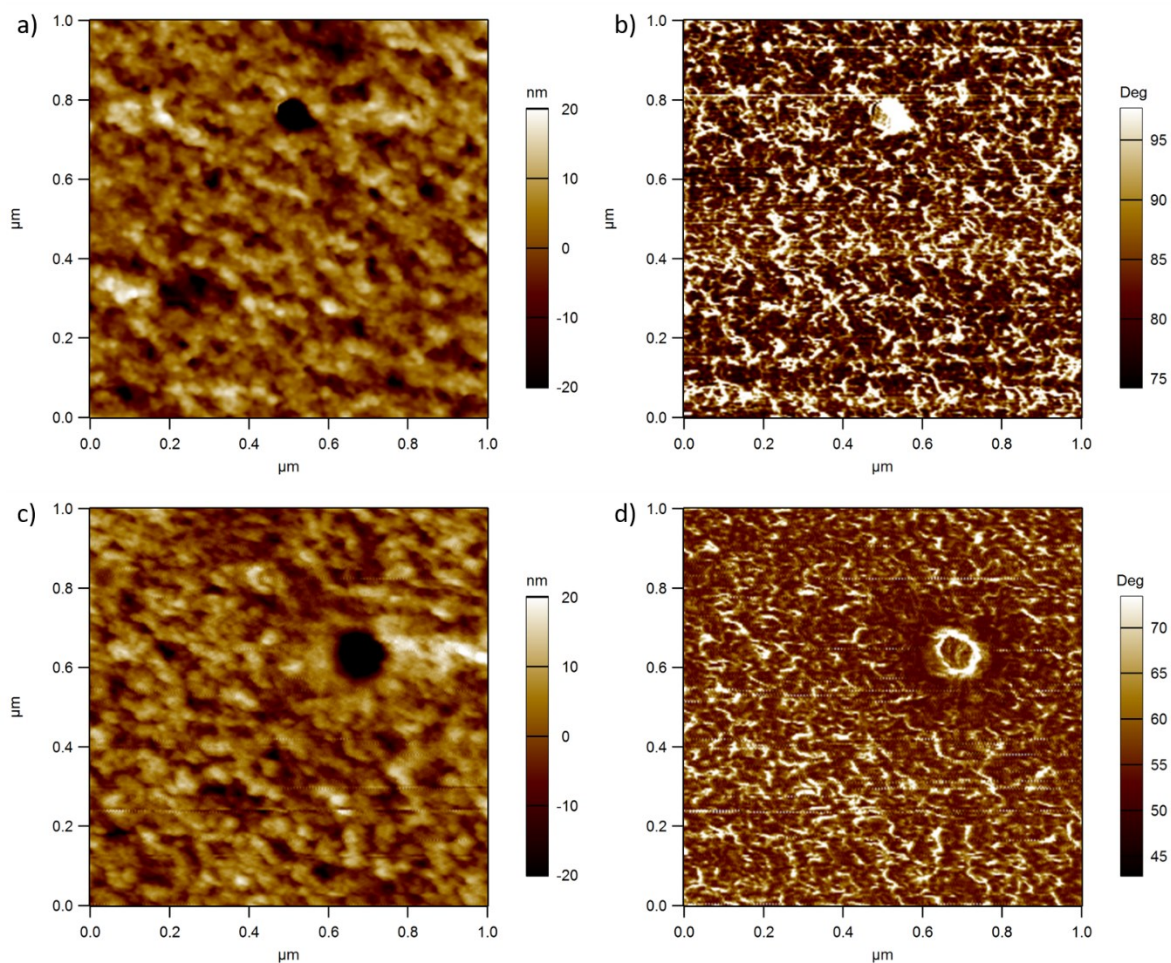


Figure 106: AFM-images of nanopore membrane surfaces having a pore density of  $10^7$  pores/cm<sup>2</sup>. AFM-images of the blank nanopore membranes are shown in (a) and (b), whereas the ATCUN-modified pores are shown in (c) and (d). Note that the figures (a) and (c) provide the topological images of the respective pore and (b) and (d) shows phase differences. In this case brighter areas show higher interactions between cantilever and pore surfaces. The resulting halo in (d) indicates softer regions and, therefore, the presence of the peptide. The AFM-images were kindly recorded by Dr. Christian Dietz (RG Stark).

The comparison between the unmodified nanopore surfaces (Figure 106a) and the ATCUN-terminated pore surfaces (Figure 106c) reveals the topological changes of the pore composition upon surface modification. Moreover, the observed phase shifts in Figure 106b for ATCUN-modified pore reveals the presence of softer regions at the entrance of the pore opening due to the presence of a bright halo located on the top of the pore opening. In contrast, the phase image of the blank nanopore (Figure 106b) shows a bright dot on the pore position. This indicates unspecific interactions of the cantilever and the pore region. With the help of AFM-imaging, a defined interaction of the cantilever for softer surface regions was shown assuming the presence of the ATCUN-modified nanopore surface.

Next, the existence of ATCUN-functionalized nanopores can be detected by confocal scanning microscopy, because the ACTUN-peptide is fluorescently labelled. Consequently, a blank nanopore is not fluorescently active, whereas ATCUN-immobilization induces fluorescent pore images surfaces under the CLSM. For this purpose, the use of a multipore membrane is crucial to enable the detection of pores under the CLSM. The Figure 107 displays the respective CLSM-images after the ATCUN-modification of a multipore membrane.

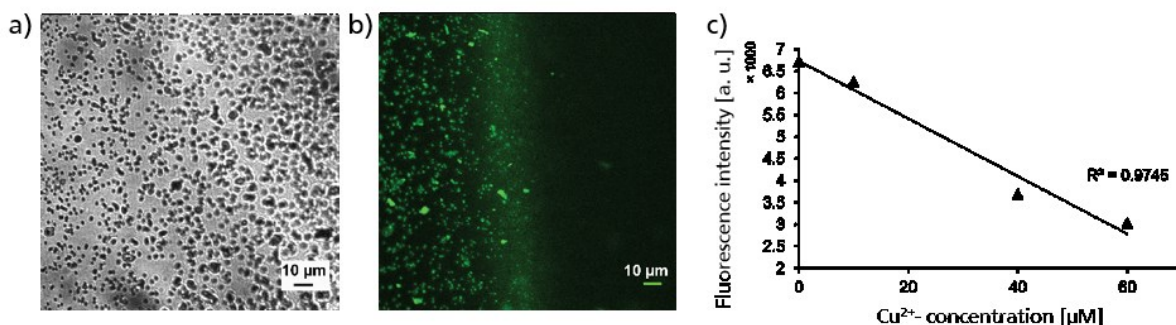


Figure 107: CLSM- images of fluorescently labelled ATCUN-moieties after the covalent attachment onto the multipore membrane ( $10^7$  pores/cm<sup>2</sup>). Here, the reflected light as well as the fluorescent emission images are shown in (a) and (b), respectively. Note that, the dark area indicated the absence of fluorescent groups, i.e., the absence of ATCUN because the etching area is not identical to the modification area. Moreover, the quantification of fluorescence reduction upon exposure to various concentrations of Cu<sup>2+</sup> ion ranging from 0 μM to 60 μM is presented and linearly fitted in (c).

Here, top-view of the ATCUN-modified pore membrane is displayed as a white-light image (Figure 107a) as well as a fluorescence image (Figure 107b). The fluorescence excitation is visualized as green colour upon the laser-irradiation at 488 nm. In comparison with Figure 107a, the etched pore surface does not provide fluorescent light onto the entire pore area. In fact, Figure 107b shows a quite sharp line of fluorescent active and inactive parts. This phenomenon is easily explained regarding the experimental setup used for the surface modification and the etching of the membranes: Prior to the surface modification, the pores are generated within the polymeric substrate. This is carried out in the etching cell (Figure 28, CHAPTER II.1). For the modification step, the membrane is clamped between the two half-cells of the measurement cell (Figure 29, CHAPTER II.2). Now, the half-cells used for the etching have a cell opening of 16 mm diameter, whereas the half-cells used for the modification steps a made of an opening of 8 mm diameter. Therefore, Figure 107a shows an area fully covered by pores, whereas Figure 107b indicates the line between etched area and modified area. This image was specially selected, because it shows not only the successful attachment of ATCUN-moieties onto the pore membrane but also gives evidence that the blank nanopore membrane does not provide initial fluorescence activity. In turn, all fluorescent irradiation originated from ATCUN-peptides immobilized on the pore membrane.

Furthermore, the accumulated fluorescent intensity was examined in dependence on the Cu<sup>2+</sup>-amount (see Figure 107c). By pipetting various Cu<sup>2+</sup>-concentrations onto the membrane, the successive fluorescent quenching was observed. In total, the addition of 60 μM Cu<sup>2+</sup>-solution reduces the fluorescence activity to more than 50%.

The re-usability was also evaluated from the visualization of the complexation/ decomplexation process in presence or absence of copper ions. Therefore, the changes of fluorescence upon copper-ion interaction was observed by focusing on the fluorescence of one pore (see Figure 108, “start”). Then, 100 μM of Cu<sup>2+</sup>-solution (MES-buffer at pH 6.5) was pipetted on to the pore surface. Immediately (after 0 min), the fluorescence was quenched to more than 50 %. After 5 minutes, a further decrease of fluorescence was noticed. Treating the membrane with 1 mM EDTA-solution provides a fluorescent signal. After the washing steps, i. e., one-time with MES-buffer and three times with pure water, the similar fluorescent read-out was obtained as the starting value indicating a reversible binding-mechanism between copper(II) ions and pore-bound ATCUN-moieties. Note that, the quenching is only caused by interaction with copper

ions, a reference point was chosen, i. e. a pore that had no contact with either copper(II) ions or EDTA. Using this strategy, the loss of fluorescence read-out owed by bleaching-effects was detectable and used as offset for the effective quenching analysis.

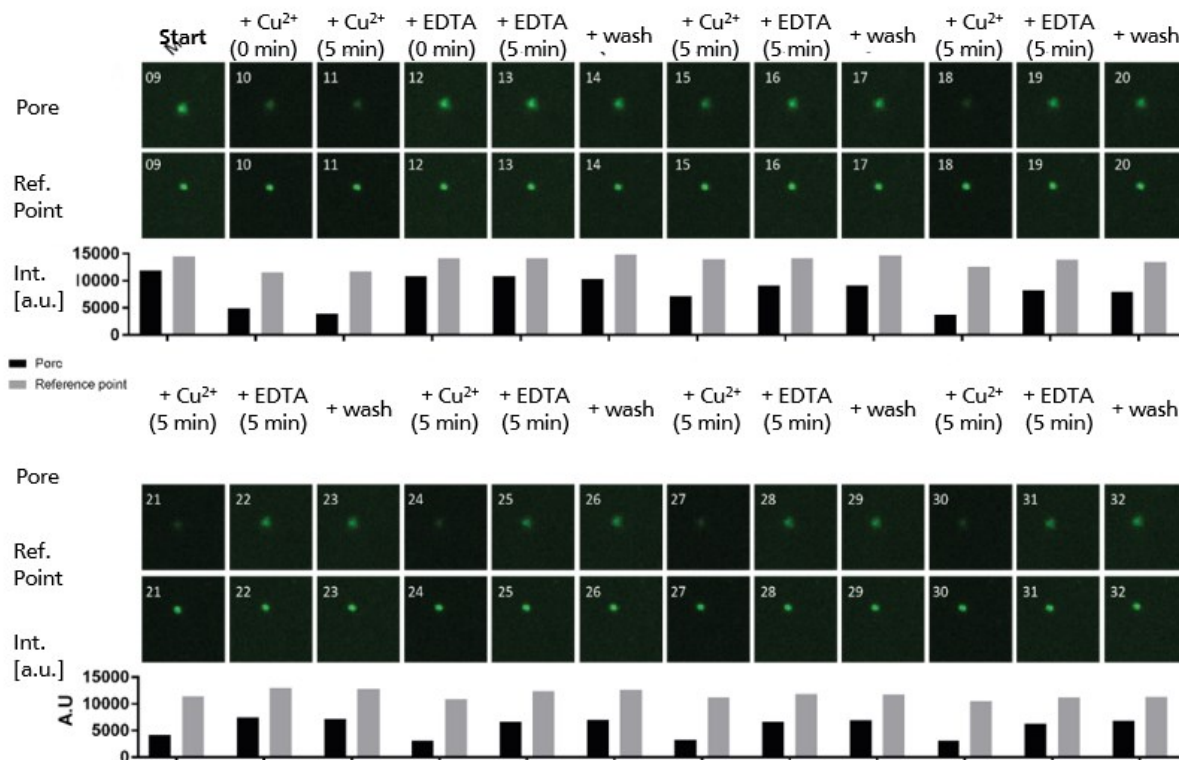


Figure 108: CLSM-images to evaluate the "on-off"-state of ATCUN-modified nanopore membranes, showing the reversibility of the ACTUN-Cu<sup>2+</sup>-interaction in presence of 100  $\mu$ M Cu<sup>2+</sup>-solution and 1 mM EDTA-solution. Note that the term '+wash' means in total one washing-step with MES-buffer (pH6.5) followed by three washing steps with pure water.

Reproducibility was tested by performing the copper ion/EDTA-treatment in an iterative series over seven cycles in total. The experimental data clearly verify the successful binding/unbinding of copper ions to the surface, exhibiting the reversible switching-behaviour of the pore. Moreover, the efficient regeneration of the nanopore surface throughout EDTA-treatment was achieved without visualizing any significant attenuations in terms of sensing performance and detection properties.

### 4.3. Conclusion

So far, the design of an ultra-sensitive and selective copper ion sensor was presented and analysed based on the self-made ATCUN-peptide that was successfully immobilized onto track-etched nanopore membranes. The sensing performance was tested in terms of sensitivity, selectivity and reproducibility. The results clearly showed the highest efficiency of ATCUN-copper binding at pH 6.5 as well as the outstanding affinity towards copper ions.

Herein, the ACTUN-peptide was covalently attached onto the nanopore-substrate and analysed by *IV*-measurements. Upon exposure to various Cu<sup>2+</sup>-electrolytes, the *IV*-curves exhibited a sigmoidal dependence between an increase of ionic transport across the pore region and the concentration of copper ions in the surrounding electrolyte solution. Moreover, limit of detection was estimated in submicromolar ranges ( $\sim$ 10 nM), whereas saturation occurred for

---

concentrations higher than 1 mM. These experiments clearly showed the detection ability of ATCUN-modified-nanopore membrane towards copper ions. Further, the selectivity measurements were performed by exposing the ACTUN-modified membrane towards various divalent metal cations, i. e.,  $\text{Ni}^{2+}$ ,  $\text{Zn}^{2+}$  and  $\text{Cu}^{2+}$ . The corresponding *IV*-measurement showed only significant current increase for the case of copper(II)-solution, whereas the nickel(II)- and zinc(II)-solution could not affect the ionic transport across the modified membrane. Moreover, the reversibility of the ATCIN- $\text{Cu}^{2+}$ -interaction was also tested upon the cyclic treatment with EDTA-solution (regenerated pores) and  $\text{Cu}^{2+}$ -solution (loaded pores). Overall, the *IV*-data demonstrated the outstanding copper sensing feature of ACTUN-modified nanopores.

Because the ATCUN-peptide is fluorescently labelled, the surface modification as well as the reversibility testes were also verified by using CLSM-imaging methods. On the one hand, the CLSM-images evidenced the covalent ATCUN-attachment onto the nanopore by inducing fluorescence into a former CLSM-inactive pore surface. On the other hand, the experimental results showed clearly the quenching effect upon the copper-interaction. Moreover, the recovery of ACTUN-moieties on the pore surface, i. e., regeneration of fluorescent activity, was visualized. This switching-behaviour accompanied by the ultrasensitive and selective  $\text{Cu}^{2+}$ -sensing could be beneficially adapted in clinical studies, where the detection of traces of target ions can be potentially employed for the early-diagnostics of diseases.

Consequently, further investigations especially regarding measurements in body fluids like human blood or serum are required in order to design efficient diagnostic devices and sustainable detection tools. Experimental studies using human serum were performed on ATCUN-modified nanopores and briefly analysed in the second section of CHAPTER VI.

---

## 5. Ultrasensitive, Electrical Biosensing of Protein Analytes by means of Nanobodies immobilised inside Track-Etched Nanopores

---

### 5.1. Introduction

Over the last two decades, the biomolecular sensing approach based on polymeric nanopores has been well-established in the scientific community. Analyte recognition is created upon the receptor attachments onto the nanopore membrane. In presence of the respective analyte, the bioconjugation occurs leading to changes, such as (partial) blockages, of the ionic current across the membrane. Meanwhile, numerous nanopore based analyte recognitions were published, whose detection mechanism rely on the specific bioconjugation reaction. Aspiring application of nanopores for the use as diagnostic devices, the interaction between analyte and receptor should be of maximum accuracy, sensitivity and selectivity.

Looking at the biological surrounding, antibodies, herein referred as AB, are the protagonists of our immune system as they interact with respective antigen-sequences of viruses, bacteria, toxins, etc. In presence of antigens, the formation of an immune complex occurs, which in turn provides further biomolecular reactions of the immune reactions. Therefore, antibodies are used as powerful tools for the detection of diseases. Siwy *et al.* used track-etched nanopores functionalized with antibodies and reported about the bio sensing of  $\gamma$ -poly(glutamic acid) for the potential monitoring of anthrax. (106)

AB-structures (Figure 109) are typically composed of heterotetrameric polypeptide-chains, namely a dimer of one heavy peptide-chain (H) and one lighter peptide chain (L). The antigen-binding domain is located at the end of each H-L-dimer. Common antibody sizes amount to  $\sim 15$  nm with a molecular mass of 150 kDa. (313) Hence, the successful incorporation of antibodies into nanopores requires a directed AB-attachment with an intact antigen-binding area. This approach is seen to be difficult as the AB-dimensions and nanopore dimensions are in the same range.

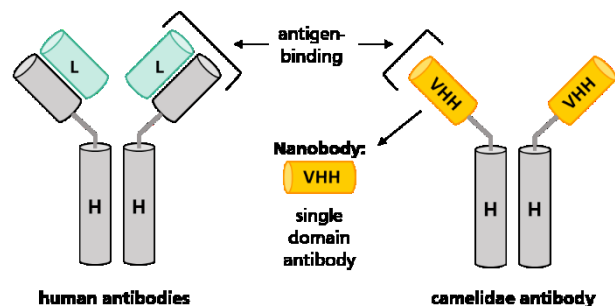


Figure 109: Antibodies (AB) composition and respective structural coherency of nanobodies (NB).

Recently, structural curiosities were found in camelid antibodies. Unlike conventional human antibodies, they consist of only one dimer of heavy chains combined by a variable antigen-binding domain, i. e., the *variable heavy homodimer* (VHH)-domain. (314) The smallest intact functional antigen-binding fragment is defined as nanobody, herein referred as NB, represented by a single domain antibody. The NB-size amounts to only a few nanometres with a molar mass of a several kilo-Daltons. Along with their truncated structure, there are several further advantages to incorporate nanobodies onto the surface of nanopores (315), such as:

- *affinity*: evidenced by kinetic binding rate constants
- *specificity*: cognate antigen-binding is in the same range as antibodies
- *stability*: storage over months
- *crystal structures*: well-established NB-epitope-interactions
- *production costs*: mg-yields from single cultures

---

These beneficial features highlighted the use of NB as research tools in biochemical and nanotechnological fields. In this study, the successful attachment of nanobodies is examined along with sensitivity and selectivity test towards cognate antigens.

## 5.2. Results and Discussion

Herein, the immobilisation of nanobodies onto the track-etched nanopores is investigated. In order to enable the maximum control of surface attachment, a new route of peptide-based click-chemistry is introduced, namely the Tag/Catcher system. Zakeri and co-workers pioneered this new class of peptide-click chemistry. Their work relies on the spontaneous formation of an intact domain by mixing a peptide fragment, herein pronounced as the ‘Tag’, with its respective protein counterpart, herein referred as the ‘Catcher’. (183)

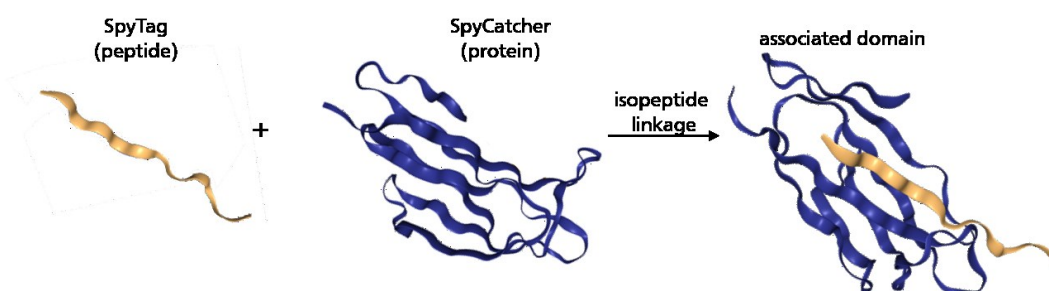


Figure 110: Formation of an intact domain using splitted SpyTag and SpyCatcher-sequences. Peptide and protein structures are adapted from protein data bank (Code: 4MLI).

The generated domain represents the permanent linkage based on the rapid and irreversible formation of an isopeptide bond between the lysine-group of the Tag and the glutamine acid group of the Catcher. (183) The detailed isopeptide mechanism is already provided in the experimental part (section 2.2.2, CHAPTER II). Among numerous Tag/Catcher-combinations, the well-established SpyTag/SpyCatcher-combination was chosen to induce a highly precise linkage between the pore substrate and the Nanobody-protein. Here, the Spy-peptide-tag consists of 13 amino acids, whereas 137 amino acids are forming the protein-catcher. (316)

The selective interaction shows no side-reactions and, therefore, it is employed onto the nanopores-substrate to couple NB with a high specificity. For this purpose, the tag-component is first attached to the pore-surface. Then, the catcher-component carrying the nanobody-moiety is exposed to the tag-terminated pore surface. The proof-of-concept is performed using nanobodies exhibiting affinity towards specific proteins.

In the beginning, the successful functionalization of two different nanobodies is monitored by *IV*-measurements. One nanobody shows strong affinity towards green fluorescent protein (GFP), herein referred as NB<sub>GFP</sub>, while the other is attracted by the red fluorescent protein mCherry, herein pronounced as NB<sub>mCherry</sub>. Therefore, the sensitivity is evaluated on both GFP and mCherry, separately.

The selectivity of the nanobodies is screened systematically by examining the *IV*-characteristics of NB<sub>GFP</sub>- and NB<sub>mCherry</sub>-functionalized nanopores towards both proteins. Because of the fluorescent activity of mCherry and GFP, the pore-bounded NB interaction with GFP and mCherry is additionally evaluated using CLSM-imaging.

A negative control experiment was also performed in order to exclude non-specific interactions. The respective experimental results are presented in the third part of this study.

### 5.2.1. Pore-Modification and Sensing Performance of Nanobodies

To this end, conically shaped single pores were functionalized with NB in three steps. The pore dimensions were estimated to be around 26 nm to 45 nm (tip size) and 550 nm to 650 nm (bulk size) using SEM-imaging of respective multipore membranes. According to Figure 111, the as-prepared nanopore surface is functionalized with amino-terminated DBCO-units using EDC-PFP-coupling chemistry. In the next step, the peptide-tag is attached through the strain-promoted cycloaddition between the DBCO-triple bond and the azido-groups of the peptide-tag. Finally, the Tag-terminated pore is treated with SpyCatcher-moieties carrying the NB-sequence in order to achieve successful NB-attachment to the pore surface.

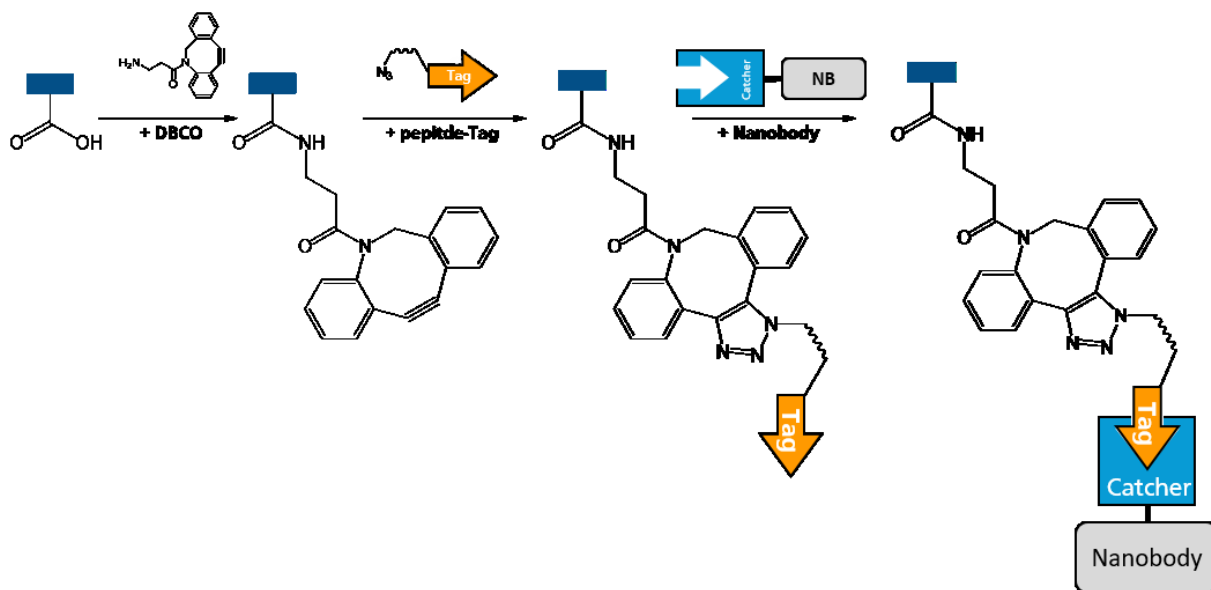


Figure 111: Modification pathway for the covalent attachment of NB-moieties onto the nanopore surface. First, the pore surface is modified with DBCO-groups using EDC/PFP-chemistry. Then, the peptide-tag is attached through a [3+2]-cycloaddition between azido-units of the peptide-tag and the DBCO-triple bond. Upon exposing the membrane to SpyCatcher-NB-moieties, the isopeptide bond formation within the Tag/Catcher-system occurs, connecting the NB with the pore surface.

The entire modification reactions were monitored by *IV*-measurements. For this purpose, the etched membranes are clamped between the two half-cells of the measurement cell and *IV*-curves are recorded prior to and after each modification step. In order to receive comparable experimental results, once the membrane is fixed between the measurement cells, the set-up remains unchanged until the entire modification and characterization process is performed.

Finally, the surface attached peptide-tag is treated with two different NB-structures having strong affinity either towards green fluorescent protein (GFP) or red fluorescent protein (mCherry). The amino sequence is provided in the appendix part. However, the peptide-tag is composed of the respective SpyTag-sequence and an  $\epsilon$ -azido group to enable successful cycloadditions with DBCO-moieties. The exact amino acid sequences are presented in the appendix part as well. The molar mass of the peptide-tag amounts to  $\sim 8.4$  kDa and carries net positive charges of +6. Further, all NB-molecules are composed of the same SpyCatcher-group. Both, the peptide-tags and the SpyCatcher-NB are custom-made molecules synthesized by

Alexander Gräwe, M. Sc. (RG Stein) and were kindly provides to be attached on the pore surface. *IV*-curves used to monitor the modification steps are displayed in Figure 112.

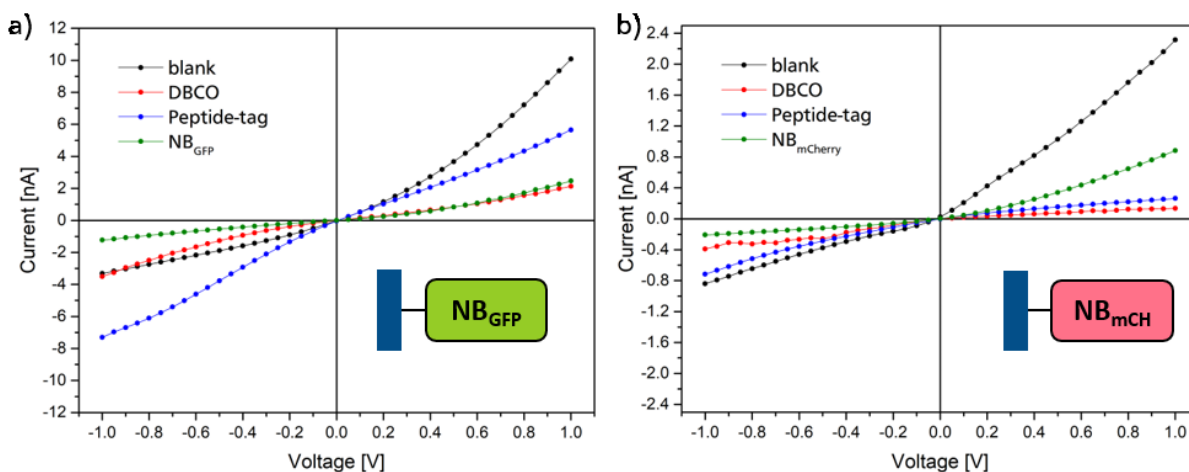


Figure 112: *IV*-curves of single pore membranes for different modification steps measured in 0.1 M KCl electrolyte (PBS, pH 7).

Figure 112a represents the modification of a conical single pore having a tip diameter of  $\sim 45$  nm and a base diameter of  $\sim 650$  nm (estimated by SEM-imaging), whereas a second pore was used in Figure 112b (tip diameter:  $\sim 26$  nm; base diameter:  $\sim 550$  nm). Both membranes were fabricated using the protocol already described in section 1.2 (CHAPTER II). In the first step, amino-terminated DBCO was attached to the pore surface using EDC/PFP-chemistry (section 2.1.1, CHAPTER II). Regarding the *IV*-curves, the DBCO-treatment resulted in a loss of ionic conductance of more than 90% due to almost uncharged DBCO-moieties located on the pore surface. Yet, a slight positive rectification is observed presumably due to the electron-rich triple bond of DBCO being attractive for cations that causes positive polarization inside the pore region, which allows anions to pass the pore more easily. In the next step, the membranes are separately exposed to a solution containing the peptide-tag. The respective *IV*-curves show a two-times higher increase of conductance accompanied by rectification ratios smaller than 1, namely  $f_{rec} = 0.66$  (Figure 112a) and  $f_{rec} = 0.36$  (Figure 112b). Here,  $f_{rec}$  is calculated as the absolute current value measured at +1V and -1V. Therefore, if  $f_{rec} > 1$ , the recorded current is mainly promoted by cationic movement. For  $f_{rec} < 1$ , the ionic flux is composed of anionic migration across the nanopore membrane. This indicates the presence of positive surface charges inside the pore region that cause a restricted cation movement across the membrane based on the underlying positive net charge (+6) of the peptide-tag. Finally, the NB-units are exposed to the single pore membranes. Upon the sufficient SpyTag/SpyCatcher-linkage, the NB<sub>GFP</sub>-molecule with a molar mass of 27.3 kDa and negative net charge (-9) is attached to the pore in Figure 112a evidenced by *IV*-curves show an increased current up to 50%. Moreover, the rectification behaviour is regenerated and reveals a positive rectification ( $f_{rec} = 1.96$ ) showed the successful attachment of NB-moieties onto the pore. Figure 112b reveals the same inversion of rectification ( $f_{rec} = 4.2$ ). Moreover, the total current value is increased from 0.2 nA to 0.9 nA after the NB-attachment caused by the higher charge state of NB<sub>mCherry</sub> (-11) compared to the charged state of NB<sub>GFP</sub> (-9). Thus, the charge-induced gain of conductance causes the observed current increase. However, comparison of Figure 112a and Figure 112b has to be treated with caution since both measurements were performed on different membranes, separately. Hence, the comparability relies only on qualitative observations.

Because the modification of nanopores with nanobodies was successful, the respective sensing performance was evaluated as the pore-bounded  $\text{NB}_{\text{GFP}}$ - and  $\text{NB}_{\text{mCherry}}$ -moieties show high affinity towards green-fluorescent proteins (GFP) and red fluorescent MCherry, respectively. NB-interactions towards their respective epitopes are already proven and briefly studied. (317, 318)

To this end, the  $\text{NB}_{\text{GFP}}$ -terminated nanopore membrane was treated with various GFP-concentrations. The respective  $IV$ -curves and conductance values are shown in the following Figure.

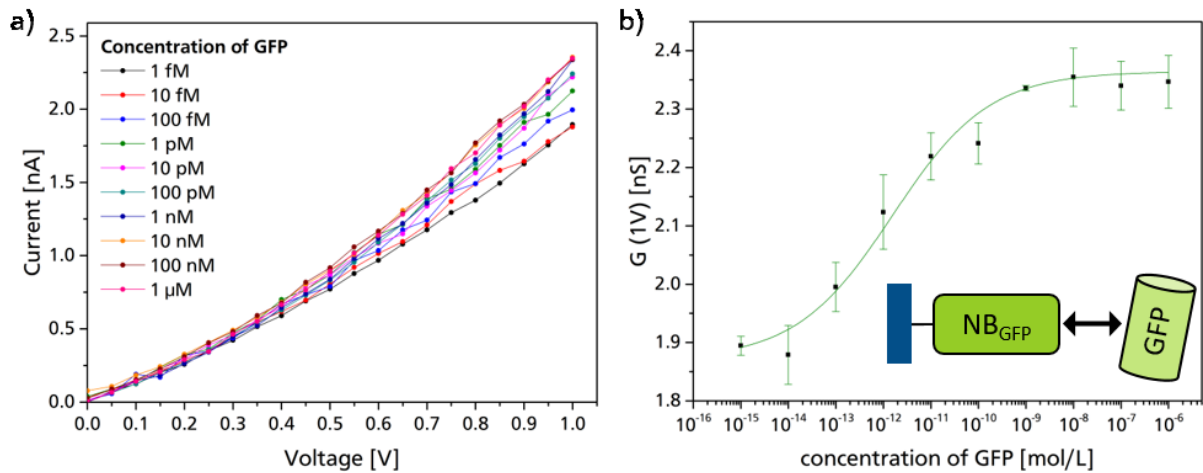


Figure 113:  $IV$ -curves for positive voltages (a) and respective conductance values at 1 V (b) of the single pore membrane functionalized with  $\text{NB}_{\text{GFP}}$ -moieties, upon exposure to different GFP-concentrations measured in 0.1 M KCl electrolyte (PBS buffer, pH 7).

Upon exposing the NB-modified single pore membrane to various GFP-concentrations, a significant gain of ionic transport is observed from 1.8 nA to 2.4 nA. The best fitting curve reveals a sigmoidal correlation between GFP-amount and transmembrane conductance as presented in Figure 113b. An approximately linear increase is obtained for GFP-concentrations between 1 fM and 1 nM being referred as the active GFP-detection area. For concentrations above 10 nM saturation is observed with only minor deviations of several pA.

However, the gain of transmembrane current with increasing GFP-amounts is due to the efficient GFP- $\text{NB}_{\text{GFP}}$ -binding, where the GFP is composed of a negative net charge (-6). Thus, the increase of GFP inside the pore region causes a higher negative surface density that reinforces the cationic movement. The GFP-protein structure is displayed in Figure 114. Although GFP is a large protein having a size  $\sim 4$  nm and a molar mass of 27 kDa, the GFP-adsorption on to the pore does not lead to pore blockage, but rather initialize the rise of the negative pore net charge, as evidenced by the positive rectification behaviour with increasing GFP-amount.

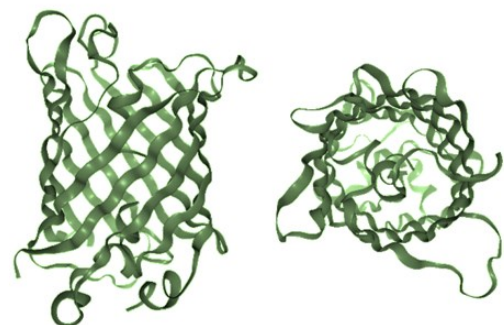


Figure 114: side-view and top-view of the crystal structure of GFP (PDB-code: 1EMA).

Further, the sensitivity towards mCherry-proteins was tested onto the NB<sub>mCherry</sub>-modified nanopore membranes and monitored by *IV*-measurements as displayed in the following Figure.

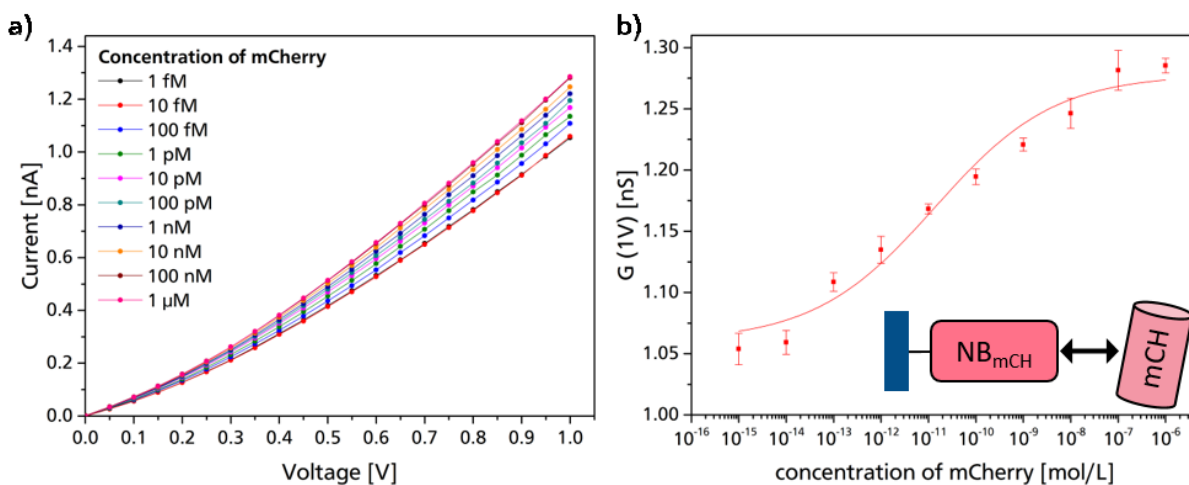


Figure 115: *IV*-curves for positive voltages (a) and respective conductance values at 1 V (b) of the single pore membrane functionalized with NB<sub>mCherry</sub>-moieties, upon exposure to different mCherry-concentrations measured in 0.1 M KCl electrolyte (PBS buffer, pH 7).

Figure 115 reveals the equivalent sigmoidal correlation between ionic transport and mCherry-concentrations. Similar to the GFP-series, the increase of transmembrane current is observed with higher protein concentration. GFP and mCherry are structurally related, having sizes of 28 kDa (mCherry) and a barrel-like scaffold (Figure 116). (319) Therefore, the linear current progress ranges from 1 fM to 10 nM, indicating an active sensing area over five orders of magnitude.

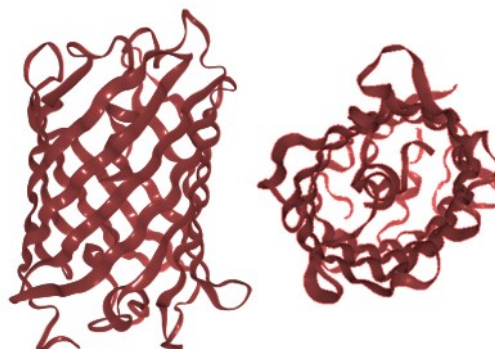


Figure 116: Side-view and top-view of the crystal structure of mCherry (PDB-code: 1EMA).

### 5.2.2. Nanobody-selectivity towards Cognate Protein-Epitopes

After sensitivity measurements, the NB-performance was also cross-tested towards the respective proteins. For this purpose, a new set of NB-modified nanopores was prepared (Figure 117) and exposed first to the solution containing the control protein (with no binding interaction towards NB) and then, after numerous washing steps, the same membrane was exposed to the correct protein-solution.

The modification pathways revealed equivalent *IV*-curves in terms on the rectification behaviour likewise every NB-modification route presented in this section (Figure 112). Therefore, modification-results were not further discussed. For Figure 117a, the used nanopore size amounts to 51 nm (tip diameter) and 680 nm (base diameter), whereas the calculated pore dimensions for the pore used in Figure 117b correspond to 42 nm for the tip size and 510 nm for the base opening.

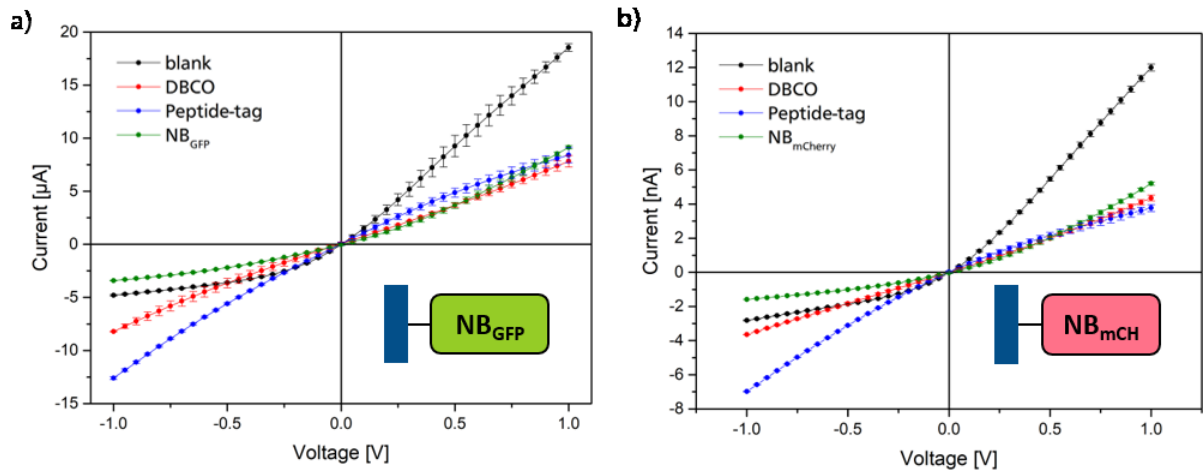


Figure 117: *IV*-curves of pore membranes for different modification steps measured in 0.1 M KCl electrolyte (PBS, pH 7).

Now, the  $NB_{GFP}$ -modified nanopore membranes treated with various concentrations of mCherry-protein. The respective *IV*-curves are presented in Figure 118a. Afterwards, the membrane was thoroughly washed with pure buffer solution in order to remove mCherry-residues. Then, the experimental series were repeated using GFP-protein. The recorded *IV*-curves are displayed in Figure 118b.

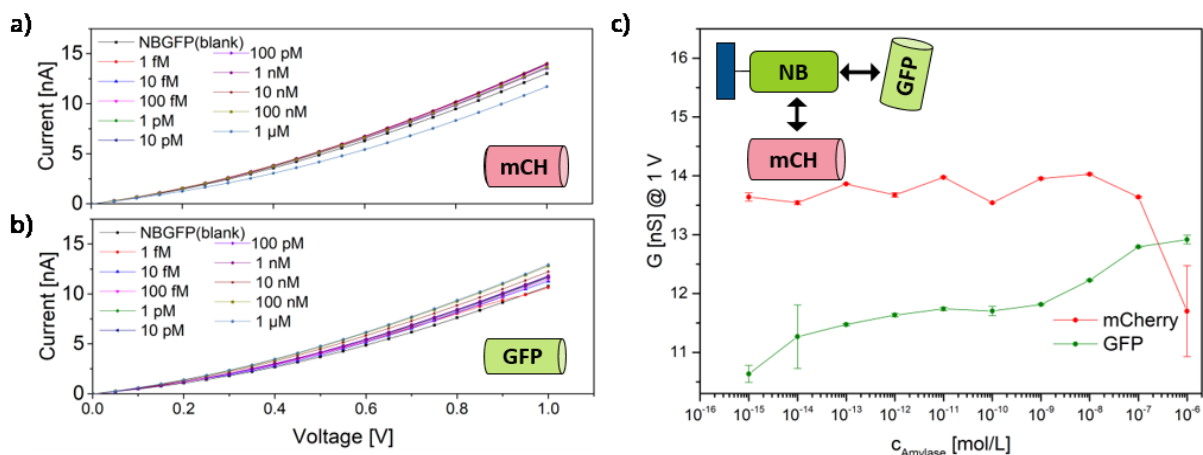


Figure 118: *IV*-curves for positive voltages of the single pore membrane functionalized with  $NB_{GFP}$ -moieties, upon exposure to different mCherry-concentrations (a) and different GFP-concentrations (b) measured in 0.1 M KCl electrolyte (PBS buffer, pH 7). Conductance values at 1 V with respect to the measured proteins (c).

In order to evaluate the correlation between the ionic current and the protein amount, the respective conductance values obtained at 1 V are plotted against the protein concentration in Figure 118c. Here, the  $NB_{GFP}$ -mCherry-interaction does not reveal any correlation. In fact, the entire conductance values fluctuate around a value of 13.7 nS. In contrast, an almost sigmoidal behaviour is obtained and expected by treating the  $NB_{GFP}$ -modified membrane with GFP. These results clearly show, the affinity of  $NB_{GFP}$  functionalized membrane with the respective analyte. However, the  $NB_{GFP}$ -GFP-correlation shows a linear area of only three orders of magnitude (1 nM to 100 nM), indicating the loss of sensitivity compared Figure 113. Although, the comparison of two individual membranes has to be treated with caution, the slight loss of sensitivity in Figure 118c could be caused by the fact, that the nanopore membrane is composed of a larger single pore (tip size of  $\sim 50$  nm, and a base diameter of  $\sim 680$  nm).

In the next step, the second single pore membrane modified with NB<sub>mCherry</sub>-moieties was exposed to various GFP-concentrations and characterized by *IV*-experiments (see Figure 119). After numerous washing steps with pure buffer, the same measurements are repeated upon exposing the membrane to different mCherry-concentrations (Figure 119a). For a better comparability, the conductance values at 1 V are correlated with the respective protein concentration (Figure 119c).

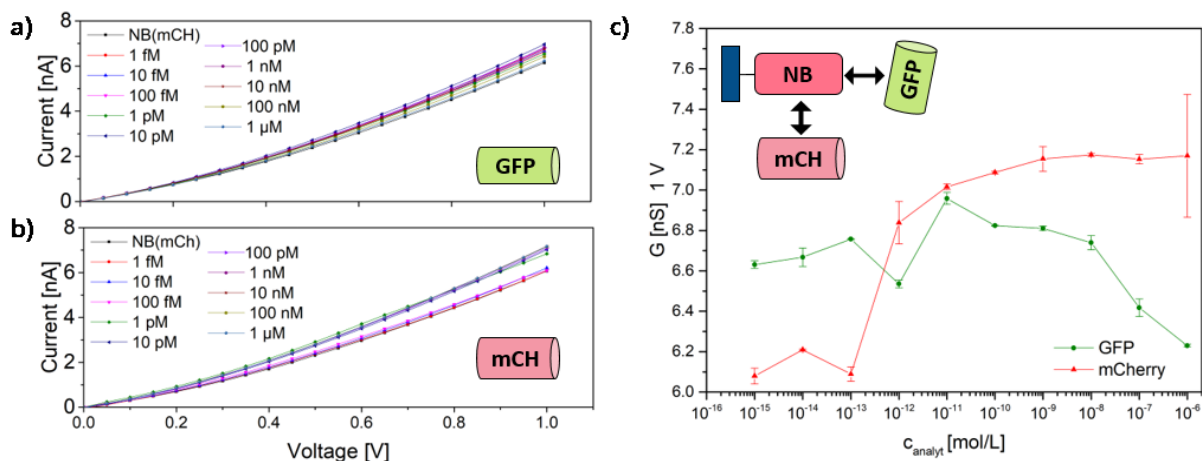


Figure 119: *IV*-curves for positive voltages of the single pore membrane functionalized with NB<sub>mCherry</sub>-moieties, upon exposure to different mCherry-concentrations (a) and different GFP-concentrations (b) measured in 0.1 M KCl electrolyte (PBS buffer, pH 7). Conductance values at 1 V with respect to the measured proteins (c).

The experimental results of NB<sub>mCherry</sub>-terminated membranes show similar selective behaviour as the previous NB<sub>GFP</sub>-series. First, by treating the NB with the unsuitable protein, i. e., GFP, no significant correlation is achieved. In fact, the ionic current shows a diffuse trend with increasing GFP-concentrations. On the contrary, an adequate sigmoidal-like correlation for the case of mCherry-solutions is observable. Moreover, the saturation is achieved for lower concentrations leading to the assumption that the larger pore size provides the reduction of sensitivity.

The selectivity results show a significant correlation between NB with their respective analytes. In contrast, the testing series using the wrong protein-analyte did not affect the ionic current substantially, even though mCherry and GFP are composed of similar protein structures. Although the results of the selectivity trial are not as precise as the previous sensitivity measurements (without intermitting cross-over measurement), the potential of NB-promoted analyte detection was undoubtedly demonstrated.

Because mCherry and GFP differ in their fluorescence wavelength, the entire selectivity tests were repeated onto multipore membranes having a pore density of 10<sup>7</sup> pores/cm<sup>2</sup> and analysed by CLSM-imaging with the help of Wadim Weber, M.Sc. (RG Stein). For this purpose, two conical multipore membranes were functionalized with NB<sub>GFP</sub>- and NB<sub>mCherry</sub>-moieties and entire selective cross-testing was repeated using GFP- and mCherry-solution, separately. Here, only the membranes became fluorescently active as soon as the NB interacts with his specific protein. In fact, neither the pore membrane nor the NB-moieties carry fluorophore-units. Therefore, a successful NB-protein interaction caused fluorescence inside the pore regions and is expected only for the following combinations: (i) NB<sub>GFP</sub>-terminated pores upon GFP-treatment and (ii) NB<sub>mCherry</sub>-terminated pores with mCherry-treatment.

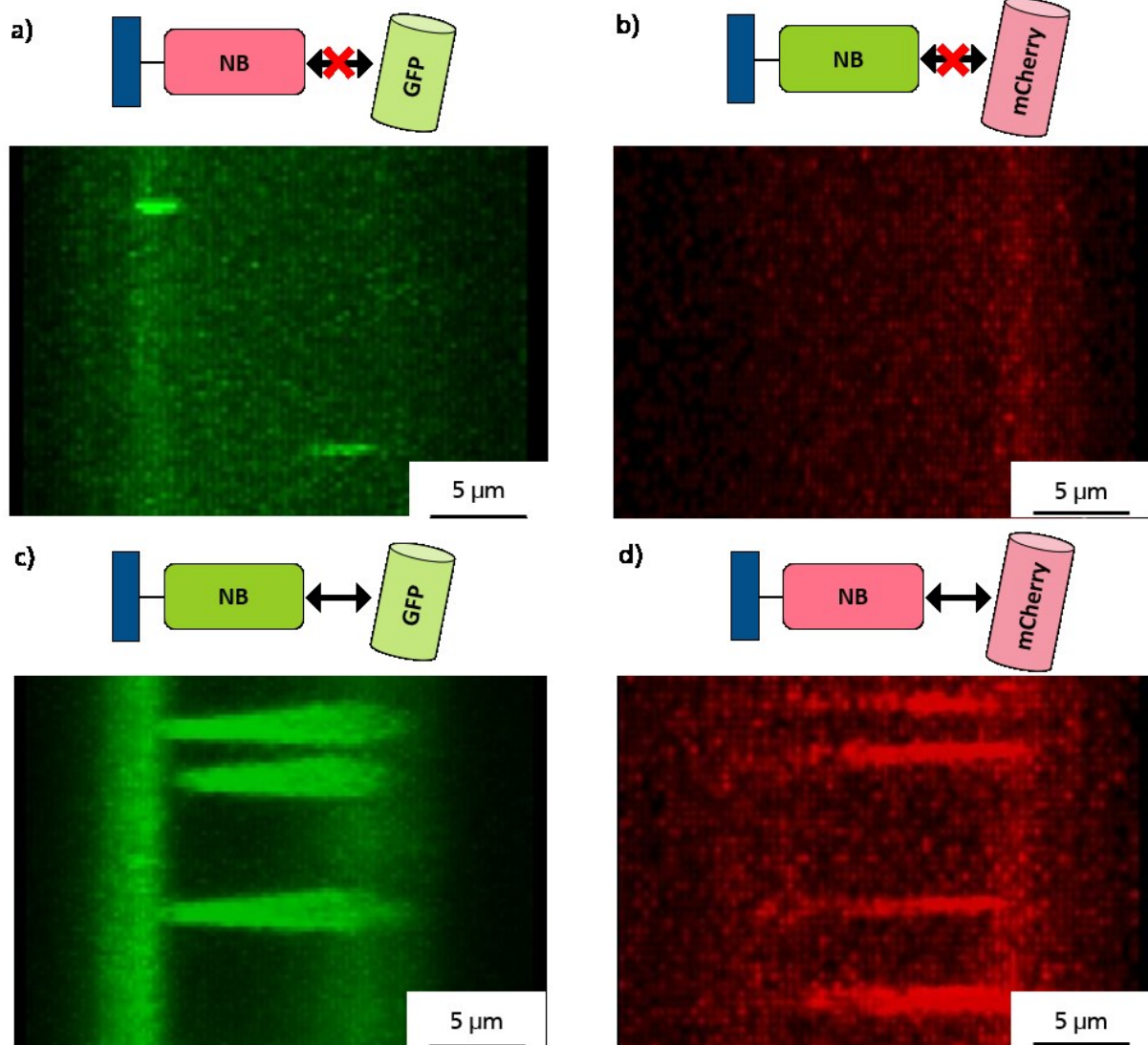


Figure 120: Cross-sectional CLSM-images of the NB-modified multipore membranes after exposing the membrane to the respective Protein-solutions. The following combinations are displayed: (a) NB<sub>GFP</sub>-membrane interacting with GFP, (b) NB<sub>mCherry</sub>-membrane interacting with mCherry, (c) NB<sub>mCherry</sub>-membrane interacting with GFP, (d) NB<sub>GFP</sub>-membrane interacting with mCherry.

Figure 120 demonstrates the cross-sectional CLSM-images of the NB-terminated membranes. To this end, the NB-terminated membranes were fixed on top of the CLSM-sample holder with one drop of agarose and were exposed to the protein solutions for 30 min. Then, the membrane was washed two times with pure buffer solutions in order to remove unbounded protein. CLSM-imaging was processed at excitation wavelength of 485 nm for the case of GFP-investigations and 587 nm for the case of mCherry-investigations.

Upon treating the NB-terminated membranes with the nonspecific protein-solution, namely NB<sub>mCherry</sub>-GFP (Figure 120a) and NB<sub>GFP</sub>-GFP (Figure 120b), the expected absence of fluorescence is noticed. On the contrary, significant fluorescence is obtained, when the membrane is treated with the correct NB-protein-interaction, namely NB<sub>GFP</sub>-GFP (Figure 120c) and NB<sub>mCherry</sub>-mCherry (Figure 120d). Due to higher quantum yields for GFP-proteins (0.65 ;(320)) compared to mCherry-proteins (0.22 (321)), GFP-emitting cross-sections resolve even the conical pore shape and show higher brightness, than mCherry-covered pore regions.

In total, the selectivity test of NB-modified single and multipores evidenced the successful linkage of NB with its respective analyte on both *IV*-measurements and CLSM-imaging. Even though GFP and mCherry are structurally related, NB having a strong affinity towards GFP did not further interact with mCherry-protein and *vice versa*.

Further, in order to examine the specificity of NB-interaction with their respective analyte, some negative control experiments were performed and are discussed below.

### 5.2.3. Negative Control Experiment

The negative control was performed using single pores modified with the peptide-tag to exclude non-specific interactions between analyte and nanopore-environment. For this purpose, a new single pore was fabricated (tip size: 52 nm, base size: 600 nm) modified with the peptide-tag and exposed to various concentrations of mCherry and GFP. Afterwards, the membrane was functionalized with NB-moieties and the entire mCherry- and GFP-series was repeated.

Upon exposing the peptide-modified membrane to GFP or mCherry-solutions, the transmembrane current is expected to remain almost unaffected, because the peptide-tag sequence does not contain recognition units neither for mCherry nor GFP. Figure 121 displays the recorded *IV*-characteristics and respective conductance obtained from the corresponding *IV*-curves at 1 V.

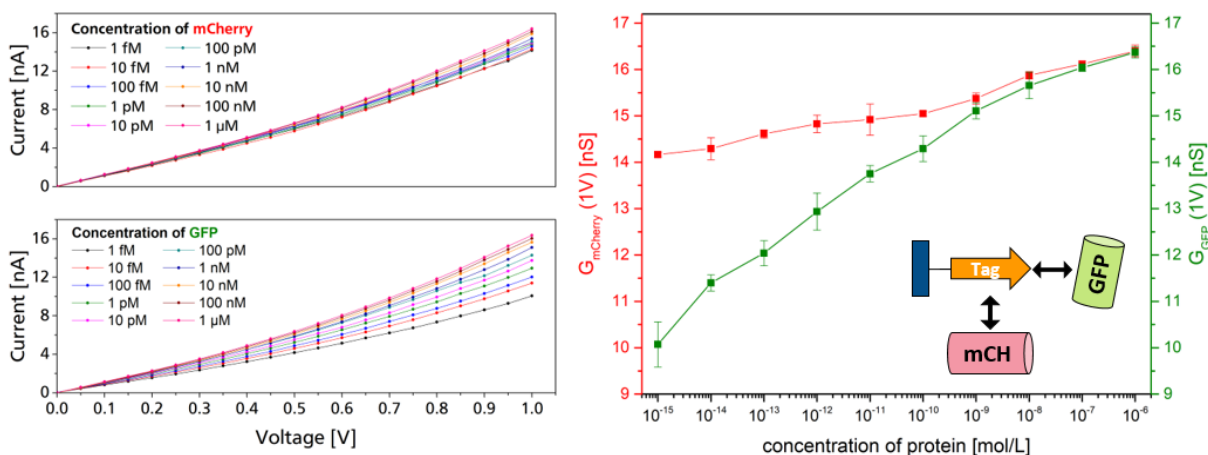


Figure 121: *IV*-curves for positive voltages of the single pore membrane functionalized with the peptide-tag, upon exposure to different mCherry-concentrations (a) and different GFP-concentrations (b) measured in 0.1 M KCl electrolyte (PBS buffer, pH 7). Conductance values at 1 V with respect to the measured proteins (c).

Contrary to the expectations, the *IV*-curves exhibit a smooth increase of current upon increasing the protein-amount inside the electrolyte presumably caused by strong electrostatic attraction between the positively charged peptide-tag (+6) with the negatively charged GFP (-9) and mCherry (-6). Regarding the rectification behaviour prior and after the mCherry- and GFP-treatment, the former *IV*-curve provides a slight positive rectification, which is in accordance with the positive charge of the peptide-tag. Upon treating the membrane either with mCherry or with GFP, the inversion of rectification emphasizes the presumption of electrostatically adsorbed proteins onto peptide-terminated pores. In fact, the total change of transmembrane current amounts to  $\sim 6$  nA, whereas mCherry-series reveals a current change of 2.5 nA. Therefore, the impact on transmembrane current is more significant for the use of GFP than for

the case of mCherry due to the higher net charge of GFP-moieties. The assumption of electrostatic interactions is underlined by the fact, that both mCherry and GFP provide an almost linear correlation with the transmembrane current values indicating the presence of non-specific interaction between the proteins and the peptide-tag.

It has to be mentioned, that the experiment was started with the mCherry-series. After numerous washing steps, the transmembrane impact was investigated using the GFP-series. For washing, the membrane was treated with 5 M Urea-solution, absolute ethanol and pure PBS-buffer solution in the given order. The urea- and EtOH-treatments were allowed to rest for 30 minutes. Urea-solutions are widely used as an efficient method to decompose secondary proteins-structures. Therefore, it is expected that sufficient treatment with urea-solution should remove all residues of GFP or mCherry from the pore surface, while the peptide-tag is not affected due to the absence of secondary structures. (322) The successful removal of protein-moieties was monitored by *IV*-measurements (Figure 122).

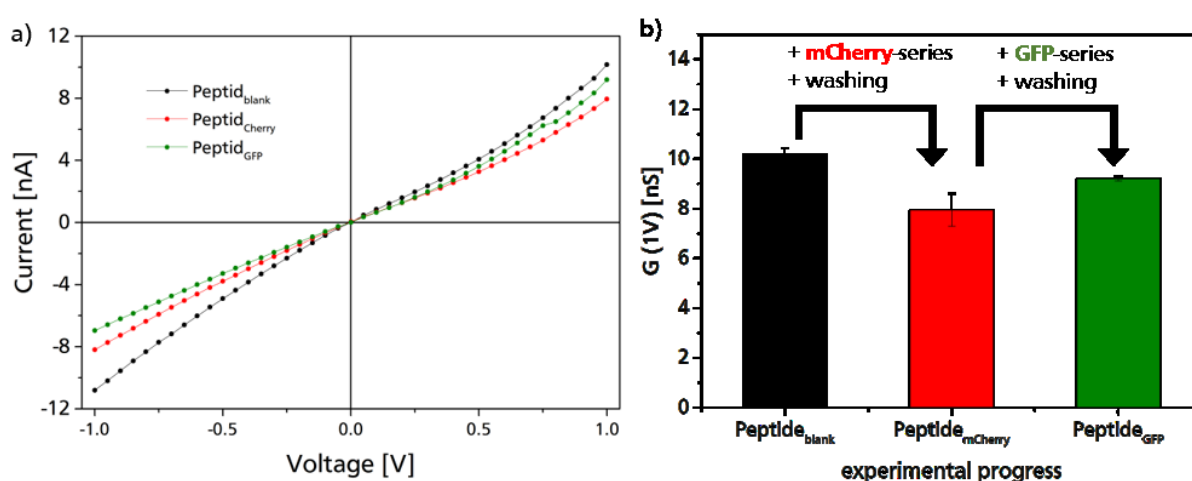


Figure 122: *IV*-curves (a) and respective conductance values (b) measured in 0.1 M KCl electrolyte (PBS buffer, pH 7) of the single pore membrane functionalized with the peptide-tag. The *IV*-curves were recorded prior to the protein exposure, herein referred to as Peptide<sub>blank</sub>-state (black graph and bar) and after the respective protein series, herein referred to as Peptide<sub>mCherry</sub>-state (red graph and bar) and Peptide<sub>GFP</sub>-state (green graph and bar). Note that after every protein series, the membrane was washed with urea, EtOH and pure buffer in order to remove protein residues.

Here, the comparison of the *IV*-values is examined prior to and after exposure to the protein. Herein, the initial *IV*-curve of the peptide-state is referred to as the Peptide<sub>blank</sub>-state (black curve, Figure 122a) and obtains a maximum current of ~10 nA as well as a slightly negative rectification due to the positive charged peptide-moieties. The red curve demonstrates the same pore after the mCherry-proceeding and washing steps. The maximum current is reduced compared to the Peptide<sub>blank</sub>-state to about 2 nA and shows a positive rectification presumably caused by insufficient removal of mCherry from the pore. However, the GFP-series was proceeded and after the washing steps, the respective *IV*-curve (green graph, Figure 122a) was recorded and is referred to as Peptide<sub>GFP</sub>-state. The absolute current value at 1 V amounts to 9.2 nA and showed again positive rectifications. Again, the initial transmembrane current could not be received. Moreover, the present positive rectification contrasts with the expectation. A sufficient regenerated pore should (i) obtain the same transmembrane conductance and (ii) also provide the same negative rectification behaviour. Therefore, it can be assumed that the electrostatic attraction between peptide-moieties and protein-groups is enormously high that both urea and EtOH could not ensure an adequate removal of the proteins from the pore surface.

The results of the negative control on peptide-modified nanopores revealed undefined interactions between peptide and proteins and are expected to have an impact on investigations onto NB-functionalized single pores as well. Therefore, the NB-functionalization was proceeded and the respective mCherry- and GFP-series is repeated. The recorded *IV*-curves are presented in the following Figure.

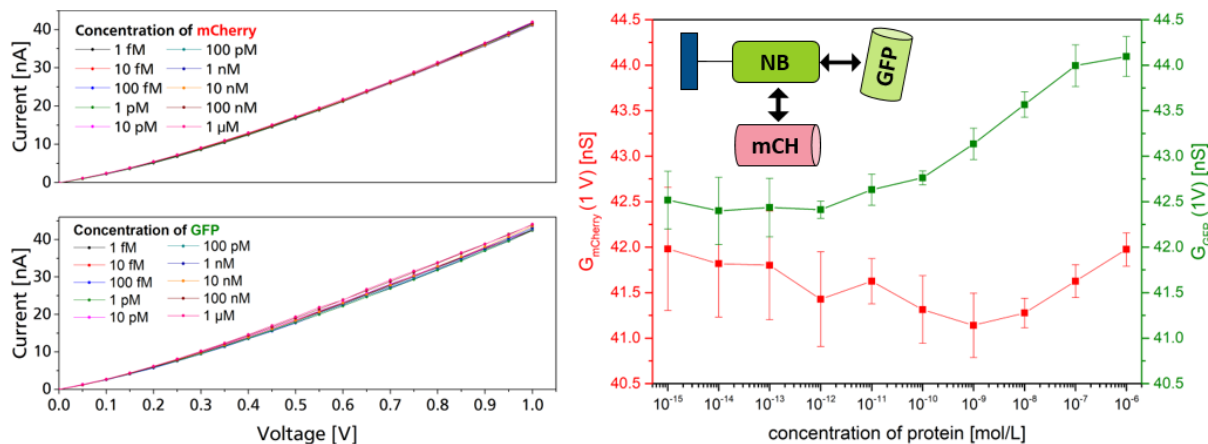


Figure 123: *IV*-curves for positive voltages of the single pore membrane functionalized with the NB-moieties with an affinity towards GFP, upon exposure to different mCherry-concentrations (a) and different GFP-concentrations (b) measured in 0.1 M KCl electrolyte (PBS buffer, pH 7). Conductance at 1 V with respect to the measured proteins (c).

The *IV*-curves recorded for the mCherry- and GFP-series were obtained in the same current range. Over all, the current values spreads over less than 1 nA (for the case of mCherry), whereas the total current change of 1.5 nA is obtained by GFP-series (see Figure 123 a and b). Since the attached NB-moieties have a strong affinity to GFP, the mCherry measurement should not affect the ionic transport at all. Here, the mCherry-treatment does not provide any clear correlation between the ionic transport across the membrane. In fact, the recorded conductance values fluctuate around an average of 41.7 nA. After the NB-immobilization, the membrane was only washed with pure buffer. Urea-treatments are not suitable, because the secondary structure of the NB-moieties would be affected. However, an adequate continuous trend is observed in the correlation of transmembrane conductance and GFP-concentrations. The linear area is valued over three orders of magnitude (10 pM and 100 nM) indicating a reduced sensitivity compared to the tests without intermediate negative control experiments (see Figure 113b).

Although negative control experiments were performed onto the single pore, the results are in accordance to the expectations and underlines the selective measurement of GFP accompanied by the inability of the NB<sub>GFP</sub>-pore to identify mCherry. However, larger errors were noticed during the entire NB-measurements compared to the error bars recorded without intermediate control experiments. This could be caused by traces of GFP and mCherry-residues that still remained inside the pore region even after the washing steps. Consequently, NB-immobilization into the pore region becomes discontinuous, because the NB-moieties can undergo either the Tag/Catcher-interaction or adsorb to remaining protein-residues inside the pore providing more fluctuations during the *IV*-measurement.

---

### 5.3. Conclusion

To sum up, this study investigated the feasibility of nanobodies as potential receptors inside track-etched nanopores.

In the first part, the successful modification of nanobodies onto nanopores was successfully presented. Moreover, the use of a new class of protein-coupling chemistry, i. e. the SpyTag/Catcher-system, was introduced and adapted on the pore-surface. To the best of my knowledge, this is the first time, that tag/catcher system enabled the directed nanobody attachment onto nanopore surfaces indicating the potential of this versatile, directed and simple modification technique.

As the immobilization of the nanobodies was successfully achieved, the sensitivities of two nanobodies towards specific proteins were examined. Firstly, the nanobody with a strong affinity towards green fluorescent proteins (NB<sub>GFP</sub>) was attached and the sensing performance towards various GFP-concentrations (1 fM to 1  $\mu$ M) was monitored by *IV*-experiments. The same sensing trial was performed using a second nanobody having a strong affinity to red fluorescent proteins (NB<sub>mCherry</sub>). To sum up, the sensitivity test revealed a strong and sigmoidal correlation between the transmembrane current and the protein-concentrations ranging over five orders of magnitude (from 1 pM to 10 nM).

Next, the selectivity of both nanobodies was tested using *IV*-measurements, upon exposing each NB-modified membrane to both protein solutions. The experimental results show that NB<sub>GFP</sub>-membranes selectively interact only with GFP-molecules, whereas mCherry did not affect the transmembrane current. The respective measurements with the NB<sub>mCherry</sub>-membranes obtained the opposite results, namely suitable current changes for the use of mCherry and fluctuating currents for the use of GFP. In addition, the identical selectivity results were obtained by analysing the same cross-test with CLSM-imaging. The selectivity test emphasizes the extraordinary specificity of nanobodies towards their respective epitopes. Although GFP and mCherry are structurally cognate in their molecular size and barrel-like scaffold, the NB<sub>GFP</sub> interacts specifically with GFP and NB<sub>mCherry</sub> only with mCherry.

In the third part, negative control experiments were performed using single pore membranes modified with the peptide-tag. Upon exposing the peptide-terminated membranes with mCherry or GFP, a significant interaction was observed, exhibiting a smooth linear correlation between the ionic conductance and the protein concentrations. In order to proceed with the NB-modification onto the membranes successfully, the single pore was roughly washed with Urea-solution. Yet, it is not excluded that negative control experiments are impacting the NB-sensing performance. Although the expected sensitivity and selectivity towards GFP was achieved, the *IV*-measurement revealed a less significant current change of only 4% (from 42.5 nA to 44.0 nA). It can be assumed that a strong interaction between the peptide-moieties and the proteins is presumably promoted by their strong electrostatic attraction. However, urea-treatments seemed to provide adequate regenerated pore-surfaces, but a complete removal of protein-residues is still challenging. Nonetheless, the qualitative proof of specific interactions between NB and their respective proteins inside the nanopore environment is evidenced by the experiment data accompanied by a loss of sensitive performance.

Overall, nanobodies offer highly selective and sensitive properties even in nanoconfined surrounding and could to be worthy candidates for the analyte detections within a clinical surrounding.

---

---

## CHAPTER VI: NANOPORE MEASUREMENTS IN REAL SYSTEMS

---

When aiming at the design of physicochemical biosensors, nanopore membranes need to be established for the on-market use. Hence, there are general requirements that have to be investigated:

- Implementation of *IV*-measurements into portable sensing devices (*Lab-on-Chip* system)
- Processing analyte recognitions within blood samples or human serum (human fluid system)

The achievements of the above mentioned parameters would be of crucial importance towards application of nanopore-based sensors. Therefore, the studies presented in this subchapter were performed in order to move one step closer to real systems.

---

### 1. Nanopore-Sensing within *Lab-on-Chip*-Systems

---

#### 1.1. Introduction

Inspired from POCT-designs, engineering and preparation of the LOC-devices has to be carried out by the sufficient incorporation of the nanopore membrane. Yet, the LOC-fabrication process should not cause changes of the morphological and geometrical pore composition.

According to the literature, the use of single pore membranes is essential for the implementation and sufficient characterization of nanopore based sensors. The first choice for reliable examinations of transmembrane current changes upon exposing the membrane to analyte-solutions are well-established *IV*-measurements. Because *IV*-results are mostly recorded in the one- or two-digit nanoampere (nA) range, the sensitive *IV*-measurements require an experimental set-up with grounding, FARADAY-cage, and surroundings with low noise-background (electrosmog). Otherwise, such sensitive currents would not protrude the *S/N*-ratio. Therefore on-market application request more robust and less-challenging signal-record. Further, single pore membranes are commercially not available as they can only be prepared in the UNILAC-accelerator at GSI-HELMHOLTZ-centre in Darmstadt. Therefore, single pore membranes are used only for research activities. However, multiporous membranes are beneficial for the on-market use as they are commercially available and provide higher current values (mA-range) during *IV*-measurements. As a consequence, the incorporation of easily assessable membranes having a higher pore density is used for the LOC-design.

Here, conically shaped nanopore membranes were fabricated and handed over to Mario El-Khoury, M. Sc. (collaborator of RG Schlaak) for the incorporation into the LOC-device. The laboratory set-up is compared with the LOC-system in terms of technical dimensions and reliable *IV*-measurements. Moreover, the ability to modify the pore surface with active ligands inside the LOC-surrounding is examined and was investigated towards respective analyte detection inside the LOC-device.

#### 1.2. Results and Discussion

As mentioned before, *IV*-measurements of multiporous membranes are difficult to characterize. Due to the semi-crystallinity of the polymeric substrate, every pore located inside the polymeric material is unique. Consequently, every pore located inside the transmembrane area is individual in its ionic transport performance that results in a superposed current read-out along

---

with higher deviations. Moreover, the surface density is higher compared to the net charge of membranes having only one pore. Therefore, diffuse *IV*-curves are recorded along with a complicated the estimation of the rectification behaviour. (204)

Therefore, the number of pores located in the transmembrane area must be as small as possible. This can be achieved by reducing the transmembrane area to a minimum or by using the membrane samples with the lowest available pore density to gain control over ionic transport across nanoporous membranes. Upon engineering nanopore-based LOC-devices, the dimension of the transmembrane area is controlled during the LOC-fabrication process. Hence, if multipore membranes having a pore density of  $10^7$  pores/cm<sup>2</sup> are used, the transmembrane area is reduced to a minimum of 5 x 5 mm<sup>2</sup>. Consequently, the pore number within the transmembrane area is ~600 pores. Taking in mind the previous results of the LBL-study (CHAPTER V.3), successful *IV*-outputs were achieved using membranes with a pore density of  $10^4$  pores/cm<sup>2</sup> as already proven in the LBL-study in section 3 (CHAPTER V). In general, the LOC-fabrication offers a powerful tool to establish *IV*-measurements of better accessible multipore membranes by incorporating them into LOC-devices.

### 1.2.1. Laboratory Set-up vs. LOC-System

The following figure demonstrates the schematic composition of the LOC compared to the laboratory set-up.

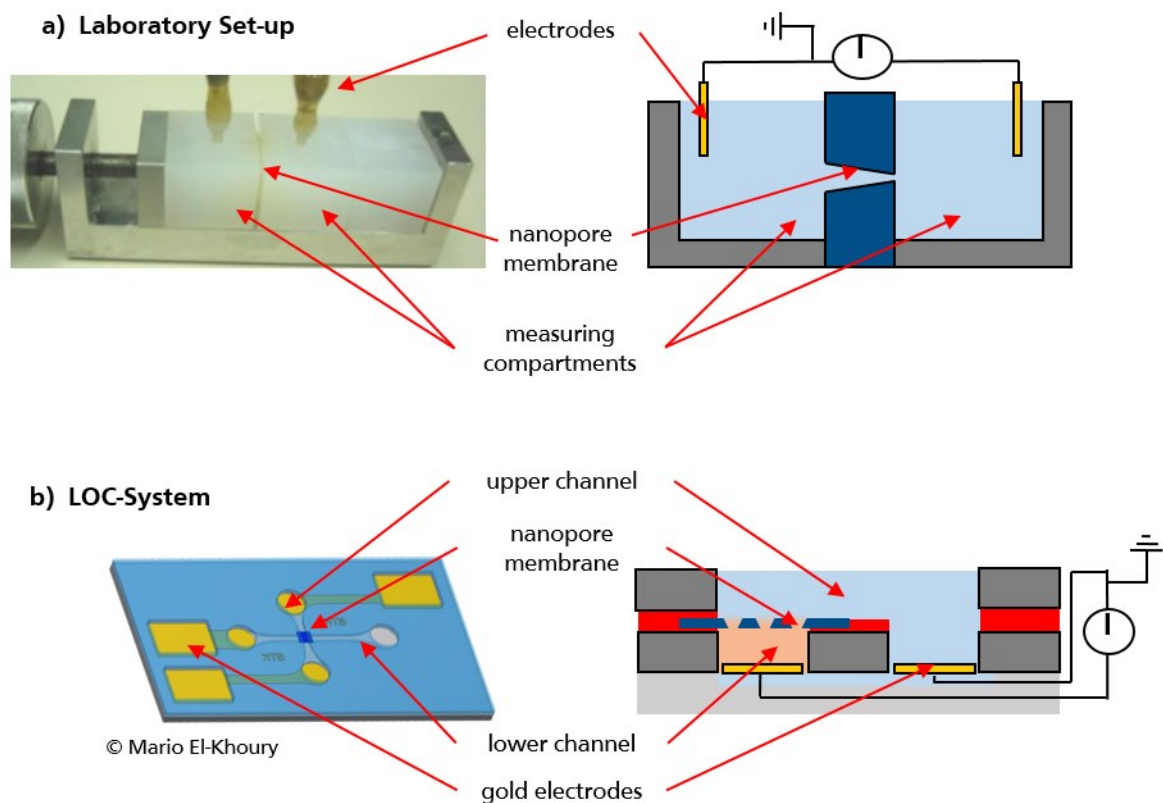


Figure 124: Comparison and construction of the laboratory set-up for the *IV*-measurement (a) and the designed nanopore-based LOC-system (b). The LOC-image is adapted with permission of Mario El-Khoury, M. Sc. (RG Schlaak).

Comparing the *IV*-setup in laboratory and LOC state, the most obvious change is the alignment in the measurement. In Figure 124a, the porous membrane is vertically clamped between the

half-cells, whereas the horizontal alignment is established in the LOC-system. Moreover, the former chambers are transferred into microfluidic channels. The perpendicular channels create an overlapping area, which is separated by the nanopore membrane. Using this construction, the overlapping area is identical to the transmembrane area for later *IV*-measurements and maximum control of transmembrane current became achievable. For a better overview, the technical data are listed in the following table.

Table 6: Technical data of the laboratory set-up and LOC-system.

	Laboratory Set-up	LOC-System
<i>dimensions (L x W x H)</i>	10 cm x 3 cm x 5 cm	23 mm x 14 mm x 1 mm
<i>size of the device</i>	150 cm <sup>3</sup>	322 mm <sup>3</sup>
<i>absolute volume</i>	3000 μL	30 μL
<i>transmembrane area</i>	50 mm <sup>2</sup>	0.0625 mm <sup>2</sup>

According to Table 6, the LOC-compact size is roughly 500-times smaller by having a 100-times smaller sample volumes than the laboratory set-up. In addition, the respective transmembrane area is reduced by around 800-times. During the miniaturization process, the accurate and precise channel fillings with electrolyte solution are required to avoid bubble-formation and osmotic pressure formation. Therefore, the sample filling is carried out using a micropipette, that ensures the filling of the equal volume fraction into both channels. The *IV*-measurement was carried out using the same picoamperemeter/voltage source as for the laboratory set-up. Here, the rod electrodes of the voltage source were connected to the gold-contacts located on the LOC-device.

The LOC-device is build-up on a glass substrate and the respective microfluidic channels are made of the photoresist ‘SU-8’ constructed using photolithographic methods. Upon LOC-fabrication, the crucial part is the layering of the upper channel onto the lower channel as the overlapping channels determine the transmembrane area. This essential step is performed through adhesive bonding. Here, a layer of negative photoresist connects the upper channel with the lower channel. In this study, the first generation of LOC was fabricated by the use of bluish ADEX-photoresist, whereas for the second generation of LOC-devices a layer of colourless Ordyl®-photoresist were used (see Figure 125).

*IV*-measurements were performed and analysed on both LOC-generations. The pH-dependant rectification behaviour as well as ligand-modification and analyte determination inside the LOC-surrounding is characterized by *IV*-curves. Note that the entire LOC-fabrication was performed by Mario El-Khoury with the provided nanopore membranes.



Figure 125: 1<sup>st</sup> and 2<sup>nd</sup> generation of the LOC-devices.

## 1.2.2. 1<sup>st</sup> Generation of LOC-devices

### pH-Dependence

First of all, the pH-dependant behaviour of unmodified pores was tested upon exposing the membrane and the LOC-device to various pH-solutions, respectively.

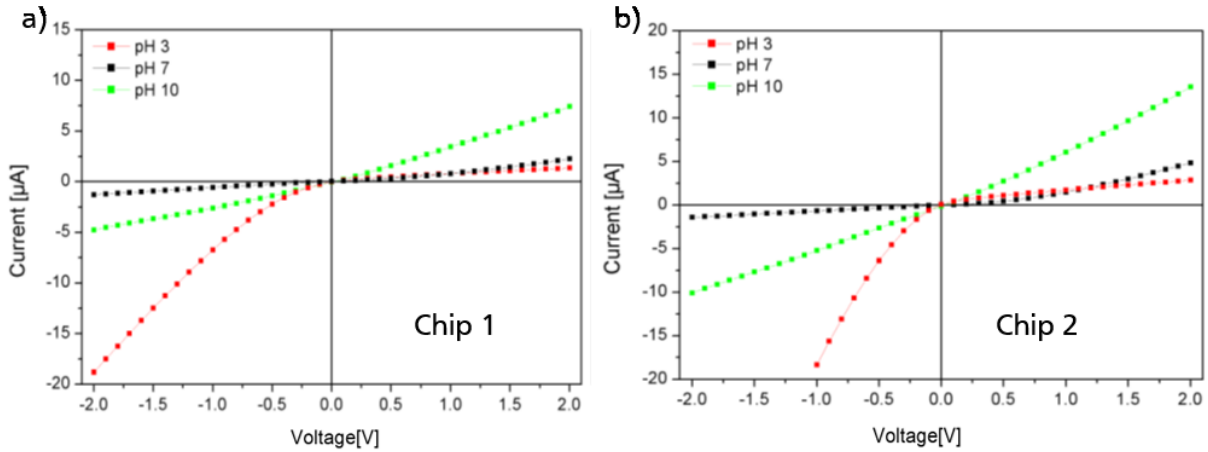


Figure 126: pH-dependent  $I/V$ -characteristics of multipore membranes having a pore density of  $10^7$  pores/cm<sup>2</sup>. The LOC is composed of a nanopore membrane area of  $5 \times 5$  mm<sup>2</sup> originated from the same multipore membrane.

Here, the  $I/V$ -curves were recorded using an acidic electrolyte (PBS buffer, pH 3). After numerous washing steps with pure water, the experiments were repeated in 0.1 M KCl electrolyte (pH 7). Additionally, the same process was carried out using alkaline electrolyte (pH 10). On the first view, both measured chips show similar  $I/V$ -characteristics. Positive rectifications are observed above pH 7 and show an enhanced rectification and rectified ion current at pH 10. For the better comparability, the respective minimum and maximum value, as well as the rectification factor  $f_{rec}$  are listed in the following table.

Table 7: List of maximum and minimum current values and respective rectification factors for the  $I/V$ -measurements of Chip 1 and Chip 2.

	pH3			pH 7			pH 10		
	$I_{max}$	$I_{min}$	$f_{rec}$	$I_{max}$	$I_{min}$	$f_{rec}$	$I_{max}$	$I_{min}$	$f_{rec}$
Chip 1	1.8 $\mu A$	-19.8 $\mu A$	0.09	3.9 $\mu A$	- 1.6 $\mu A$	2.44	8.6 $\mu A$	-5.0 $\mu A$	1.72
Chip 2	2.6 $\mu A$	-38.0 $\mu A$	0.07	4.9 $\mu A$	- 3.1 $\mu A$	1.58	12.6 $\mu A$	-10.1 $\mu A$	1.24

Comparing  $f_{rec}$ -values at pH 3, a positive rectification behaviour ( $f_{rec} < 1$ ) is recorded, while for more basic solutions the rectification behaviour is inverted ( $f_{rec} > 1$ ). This leads to the assumption that the surface polarity inside the pore region got switched upon changing the pH surrounding. In acidic surroundings, the pore surface is covered by protonated uncharged COOH-moieties. Hence, the  $I/V$ -measurements of unmodified pores should be linear and neither anionic nor cationic discrimination should occur. Now, the LOC-measurement could lead to the presumption, that initial positive surfaces charges are present originated by the LOC-materials. The LOC-device is mainly based on photoresist like SUEX or ADEX made up of epoxide resins (323), whose active residues could still carry active epoxy-groups, which are positively charged in the acidic medium and, thus, cause the negative rectification. However, while the pH is changed towards neutral and basic ranges, the expected positive rectification behaviour ( $f_{rec}$

>1) is observed for all used LOC-devices. To this end, this is the first-time a rectification behaviour with multipore membranes embedded into LOC-devices was recorded.

### Modification and Sensorial Performance using 1<sup>st</sup> LOC-Generation

After the successful investigation of pH-dependant rectification behaviour in the multipore membrane was demonstrated, molecular ligands were attached to the pore surface inside the LOC-device to detect respective analytes. The chosen modification pathway was adapted from the already presented covalent attachment of NTA-groups onto nanopores in CHAPTER V.1, because of the simple modification and the reliable results.

Therefore, the identical modification pathway was adapted onto the LOC-integrated multipore membrane and the reaction process is monitored by *IV*-measurements. Figure 127 demonstrates the first *IV*-measurements onto nanopores integrated into the 1<sup>st</sup>-generation of the LOC-devices upon exposing them to various histamine concentrations. For a better overview, only the *IV*-curve for positive voltages is presented as the entire recorded *IV*-curve (from -1V to 1 V) is point symmetrical. After NTA-modification and Ni<sup>2+</sup>-loading, the recorded current values at +1 V are around 4.5  $\mu$ A. According to the experiments onto single pores, the treatment with histamine solution causes the decomplexation of Ni<sup>2+</sup>-moieties from the NTA-modified nanopore surface, resulting in a gain of ionic current. As shown in Figure 127, the increase of histamine amount provides the expected current gain but the increased current flow is not consistent by increasing the Hm-concentration, suggesting an insufficient detection of histamine inside the LOC-device.

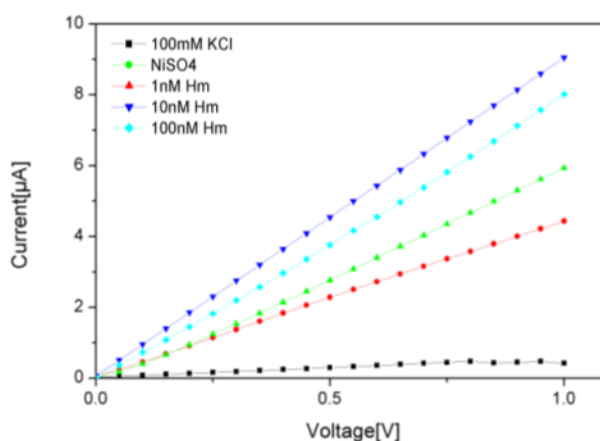


Figure 127: *IV*-curves monitoring the successful modification and histamine detection inside the 1<sup>st</sup> generation of LOC-chips.

However, during the histamine measurements, the dissolution of the binding agent inside the LOC-device occurred and the microfluidic channels became clogged. Consequently, the sufficient filling of the microfluidic channels was not possible and the histamine series was aborted.

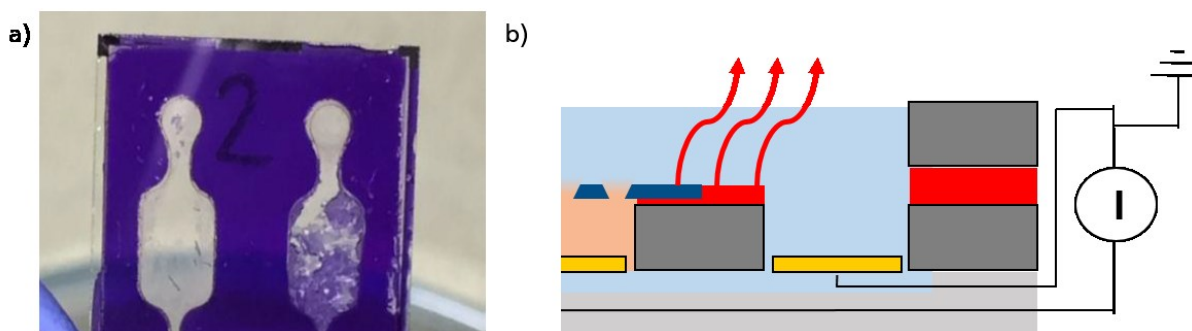


Figure 128: Demonstration of the leaking ADEX-material of the upper microfluidic chamber (a) and respective scheme indicating the presence of free adhesive residues that are dissolved upon intensive contact with modification mixtures and electrolyte solutions.

The leaking bluish ADEX-material is shown in Figure 128(a), and could be due to the fact that some free adhesive residues at the upper microfluidic channel were dissolved upon immersing the LOC-device into ethanolic modification mixture (NTA-modification solution was carried out in an ethanolic-water mixture) and aqueous electrolyte.

In general, the histamine detection was performed on both LOC-devices (Chip 1 and 2) but no reliable results were obtained. It can be assumed that the failure of the ADEX-bonding is mainly causing the fluctuating correlation between the ionic transports on increasing the histamine concentration.

Moreover, due to the instable adhesive binding an alternative chip, i. e., 2<sup>nd</sup> generation of the LOC-system was designed accompanied by the repeating tests towards pH-dependant rectifying behaviour as well as the ligand-modification and histamine detection within the LOC-system.

### 1.2.3. 2<sup>nd</sup> Generation of LOC-devices

The investigation of 2<sup>nd</sup> LOC-generation was highly motivated based on the previous study with the 1<sup>st</sup> LOC-generation to gain control over the dissolved bonding layers. Therefore, the LOC-fabrication was performed by exchanging the ADEX- into Ordyl®-photoresist. The former bluish LOC-device became colourless having the advantage to detect insufficient wetting of the microfluidic channels (see Figure 125).

According to the examination of the 1<sup>st</sup> LOC-generation, the pH-induced change of rectification behaviour was investigated on the 2<sup>nd</sup> LOC-generation as displayed in Figure 129.

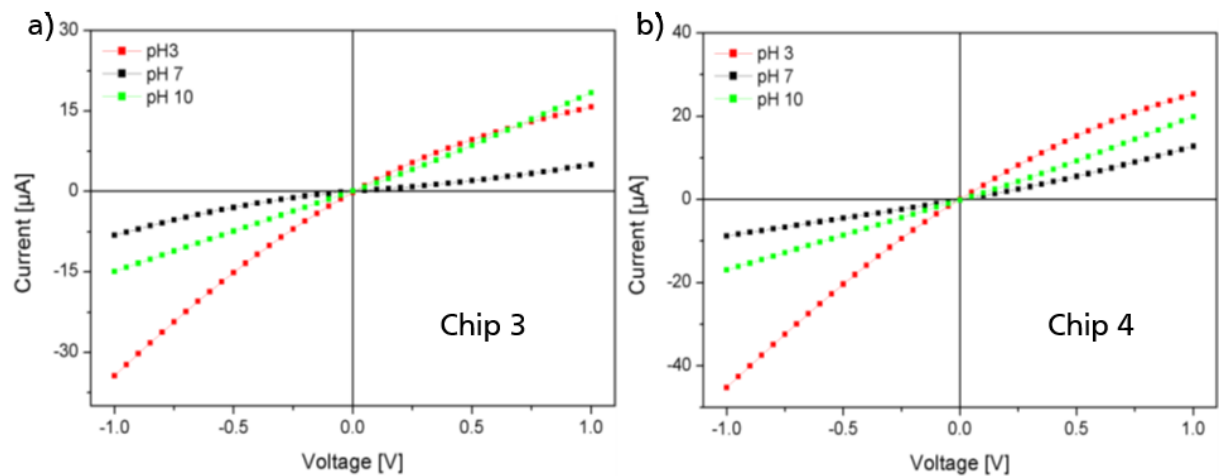


Figure 129: pH-dependent  $I/V$ -characteristics of multipore membranes having a pore density of  $10^7$  pores/cm<sup>2</sup>. LOC is composed of a nanopore membrane piece of  $5 \times 5$  mm<sup>2</sup> taken from the same multipore membrane already used for the 1<sup>st</sup> LOC-generation.

For a better comparability, the specific current values at 1 V and -1 V are listed in the table below.

Table 8: Maximum and minimum current values and respective rectification factors for the  $I/V$ -measurements of Chip 3 and Chip 4.

	pH 3			pH 7			pH 10		
	$I_{\max}$	$I_{\min}$	$f_{\text{rec}}$	$I_{\max}$	$I_{\min}$	$f_{\text{rec}}$	$I_{\max}$	$I_{\min}$	$f_{\text{rec}}$
Chip 3	15.1 $\mu\text{A}$	-31.7 $\mu\text{A}$	0.32	6.2 $\mu\text{A}$	- 6.9 $\mu\text{A}$	0.90	16.4 $\mu\text{A}$	-14.9 $\mu\text{A}$	1.10

Chip 4	23.2 $\mu\text{A}$	-42.3 $\mu\text{A}$	0.55	9.9 $\mu\text{A}$	- 8.9 $\mu\text{A}$	1.11	21.0 $\mu\text{A}$	-19.2 $\mu\text{A}$	1.09
--------	--------------------	---------------------	------	-------------------	---------------------	------	--------------------	---------------------	------

The embedded nanopore pieces inside the 1<sup>st</sup> and the 2<sup>nd</sup> LOC-generation are obtained from the same multipore membrane. Regarding the pH-dependant ionic response, a slightly positive rectification behaviour is observed in neutral and basic surrounding. In contrast, the use of acidic electrolytes (pH 3) reveals the negative rectification behaviour and by comparing with the 1<sup>st</sup> LOC-generation the  $f_{rec}$ -values are slightly enhanced, indicating a low positive net charge inside the 2<sup>nd</sup> LOC-generation. Because the use of Ordyl®-promoted bonding instead of ADEX, there is no difference between both LOC-generations. Now, Ordyl®-compounds are based on acrylate resins and known to be robust and stable upon exposure to acidic or basic surrounding. (324) Therefore, it could be assumed that Ordyl®-compounds are highly polymerized, leading to inactive ends and, thus, promote less surface charge compared to ADEX-films.

Moving on to the modification and analyte detection step, the 2<sup>nd</sup> LOC-generation (Chip 3 and 4) was first functionalized with NTA-moieties and monitored through *IV*-measurements as displayed in Figure 130. For a better overview, only the *IV*-curve for positive voltages is presented as the entire recorded *IV*-curve (from -1V to 1 V) is pointsymmetrical.

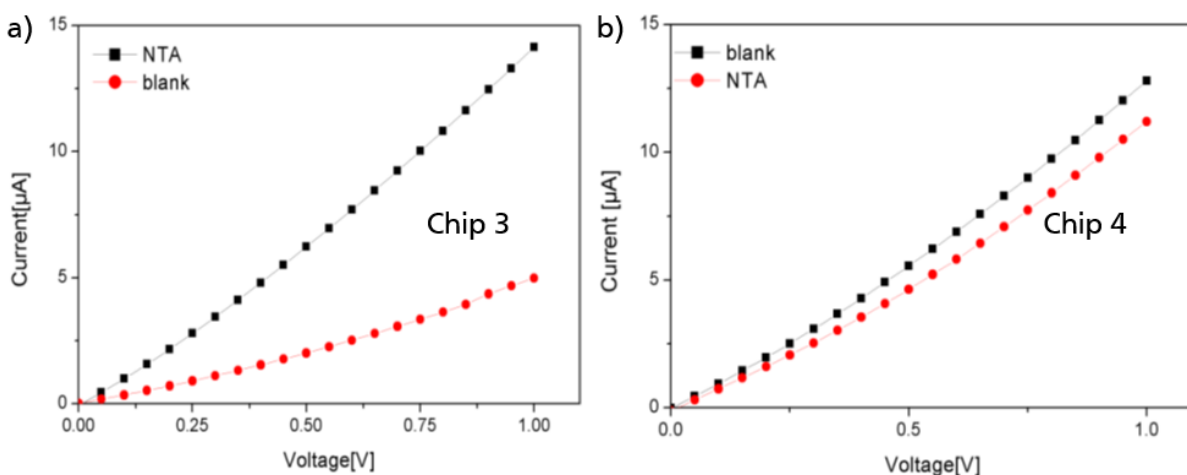


Figure 130: *IV*-curves of Chip 3 (a) and Chip 4 (b) measured in 0.1 M KCl-electrolyte to monitor the NTA-modification procedure inside the 2<sup>nd</sup> LOC-generation.

The successful attachment of NTA-moieties is evidenced by an increase in ionic current due to the enhanced negative surface charge. Because the NTA-modification magnifies the number of negatively charged  $\text{COO}^-$ -groups, an enhanced surface charge was expected, leading to an increased current value and a gain of positive rectification behaviour. Hence, the results coincide with the expectations, evidencing a successful NTA-attachment onto the pore surface.

Afterwards, the NTA-modified nanopore is treated with  $\text{Ni}^{2+}$ -solution according to the procedure for the 1<sup>st</sup> LOC-generation. The respective *IV*-curves are displayed in Figure 131. For a better overview, only the *IV*-curve for positive voltages is presented as the entire recorded *IV*-curve (from -1V to 1 V) is pointsymmetrical.

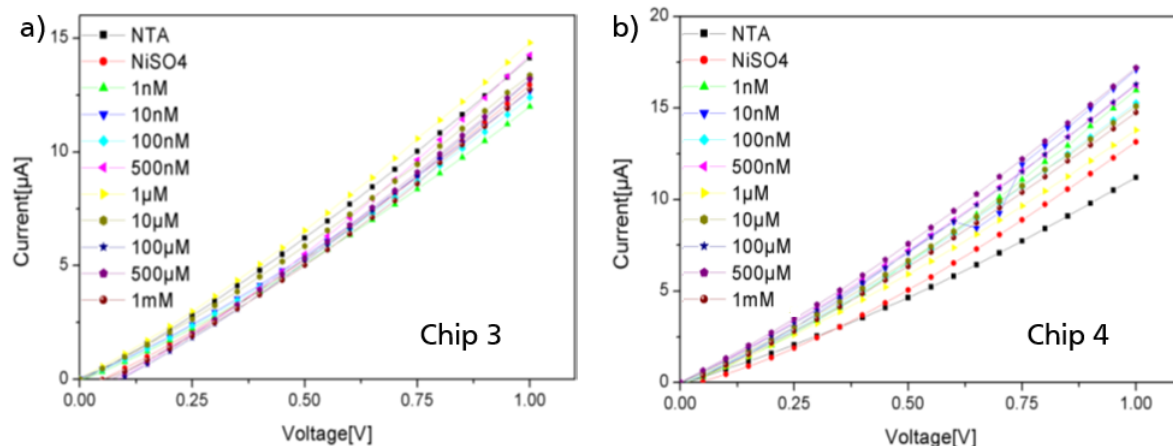


Figure 131:  $I$ - $V$  curves of Chip 3 (a) and Chip 4 (b) measured in 0.1 M KCl-electrolyte to monitor the histamine detection inside the 2<sup>nd</sup> LOC-generation.

Upon increasing the histamine concentration in the electrolyte, the expected current increase is observed. The modification of Chip 3 provided sufficient  $I$ - $V$  curves ranging from  $\sim 12 \mu\text{A}$  to  $\sim 15 \mu\text{A}$ . However, the histamine detection of Chip 4 is wider expanded  $5 \mu\text{A}$  (from  $\sim 12 \mu\text{A}$  to  $\sim 17 \mu\text{A}$ ).

Regarding the correlation between the ionic current and the histamine amount, a continuously increasing trace is observed along with some deviations. To gain a better insight about the real histamine detection performance, conductance values (obtained at 1 V) are plotted against the Hm-concentration (see Figure 132).

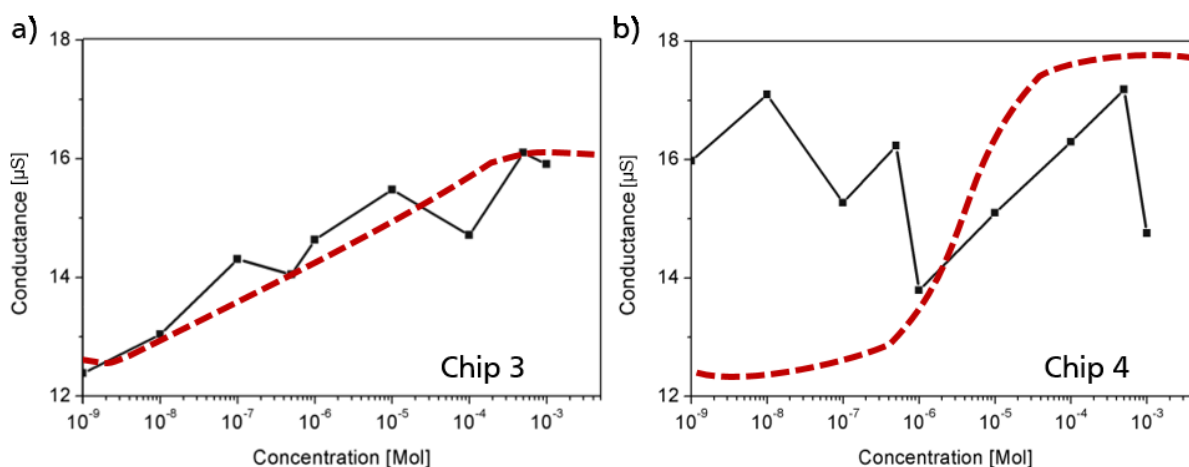


Figure 132: Conductance values of Chip 3 (a) and Chip 4 (b) at 1 V measured in 0.1 M KCl-electrolyte to monitor the histamine detection inside the 2<sup>nd</sup> LOC-generation. Note that the dashed line is the assumed sigmoidal correlation between conductance and histamine amount

From Figure 132a, Chip 3 showed a slight but continuous gain of conductance upon increasing histamine amount along with minor deviations. However, a linear trend representing the active sensing area is not achieved. However, the dashed line demonstrates a possible sigmoidal fit, indicating the feasible match with the respective conductance results. In contrast, chip 4 (see Figure 132b) provides no trend at all. In fact, the respective conductance values are fluctuating in a random order between  $14 \mu\text{S}$  and  $17 \mu\text{S}$ , revealing no match with the possible sigmoidal curve.

---

### 1.3. Conclusion

In general, the experimental results show clearly the successful incorporation of nanopore membranes into LOC-devices. Moreover, the fabrication process did not influence the ionic transport as evidenced by the record of *IV*-curves of LOC-devices which provide significant rectification behaviour.

The pH-dependant ionic transport across the nanopore membranes embedded inside LOC-devices was tested. The expected increase of current flow and rectification was observed upon changing the pH from neutral to basic surrounding. On the contrary, the measurements in acidic electrolytes revealed the presence of positive surface charges that could be originated from the LOC-material SUEX and the binding-components ADEX and Ordyl®, respectively.

Moreover, the modification and analyte detection were performed inside the LOC-devices. Here, the ADEX-bonding step was replaced with Ordyl®-photoresist. The modification step was successfully monitored by *IV*-measurements, evidencing a sufficient modification of NTA-moieties onto the pore surface. Here, the 1<sup>st</sup> LOC-generation provided insufficient results because leaking of the ADEX-film was observed that caused a blockage of the microfluidic channels. Therefore, the entire study was repeated on ADEX-free LOC-devices (2<sup>nd</sup> generation). By exposing various histamine-amounts to the LOC-devices bearing NTA-modified pore areas, an adequate gain of current response was observed. This observation matched with the former study performed on single pore membranes inside the laboratory set-up. Thus, the histamine detection is assumed as a proof-of-concept with respect to the nanopore based LOC-sensor design. Still, there are many parameters that has to be improved. Further variations of LOC-materials should be examined in order to avoid any interactions between the electrolyte solution and the ionic transport during *IV*-measurements.

The experimental data shows the feasibility to incorporate nanopore membranes into LOC-devices and provided reliable *IV*-measurements with adequate detection performances. This study is assumed to be a proof-of-concept in the development of nanopore-based biosensors. Further studies should focus on reproducibility and reliability as well as on the use of real body fluids in order to investigate sensing concepts inside LOC-systems.

## 2. Nanopore-Sensing in Human Body Fluids

### 2.1. Introduction

Upon the development of sensing devices for the early diagnostics of ALZHEIMER's disease, herein referred as AD, the sensing performance of ATCUN-modified nanopores was switched from aqueous measuring medium to a real system such as blood samples. Regarding the blood composition, the cell ingredients like leucocytes or thrombocytes could cause blocking effects when nanopore membranes are exposed to blood samples. For instance, the spatial dimensions of leucocytes range from  $7\ \mu\text{m}$  to  $20\ \mu\text{m}$  being 100-times larger than the base opening of conical nanopores ( $\sim 400\ \text{nm}$ ). (325) Regarding human serum, the fluid is cell free upon sufficient plasma separation and consists mainly of albumin proteins, lipid molecules and water. Therefore, the use of human serum as measuring method could be a promising medium to analyse receptor-modified nanopores aiming their application as diagnostic device.

To evaluate the use of human serum (HS) as potential electrolyte in *IV*-measurements, commercially available human serum from male AB-plasma was purchased. (326) To gain more information about the impact of HS as potential measuring medium, *IV*-curves were recorded on blank nanopores as well as on ATCUN-functionalized membranes using common aqueous KCl-electrolyte (100 mM) and HS-based electrolyte, respectively. Upon exposure to  $\text{Cu}^{2+}$ -ions, the sensitivity, selectivity and reversibility of the ATCUN- $\text{Cu}^{2+}$ -binding ability was examined by *IV*-measurements in HS-based electrolytes.

The  $\text{Cu}^{2+}$ -sensing ability using ATCUN-modified nanopores was previously tested in aqueous solutions, i. e., 100 mM KCl-electrolyte (MES buffered, pH 6.5) as described in the section 4 (CHAPTER V). The experimental results showed a proof-of-concept, but further investigations have to be carried out to establish applications in real systems. The following study is mainly based on the previous investigations of  $\text{Cu}^{2+}$ -sensing performances on ATCUN-modified single pores. Now, the former aqueous medium is extended to real systems. For this purpose, the complexity of the used electrolyte solution is stepwise increased (see Figure 133).

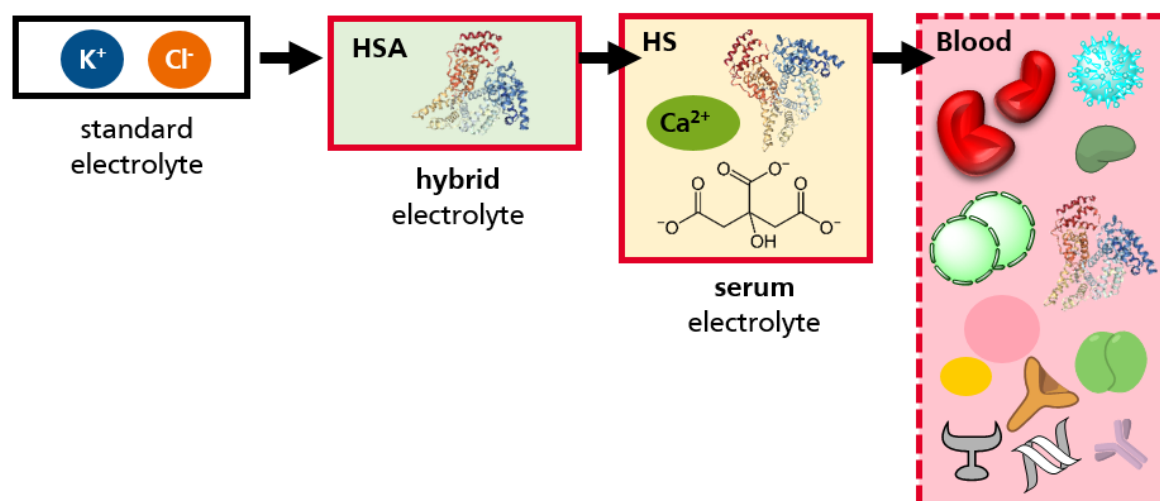


Figure 133: Classes of possible experimental media. The classical electrolyte used for *IV*-measurements consists of 100 mM KCl-solution. The electrolyte complexity is stepwise increased from electrolyte based on human serum albumin (HSA) to human serum (HS) solutions with aiming to perform measurements in blood samples (dotted line).

Standardly, the single pore membranes are used as sensing substrates because of of maximum control over ionic transport and ease of monitoring the current changes by *IV*-measurements.

But the single-pore membranes are not commercially available. Aiming the design of sensing devices for the later clinical applications, the research focus could be extended to the use of low fluence nanopore membranes due to two essential advantages. First, low density porous membranes are commercially available ( $10^4$  pores/cm<sup>2</sup> and higher) and, second, the rectification behaviour of conically shaped pores in commercially available membranes is resolvable through *IV*-measurements. Therefore, the upcoming measurements are all carried out using conically shaped nanoporous membranes having a pore density of  $10^4$  pores/cm<sup>2</sup>.

## 2.2. Results and Discussions

In the beginning, the copper-binding performance is analysed in a hybrid-electrolyte-solution as well as by using the commercially available humane serum (see section 1.2.2 and 1.2.3). To this end, the sensitivity, selectivity as well as the reversibility was tested in the same way as already performed with the KCl-electrolyte solutions in Chapter V.4.

### 2.2.1. Copper (II)-Sensing in Human Serum (HS)

In this section, a few preliminary tests were conducted to slowly approach the new measurement medium. In order to investigate changes in *IV*-characteristics of an unmodified membrane and to avoid contaminations of the already modified oligopore with ingredients of the human serum, a second oligopore membrane was fabricated in the identical etching time (1450 s) having the same pore density and shape as the previous one (average tip diameter  $36 \text{ nm} \pm 4 \text{ nm}$ ; average base diameter  $520 \text{ nm} \pm 26 \text{ nm}$ )

Figure 134 demonstrates the *IV*-curves of the unmodified conical oligopore membrane upon exposure to various electrolyte solutions. Here, a negative control experiment was carried out using distilled pure water ( $18.2 \text{ M}\Omega$ ,  $25 \text{ }^\circ\text{C}$ ), providing almost no current record. As positive control measurement serves the *IV*-curve presenting the positive rectification behaviour with a maximum current of  $1.6 \text{ }\mu\text{A}$  (at  $+1 \text{ V}$ ) obtained in  $0.1 \text{ M}$  KCl-electrolyte (standard electrolyte). The  $\mu\text{A}$ -current is recorded, because in this series the half-cells with the wider opening ( $8 \text{ mm}$  diameter) were used. Therefore, the number of nanopores is enlarged and provides the higher current values.

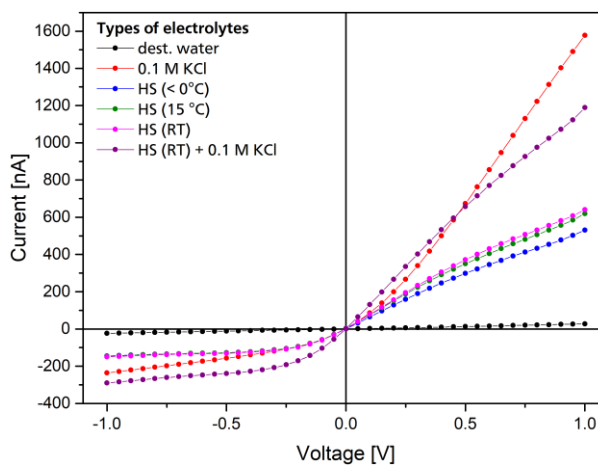


Figure 134: *IV*-curve of the unmodified oligopore membrane with respect to various electrolyte solutions: distilled water,  $100 \text{ mM}$  KCl-electrolyte and human serum-electrolytes at different temperature.

Because the human serum samples are stored in the freezer (at  $-40^\circ\text{C}$ ), the *IV*-measurement of HS-based electrolyte solutions should be carried out at room temperature with a completely molten serum sample. According to Figure 134, the samples that were immediately taken out of the freezer obtain a lower conductance than those measured at room temperature (RT). In addition, the ionic transport in the standard electrolyte is two-times higher than the one of pure HS-electrolyte. To ensure enough electrolyte conductance,  $100 \text{ mM}$  KCl-salt was added to the HS-sample. The respective *IV*-curve revealed high ionic transport ( $\sim 1 \text{ }\mu\text{A}$  at  $1 \text{ V}$ ). The reduced

current transport could be due to the fact that HS-samples consists of aqueous and organic ingredients affecting the solubility of KCl-salt. Hence, further *IV*-measurement were carried out in HS-electrolyte solutions containing 0.1M KCl.

During the pretests, the enhanced viscosity of HS-samples was observed that required a more careful and bubble-free handling, especially in terms of the filling of HS-electrolyte into the measurement cell as well as washing out of the cell after measurement. Therefore, the copper-sensing performance of ATCUN-modified oligopore was carried out using various HS-ratios und using a smaller half-cell (8 mm diameter). The *IV*-curves displayed in Figure 135 monitor the successful modification of the pore membrane having the same readout as the nanopore used in CHAPTER V.4 (Figure 103). In the beginning, the nanopore behaves cation selective as indicated by the positive rectification behaviour. Upon the attachment of ethylene diamine (EDA), the former negatively charged surface became neutral. Therefore, an equivalent passage of cations and anions is enabled leading to an enhanced conductance as well as a linear *IV*-curve. The ATCUN-immobilization induces a positively charged surface accompanied by a hindered cationic movement across the pore region as indicated by the inverted *IV*-curve compared to the unmodified blank state.

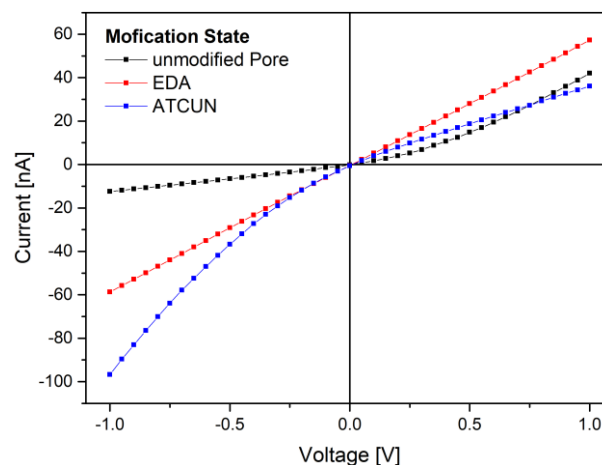


Figure 135: *IV*-curves demonstrating the ATCUN-modification onto a blank conical pore membrane having  $10^4$  pores/cm<sup>2</sup>.

First, the ATCUN-Cu<sup>2+</sup>-interaction was repeated under the same conditions as in CHAPTER V.4 regarding the sensitivity and selectivity towards copper ion detection as well as the re-usability and are presented in the following Figure.

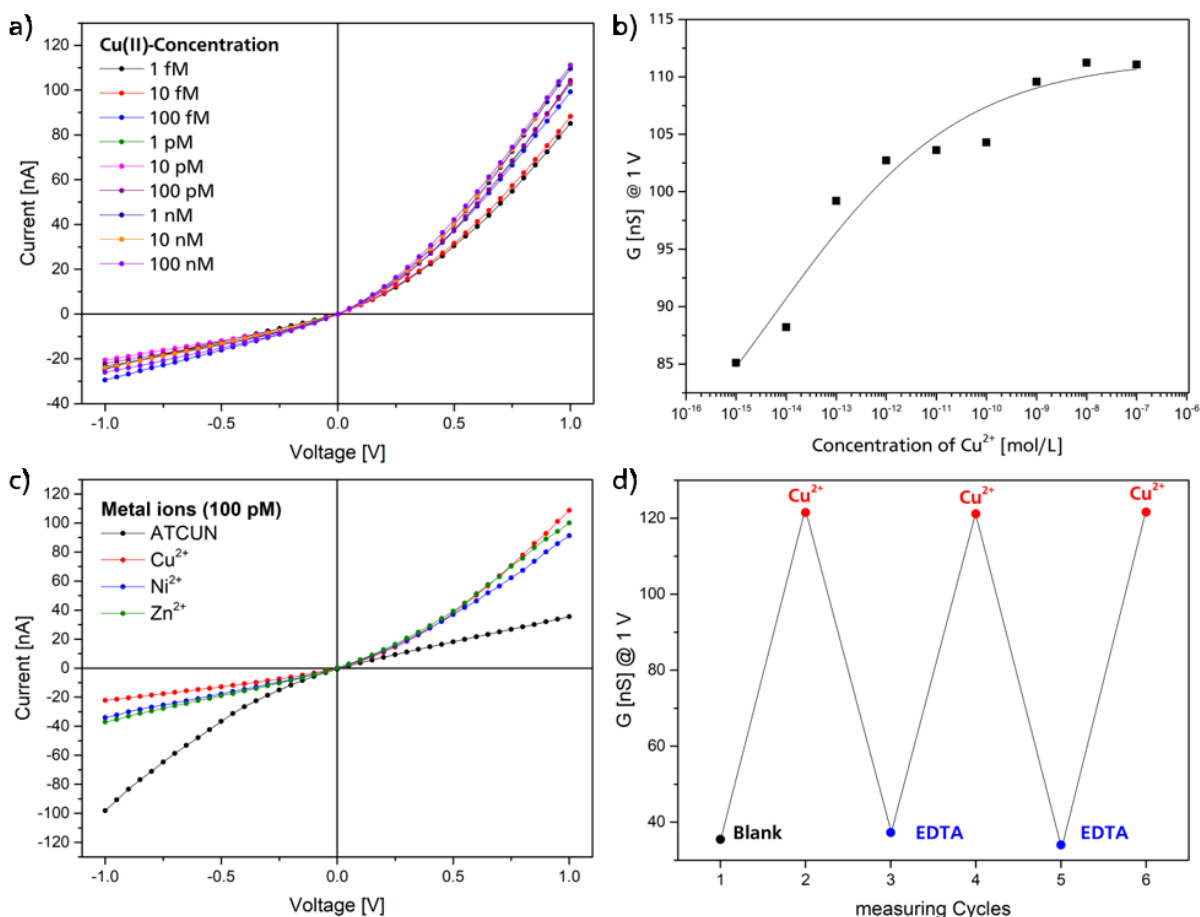


Figure 136: *IV*-curve of the ATCUN-modified membrane having  $10^4$  pores/cm<sup>2</sup> upon exposure to various Cu<sup>2+</sup>-concentrations in the electrolyte solution (100 mM KCl, MES buffer, pH 6.5) (a). The underlying conductance values are obtained from the corresponding *IV*-data at 1 V with respect to the tested Cu<sup>2+</sup>-concentrations (b). *IV*-curve of the ATCUN-modified oligopore upon exposure to various divalent metal ions (100 pM) in the electrolyte solution (100 mM KCl, MES buffer, pH 6.5) (c). Conductance values at 1 V shows the reversible complexation/decomplexation of Cu<sup>2+</sup>-ions. Here, on exposure to 100 pM Cu<sup>2+</sup>-concentration in the electrolyte solution (100 mM KCl, MES buffer, pH 6.5) exhibits the current increase (red dots) due to the enhance surface charge of the pore upon generation of ATCUN-Cu-moieties on the pore surface. Treatment with 1 mM EDTA-solution causes the removal of Cu<sup>2+</sup>-ions from the pore surface, inducing a recovery of pore surface (blue dots).

Regarding the results of the sensitivity test, the gain of ionic transport with increasing Cu<sup>2+</sup>-amount is in agreement with the trend resulting from the Cu<sup>2+</sup>-sensitivity experiments in Chapter V.4, along with an absolute increased current flow with respect to the up-scaled pore density as wider half-cells were used. Hence, the conductance values at 1 V did not show an adequate dependence between ionic transport and Cu<sup>2+</sup>-amount. In detail, Figure 136b demonstrates a successive current increase of almost 30%. The results show a good copper-response-ratio but the linear zone that corresponds to the active Cu<sup>2+</sup>-sensing area is smaller (1 pM to 1 nM) compared to the linear zone of the former experiment in CHAPTER V.4 (1 fM to 1 nM). The respective selectivity measurements are presented in Figure 136c. Here, the ATCUN-terminated membrane is exposed to various divalent metal ion solutions having a concentration of 100 pM. Herein, for each *IV*-measurement, the pore was exposed to 1 mM EDTA solution to enable the efficient removal of respective bivalent metal ions. The experiments show the current increase of 60% for the use of copper ions, whereas the current value for nickel and zinc ions caused only a marginal current change of 55% and 52%, respectively. The presence of copper ions resulted highest current change compared to the other metal ions. At least, the reversibility

for the ACTUN-Cu<sup>2+</sup>-interaction examined on the pore membrane is shown in Figure 136d. The exposure to electrolytes in the presence and absence of Cu<sup>2+</sup>-ions was repeated over 6 cycles. The *IV*-values provide stable signals in the range of 120 nS in presence of Cu<sup>2+</sup>-ions. Whereas the membrane gets fully regenerated upon treatment with EDTA (~35 nA) underlining the adequate reproducibility of the complexation/decomplexation between ATCUN-moieties and Cu<sup>2+</sup>-ions, when oligopores membranes were used.

Consequently, further investigations regarding the expansion from aqueous KCl-solution to electrolytes based on human serum were carried out using the same oligopore to evaluate the potential application towards real systems. Therefore, the copper sensing performance is carried out in electrolyte containing human serum and is discussed briefly in the next section.

First, the Cu<sup>2+</sup>-series was performed in HS-electrolyte with the addition of 100 mM KCl. Then, the same study was performed using 1:2 ratio and 1:10-ratio (HS/water), separately. The following picture demonstrates the Cu<sup>2+</sup>-sensing series with respect to the HS/water-ratio. Note that after each series, the membrane was carefully washed with EDTA-solution, MES-buffer and corresponding electrolyte solution.

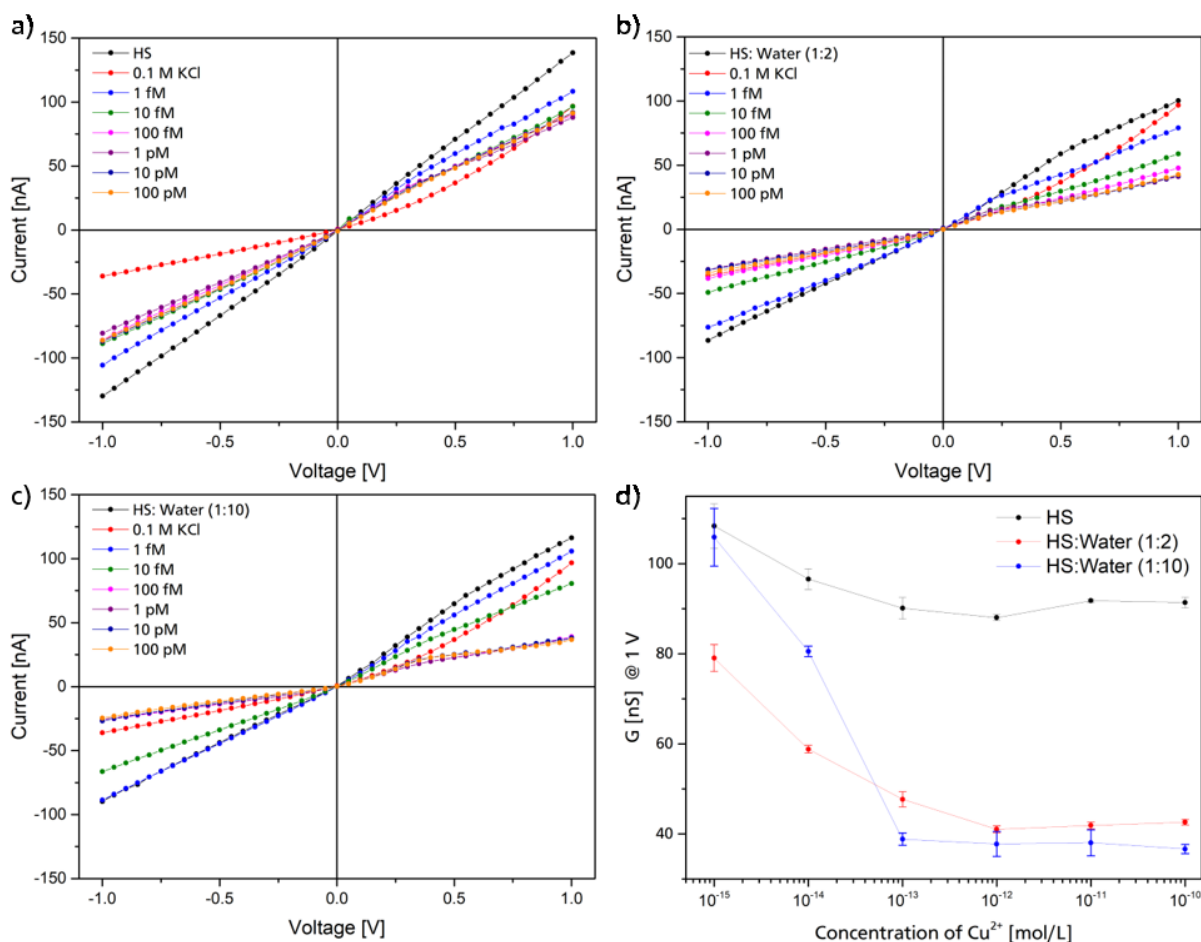


Figure 137: *IV*-measurements using the ATCUN-modified oligopore membrane upon exposure to different Cu<sup>2+</sup>-concentrations with respect to the electrolyte composition: 100 mM KCl solved in pure HS-solution (a); 100 mM KCl solved in 1:2 diluted HS-water-solution (b) and 100 mM KCl solved in diluted 1:10 HS-water-solution (c). The underlying conductance values at 1 V are presented with respect to the electrolyte composition and Cu<sup>2+</sup>-amount (d).

The use of HS-based electrolytes causes two significant changes when compared to the water-based measurements. First, the *IV*-curves show more linear characteristics compared to the *IV*-

curves obtained by  $\text{Cu}^{2+}$ -series in aqueous electrolyte. Second, the current transport is inverted. Here, the current response is decreased upon exposure to increasing  $\text{Cu}^{2+}$ -concentrations. Briefly, the measurement in pure HS-electrolyte provides a 20%-decrease of conductance, whereas the use of 1:2 and 1:10-diluted HS-electrolyte reduces the conductance to about 50% and 70%, respectively. In addition, for concentrations of 1 pM and higher, all experiments show a kind of saturation effect due to stagnating current values with only minor changes in the range of 4% and 9%. Overall, the results of the 1:2-dilution series provides smooth experimental data in terms of low deviations, i.e., low error bars, as well as the continuous reduction of ionic flux, revealing a detection area between 10 fM and 1 pM  $\text{Cu}^{2+}$ -amount. Consequently, further experimental studies require a soft dilution of pure HS-samples to obtain adequate measurements.

Concluding the use of HS-based electrolytes, the inverted ionic transport upon increasing the  $\text{Cu}^{2+}$ -amount could be due to specific interactions between the ATCUN- $\text{Cu}^{2+}$ -moieties located on the nanopore surface and the HS-ingredients. Regarding the composition of human serum, it contains protein, i.e., human serum albumin (HSA) in high quantity. It is suggested that HSA interacts with the copper-loaded nanopore region. However, the design of the ATCUN-motif originated from a certain protein sequence located inside the albumin protein of the human blood. This region is responsible for the effective transportation of cupric ions within the human body and therefore, probably responsible for the inverted *IV*-results. (327)

Now that the  $\text{Cu}^{2+}$ -sensitivity in HS medium has been ensured, selectivity tests towards other divalent metal ions was carried out using 100 pM  $\text{Ni}^{2+}$ - and  $\text{Zn}^{2+}$ -amount dissolved in 1:2-diluted HS-electrolyte (1:2) and displayed in Figure 138a. Moreover, the reversibility between ATCUN-terminated pore surface and  $\text{Cu}^{2+}$ -ions was evaluated in Figure 138b.

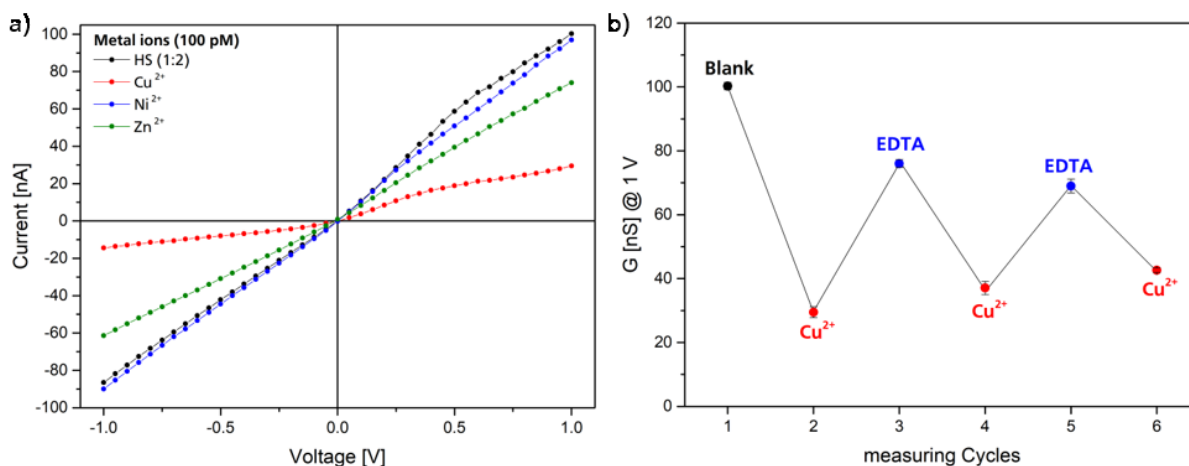


Figure 138: *IV*-curve of the ATCUN-modified oligopore upon exposure to various divalent metal ions (100 pM) in the HS-based electrolyte solution (100mM KCl, 1:2-ratio of HS and water) (a). Conductance values at 1V show the reversible complexation/ decomplexation of  $\text{Cu}^{2+}$ -ions. Here, on exposure to 100 pM  $\text{Cu}^{2+}$ -amount in the HS-based electrolyte solution provides the current reduction (red dots) due to the suggested HSA-interaction upon the generation of ATCUN- $\text{Cu}$ -moieties. The on-going treatment with 1mM EDTA-solution leads to the removal of  $\text{Cu}^{2+}$ -ions from the pore surface, inducing a recovery of ATCUN moieties (blue dots).

Regarding the selectivity measurements, the maximum ionic current decrease of up to 70% is observed for the use of  $\text{Cu}^{2+}$ -ions, as expected. On the contrary, treating the membrane with nickel ions did not show significant current changes (< 5%), whereas the measurement in presence of zinc ions leads to minor reduced current flow (~20%). Although the composition

of the electrolyte is HS-based, the experimental data demonstrates still a significant selectivity towards copper ions (Figure 138a).

Moving on to the reversibility test shown in Figure 138b, the experimental procedure was performed to record the reversibility of  $\text{Cu}^{2+}$ -adsorption and -desorption in dependence of EDTA-solution. Now, the results showed an adequate re-usability of the ACTUN-modified membrane even in HS-based electrolytes. Treating the ATCUN-modified membrane with  $\text{Cu}^{2+}$ -ions causes the expected current decrease, whereas the treatment with EDTA-solution provides the regeneration of the ATCUN on the pore surface. Hence, the current value deviates from the starting current value (100 nA) after the EDTA-treatment. In fact, the current values are reduced to about 20% compared to the blank state, suggesting insufficiently removal of  $\text{Cu}^{2+}$ -ions from the pore surface. Therefore, the exposure time for the EDTA treatment was increased to 1 h in the next measuring cycle. But the complete regeneration of the current value could not be reached. In fact, the current value is balanced by around 80 nA suggesting that albumin residues are still in the pore walls which can not be washed out by EDTA-treatment. Nevertheless, the reproducibility is evidenced even in presence of albumin proteins.

To gain more insights into the specific interaction in HS-based measurements, first, it should be excluded that simply the use of a HS-based  $\text{Cu}^{2+}$ -series does not affect the ionic transport at all (negative control experiment) and, second, it has to be investigated, whether HSA is responsible for the inverted IV-characteristics.

### 2.2.2. Copper (II)-Sensing in Human Albumin Electrolyte

In order to investigate the effect of human serum towards nanopores, a third nanopore membrane was prepared under the same etching conditions as the previous one to ensure a similar pore geometry (tip diameter: 32 nm; base diameter: 600 nm). The as-prepared oligopore membrane was fixed in the IV-cell and the entire  $\text{Cu}^{2+}$ -series was carried out using the HS-based electrolyte (1:2-diluted HS:water). The resulting IV-curves are presented in the inset of Figure 139. Here, the error bars of the higher diluted range are enlarged, presumably caused by dilution errors. In contrast, higher concentrated  $\text{Cu}^{2+}$ -amounts show only marginal error-values, because even small fluctuations could cause measurable effects in such low concentrations. The experimental data display no clear correlation between ionic transport behaviour and the increasing  $\text{Cu}^{2+}$ -amount. All data are scattering around the average current value of  $\sim 17$  nA, exhibiting no specific interaction of the HS-based electrolyte with the nanopore surface.

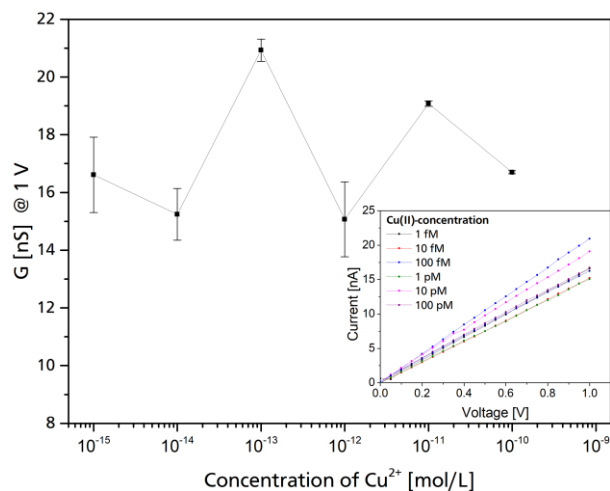


Figure 139: Conductance and IV-curves for positive applied voltages using unmodified oligopores with respect to various  $\text{Cu}^{2+}$ -amounts solved in 0.1 M KCl electrolyte solution (1:2-diluted HS-water-mixture).

Once the negative control study revealed only nonspecific interactions of HS-ingredients with the unmodified membrane, further experiments were performed to investigate the impact of human serum albumin (HSA) as measuring medium with ATCUN-peptides modified membrane. The following Figure 138 display the IV-characteristics of the ACTUN-terminated

membrane upon exposure to  $\text{Cu}^{2+}$ -series with HS-based electrolyte (1:2-diluted HS-water-mixture) and then with HSA-based electrolyte (Figure 140b).

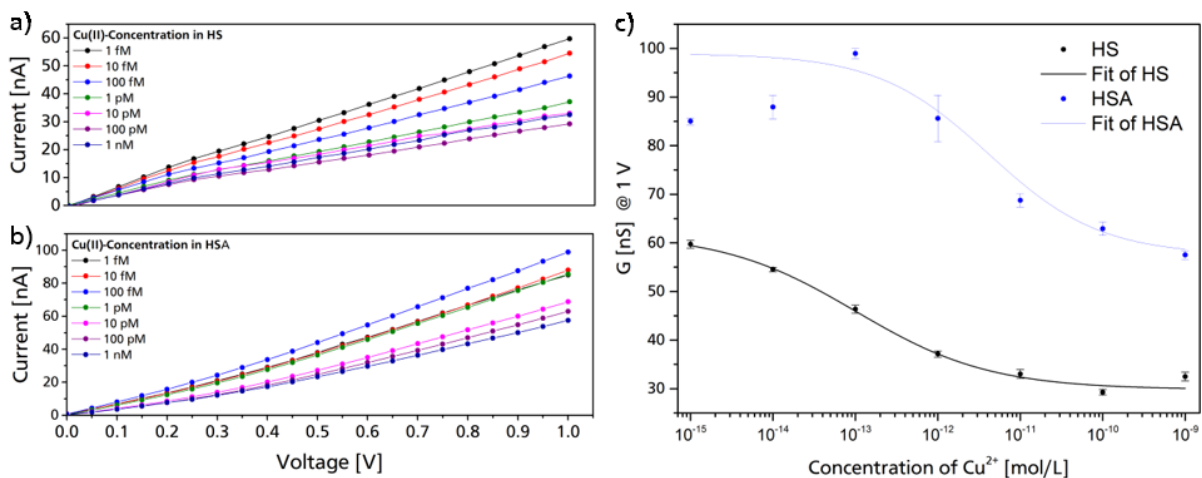


Figure 140:  $I/V$ -curves for positive applied voltages of the ACTUN-modified oligopores with respect to various  $\text{Cu}^{2+}$ -amounts dissolved in HS-based electrolyte solution containing 0.1M KCl in 1:2-diluted HS-water-mixture (a) and dissolved in HSA-based electrolyte consisting of 0.1M KCl in aqueous 150 mM HSA-solution (b).

From the supplier's certificate of analysis the natural amount of HAS of human serum ranges from 50 to 75  $\mu\text{M}$ . (330) However, the HSA-amount can further vary with respect to the age. Therefore the HAS amount of the used HAS-based electrolyte was set to 17  $\mu\text{M}$  being in the same range of natural HSA-amount of 1:2-diluted HS-water-mixture. Moreover, the measurement was first performed with HSA-based electrolyte and then after numerous washing steps (with EDTA, water and pure electrolyte), the HS-based  $\text{Cu}^{2+}$ -series was carried out.

Figure 140a and b demonstrate similar  $I/V$ -curves using of HS- or HSA-based electrolytes. The ionic flux is dropped upon increasing the  $\text{Cu}^{2+}$ -concentration in both electrolyte as evidenced from Figure 140c. Here, for the case of HSA-based measurements, the total decrease of conductance (at 1 V) amounts to almost 40%, whereas a reduction of  $\sim 50\%$  is obtained by using HS-based electrolyte. The HS-measurements provides a sigmoidal trend between  $\text{Cu}^{2+}$ -amount and conductance, whereas the HSA-experiments provides higher scattered data points around the sigmoidal fit. Nonetheless, the sloping correlation between various concentrations of copper ions and the ionic response is obvious for the use of both electrolytes with increasing  $\text{Cu}^{2+}$ -amount in contrast to the an increase of conductance in aqueous electrolytes.

Regarding Figure 140c, the experimental data provide higher deviations when using HSA-based electrolyte compared to the HS-based measurements, indicating higher disturbances through  $I/V$ -measurements. During the HSA-experiments, a lower surface tension of the electrolyte was noticed upon addition of HAS that caused bubble formation while HAS-electrolyte was filled in the half-chambers. Absolom *et al.* reported the effect of surface tension in the presence of respective proteins which lead to an enhanced foam formation at the peptide-air-interface. (328) Now, the filling into the measurement cell was more difficult in order to avoid bubble formation inside the cell. Moreover, the applied voltage leads to ionic movements inside the HSA-medium, that could further disturb the  $I/V$ -measurements. By considering the first  $\text{Cu}^{2+}$ -series which was carried out in pure HS, larger error bars were also observed which become smaller upon the dilution with water (see Figure 137d). In this study, experimental data of Figure 137 show clearly the requirement of diluted HS-samples, in order to obtain more

precise and less scattering experimental results. Hence, reports about the HSA-level in human serum deduce a broad HSA-range between  $50 \mu\text{M}$  (329) and  $75 \mu\text{M}$  (330). Note that the HSA-amount can further vary with respect to the age and sex of the donor. Therefore, the HAS-amount was set at  $17 \mu\text{M}$  being equal to the HSA-amount of a 1:2 diluted HS-sample. However, the measurements in HSA-based electrolyte do not provide the same current values but obtain the same correlation. Therefore, it can be assumed that the used HSA -amount of  $17 \mu\text{M}$  differs significantly from the real HSA-level in HS-samples. Nonetheless, the comparison of HSA- and HS-based  $\text{Cu}^{2+}$ -series suggests that the inverted conductivity response is due to the presence of albumin. Based on previous studies, the interaction between copper and ATCUN is well-known. In HS-surroundings, the addition of  $\text{Cu}^{2+}$ -ions lead to the formation of a preliminary albumin- $\text{Cu}^{2+}$ -complex that is attached to the pore surface instead of the single  $\text{Cu}^{2+}$ -adsorption. According to the Figure 139, the adsorbed albumin- $\text{Cu}^{2+}$ -pair leads to a decrease of effective current flow due to the spatial expansion of ATCUN- $\text{Cu}^{2+}$ -albumin moieties.

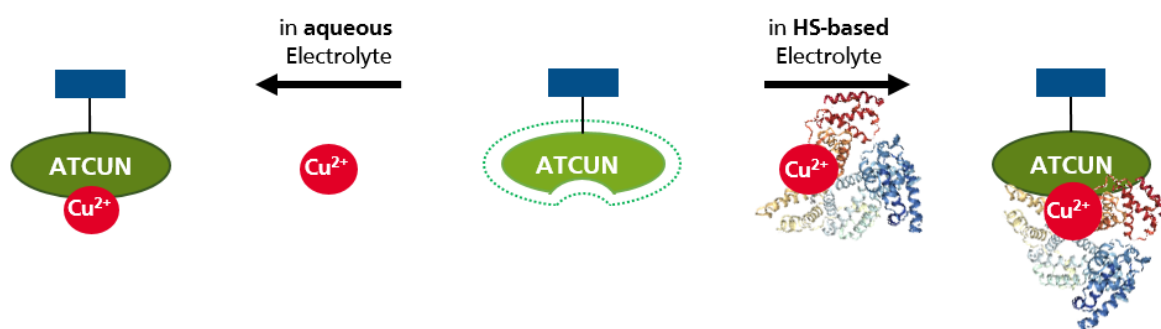


Figure 141: Suggested interaction between  $\text{Cu}^{2+}$ -moieties and ATCUN-modified pore surface. For the case of performing the  $\text{Cu}^{2+}$ -series in aqueous electrolyte, the adsorption of  $\text{Cu}^{2+}$ -ions leads to an increased surface net charge. For the use of HS-based electrolytes, the presence of albumin protein provides the formation of ATCUN- $\text{Cu}^{2+}$ -albumin groups, causing a decrease of current due to the huge spatial expansion.

The interaction of Albumin-bounded  $\text{Cu}^{2+}$ -ions with ATCUN is specific, because the HS-based  $\text{Cu}^{2+}$ -series performed on unmodified nanopores reveals only undefined interactions with the blank pore surface. Hence, it can be assumed upon treating the ATCUN-modified pore with copper ions in HS/HAS-based electrolytes, the HSA interacts with the  $\text{Cu}^{2+}$ -ions being bounded to the pore surface causing to the inverted ionic response.

### 2.3. Conclusion

In summary, the  $\text{Cu}^{2+}$ -sensing ability in human serum samples was tested using ATCUN-modified oligopore membranes by *IV*-measurements. The experimental data demonstrated the successful and curtail proof-of-concept of using modified nanopore membranes as sensing devices in human body fluids.

The fabrication of membranes having a higher density is faster due to reduced etching times. Promoted by an enhanced contact area during pore etching fabrication shortened etching times compared to the single pore membranes are required. Moreover, the use of oligopore membranes is more economical. Here, one membrane piece offers the possibility to manufacture several sensor devices. Because the fabrication of a nanopore based sensor required indeed at least only one intact pore to obtain significant results.

Sensitivity measurements were performed in aqueous 0.1 M KCl-electrolyte and by switching the measuring medium to a real system, i. e., commercially available human serum. The

---

experimental data demonstrated clearly that  $\text{Cu}^{2+}$ -sensing performance has been achieved in diluted HS-based electrolyte. Here, one part of HS was diluted with two parts of water in order to reduce deviations during the *IV*-measurements. In addition, the ionic transport is decreased upon exposure to  $\text{Cu}^{2+}$ -ions, indicating an inverted, i. e., sloping conductive readout is detected, in contrast to the measurements in aqueous electrolytes. This is because HS-samples contain human serum albumin (HSA) proteins. Further experiments were performed in HSA-based electrolytes displaying a sloping conductance trend only due to the HSA-presence. Albumin proteins offer a high affinity to copper ions to form an albumin-copper complex in the electrolyte upon  $\text{Cu}^{2+}$ -addition. Since the  $\text{Cu}^{2+}$ -binding domain of ATCUN was derived from the HSA-protein. Performing the  $\text{Cu}^{2+}$ -measurements assumes that the entire  $\text{Cu}^{2+}$ -albumin-pair is attached to the pore surface forming a sort of ATCUN- $\text{Cu}^{2+}$ -albumin sandwich-complex. Consequently, high  $\text{Cu}^{2+}$ -amount induces the adsorption of more and more  $\text{Cu}^{2+}$ -Albumin-moieties onto the ATCUN-modified pore surface and subsequent reduction in the current flow. This assumption harmonizes with the experimental data and explains sufficiently the contrary effect that occurred when the  $\text{Cu}^{2+}$ -series is measured in HS-based electrolytes instead of aqueous electrolytes.

Moreover, the selectivity and reversibility test determined the feasibility of specific  $\text{Cu}^{2+}$ -recognition. In addition, the stable signal readout was achieved upon exposing the membrane with EDTA-solution, indicating the reversible ATCUN- $\text{Cu}^{2+}$ -interaction even in presence of HSA-proteins.

Overall, the specific  $\text{Cu}^{2+}$ -detection in human serum was achieved by a sensitivity (detection area 100 fM - 1pM), essential selectivity towards other divalent metal ions ( $\text{Ni}^{2+}$ -and  $\text{Zn}^{2+}$ -ions) as well as reversible  $\text{Cu}^{2+}$ -binding interaction with the pore surface. In fact, the entire study was obtained on performing more than 200 single *IV*-measurements on one certain membrane which represented a stable and robust substrate and measurement method. In summary, the experimental data represent the successful and curtail proof-of-concept in the sense of using modified nanopore membranes as sensing devices in human body fluids for the early state diagnostic of diseases.

---

## CHAPTER VII: SUMMARY AND OUTLOOK

---

Nanopore-based devices have become one of the major impulses regarding biomolecular detection systems. However, the use of track etched nanopores is mainly performed on a basic research level and efforts towards clinical applications are still challenging. Therefore, this thesis deals with the scientific approach of track-etched nanopores for their applicability in real systems. Aiming the design of nanopore-based sensors, the investigations were performed by taking in account three main parts. CHAPTER IV deals with the investigations of the nanopore material itself. CHAPTER V was mainly focused on the development of novel analyte recognition mechanisms. Finally, CHAPTER VI describes the feasibility of nanopore-based analyte detection in real systems.

Firstly, the nanopore materials were investigated, because nanopore applications require substrate materials that enable reproducible nanopores fabrications regarding their geometrical dimensions and polymer etching abilities. Therefore, two different nanopore materials were examined and compared with the track-etched nanopore in standard PET-substrates irradiated at the GSI-facility (CHAPTER IV).

Here, the track-etching parameters of commercially available PET-membranes (*ip4ip S.A.*, Belgium) were investigated. The results showed discontinuous pores inside the membrane matrix, suggesting that the underlying latent ion tracks are less distinctive. It is assumed that the use of accelerated low energy argon ions provides insufficiently formed damaged zones that reinforce annealing effects after irradiation during the membrane storage. On the contrary, GSI-membranes exhibited good etching abilities even after the storage of several months and even years caused by the highly reactive latent tracks generated by swift heavy ion irradiation with gold-nuclei ( $\text{Au}^{26+}$ ). Overall, a track-to-bulk etching ratio was estimated to be around  $\sim 20:1$ , whereas GSI-membranes offer a track-to-bulk ratio of more than  $1000:1$ . Due to the insufficient etching behaviour, another strategy was tested to enable conical nanopores inside commercial membranes. For this purpose, etched membranes with cylindrical nanopores were purchased by the same company. Then, the membranes were post-treated from one side with DMF-solvent acting as a swelling agent. Afterwards, *IV*-measurements revealed a rectification behaviour of the former cylindrical pores indicating successful DMF-promoted conical pore shaping. Further, the DMF-treated membranes were modified with EDA-moieties to examine modification-features of commercial nanopores. As a result, the *IV*-curves provide an inversion of rectification indicating a successful attachment of positively charged EDA-moieties onto the pore surface. Overall, the generation of conical nanopores inside commercial membranes were established but the requirement of a post-shaping step promoted by hazardous DMF is not suitable for practical applications. With the use of commercial membranes, the demand of nanopore membranes for the economical application can be satisfied, but conical pores are only achievable with additional post-treatments.

Further, the fabrication of nanopore inside biodegradable membranes composed of poly(lactic acid) (PLA) was evaluated as possible eco-friendly substrates. The track-etching was screened by testing different etching conditions. Although various etchants, temperatures, concentrations and etching times were examined, no continuous pore formation was achieved, but cones of several  $\mu\text{m}$  size were obtained. The calculation of track-to-bulk etching ratio ( $v_t/v_b \sim 1.1$ ) revealed that no selective track etching occurred during the pore fabrication. It is suggested that amorphous regions inside biodegradable polymers are predominantly being responsible for the low track-etching rates. It is assumed that even irradiation of swift heavy ions do not provide

---

sufficient structural changes along the penetration track of the accelerated ions. In summary, non-selective track-to-bulk etching and, thus, no useful pore formation was obtained.

CHAPTER V deals with the development of unprecedented receptor-analyte interactions in order to magnify the limits of suitable biomarker detections with nanopores.

By modifying the nanopore surface with nickel-binding NTA-moieties, the label-free and selective detection of histamine was achieved with a detection limit in the submicromolar-range. Therefore, the nanopore-based histamine level detection serves as a powerful diagnostic tool, because histamine plays a critical role as neurotransmitter within the synaptic cleft of neurons being out of control in allergic reactions.

A further look on the neuronal system reveals the huge impact of potassium ions for the efficient neuronal signal transduction. Therefore, monitoring the potassium level provides important insights into neuropathological processes within the human body. In this context, the selective potassium ion detection was achieved by decorating the pore surface with oligoethylene glycol-moieties to monitor the potassium sensing performance with *IV*-measurements. Due to the pseudo-crown ether scaffold of the attached surface groups, the membrane was efficiently complexing potassium ions that provide specific changes in transmembrane ion current, while other alkali ions did not affect the transmembrane current. Overall, the potassium capturing with pseudo-crown ethers attached on the nanopore surface was successfully observed, and could be potentially expanded onto other alkali ions by simply varying the pseudo-crown size. Further, modification of nanopores was obtained by depositing polyelectrolyte layers inside nanopores. Through the Layer-by-Layer (LBL) technique, the alternating multilayers of cationic poly(allylamine hydrochloride) (PAH) and anionic poly(acrylic acid) (PAA) provided a step-wise reduction of effective pore diameter as evidenced by a step-wise decrease of ionic transport across the nanopore. However, by exposing the membrane to silver ions, specific reorganization occurred due to the formation of amino-silver complexes that enables a reorganisation of the LBL-structure as detected from the changes in transmembrane current. Further, the electrostatic LBL-deposition was extended to a three-component system by a supplementary deposition of poly(4-vinylpyridine)-moieties promoted by *H*-bridges. The resulting LBL-assembly is interconnected by EDC-coupling chemistry. On further pH-induced wash-out of PVP-moieties, the porous transition of interconnected layers occurs, which was successfully monitored by a gain of transmembrane current. In sum, the electrostatic-bounded LBL-modification enables the precise control inside the nanoconfined pore environment. Moreover, the transformation of LBL-assemblies into a covalent linkage with the nanopore surface along with the sacrificial use of PVP is considered as a proof-of-concept that can be implemented in stimuli-triggered release of drugs.

Further, an ultrasensitive and selective copper-detection was obtained by the covalent attachment of copper-binding peptide-motif (ATCUN) onto the nanopore surface. The experimental results demonstrated the sensitivity beyond nanomolar  $\text{Cu}^{2+}$ -concentrations and significant selectivity towards similar divalent cations like  $\text{Zn}^{2+}$ - and  $\text{Ni}^{2+}$ -ions. Additionally, *IV*-characteristics showed the sustainable re-usability of the ATCUN-modified pore, upon performing numerous cycles of  $\text{Cu}^{2+}$ -complexation and EDTA-induced  $\text{Cu}^{2+}$ -decomplexation. Overall, the ATCUN-study provides extraordinary sensitivity, excellent selectivity and high stability towards specific copper-recognition. Hence, copper ions level monitoring can provide useful information about the health level of patients, because copper ions regulate the complex plaque-formation within the human brain being well-known as one of the major symptoms of

---

ALZHEIMER's disease. Therefore, the ACTUN-promoted  $\text{Cu}^{2+}$ -recognition can be adapted as an early diagnosis method for neurodegenerative diseases.

However, when the diagnostic features are desired, the fundamental part of antibodies is indispensable being the central mechanism of detection biomarkers and pathogens in the human body. The antibody-antigen interaction is the core of the immune system and the base of numerous commercial diagnosis tests. The antibody size is in the several nanometre range, therefore, the precise anchoring of antibodies inside nanopores is challenging. Herein, nanobodies, which are defined as single domain antibodies, are suitable moieties to be attached on the pore surface as they combine beneficial size of few nanometres and display the same specificity toward the respective biomarkers as their larger relatives. In order to enable the covalent and highly directed attachment of nanobodies the use of a novel Tag/Catcher-system was investigated. Firstly, the Tag-component was decorated onto the pore surface. Then, by exposing the membrane to the Catcher-sequence carrying nanobody-structure, the spontaneous isopeptide-formation occurs between Tag- and Catcher-moieties, and causes an irreversible conjugation of the nanobody to the nanopore. To this end, nanobodies with high affinity towards fluorescent proteins were used as model systems and their successful interaction was evidenced by *IV*-measurements as well as with CLSM-imaging methods. Moreover, selectivity measurements were performed with protein analytes having similar protein sizes and scaffolds. The respective experimental data showed only the specific nanobody-protein interactions. The high selectivity was accompanied by a sensitivity over five order of magnitude in the nanomolar range suggesting future implementation of nanobody-promoted detections of analytes as a powerful candidate for clinical studies.

Aiming towards the medical application of nanopore-based biomolecular sensing, the feasible analyte detection requires reliable tests in real systems, which was described in CHAPTER VI.

In this context, the nanopore membranes were integrated in custom-made LOC-devices. The already investigated histamine detection method was implemented inside the LOC-surrounding using multiporous membranes. The sensitivity of the system revealed several construction problems and leaking effects of internal adhesive layers in the first generation of LOC-devices. Therefore, the manufacture was improved by using a more suitable bonding component and the respective results of the 2<sup>nd</sup> LOC-generation provided an adequate correlation between histamine concentration and changes in the transmembrane current in a nanomolar sensing range over three order of magnitudes. However, further improvements are still required to achieve more significant correlations between the analyte concentration and transmembrane current.

Furthermore, the medical use of nanopore based devices was tested with the desire of reliable analyte detections in real measuring media. For this purpose, the second part of CHAPTER VI is about the implementation of nanopore system for biomolecular recognitions inside human serum samples. For this purpose, nanopore membranes were decorated with ATCUN-moieties and the copper ion recognition was performed in human serum (HS)-based electrolytes. Remarkably, the experimental data show an inverted correlation of copper ions and ionic current in comparison to the water-based  $\text{Cu}^{2+}$ -measurements provided in Chapter V. It was suggested, that the HSA-presence could cause the inversed  $\text{Cu}^{2+}$ -current-correlation, because the human serum albumin (HSA) protein is the main ingredient of HS as well as the origin of the ATCUN-structure was adapted from HSA. Therefore, the entire  $\text{Cu}^{2+}$ -study was repeated in electrolyte solutions composed of human serum albumin and KCl electrolytes. As expected, the inverted correlation was reproduced, evidencing the special interfering role of HSA inside

---

nanopore-based detections. Nonetheless, the experimental data proved the successful detection of analytes inside human serum samples, serving as a starting point for further medical trials.

Aspiring future activities, this thesis brought the application of nanopore based biosensors one step further to implement them in medical application. However, there is still need for improvement.

Regarding the nanopore material, further tests should rely on commercial membranes to enable an upscaling of nanopore membranes. Hence, the application would require a higher plastic consumption. Therefore, future studies have to evaluate the feasibility to use and irradiate recycled PET-membranes as potential nanopore substrates.

The need of highly precise and specific detection of biomarkers is still unsatisfied. One promising tool is presented by using nanobodies as active receptors inside the nanopore. Their synthesis is already well-established and their affinity towards analytes provides not only maximum accuracy but is also adjustable. Therefore, nanobodies carrying affinities towards real biomarkers should be investigated and transferred to the nanopore regime. Further, the sufficient monitoring of the health state does not only depend on one single laboratory value. Therefore, research impulse should aim towards the simultaneous detection of multiple analytes using a nanopore membrane being functionalized with several receptors. Besides the detection of one specific biomarker, the focus relies on further related inflammation values, like the level of C-reactive protein. In this way, the practicability in the clinical surrounding would be enabled. In addition, analytical trials of nanopore-based receptor-analyte-interactions should be expanded towards measurements in the HS-based environment. Preliminary studies need be carried out in HS-samples of healthy probands but also HS-donations of real patients must be considered along with the aim of successful analyte detection inside full blood samples, presumably after blood filtration steps.

Moreover, the active biomarker detection inside Lab-on-Chip-(LOC) devices would be the goal in the frame of clinical studies. For this, the LOC-system must be transferred at first into a closed aperture to avoid contaminations of the samples during the measurement. Aiming the successful analyte detection inside full blood samples, the invention of suitable washing-features is also required.

In this context, the vision of a nanopore-based biosensor is achievable if above-mentioned challenges are sufficiently overcome.

---

## References

---

1. Miles, B. N.; Ivanov, A. P.; Wilson, K. A.; Doğan, F.; Japrun, D.; Edel, J. B. Single molecule sensing with solid-state nanopores: novel materials, methods, and applications. *Chemical Society reviews* **2013**, *42* (1), 15–28.
2. Lepoitevin, M.; Jamilloux, B.; Bechelany, M.; Balanzat, E.; Janot, J.-M.; Balme, S. Fast and reversible functionalization of a single nanopore based on layer-by-layer polyelectrolyte self-assembly for tuning current rectification and designing sensors. *RSC Adv.* **2016**, *6* (38), 32228–32233.
3. Jessell, T. M.; Kandel, E. R. Synaptic Transmission: A Bidirectional and Self-Modifiable Form of Cell-Cell Communication. *Cell* **1993**, *72*, 1.
4. Majd, S.; Yusko, E. C.; Billeh, Y. N.; Macrae, M. X.; Yang, J.; Mayer, M. Applications of biological pores in nanomedicine, sensing, and nanoelectronics. *Current opinion in biotechnology* **2010**, *21* (4), 439–476.
5. Bauer, W. R.; Nadler, W. Molecular transport through channels and pores: Effects of in-channel interactions and blocking. *PNAS* **2006**, *103* (31), 11446.
6. Bayley, H.; Cremer, P. S. Stochastic sensors inspired by biology. *Nature [Online]* **2001**, *413*, 226.
7. Astier, Y.; Bayley, H.; Howorka, S. Protein components for nanodevices. *Current opinion in chemical biology* **2005**, *9* (6), 576–584.
8. *Cambridge Dictionary*; Cambridge University Press, 4th: 2013.
9. ISO/TS 27687:2008 (E). *Nanotechnologies — Terminology and definitions for nano-objects — Nanoparticle, nanofibre and nanoplate*; International Organization for Standardization.
10. Eijsink, V. G. H.; Axelsson, L.; Diep, D. B.; Håvarstein, L. S.; Holo, H.; Nes, I. F. Production of class II bacteriocins by lactic acid bacteria; an example of biological warfare and communication. *Antonie van Leeuwenhoek* **2002**, *81* (1-4), 639–654.
11. Beckstein, O.; Sansom, Mark S. P. The influence of geometry, surface character, and flexibility on the permeation of ions and water through biological pores. *Phys. Biol.* **2004**, *1*, 42.
12. Fujiyoshi, Y.; Mitsuoka, K.; Groot, B. L. de; Philippsen, A.; Grubmüller, H.; Agre, P.; Engel, A. Structure and function of water channels. *Current opinion in structural biology* **2002**, *12* (4), 509.
13. Pérez-Mitta, G.; Albesa, A. G.; Trautmann, C.; Toimil-Molares, M. E.; Azzaroni, O. Bioinspired integrated nanosystems based on solid-state nanopores: "iontronic" transduction of biological, chemical and physical stimuli. *Chemical science* **2017**, *8* (2), 890–913.
14. Bertozzi, C.; Zimmermann, I.; Engeler, S.; Hilf, R. J. C.; Dutzler, R. Signal Transduction at the Domain Interface of Prokaryotic Pentameric Ligand-Gated Ion Channels. *PLoS biology* **2016**, *14* (3), e1002393.
15. Goswitz, V. C.; Brooker, R. J. Structural features of the uniporter/symporter/ antiporter superfamily. *Protein Sci.* **1995**, *4* (3), 534.
16. Beck, M.; Hurt, E. The nuclear pore complex: understanding its function through structural insight. *Nature reviews. Molecular cell biology* **2017**, *18* (2), 73–89.
17. Hediger, M. A.; Cléménçon, B.; Burrier, R. E.; Bruford, E. A. The ABCs of membrane transporters in health and disease (SLC series): Introduction | Elsevier Enhanced Reader. *Mol. Aspects Med.* **2013**, *34*, 95–107.
18. J. L. Popot and D. M. Engelman. Membrane protein folding and oligomerization: the two-stage model. *Biochemistry* **1990**, *29* (17), 4031–4037.
19. Steck, T. L. The Organization of Proteins in the Human Red Blood Cell Membrane. *J. Cell Biol.* **1974**, *62*, 1–19.
20. Seino, S. ATP-sensitive potassium channels: a model of heteromultimeric potassium channel/receptor assemblies. *Ann. Rev. Physiol.* **1999**, *61*, 337–362.
21. Simms, B. A.; Zamponi, G. W. Neuronal voltage-gated calcium channels: structure, function, and dysfunction. *Neuron* **2014**, *82* (1), 24–45.
22. Kellenberger, S.; Schild, L. Epithelial sodium channel/degnerin family of ion channels: a variety of functions for a shared structure. *Physiol. Rev.* **2002**, *82* (3), 735–767.
23. Keil, L. M. R.; Möller, F. M.; Kieß, M.; Kudella, P. W.; Mast, C. B. Proton gradients and pH oscillations emerge from heat flow at the microscale. *Nature communications* **2017**, *8* (1), 1897.
24. Mummert, H.; Gradmann, D. Action potentials in *Acetabularia*: measurement and simulation of voltage-gated fluxes. *The Journal of membrane biology* **1991**, *124* (3), 265–273.
25. Steller, L.; Kreir, M.; Salzer, R. Natural and artificial ion channels for biosensing platforms. *Analytical and bioanalytical chemistry* **2012**, *402* (1), 209–230.
26. Dryer, S. E. Na<sup>+</sup>-activated K<sup>+</sup> channels: a new family of large-conductance ion channels ion channels. *Trends Neurosci.* **1994**, *17* (4), 155–160.

- 
27. Hamill, O. P.; Marty, A.; Neher, E.; Sakmann, B.; Sigworth, F. J. Improved patch-clamp techniques for high-resolution current recording from cells and cell-free membrane patches. *Pflugers Archiv : European journal of physiology* **1981**, *391* (2), 85–100.
  28. Sakmann, B.; Neher, E. Patch Clamp Techniques for Studying Ionic Channels in Excitable Membranes. *Annu. Rev. Physiol.* **1984**, *46*, 455–472.
  29. Collingridge, G. L.; Olsen, R. W.; Peters, J.; Spedding, M. A nomenclature for ligand-gated ion channels | Elsevier Enhanced Reader. *Neuropharmacology* **2009**, *56* (1), 2–5.
  30. Unwin, N. Neurotransmitter Action: Opening of Ligand-Gated Ion Channels. *Cell [Online]* **1993**, *72*, 31–41.
  31. Chen, M.; Khalid, S.; Sansom, M. S. P.; Bayley, H. Outer membrane protein G: Engineering a quiet pore for biosensing. *PNAS* **2008**, *105* (17), 6272–6277.
  32. Venkatesan, B. M.; Bashir, R. Nanopore sensors for nucleic acid analysis. *Nat. Nanotechnol.* **2011**, *6* (10), 615–624.
  33. Bill, R. M.; Henderson, P. J. F.; Iwata, S.; Kunji, E. R. S.; Michel, H.; Neutze, R.; Newstead, S.; Poolman, B.; Tate, C. G.; Vogel, H. Overcoming barriers to membrane protein structure determination. *Nature biotechnology* **2011**, *29* (4), 335–340.
  34. Saeui, C. T.; Mathew, M. P.; Liu, L.; Urias, E.; Yarema, K. J. Cell Surface and Membrane Engineering: Emerging Technologies and Applications. *Journal of functional biomaterials* **2015**, *6* (2), 454–485.
  35. Jackman, J.; Knoll, W.; Cho, N.-J. Biotechnology Applications of Tethered Lipid Bilayer Membranes. *Materials* **2012**, *5* (12), 2637–2657.
  36. Köper, I. Insulating tethered bilayer lipid membranes to study membrane proteins. *Molecular bioSystems* **2007**, *3* (10), 651–657.
  37. Hou, X.; Jiang, L. Learning from nature: building bio-inspired smart nanochannels. *ACS nano* **2009**, *3* (11), 3339–3342.
  38. Kowalczyk, S. W.; Blosser, T. R.; Dekker, C. Biomimetic nanopores: learning from and about nature. *Trends in biotechnology* **2011**, *29* (12), 607–614.
  39. Dekker, C. Solid-state nanopores. *Nat. Nanotechnol.* **2007**, *2* (4), 209–215.
  40. Storm, A. J.; Chen, J. H.; Ling, X. S.; Zandbergen, H. W.; Dekker, C. Fabrication of solid-state nanopores with single-nanometre precision. *Nature materials* **2003**, *2* (8), 537–540.
  41. Balme, S.; Janot, J.-M.; Berardo, L.; Henn, F.; Bonhenry, D.; Kraszewski, S.; Picaud, F.; Ramseyer, C. New bioinspired membrane made of a biological ion channel confined into the cylindrical nanopore of a solid-state polymer. *Nano letters* **2011**, *11* (2), 712–716.
  42. Zhang, H.; Tian, Y.; Jiang, L. From symmetric to asymmetric design of bio-inspired smart single nanochannels. *Chem. Commun.* **2013**, *49* (86), 10048.
  43. Wanunu, M.; Meller, A. Chemically modified solid-state nanopores. *Nano letters* **2007**, *7* (6), 1580–1585.
  44. Tang, Z.; Lu, B.; Zhao, Q.; Wang, J.; Luo, K.; Yu, D. Surface modification of solid-state nanopores for sticky-free translocation of single-stranded DNA. *Small (Weinheim an der Bergstrasse, Germany)* **2014**, *10* (21), 4332–4339.
  45. Lepoitevin, M.; Ma, T.; Bechelany, M.; Janot, J.-M.; Balme, S. Functionalization of single solid state nanopores to mimic biological ion channels: A review. *Adv. Colloid Interface Sci.* **2017**, *250*, 195–213
  46. Chen, Q.; Liu, Z. Fabrication and Applications of Solid-State Nanopores. *Sensors (Basel, Switzerland)* **2019**, *19* (8), 1886 (1-29).
  47. Zhang, Q.; Cheng, Y.; Cao, P.; Gu, Z. Solid-state nanopores for ion and small molecule analysis. *Chinese Chemical Letters* **2019**, *30* (9), 1607–1617.
  48. van den Berg, A.; Wessling, M. Silicon for the perfect membrane. *Nature* **2007**, *445*, 726.
  49. Lee, W.; Park, S.-J. Porous anodic aluminum oxide: anodization and templated synthesis of functional nanostructures. *Chem. Rev.* **2014**, *114* (15), 7487–7556.
  50. Gierak, J.; Madouri, A.; Bianche, A. L.; Bourhis, E.; Patriarche, G.; Ulysse, C.; Lucot, D.; Lafosse, X.; Auvray, L.; Bruchhaus, L.; Jede, R. Sub-5nm FIB direct patterning of nanodevices. *Microelectronic Engineering* **2007**, *84* (5-8), 779–783.
  51. Bianche, A.-L.; Gierak, J.; Bourhis, É.; Madouri, A.; Lafosse, X.; Patriarche, G.; Oukhaled, G.; Ulysse, C.; Galas, J.-C.; Chen, Y.; Auvray, L. Focused ion beam sculpted membranes for nanoscience tooling. *Microelectronic Engineering* **2006**, *83* (4-9), 1474–1477.
  52. Farimani, A. B.; Min, K.; Aluru, N. R. DNA base detection using a single-layer MoS<sub>2</sub>. *ACS nano* **2014**, *8* (8), 7914–7922.
  53. White, R. J.; Ervin, E. N.; Yang, T.; Chen, X.; Daniel, S.; Cremer, P. S.; White, H. S. Single ion-channel recordings using glass nanopore membranes. *J. Am. Chem. Soc.* **2007**, *129* (38), 11766–11775.
-

54. Wei, C.; Bard, A. J.; Feldberg, S. W. Current Rectification at Quartz Nanopipet Electrodes. *Anal. Chem.* **1997**, *69* (2), 4627-4633.
55. Zhang, Z.; Wen, L.; Jiang, L. Bioinspired smart asymmetric nanochannel membranes. *Chemical Society reviews* **2018**, *47* (2), 322–356.
56. Jiang, Z.; Mihovilovic, M.; Chan, J.; Stein, D. Fabrication of nanopores with embedded annular electrodes and transverse carbon nanotube electrodes. *Journal of physics. Condensed matter : an Institute of Physics journal* **2010**, *22* (45), 454114.
57. Liu, Z. Trapping sound at corners. *Nature materials* **2019**, *18* (2), 98–99.
58. Ali, M.; Yameen, B.; Neumann, R.; Ensinger, W.; Knoll, W.; Azzaroni, O. Biosensing and supramolecular bioconjugation in single conical polymer nanochannels. Facile incorporation of biorecognition elements into nanoconfined geometries. *J. Am. Chem. Soc.* **2008**, *130* (48), 16351–16357.
59. Chuah, K.; Wu, Y.; Vivekchand, S. R. C.; Gaus, K.; Reece, P. J.; Micolich, A. P.; Gooding, J. J. Nanopore blockade sensors for ultrasensitive detection of proteins in complex biological samples. *Nature communications* **2019**, *10* (1), 2109.
60. Haque, F.; Li, J.; Wu, H.-C.; Liang, X.-J.; Guo, P. Solid-State and Biological Nanopore for Real-Time Sensing of Single Chemical and Sequencing of DNA. *Nano today* **2013**, *8* (1), 56–74.
61. Siwy, Z.; Trofin, L.; Kohli, P.; Baker, L. A.; Trautmann, C.; Martin, C. R. Protein biosensors based on biofunctionalized conical gold nanotubes. *J. Am. Chem. Soc.* **2005**, *127* (14), 5000–5001.
62. Wang, J.; Hou, J.; Zhang, H.; Tian, Y.; Jiang, L. Single Nanochannel-Aptamer-Based Biosensor for Ultrasensitive and Selective Cocaine Detection. *ACS Appl. Mater. Interfaces* **2018**, *10* (2), 2033–2039.
63. Heins, E. A.; Siwy, Z. S.; Baker, L. A.; Martin, C. R. Detecting single porphyrin molecules in a conically shaped synthetic nanopore. *Nano Lett.* **2005**, *5* (9), 1824–1829.
64. Ali, M.; Ramirez, P.; Duznovic, I.; Nasir, S.; Mafe, S.; Ensinger, W. Label-free histamine detection with nanofluidic diodes through metal ion displacement mechanism. *Colloids Surf., B* **2017**, *150*, 201–208.
65. Harrell, C. C.; Choi, Y.; Horne, L. P.; Baker, L. A.; Siwy, Z. S.; Martin, C. R. Resistive-pulse DNA detection with a conical nanopore sensor. *Langmuir* **2006**, *22* (25), 10837–10843.
66. Fischer, N. O.; Tarasow, T. M.; Tok, J. B.-H. Protein detection via direct enzymatic amplification of short DNA aptamers. *Anal. Biochem.* **2008**, *373* (1), 121–128.
67. Tian, Y.; Hou, X.; Wen, L.; Guo, W.; Song, Y.; Sun, H.; Wang, Y.; Jiang, L.; Zhu, D. A biomimetic zinc activated ion channel. *Chem. Commun.* **2010**, *46* (10), 1682–1684.
68. Ali, M.; Ahmed, I.; Ramirez, P.; Nasir, S.; Mafe, S.; Niemeyer, C. M.; Ensinger, W. Lithium Ion Recognition with Nanofluidic Diodes through Host-Guest Complexation in Confined Geometries. *Anal. Chem.* **2018**, *90* (11), 6820–6826.
69. Fleischer, R. L.; Price, P. B.; Symes, E. M. Novel Filter for Biological Materials. *Science (New York, N.Y.)* **1964**, *143* (3603), 249–250.
70. Apel, P. Track etching technique in membrane technology. *Radiation Measurements* **2001**, *34*, 559–566.
71. Ferain, E.; Legras, R. Efficient production of nanoporous particle track etched membranes with controlled properties. *Radiat. Meas.* **2001**, *34* (1-6), 585–588.
72. Ali, M.; Schiedt, B.; Healy, K.; Neumann, R.; Ensinger, W. Modifying the surface charge of single track-etched conical nanopores in polyimide. *Nanotechnology* **2008**, *19* (8), 85713.
73. Kravets L. I.; Dmitriev S. N.; Apel P. Yu. Production and Properties of Polypropylene Track Membranes. *Collect. Czech. Commun.* **1997**, *62*, 752.
74. Apel, P. Y.; Ramirez, P.; Blonskaya, I. V.; Orelovitch, O. L.; Sartowska, B. A. Accurate characterization of single track-etched, conical nanopores. *Physical chemistry chemical physics : PCCP* **2014**, *16* (29), 15214–15223.
75. Cornelius, T. W.; Apel, P. Y.; Schiedt, B.; Trautmann, C.; Toimil-Molares, M. E.; Karim, S.; Neumann, R. Investigation of nanopore evolution in ion track-etched polycarbonate membranes. *Nuclear Instruments and Methods in Physics Research Section B: Beam Interactions with Materials and Atoms* **2007**, *265* (2), 553–557
76. Nguyen, G.; Howorka, S.; Siwy, Z. S. DNA strands attached inside single conical nanopores: ionic pore characteristics and insight into DNA biophysics. *The Journal of membrane biology* **2011**, *239* (1-2), 105–113.
77. Apel, P. Y. Fabrication of functional micro- and nanoporous materials from polymers modified by swift heavy ions. *Radiation Physics and Chemistry* **2019**, *159*, 25–34.
78. Siwy, Z.; Apel, P.; Dobrev, D.; Neumann, R.; Spohr, R.; Trautmann, C.; Voss, K. Ion transport through asymmetric nanopores prepared by ion track etching. *Nucl. Instrum. Methods Phys. Res., Sect. B* **2003**, *208*, 143–148.

- 
79. Toimil-Molares, M. E. Characterization and properties of micro- and nanowires of controlled size, composition, and geometry fabricated by electrodeposition and ion-track technology. *Beilstein journal of nanotechnology* **2012**, *3*, 860–883.
  80. Adla, A.; Fuess, H.; Trautmann, C. Characterization of heavy ion tracks in polymers by transmission electron microscopy. *Journal of Polymer Science: Part B: Polymer Physics* **2003**, *41*, 2982–2901.
  81. Ziegler, J. F.; Ziegler, M. D.; Biersack, J. P. SRIM – The stopping and range of ions in matter (2010). *Nuclear Instruments and Methods in Physics Research Section B: Beam Interactions with Materials and Atoms* **2010**, *268* (11–12), 1818–1823.
  82. *Applications of ionizing radiation in materials processing*; Sun, Y., Chmielewski, A. G., Eds.; Institute of Nuclear Chemistry and Technology: Warszawa, **2017**.
  83. Siwy, Z.; Fuliński, A. Fabrication of a synthetic nanopore ion pump. *Physical review letters* **2002**, *89* (19), 198103.
  84. Apel, P.Y.; Blonskaya, I. V.; Orelovitch, O. L.; Dmitriev, S. N. Diode-like ion-track asymmetric nanopores: Some alternative methods of fabrication. *Nuclear Instruments and Methods in Physics Research Section B: Beam Interactions with Materials and Atoms* **2009**, *267* (6), 1023–1027.
  85. Cornelius, T. W.; Schiedt, B.; Severin, D.; Pépy, G.; Toulemonde, M.; Apel, P. Y.; Boesecke, P.; Trautmann, C. Nanopores in track-etched polymer membranes characterized by small-angle x-ray scattering. *Nanotechnology* **2010**, *21* (15), 155702.
  86. Trautmann, C.; Bruechle, W.; Spohr, R.; Vetter, J.; Angert, N. Pore geometry of etched ion tracks in polyimide. *Nuclear Instruments and Methods in Physics Research B* **1996**, *111*, 70–74.
  87. Ferain, E.; Legras, R. Pore shape control in nanoporous particle track etched membrane. *Nucl. Instrum. Methods Phys. Res., Sect. B* **2001**, *174* (1–2), 116–122.
  88. Apel, P. Y.; Blonskaya, I. V.; Orelovitch, O. L.; Ramirez, P.; Sartowska, B. A. Effect of nanopore geometry on ion current rectification. *Nanotechnology* **2011**, *22* (17), 175302.
  89. Nguyen, Q. H.; Ali, M.; Bayer, V.; Neumann, R.; Ensinger, W. Charge-selective transport of organic and protein analytes through synthetic nanochannels. *Nanotechnology* **2010**, *21* (36), 365701.
  90. Spohr, R. Etch hints for polymers with high track-etch-rate.PDF. European Research Training Network EuNITT **2014**, 1–10.
  91. Apel, P. Y.; Blonskaya, I. V.; Lizunov, N. E.; Olejniczak, K.; Orelovitch, O. L.; Sartowska, B. A.; Dmitriev, S. N. Asymmetrical nanopores in track membranes: Fabrication, the effect of nanopore shape and electric charge of pore walls, promising applications. *Russ J Electrochem* **2017**, *53* (1), 58–69.
  92. Ali, M.; Ramirez, P.; Nguyen, H. Q.; Nasir, S.; Cervera, J.; Mafe, S.; Ensinger, W. Single cigar-shaped nanopores functionalized with amphoteric amino acid chains: experimental and theoretical characterization. *ACS nano* **2012**, *6* (4), 3631–3640.
  93. Scopece, P.; Baker, L. A.; Ugo, P.; Martin, C. R. Conical nanopore membranes: solvent shaping of nanopores. *Nanotechnology* **2006**, *17* (15), 3951–3956.
  94. Mo, D.; Liu, J. D.; Duan, J. L.; Yao, H. J.; Latif, H.; Cao, D. L.; Chen, Y. H.; Zhang, S. X.; Zhai, P. F.; Liu, J. Fabrication of different pore shapes by multi-step etching technique in ion-irradiated PET membranes. *Nuclear Instruments and Methods in Physics Research Section B: Beam Interactions with Materials and Atoms* **2014**, *333*, 58–63.
  95. Xiao, K.; Chen, L.; Xie, G.; Li, P.; Kong, X.-Y.; Wen, L.; Jiang, L. A bio-inspired dumbbell-shaped nanochannel with a controllable structure and ionic rectification. *Nanoscale* **2018**, *10* (15), 6850–6854.
  96. Gilles, F. M.; Tagliazucchi, M.; Azzaroni, O.; Szleifer, I. Ionic Conductance of Polyelectrolyte-Modified Nanochannels: Nanoconfinement Effects on the Coupled Protonation Equilibria of Polyprotic Brushes. *J. Phys. Chem. C* **2016**, *120* (9), 4789–4798.
  97. Huffmann, K. R.; Casey, D. J. Effect of carboxyl end groups on hydrolysis of polyglycolic acid. *Journal of Polymer Science: Polymer Chemistry* **1985**, *23*, 1939–1954.
  98. *Chemically Modified Nanopores and Nanochannels. Chapter 2: Theoretical Basis for Structure and Transport in Nanopores and Nanochannels*; Tagliazucchi, M., Szleifer, I., Eds.; Elsevier, **2017**.
  99. Bard, A. J.; Faulkner, L. R. *Electrochemical Methods: Fundamentals and Applications*, 2nd ed.; John Wiley & Sons: New York, **2001**.
  100. Akoum, F.; Parodi, O. Electrostatic interactions inside the aqueous core of spherical reversed micelles (L2 phase). *J. Phys. France* **1985**, *46* (10), 1675–1681.
  101. Ali, M.; Ramirez, P.; Tahir, M. N.; Mafe, S.; Siwy, Z.; Neumann, R.; Tremel, W.; Ensinger, W. Biomolecular conjugation inside synthetic polymer nanopores via glycoprotein-lectin interactions. *Nanoscale* **2011**, *3* (4), 1894–1903.
-

102. Harrell, C. C.; Kohli, P.; Siwy, Z.; Martin, C. R. DNA-nanotube artificial ion channels. *Journal of the American Chemical Society* **2004**, *126* (48), 15646–15647.
103. Wei, R.; Gatterdam, V.; Wieneke, R.; Tampé, R.; Rant, U. Stochastic sensing of proteins with receptor-modified solid-state nanopores. *Nature nanotechnology* **2012**, *7* (4), 257–263.
104. Tagliazucchi, M.; Szleifer, I. Transport mechanisms in nanopores and nanochannels: can we mimic nature? *Mater. Today* **2015**, *18* (3), 131–142.
105. Ali, M.; Neumann, R.; Ensinger, W. Sequence-specific recognition of DNA oligomer using peptide nucleic acid (PNA)-modified synthetic ion channels: PNA/DNA hybridization in nanoconfined environment. *ACS nano* **2010**, *4* (12), 7267–7274.
106. Vlassioux, I.; Kozel, T. R.; Siwy, Z. S. Biosensing with nanofluidic diodes. *Journal of the American Chemical Society* **2009**, *131* (23), 8211–8220.
107. Ali, M.; Mafe, S.; Ramirez, P.; Neumann, R.; Ensinger, W. Logic gates using nanofluidic diodes based on conical nanopores functionalized with polyprotic acid chains. *Langmuir : the ACS journal of surfaces and colloids* **2009**, *25* (20), 11993–11997.
108. Sun, Z.; Han, C.; Song, M.; Wen, L.; Tian, D.; Li, H.; Jiang, L. Fabrication of cysteine-responsive biomimetic single nanochannels by a thiol-yne reaction strategy and their application for sensing in urine samples. *Advanced materials (Deerfield Beach, Fla.)* **2014**, *26* (3), 455–460.
109. Cho, K. L.; Lomas, H.; Hill, A. J.; Caruso, F.; Kentish, S. E. Spray assembled, cross-linked polyelectrolyte multilayer membranes for salt removal. *Langmuir : the ACS journal of surfaces and colloids* **2014**, *30* (29), 8784–8790.
110. Coceancigh, H.; Tran-Ba, K.-H.; Siepser, N.; Baker, L. A.; Ito, T. Longitudinally Controlled Modification of Cylindrical and Conical Track-Etched Poly(ethylene terephthalate) Pores Using an Electrochemically Assisted Click Reaction. *Langmuir : the ACS journal of surfaces and colloids* **2017**, *33* (43), 11998–12006.
111. Ali, M.; Yameen, B.; Cervera, J.; Ramírez, P.; Neumann, R.; Ensinger, W.; Knoll, W.; Azzaroni, O. Layer-by-layer assembly of polyelectrolytes into ionic current rectifying solid-state nanopores: insights from theory and experiment. *Journal of the American Chemical Society* **2010**, *132* (24), 8338–8348.
112. Azzaroni, O.; Lau, K. H. A. Layer-by-Layer Assemblies in Nanoporous Templates: Nano-Organized Design and Applications of Soft Nanotechnology. *Soft matter [Online]* **2011**, *7* (19), 8709–8724.
113. Alem, H.; Duwez, A.-S.; Lussis, P.; Lipnik, P.; Jonas, A. M.; Demoustier-Champagne, S. Microstructure and thermo-responsive behaviour of poly(N-isopropylacrylamide) brushes grafted in nanopores of track-etched membranes. *Journal of Membrane Science* **2008**, *308* (1-2), 75–86..
114. Jirage, K. B. Nanotubule-Based Molecular-Filtration Membranes. *Science* **1997**, *278* (5338), 655–658.
115. Kohli, P.; Harrell, C. C.; Cao, Z.; Gasparac, R.; Tan, W.; Martin, C. R. DNA-functionalized nanotube membranes with single-base mismatch selectivity. *Science (New York, N.Y.)* **2004**, *305* (5686), 984–986.
116. Martin, C. R.; Nishizawa, M.; Jirage K.; Kang, M.; Lee, S. B. Controlling Ion-Transport Selectivity in Gold Nanotubule Membranes. *Adv. Mater.* **2001**, *13* (18), 1351–1362.
117. Zhang, X.-J.; Wang, X.-W.; Da, X.-D.; Shi, Y.; Liu, C.; Sun, F.; Yang, S.; Zhang, W.-B. A Versatile and Robust Approach to Stimuli-Responsive Protein Multilayers with Biologically Enabled Unique Functions. *Biomacromolecules* **2018**, *19* (3), 1065–1073.
118. Wang, J.; Martin, C. R. A new drug-sensing paradigm based on ion-current rectification in a conically shaped nanopore. *Nanomedicine (London, England)* **2008**, *3* (1), 13–20.
119. Wharton, J. E.; Jin, P.; Sexton, L. T.; Horne, L. P.; Sherrill, S. A.; Mino, W. K.; Martin, C. R. A method for reproducibly preparing synthetic nanopores for resistive-pulse biosensors. *Small (Weinheim an der Bergstrasse, Germany)* **2007**, *3* (8), 1424–1430.
120. Siwy, Z. S. Ion-Current Rectification in Nanopores and Nanotubes with Broken Symmetry. *Adv. Funct. Mater.* **2006**, *16* (6), 735–746.
121. Ali, M.; Ahmed, I.; Ramirez, P.; Nasir, S.; Mafe, S.; Niemeyer, C. M.; Ensinger, W. A redox-sensitive nanofluidic diode based on nicotinamide-modified asymmetric nanopores. *Sensors and Actuators B: Chemical* **2017**, *240*, 895–902.
122. M. Ali; W. Ensinger; R. Neumann; B. Schiedt; GSI; Darmstadt; Germany. Chemical Modification of track-etched dingle conical nanopores inducing inversed inner wall polarity **2007**, 1–2.
123. Lepoitevin, M.; Bechelany, M.; Balanzat, E.; Janot, J.-M.; Balme, S. Non-Fluorescence label protein sensing with track-etched nanopore decorated by avidin/biotin system. *Electrochimica Acta* **2016**, *211*, 611–618.
124. Gamry Instruments (2020): "Basics of Electrochemical Impedance Spectroscopy"; URL: <https://www.gamry.com/application-notes/EIS/basics-of-electrochemical-impedance-spectroscopy/> (Assesed on 10<sup>th</sup> January 2020).

- 
125. Apel, P. Y.; Bashevoy, V. V.; Blonskaya, I. V.; Lizunov, N. E.; Orelovitch, O. L.; Trautmann, C. Shedding light on the mechanism of asymmetric track etching: an interplay between latent track structure, etchant diffusion and osmotic flow. *Physical chemistry chemical physics: PCCP* **2016**, *18* (36), 25421–25433.
  126. Scully, J. R.; Silverman, D. C.; Kendig, M. W. *Electrochemical impedance : analysis and interpretation*, ASTM STP 118; American Society for Testing and Materials: Philadelphia, Pa, **1993**.
  127. Das deutsche zentrum für Luft- und Raumfahrttechnik (2012); "Wagner, N. Einführung in die elektrochemische Impedanzspektroskopie (EIS). " URL: [https://elib.dlr.de/89946/1/DLR\\_Wagner\\_EIS\\_Grundlagen\\_und\\_Anwendungen.pdf](https://elib.dlr.de/89946/1/DLR_Wagner_EIS_Grundlagen_und_Anwendungen.pdf) (Assesed on 12th January 2020).
  128. Chien, M.-C.; Wang, G.-J.; Yu, M.-C. Nanopore Size Estimation by Electrochemical Impedance Spectroscopy Analysis. *Jap. Journal of Applied Physics* **2008**, *47* (9), 7459–7463.
  129. Kant, K.; Yu, J.; Priest, C.; Shapter, J. G.; Losic, D. Impedance nanopore biosensor: influence of pore dimensions on biosensing performance. *The Analyst* **2014**, *139* (5), 1134–1140.
  130. MacDonald, M. A.; Andreas, H. A. Method for equivalent circuit determination for electrochemical impedance spectroscopy data of protein adsorption on solid surfaces. *Electrochimica Acta* **2014**, *129*, 290–299.
  131. MacDonald, M. A.; Andreas, H. A. Impact of Electrochemical Impedance Spectroscopy Experimental Variables on Adsorbed Protein Films, as Illustrated by Bovine Serum Albumin. *Electroanalysis* **2015**, *27* (8), 1944–1951.
  132. Ma, T.; Balanzat, E.; Janot, J.-M.; Balme, S. Single conical track-etched nanopore for a free-label detection of OSCS contaminants in heparin. *Biosensors & bioelectronics* **2019**, *137*, 207–212.
  133. United Nations (2019): "17 Goals to Transform Our World" URL: <https://www.un.org/sustainabledevelopment/> (assessed on 15<sup>th</sup> December 2019).
  134. McClure, P.; Elnakib, A.; Abou El-Ghar, M.; Khalifa, F.; Soliman, A.; El-Diasty, T.; Suri, J. S.; Elmaghraby, A.; El-Baz, A. In-vitro and in-vivo diagnostic techniques for prostate cancer: a review. *Journal of biomedical nanotechnology* **2014**, *10* (10), 2747–2777.
  135. Webb, A. *Introduction to Biomedical Imaging*; John Wiley @ Sons: Piscataway, 2003.
  136. Talagala, S. L.; Lowe, I. J. Introduction to magnetic resonance imaging. *Concepts Magn. Reson.* **1991**, *3*, 145–159.
  137. Brown, B.; Adhikari, S.; Marx, J.; Lander, L.; Todd, G. L. Introduction of ultrasound into gross anatomy curriculum: perceptions of medical students. *The Journal of emergency medicine* **2012**, *43* (6), 1098–1102.
  138. Chi, X.; Huang, D.; Zhao, Z.; Zhou, Z.; Yin, Z.; Gao, J. Nanoprobes for in vitro diagnostics of cancer and infectious diseases. *Biomaterials* **2012**, *33* (1), 189–206.
  139. Luppa, P. B.; Müller, C.; Schlichtiger, A.; Schlebusch, H. Point-of-care testing (POCT): Current techniques and future perspectives. *TrAC Trends in Analytical Chemistry* **2011**, *30* (6), 887–898.
  140. Jia, C.-P.; Zhong, X.-Q.; Hua, B.; Liu, M.-Y.; Jing, F.-X.; Lou, X.-H.; Yao, S.-H.; Xiang, J.-Q.; Jin, Q.-H.; Zhao, J.-L. Nano-ELISA for highly sensitive protein detection. *Biosensors & bioelectronics* **2009**, *24* (9), 2836–2841.
  141. Suzuki, K.; Sawada, T.; Murakami, A.; Matsui, T.; Tohma, S.; Nakazono, K.; Takemura, M.; Takasaki, Y.; Mimori, T.; Yamamoto, K. High diagnostic performance of ELISA detection of antibodies to citrullinated antigens in rheumatoid arthritis. *Scandinavian journal of rheumatology* **2003**, *32* (4), 197–204.
  142. Voller, A.; Bartlett, A.; Bidwell, D. E.; Clark, M. F.; Adams, A. N. The Detection of Viruses by Enzyme-Linked Immunosorbent Assay (ELISA). *J. Gen. Virol.* **33**, 1976, 165–167.
  143. Swart, N.; Pool, E. Rapid detection of selected steroid hormones from sewage effluents using an ELISA in the Kuils River water catchment area, South Africa. *Journal of immunoassay & immunochemistry* **2007**, *28* (4), 395–408.
  144. Valli, H. A competitive ELISA to detect brevetoxins from *Karenia brevis* (formerly *Gymnodinium breve*) in seawater, shellfish, and mammalian body fluid. *Environ. Health Perspect.* **2002**, *110* (2), 179–185.
  145. Ubeira, F. M.; Muiño, L.; Valero, M. A.; Periago, M. V.; Pérez-Crespo, I.; Mezo M., González-Warleta, M.; Romarís, F.; Paniagua, E.; Cortizo, S.; Llovo, J.; Más-Coma, S. MM3-ELISA Detection of Fasciola hepatica Coproantigens in Preserved Human Stool Samples. *Am. J. Trop. Med. Hyg.* **2009**, *81* (1), 156–168.
  146. Hulanicki, A.; Geab, S.; Ingman, F. Chemical Sensors: Definitions and Classification. *Pure Appl. Chem.* **1991**, *63* (9), 1247–1250.
  147. Stetter, J. R.; Penrose, W. R.; Yao, S. Sensors, Chemical Sensors, Electrochemical Sensors, and ECS. *Journal of the Electrochemical Society* **2003**, *150* (2), 11–16.
  148. Mehrotra, P. Biosensors and their applications - A review. *Journal of oral biology and craniofacial research* **2016**, *6* (2), 153–159.
  149. Sawant, S. N. Development of Biosensors From Biopolymer Composites. *Biopolymer Composites in Electronics*; Elsevier, **2017**; 353–383.
-

- 
150. *Metal oxide nanostructures and their applications*; Umar, A., Hahn, Y.-B., Eds.; Nanotechnology book series 25; American Scientific Publ: Los Angeles, Calif., **2010**.
151. Altshuler, B. Modeling of dose-response relationships. *Environmental Health Perspectives* **1981**, *42*, 23–27.
152. Ponamoreva, O. N.; Kamanina, O. A.; Alferov, V. A.; Machulin, A. V.; Rogova, T. V.; Arlyapov, V. A.; Alferov, S. V.; Suzina, N. E.; Ivanova, E. P. Yeast-based self-organized hybrid bio-silica sol-gels for the design of biosensors. *Biosensors & bioelectronics* **2015**, *67*, 321–326.
153. *Top 15 der umsatzstärksten Segmente der globalen Medizintechnikindustrie\* im Jahr 2017 und Prognose für das Jahr 2024 (in Milliarden US-Dollar).*" Statista Chart, 26th **2018**.
154. **Luppa, P. B.; Schlebusch, H. POCT. Patientennahe Labordiagnostik, 1. Aufl.; Springer-Verlag: s.l., 2008.**
155. Vashist, S. K.; Luong, J. H. T. An Overview of Point-of-Care Technologies Enabling Next-Generation Healthcare Monitoring and Management. In *Point-of-Care Technologies Enabling Next-Generation Healthcare Monitoring and Management*; Vashist, S. K., Luong, J. H.T., Eds.; Springer International Publishing: Cham, **2019**; 1–25.
156. Hawkins, R. C. Laboratory Turnaround Time: Clin Biochem Rev Vol 28 November 2007. *Clin. Biochem. Rev.* **2007**, *28* (4), 179–194.
157. Bishop, J. D.; Hsieh, H. V.; Gasperino, D. J.; Weigl, B. H. Sensitivity enhancement in lateral flow assays: a systems perspective. *Lab on a chip* **2019**, *19* (15), 2486–2499.
158. Yetisen, A. K.; Akram, M. S.; Lowe, C. R. Paper-based microfluidic point-of-care diagnostic devices. *Lab on a chip* **2013**, *13* (12), 2210–2251.
159. Hu, J.; Wang, S.; Wang, L.; Li, F.; Pingguan-Murphy, B.; Lu, T. J.; Xu, F. Advances in paper-based point-of-care diagnostics. *Biosensors & bioelectronics* **2014**, *54*, 585–597.
160. Mudanyali, O.; Dimitrov, S.; Sikora, U.; Padmanabhan, S.; Navruz, I.; Ozcan, A. Integrated rapid-diagnostic-test reader platform on a cellphone. *Lab on a chip* **2012**, *12* (15), 2678–2686.
161. Vashist, S. K.; Luppa, P. B.; Yeo, L. Y.; Ozcan, A.; Luong, J. H. T. Emerging Technologies for Next-Generation Point-of-Care Testing. *Trends in biotechnology* **2015**, *33* (11), 692–705.
162. Drese, K. S. „Lab on a Chip“. *Wien klin Mag* **2019**, *22* (4), 172–177.
163. Chin, C. D.; Linder, V.; Sia, S. K. Commercialization of microfluidic point-of-care diagnostic devices. *Lab on a chip* **2012**, *12* (12), 2118–2134.
164. Nge, P. N.; Rogers, C. I.; Woolley, A. T. Advances in microfluidic materials, functions, integration, and applications. *Chemical reviews* **2013**, *113* (4), 2550–2583.
165. Neoh, K. H.; Hassan, A. A.; Chen, A.; Sun, Y.; Liu, P.; Xu, K.-F.; Wong, A. S. T.; Han, R. P. S. Rethinking liquid biopsy: Microfluidic assays for mobile tumor cells in human body fluids. *Biomaterials* **2018**, *150*, 112–124.
166. Manz, A.; Graber, N.; Widmer, H. M. Miniaturized total chemical analysis systems: A novel concept for chemical sensing. *Sens. Actuators, B* **1990**, *1*, 244–248.
167. Zhuang, B.; Gan, W.; Liu, P. Integrated microfluidic systems for genetic analysis. In *Integrated microfluidic systems: - Microfluidic Devices for Biomedical Applications*; Zhuang, B., Gan, W., Liu, P., Eds.; Elsevier, 2013; 465-494e.
168. Hou, X.; Guo, W.; Jiang, L. Biomimetic smart nanopores and nanochannels. *Chemical Society reviews* **2011**, *40* (5), 2385–2401.
169. Apel, P. Y.; Korchev, Y. E.; Siwy, Z.; Spohr, R.; Yoshida, M. Diode-like single-ion trak membrane prepared by electro-stopping. *Nuclear Instruments and Methods in Physics Research B* **2001**, *184* (3), 337–346.
170. Siwy, Z.; Apel, P.; Baur, D.; Dobrev, D. D.; Korchev, Y. E.; Neumann, R.; Spohr, R.; Trautmann, C.; Voss, K.-O. Preparation of synthetic nanopores with transport properties analogous to biological channels. *Surface Science* **2003**, *532-535*, 1061–1066.
171. Siwy, Z.; Dobrev, D.; Neumann, R.; Trautmann, C.; Voss, K. Electro-responsive asymmetric nanopores in polyimide with stable ion-current signal. *Applied Physics A: Materials Science & Processing* **2003**, *76* (5), 781–785.
172. Ali, M.; Bayer, V.; Schiedt, B.; Neumann, R.; Ensinger, W. Fabrication and functionalization of single asymmetric nanochannels for electrostatic/hydrophobic association of protein molecules. *Nanotechnology* **2008**, *19* (48), 485711.
173. Ragupathy, L.; Millar, D. G.; Tirelli, N.; Cellesi, F. An Orthogonal Click-Chemistry Approach to Design Poly(glycerol monomethacrylate)-based Nanomaterials for Controlled Immunostimulation: Immune Active Poly(glycerol monomethacrylate). *Macromolecular bioscience* **2014**, *14* (11), 1528–1538.
174. Karlsson, S.; Högberg, H.-E. Asymmetric 1,3-Dipolar Cycloadditions for the construction of enantiomerically pure heterocycles. A review. *Organic Preparations and Procedures International* **2001**, *33* (2), 103–172.
-

- 
175. Hein, J. E.; Fokin, V. V. Copper-catalyzed azide-alkyne cycloaddition (CuAAC) and beyond: new reactivity of copper(I) acetylides. *Chemical Society reviews* **2010**, *39* (4), 1302–1315.
176. Agard, N. J.; Prescher, J. A.; Bertozzi, C. R. A strain-promoted 3 + 2 azide-alkyne cycloaddition for covalent modification of biomolecules in living systems. *Journal of the American Chemical Society* **2004**, *126* (46), 15046–15047.
177. Meier, H.; Petersen, H.; Kolshorn, H. Die Ringspannung von Cycloalkinen und ihre spektroskopischen Auswirkungen. *Chem. Ber.* **1980**, *113*, 2398–2409.
178. McIver Jr., J. W.; Komornicki, A. Structure of transition states in organic reactions. General theory and an application to the cyclobutene-butadiene isomerization using a semiempirical molecular orbital method. *JACS* **1972**, *94* (8).
179. Shea, K. J.; Kim, J. S. Influence of strain on chemical reactivity. Relative reactivity of torsionally strained double bonds in 1,3-dipolar cycloadditions. *JACS* **1992**, *114* (12), 4846–4855.
180. Campbell-Verduyn, L. S.; Mirfeizi, L.; Schoonen, A. K.; Dierckx, R. A.; Elsinga, P. H.; Feringa, B. L. Strain-promoted copper-free "click" chemistry for <sup>18</sup>F radiolabeling of bombesin. *Angewandte Chemie (International ed. in English)* **2011**, *50* (47), 11117–11120.
181. Kang, H. J.; Baker, E. N. Intramolecular isopeptide bonds: protein crosslinks built for stress? *Trends in biochemical sciences* **2011**, *36* (4), 229–237.
182. Tan, L. L.; Hoon, S. S.; Wong, F. T. Kinetic Controlled Tag-Catcher Interactions for Directed Covalent Protein Assembly. *PLOS ONE* **2016**, *11* (10), e0165074.
183. Zakeri, B.; Fierer, J. O.; Celik, E.; Chittock, E. C.; Schwarz-Linek, U.; Moy, V. T.; Howarth, M. Peptide tag forming a rapid covalent bond to a protein, through engineering a bacterial adhesin. *Proceedings of the National Academy of Sciences of the United States of America* **2012**, *109* (12), E690-7.
184. Reddington, S. C.; Howarth, M. Secrets of a covalent interaction for biomaterials and biotechnology: SpyTag and SpyCatcher. *Current opinion in chemical biology* **2015**, *29*, 94–99.
185. Tran, H. A. Erlenmeyer flask. *The Journal of clinical endocrinology and metabolism* **2004**, *89* (10), 4827–4828.
186. Chang, M.-Y.; Tsai, C.-Y.; Chan, C.-K. mCPBA-mediated conjugation of dibenzosuberone and amines or carboxylic acids. *Tetrahedron* **2015**, *71* (3), 424–430.
187. Soto Espinoza, S. L.; Arbeitman, C. R.; Clochard, M. C.; Grasselli, M. Functionalization of nanochannels by radio-induced grafting polymerization on PET track-etched membranes. *Radiation Physics and Chemistry* **2014**, *94*, 72–75.
188. Borges, J.; Mano, J. F. Molecular interactions driving the layer-by-layer assembly of multilayers. *Chem. Rev.* **2014**, *114* (18), 8883–8942.
189. Gentile, P.; Carmagnola, I.; Nardo, T.; Chiono, V. Layer-by-layer assembly for biomedical applications in the last decade. *Nanotechnology* **2015**, *26* (42), 422001.
190. Tsuge, Y.; Moriya, T.; Shiratori, S. Porous Transition of Polyelectrolyte Film through Reaction-Induced Phase Separation Caused by Interaction with Specific Metal Ions. *Langmuir : the ACS journal of surfaces and colloids* **2016**, *32* (28), 7219–7227.
191. Li, Q.; Quinn, J. F.; Caruso, F. Nanoporous Polymer Thin Films via Polyelectrolyte Templating. *Adv. Mater.* **2005**, *17* (17), 2058–2062.
192. Roitershtein, D. M.; Vinogradov, A. A.; Lyssenko, K. A.; Nifant'ev, I.E. Self-assembly of heteroleptic tetranuclear carboxylate complexes of yttrium and lanthanides during hydrolysis and oxidation of rare earth homoleptic carboxylates. *Inorganic Chemistry Communications* **2017**, *84*, 225–228.
193. Schmidt, T. G. M.; Koepke, J.; Frank, R.; Skerra, A. Molecular Interaction Between the Strep-tag Affinity Peptide and its Cognate Target, Streptavidin. *J. Mol. Biol.* **1996**, *255*, 753–766.
194. Demoustier-Champagne, S.; Delvaux, M. Preparation of polymeric and metallic nanostructures using a template-based deposition method. *Materials Science and Engineering: C* **2001**, *15* (1-2), 269–271.
195. Yu, S.; Welp, U.; Hua, L. Z.; Rydh, A.; Kwok, W. K.; Wang, H. H. Fabrication of Palladium Nanotubes and Their Application in Hydrogen Sensing. *Chem. Mater.* **2005**, *17* (13), 3445–3450.
196. Muench, F.; Bohn, S.; Rauber, M.; Seidl, T.; Radetinac, A.; Kunz, U.; Lauterbach, S.; Kleebe, H.-J.; Trautmann, C.; Ensinger, W. Polycarbonate activation for electroless plating by dimethylaminoborane absorption and subsequent nanoparticle deposition. *Appl. Phys. A* **2014**, *116* (1), 287–294.
197. Muench, F.; Kunz, U.; Neetzel, C.; Lauterbach, S.; Kleebe, H.-J.; Ensinger, W. 4-(Dimethylamino)pyridine as a powerful auxiliary reagent in the electroless synthesis of gold nanotubes. *Langmuir : the ACS journal of surfaces and colloids* **2011**, *27* (1), 430–435.
198. C.R. Martin, M. Nishizawa, K. Jirage, M.S. Kang, S.B. Lee. Controlling ion-transport selectivity in gold 'nanotubule' membranes. *Membr. Technol.* **2001**, *13* (18), 1351–1362.
-

199. Muench, F.; Oezaslan, M.; Rauber, M.; Kaserer, S.; Fuchs, A.; Mankel, E.; Brötz, J.; Strasser, P.; Roth, C.; Ensinger, W. Electroless synthesis of nanostructured nickel and nickel–boron tubes and their performance as unsupported ethanol electrooxidation catalysts. *Journal of Power Sources* **2013**, *222*, 243–252.
200. Rohan, J. F.; Ahern, B. M.; Nagle, L. C. DMAB Oxidation for Electroless Deposition from Alkaline Solutions. In *ECS Transactions*; ECS, **2005**; 1–9.
201. Stuart, B. H. *Infrared spectroscopy. Fundamentals and applications*; Analytical techniques in the sciences; Wiley: Chichester, **2008**.
202. Lin, C.-Y.; Yeh, L.-H.; Siwy, Z. S. Voltage-Induced Modulation of Ionic Concentrations and Ion Current Rectification in Mesopores with Highly Charged Pore Walls. *The journal of physical chemistry letters* **2018**, *9* (2), 393–398.
203. Ali, M.; Ramirez, P.; Mafé, S.; Neumann, R.; Ensinger, W. A pH-tunable nanofluidic diode with a broad range of rectifying properties. *ACS nano* **2009**, *3* (3), 603–608.
204. Ramirez, P.; Gomez, V.; Cervera, J.; Nasir, S.; Ali, M.; Ensinger, W.; Siwy, Z.; Mafe, S. Voltage-controlled current loops with nanofluidic diodes electrically coupled to solid state capacitors. *RSC Adv.* **2016**, *6* (60), 54742–54746.
205. Lu, Y.; Zhang, D.; Zhang, Q.; Huang, Y.; Luo, S.; Yao, Y.; Li, S.; Liu, Q. Impedance spectroscopy analysis of human odorant binding proteins immobilized on nanopore arrays for biochemical detection. *Biosensors & bioelectronics* **2016**, *79*, 251–257.
206. Nguyen, Q. H.; Ali, M.; Nasir, S.; Ensinger, W. Transport properties of track-etched membranes having variable effective pore-lengths. *Nanotechnology* **2015**, *26* (48), 485502.
207. Eral, H. B.; 't Mannetje, D. J. C. M.; Oh, J. M. Contact angle hysteresis: a review of fundamentals and applications. *Colloid Polym Sci* **2013**, *291* (2), 247–260.
208. Ferain, E.; Legras, R. Characterisation of nanoporous particle track etched membrane. *Nucl. Instrum. Methods Phys. Res., Sect. B* **1997**, *131* (1-4), 97–102.
209. Clochard, M.-C.; El Jouad, M.; Bizière, N.; Chung, P. D.; Drouhin, H.-J.; Balanzat, E.; Lairez, D.; Viret, M.; Wegrowe, J.-E. Magnetic nanoconstrictions made from nickel electrodeposition in polymeric bi-conical tracks: Magneto-transport behaviour. *Radiation Physics and Chemistry* **2014**, *94*, 66–71.
210. Orelovich, O. L.; Apel, P. Y. Methods for Preparing Samples of Track Membranes for Scanning Electron Microscopy. *Instrum. Exp. Tech.* **2001**, *44*, 111–114.
211. Toseland, C. P. Fluorescent labeling and modification of proteins. *Journal of chemical biology* **2013**, *6* (3), 85–95.
212. Martynov, V. I.; Pakhomov, A. A.; Popova, N. V.; Deyev, I. E.; Petrenko, A. G. Synthetic Fluorophores for Visualizing Biomolecules in Living Systems. *Acta Naturae* **2016**, *8* (4), 33–46.
213. Day, R. N.; Davidson, M. W. The fluorescent protein palette: tools for cellular imaging. *Chemical Society reviews* **2009**, *38* (10), 2887–2921.
214. Hierl, P. M.; Herman, Z.; Wolfgang, R. Chemical Accelerator Studies of Isotope Effects on Collision Dynamics of Ion–Molecule Reactions: Elaboration of a Model for Direct Reactions. *The Journal of Chemical Physics* **1970**, *53* (2), 660–673.
215. Track etching technique in membrane technology | It4ip. <https://www.it4ip.be/track-etching-technology/>).
216. Toulemonde, M.; Trautmann, C.; Balanzat, E.; Hjort, K.; Weidinger, A. Track formation and fabrication of nanostructures with MeV-ion beams. *Nuclear Instruments and Methods in Physics Research Section B: Beam Interactions with Materials and Atoms* **2004**, *216*, 1–8.
217. Nasir, S. Stimuli-Triggered Ionic and Molecular Transport through Track-Etched Nanopores. *Ph. D. Dissertation* **2014**.
218. Sartowska, B.; Starosta, W.; Apel, P.; Orelovitch, O.; Blonskaya, I. Polymeric Track Etched Membranes - Application for Advanced Porous Structures Formation. *Acta Phys. Pol. A* **2013**, *123* (5), 819–821.
219. Spohr, R.; Bethge, K. *Ion Tracks and Microtechnology: Principles and Applications*; Vieweg+Teubner Verlag, **1990**.
220. Fink, D. *Transport Processes in Ion-Irradiated Polymers*; Springer Series in Materials Science 65; Springer: Berlin, Heidelberg, **2004**.
221. Institute for Bioplastics and Biocomposites: "Biopolymers-Facts-Statistics" (2019); URL: [https://www.ifbb-hannover.de/files/IfBB/downloads/faltblaetter\\_broschueren/Biopolymers-Facts-Statistics-2018.pdf](https://www.ifbb-hannover.de/files/IfBB/downloads/faltblaetter_broschueren/Biopolymers-Facts-Statistics-2018.pdf) (Assesed on 2nd February 2020).
222. Lasprilla, A. J. R.; Martinez, G. A. R.; Lunelli, B. H.; Jardini, A. L.; Filho, R. M. Poly-lactic acid synthesis for application in biomedical devices - a review. *Biotechnology advances* **2012**, *30* (1), 321–328.
223. Formnext Magazin (2020); "Additive Fertigung bereichert die Medizintechnik". URL: <https://fon-mag.de/highlight-stories/hintergrund-medizintechnik/?L=0>. (assessed on 2<sup>nd</sup> February 2020).

224. Olayo-Valles, R.; Lund, M. S.; Leighton, C.; Hillmyer, M. A. Large area nanolithographic templates by selective etching of chemically stained block copolymer thin films. *J. Mater. Chem.* **2004**, *14* (18), 2729.
225. Rzaev, J.; Hillmyer, M. A. Nanochannel array plastics with tailored surface chemistry. *J. Am. Chem. Soc.* **2005**, *127* (38), 13373–13379.
226. Cummins, C.; Mokarian-Tabari, P.; Holmes, J. D.; Morris, M. A. Selective etching of polylactic acid in poly(styrene)-block-poly(d,l) lactide diblock copolymer for nanoscale patterning. *J. Appl. Polym. Sci.* **2014**, *131* (18), 40798 (1-12).
227. Chen, L.; Zhao, H.-B.; Ni, Y.-P.; Fu, T.; Wu, W.-S.; Wang, X.-L.; Wang, Y.-Z. 3D printable robust shape memory PET copolyesters with fire safety via  $\pi$ -stacking and synergistic crosslinking. *J. Mater. Chem. A [Online]* **2019**, *7* (28), 17037–17045.
228. Menges, G.; Haberstroh, E.; Michaeli, W.; Schmachtenberg, E. *Menges Werkstoffkunde Kunststoffe*, 1. Aufl.; Carl Hanser Fachbuchverlag: s.l., **2014**.
229. Ali, M.; Nasir, S.; Ramirez, P.; Cervera, J.; Mafe, S.; Ensinger, W. Carbohydrate-Mediated Biomolecular Recognition and Gating of Synthetic Ion Channels. *J. Phys. Chem. C* **2013**, *117* (35), 18234–18242.
230. Ali, M.; Nasir, S.; Nguyen, Q. H.; Sahoo, J. K.; Tahir, M. N.; Tremel, W.; Ensinger, W. Metal ion affinity-based biomolecular recognition and conjugation inside synthetic polymer nanopores modified with iron-terpyridine complexes. *J. Am. Chem. Soc.* **2011**, *133* (43), 17307–17314.
231. Ali, M.; Schiedt, B.; Neumann, R.; Ensinger, W. Biosensing with functionalized single asymmetric polymer nanochannels. *Macromolecular bioscience* **2010**, *10* (1), 28–32.
232. Tahir, M. N.; Ali, M.; Andre, R.; Müller, W. E. G.; Schröder, H.-C.; Tremel, W.; Ensinger, W. Silicatein conjugation inside nanoconfined geometries through immobilized NTA-Ni(II) chelates. *Chemical communications (Cambridge, England)* **2013**, *49* (22), 2210–2212.
233. Ali, M.; Ahmed, I.; Ramirez, P.; Nasir, S.; Cervera, J.; Niemeyer, C. M.; Ensinger, W. Fluoride-induced modulation of ionic transport in asymmetric nanopores functionalized with "caged" fluorescein moieties. *Nanoscale* **2016**, *8* (16), 8583–8590.
234. Liu, Q.; Xiao, K.; Wen, L.; Dong, Y.; Xie, G.; Zhang, Z.; Bo, Z.; Jiang, L. A fluoride-driven ionic gate based on a 4-aminophenylboronic acid-functionalized asymmetric single nanochannel. *ACS nano* **2014**, *8* (12), 12292–12299.
235. Nie, G.; Sun, Y.; Zhang, F.; Song, M.; Tian, D.; Jiang, L.; Li, H. Fluoride responsive single nanochannel: click fabrication and highly selective sensing in aqueous solution. *Chemical science* **2015**, *6* (10), 5859–5865.
236. Sun, Z.; Zhang, F.; Zhang, X.; Tian, D.; Jiang, L.; Li, H. Chiral recognition of Arg based on label-free PET nanochannel. *Chemical communications (Cambridge, England)* **2015**, *51* (23), 4823–4826.
237. Ali, M.; Nasir, S.; Ensinger, W. Stereoselective detection of amino acids with protein-modified single asymmetric nanopores. *Electrochimica Acta* **2016**, *215*, 231–237.
238. Han, C.; Hou, X.; Zhang, H.; Guo, W.; Li, H.; Jiang, L. Enantioselective recognition in biomimetic single artificial nanochannels. *J. Am. Chem. Soc.* **2011**, *133* (20), 7644–7647.
239. Ali, M.; Ahmed, I.; Ramirez, P.; Nasir, S.; Niemeyer, C. M.; Mafe, S.; Ensinger, W. Label-Free Pyrophosphate Recognition with Functionalized Asymmetric Nanopores. *Small (Weinheim an der Bergstrasse, Germany)* **2016**, *12* (15), 2014–2021.
240. Han, C.; Su, H.; Sun, Z.; Wen, L.; Tian, D.; Xu, K.; Hu, J.; Wang, A.; Li, H.; Jiang, L. Biomimetic ion nanochannels as a highly selective sequential sensor for zinc ions followed by phosphate anions. *Chemistry (Weinheim an der Bergstrasse, Germany)* **2013**, *19* (28), 9388–9395.
241. Kandel, J. H.; Schwartz, T. M. *Principles of Neural Science*, 5th; McGraw-Hill: New York, **2012**.
242. Webster, R. A. *Neurotransmitters, drugs, and brain function*; Wiley: Chichester, New York, **2001**.
243. Gelfand, E. W. Role of histamine in the pathophysiology of asthma: immunomodulatory and anti-inflammatory activities of H1-receptor antagonists. *The American Journal of Medicine* **2002**, *113* (9), 2–7.
244. Falus, A.; Merétey, K. Histamine: an early messenger in inflammatory and immune reactions. *Immunology Today* **1992**, *13* (5), 154–156.
245. Schwartz, J.-C.; Pollard, H.; Quach, T. T. Histamine as a Neurotransmitter in Mammalian Brain: Neurochemical Evidence. *Journal of Neurochemistry* **1980**, *35* (1), 26–33.
246. Maintz, L.; Novak, N. Histamine and histamine intolerance. *The American journal of clinical nutrition* **2007**, *85* (5), 1185–1196.
247. Pradhan, T.; Jung, H. S.; Jang, J. H.; Kim, T. W.; Kang, C.; Kim, J. S. Chemical sensing of neurotransmitters. *Chemical Society reviews* **2014**, *43* (13), 4684–4713.
248. White, M. V. The role of histamine in allergic diseases. *Journal of Allergy and Clinical Immunology* **1990**, *86* (4), 599–605.

249. Antoine, F. R.; Wei, C.-I.; Otwell, W. S.; Sims, C. A.; Littell, R. C.; Hogle, A. D.; Marshall, M. R. Gas chromatographic analysis of histamine in mahi-mahi (*Coryphaena hippurus*). *Journal of agricultural and food chemistry* **2002**, *50* (17), 4754–4759.
250. Li, Y.; Kobayashi, M.; Furui, K.; Soh, N.; Nakano, K.; Imato, T. Surface plasmon resonance immunosensor for histamine based on an indirect competitive immunoreaction. *Analytica Chimica Acta* **2006**, *576* (1), 77–83.
251. Niwa, O.; Kurita, R.; Hayashi, K.; Horiuchi, T.; Torimitsu, K.; Maeyama, K.; Tanizawa, K. Continuous measurement of histamine from rat basophilic leukemia cells (RBL-2H3) with an on-line sensor using histamine oxidase. *Sensors and Actuators B: Chemical* **2000**, *67* (1-2), 43–51.
252. Oshikawa, Y.; Furuta, K.; Tanaka, S.; Ojida, A. Cell Surface-Anchored Fluorescent Probe Capable of Real-Time Imaging of Single Mast Cell Degranulation Based on Histamine-Induced Coordination Displacement. *Analytical chemistry* **2016**, *88* (3), 1526–1529.
253. Seto, D.; Soh, N.; Nakano, K.; Imato, T. Selective fluorescence detection of histamine based on ligand exchange mechanism and its application to biomonitoring. *Analytical Biochemistry* **2010**, *404* (2), 135–139.
254. Cervera, J.; Schiedt, B.; Ramírez, P. A Poisson/Nernst-Planck model for ionic transport through synthetic conical nanopores. *Europhys. Lett.* **2005**, *71* (1), 35–41.
255. Cervera, J.; Schiedt, B.; Neumann, R.; Mafé, S.; Ramírez, P. Ionic conduction, rectification, and selectivity in single conical nanopores. *The Journal of Chemical Physics* **2006**, *124* (10), 104706.
256. Ramírez, P.; Apel, P. Y.; Cervera, J.; Mafé, S. Pore structure and function of synthetic nanopores with fixed charges: tip shape and rectification properties. *Nanotechnology* **2008**, *19* (31), 315707.
257. N. A. Kostromina, N. A.; Tikhonov, V. P. PMR study of the complex formation of L-histidine with nickel(II). *Theor. Exp. Chem.* **1981**, *16* (4), 396–402.
258. Rao, B.; Mathur, H. B. Thermodynamics of the interaction of transition metal ions with histamine. *Journal of Inorganic and Nuclear Chemistry* **1971**, *33* (3), 809–816.
259. Drożdżewski, p.; Kordon, E. Isotopic labelling studies on far-infrared spectra of nickel–histamine complexes. *Spectrochim. Acta, Part A* **2000**, *56* (12), 2459–2464.
260. Tagliazucchi, M.; Szleifer, I. How Does Confinement Change Ligand-Receptor Binding Equilibrium? Protein Binding in Nanopores and Nanochannels. *J. Am. Chem. Soc.* **2015**, *137* (39), 12539–12551.
261. Karnik, R.; Castelino, K.; Fan, R.; Yang, P.; Majumdar, A. Effects of biological reactions and modifications on conductance of nanofluidic channels. *Nano Lett.* **2005**, *5* (9), 1638–1642.
262. Karnik, R.; Fan, R.; Yue, M.; Li, D.; Yang, P.; Majumdar, A. Electrostatic control of ions and molecules in nanofluidic transistors. *Nano Lett.* **2005**, *5* (5), 943–948.
263. Daiguji, H.; Yang, P.; Majumdar, A. Ion Transport in Nanofluidic Channels. *Nano Lett.* **2004**, *4* (1), 137–142.
264. Wang, P.; Wang, M.; Liu, F.; Ding, S.; Wang, X.; Du, G.; Liu, J.; Apel, P.; Kluth, P.; Trautmann, C.; Wang, Y. Ultrafast ion sieving using nanoporous polymeric membranes. *Nature communications* **2018**, *9* (1), 569.
265. Payandeh, J.; Scheuer, T.; Zheng, N.; Catterall, W. A. The crystal structure of a voltage-gated sodium channel. *Nature* **2011**, *475* (7356), 353–358.
266. Essen, L.-O.; Koert, U. Ion-channel engineering. *Annu. Rep. Prog. Chem., Sect. C: Phys. Chem.* **2008**, *104*, 165.
267. Hou, X.; Guo, W.; Xia, F.; Nie, F.-Q.; Dong, H.; Tian, Y.; Wen, L.; Wang, L.; Cao, L.; Yang, Y.; Xue, J.; Song, Y.; Wang, Y.; Liu, D.; Jiang, L. A biomimetic potassium responsive nanochannel: G-quadruplex DNA conformational switching in a synthetic nanopore. *J. Am. Chem. Soc.* **2009**, *131* (22), 7800–7805.
268. Haydon, D. A.; Hladky, S. B. Ion transport across thin lipid membranes: a critical discussion of mechanisms in selected systems. *Quarterly reviews of biophysics* **1972**, *5* (2), 187–282.
269. Wong, K. H.; Yagi, K.; Smid, J. Ion transport through liquid membranes facilitated by crown ethers and their polymers. *Journal of Membrane Biology* **1974**, *18* (3-4), 379–397.
270. Pérez-Mitta, G.; Albesa, A. G.; Knoll, W.; Trautmann, C.; Toimil-Molares, M. E.; Azzaroni, O. Host-guest supramolecular chemistry in solid-state nanopores: potassium-driven modulation of ionic transport in nanofluidic diodes. *Nanoscale* **2015**, *7* (38), 15594–15598.
271. Ali, M.; Ahmed, I.; Ramirez, P.; Nasir, S.; Cervera, J.; Mafe, S.; Niemeyer, C. M.; Ensinger, W. Cesium-Induced Ionic Conduction through a Single Nanofluidic Pore Modified with Calixcrown Moieties. *Langmuir : the ACS journal of surfaces and colloids* **2017**, *33* (36), 9170–9177.
272. Bandyopadhyay, K.; Shu, L.; Liu, H.; Echegoyen, L. Selective K<sup>+</sup> Recognition at the Interface during Self-Assembly of a Bis-Podand Thiol on a Gold Surface. *Langmuir* **2000**, *16* (6), 2706–2714.
273. Herranz, M. A.; Colonna, B.; Echegoyen, L. Metal ion recognition and molecular templating in self-assembled monolayers of cyclic and acyclic polyethers. *PNAS* **2002**, *99* (8), 5040–5047.
274. Moins, S.; Martins, J. C.; Krumpmann, A.; Lemaure, V.; Cornil, J.; Delbosc, N.; Decroly, A.; Dubois, P.; Lazzaroni, R.; Gohy, J.-F.; Coulembier, O. Potential of polymethacrylate pseudo crown ethers as solid state polymer electrolytes. *Chemical communications (Cambridge, England)* **2017**, *53* (51), 6899–6902.

- 
275. Ramírez, P.; Gómez, V.; Cervera, J.; Schiedt, B.; Mafé, S. Ion transport and selectivity in nanopores with spatially inhomogeneous fixed charge distributions. *The Journal of Chemical Physics* **2007**, *126* (19), 194703.
276. Flink, S.; van Veggel, F. C. J. M.; Reinhoudt, D. N. Recognition of Cations by Self-Assembled Monolayers of Crown Ethers. *J. Phys. Chem. B* **1999**, *103* (31), 6515–6520.
277. Park, K.; Choi, D.; Hong, J. Nanostructured Polymer Thin Films Fabricated with Brush-based Layer-by-Layer Self-assembly for Site-selective Construction and Drug release. *Sci. Rep.* **2018**, *8* (1), 3365.
278. Jafri, S. H. M.; Dutta, J.; Sweatman, D.; Sharma, A. B. Current-voltage characteristics of layer-by-layer self-assembled colloidal thin films. *Appl. Phys. Lett.* **2006**, *89* (13), 133123.
279. Cheng, C.; Yaroshchuk, A.; Bruening, M. L. Fundamentals of selective ion transport through multilayer polyelectrolyte membranes. *Langmuir* **2013**, *29* (6), 1885–1892.
280. Duong, P. H.H.; Zuo, J.; Chung, T.-S. Highly crosslinked layer-by-layer polyelectrolyte FO membranes: Understanding effects of salt concentration and deposition time on FO performance. *J. Membr. Sci.* **2013**, *427*, 411–421
281. Zhao, Y.; Janot, J.-M.; Balanzat, E.; Balme, S. Mimicking pH-Gated Ionic Channels by Polyelectrolyte Complex Confinement Inside a Single Nanopore. *Langmuir : the ACS journal of surfaces and colloids* **2017**, *33* (14), 3484–3490.
282. Ma, T.; Gaigalas, P.; Lepoitevin, M.; Plikusiene, I.; Bechelany, M.; Janot, J.-M.; Balanzat, E.; Balme, S. Impact of Polyelectrolyte Multilayers on the Ionic Current Rectification of Conical Nanopores. *Langmuir* **2018**, *34* (11), 3405–3412.
283. Transport of proteins through gel-filled porous membranes. Kapur, V., Charkoudian, J.; Anderson, J. L. *J. Membr. Sci.* **1997**, *131*, 143–153.
284. Bagheripour, E.; Moghadassi, A. R.; Parvzian, F.; Hosseini, S. M.; van der Bruggen, B. Tailoring the separation performance and fouling reduction of PES based nanofiltration membrane by using a PVA/Fe<sub>3</sub>O<sub>4</sub> coating layer. *Chemical Engineering Research and Design* **2019**, *144*, 418–428.
285. Richardson, J. J.; Cui, J.; Björnmalm, M.; Braunger, J. A.; Ejima, H.; Caruso, F. Innovation in Layer-by-Layer Assembly. *Chemical reviews* **2016**, *116* (23), 14828–14867.
286. Richardson, J. J.; Björnmalm, M.; Caruso, F. Multilayer assembly. Technology-driven layer-by-layer assembly of nanofilms. *Science (New York, N.Y.)* **2015**, *348* (6233), 2491.
287. Lutkenhaus, J. L.; Hammond, P. T. Electrochemically enabled polyelectrolyte multilayer devices: from fuel cells to sensors. *Soft matter* **2007**, *3* (7), 804.
288. Lutkenhaus, J. L.; McEnnis, K.; Hammond, P. T. Nano- and Microporous Layer-by-Layer Assemblies Containing Linear Poly(ethylenimine) and Poly(acrylic acid). *Macromolecules* **2008**, *41* (16), 6047–6054.
289. Mendelsohn, J. D.; Barrett, C. J.; Chan, V. V.; Pal, A. J.; Mayes, A. M.; Rubner, M. F. Fabrication of Microporous Thin Films from Polyelectrolyte Multilayers. *Langmuir* **2000**, *16* (11), 5017–5023.
290. Tsuge, Y.; Moriya, T.; Shiratori, S. Porous Transition of Polyelectrolyte Film through Reaction-Induced Phase Separation Caused by Interaction with Specific Metal Ions. *Langmuir : the ACS journal of surfaces and colloids* **2016**, *32* (28), 7219–7227.
291. Zykwinska, A.; Radji-Taleb, S.; Cuenot, S. Layer-by-layer functionalization of carbon nanotubes with synthetic and natural polyelectrolytes. *Langmuir* **2010**, *26* (4), 2779–2784.
292. Ferreira, Q.; Gomes, P. J.; Ribeiro, P. A.; Jones, N. C.; Hoffmann, S. V.; Mason, N. J.; Oliveira, O. N.; Raposo, M. Determination of degree of ionization of poly(allylamine hydrochloride) (PAH) and poly(1-(3-carboxy-4-hydroxyphenylazo)benzene sulfonamido-1,2-ethanediyl, sodium salt (PAZO) in layer-by-layer films using vacuum photoabsorption spectroscopy. *Langmuir* **2013**, *29* (1), 448–455.
293. Köhler, K.; Möhwald, H.; Sukhorukov, G. B. Thermal behaviour of polyelectrolyte multilayer microcapsules: 2. Insight into molecular mechanisms for the PDADMAC/PSS system. *The journal of physical chemistry. B* **2006**, *110* (47), 24002–24010.
294. Decher, G.; Schlenoff, J. *Multilayer Thin Films. Sequential Assembly of Nanocomposite Materials*, 2. ed.; John Wiley & Sons: Hoboken, **2012**.
295. Harris, J. J.; DeRose, P. M.; Bruening, M. L. Synthesis of Passivating, Nylon-Like Coatings through Cross-Linking of Ultrathin Polyelectrolyte Films. *J. Am. Chem. Soc.* **1999**, *121* (9), 1978–1979.
296. Zhou, Y.; Chen, C.-C.; Baker, L. A. Heterogeneity of multiple-pore membranes investigated with ion conductance microscopy. *Analytical chemistry* **2012**, *84* (6), 3003–3009.
297. Rostovtseva, T. K.; Bashford, C. L.; Alder, G. M.; Hill, G. N.; McGiffert, C.; Apel, P. Y.; Lowe, G.; Pasternak, C. A. Diffusion through Narrow Pores: Movement of Ions, Water and Nonelectrolytes through Track-etched PETP Membranes. *J. Membr. Biol.* **1996**, *151* (1), 29–43.
298. Lee, S. B.; Martin, C. R. pH-Switchable, Ion-Permeable Gold Nanotubule Membrane Based on Chemisorbed Cysteine. *Anal. Chem.* **2001**, *73* (4), 768–775.
-

- 
299. Lee, S. B.; Martin, C. R. Controlling the Transport Properties of Gold Nanotubule Membranes Using Chemisorbed Thiols. *Chem. Mater.* **2001**, *13* (10), 3236–3244.
300. Dalvie, S. K.; Baltus, R. E. Transport studies with porous alumina membranes. *J. Membr. Sci.* **1992**, *71*, 247–255.
301. Clark, K.; Penner-Hahn, J. E.; Whittaker, M. M.; Whittaker, J. W. Oxidation-state assignments for galactose oxidase complexes from x-ray absorption spectroscopy. Evidence for copper(II) in the active enzyme. *J. Am. Chem. Soc.* **1990** *112* (17), 6433–6434.
302. Georgopoulos, P. G.; Roy, A.; Yonone-Lioy, M. J.; Opiekun, R. E.; Lioy, P. J. Environmental copper: its dynamics and human exposure issues. *Journal of toxicology and environmental health. Part B, Critical reviews* **2001**, *4* (4), 341–394.
303. Di Wu; Sedgwick, A. C.; Gunnlaugsson, T.; Akkaya, E. U.; Yoon, J.; James, T. D. Fluorescent chemosensors: the past, present and future. *Chemical Society reviews* **2017**, *46* (23), 7105–7123.
304. Donnelly, P. S.; Xiao, Z.; Wedd, A. G. Copper and Alzheimer's disease. *Current opinion in chemical biology* **2007**, *11* (2), 128–133.
305. Brown, D. R.; Kozłowski, H. Biological inorganic and bioinorganic chemistry of neurodegeneration based on prion and Alzheimer diseases. *Dalton transactions (Cambridge, England)* **2004**, No. 13, 1907–1917.
306. Bush, A. I.; Masters, C. L.; Tanzi, R. E. Copper, beta-amyloid, and Alzheimer's disease: tapping a sensitive connection. *PNAS* **2003**, *100* (20), 11193–11194.
307. Cherny, R. A.; Atwood, C. S.; Xilinas, M. E.; Gray, D. N.; Jones, W. D.; McLean, C. A.; Barnham, K. J.; Volitakis, I.; Fraser, F. W.; Kim, Y.-S.; Huang, X.; Goldstein, L. G.; Moir, R. D.; Lim, J. T.; Beyreuther, K.; Zheng, H.; Tanzi, R. E.; Masters, C. L.; Bush, A. Treatment with a Copper-Zinc Chelator Markedly and Rapidly Inhibits  $\beta$ -Amyloid Accumulation in Alzheimer's Disease Transgenic Mice. *Neuron* **2001**, *30* (3), 665–676.
308. Squitti, R.; Ghidoni, R.; Simonelli, I.; Ivanova, I. D.; Colabufo, N. A.; Zuin, M.; Benussi, L.; Binetti, G.; Cassetta, E.; Rongioletti, M.; Siotto, M. Copper dyshomeostasis in Wilson disease and Alzheimer's disease as shown by serum and urine copper indicators. *Journal of trace elements in medicine and biology : organ of the Society for Minerals and Trace Elements (GMS)* **2018**, *45*, 181–188.
309. Hirayama, T.; van de Bittner, G. C.; Gray, L. W.; Lutsenko, S.; Chang, C. J. Near-infrared fluorescent sensor for in vivo copper imaging in a murine Wilson disease model. *PNAS* **2012**, *109* (7), 2228–2233.
310. Harford, C.; Sarkar, B. Amino Terminal Cu(II)- and Ni(II)-Binding (ATCUN) Motif of Proteins and Peptides: Metal Binding, DNA Cleavage, and Other Properties †. *Acc. Chem. Res.* **1997**, *30* (3), 123–130.
311. Papp, S.; Jággerszki, G.; Gyurcsányi, R. E. Ion-Selective Electrodes Based on Hydrophilic Ionophore-Modified Nanopores. *Angewandte Chemie (International ed. in English)* **2018**, *57* (17), 4752–4755.
312. Zheng, Y.; Gattás-Asfura, K. M.; Li, C.; Andreopoulos, F. M.; Pham, S. M.; Leblanc, R. M. Design of a Membrane Fluorescent Sensor Based on Photo-Cross-Linked PEG Hydrogel. *J. Phys. Chem. B* **2003**, *107* (2), 483–488.
313. Wildanger, D.; Medda, R.; Kastrop, L.; Hell, S. W. A compact STED microscope providing 3D nanoscale resolution. *Journal of microscopy* **2009**, *236* (1), 35–43.
314. Wang, Y.; Fan, Z.; Shao, L.; Kong, X.; Hou, X.; Tian, D.; Sun, Y.; Xiao, Y.; Yu, L. Nanobody-derived nanobiotechnology tool kits for diverse biomedical and biotechnology applications. *International journal of nanomedicine* **2016**, *11*, 3287–3303.
315. Muyldermans, S. Nanobodies: natural single-domain antibodies. *Annual review of biochemistry* **2013**, *82*, 775–797.
316. Gao, X.; Fang, J.; Xue, B.; Fu, L.; Li, H. Engineering Protein Hydrogels Using SpyCatcher-SpyTag Chemistry. *Biomacromolecules* **2016**, *17* (9), 2812–2819.
317. Kubala, M. H.; Kovtun, O.; Alexandrov, K.; Collins, B. M. Structural and thermodynamic analysis of the GFP:GFP-nanobody complex. *Protein science : a publication of the Protein Society* **2010**, *19* (12), 2389–2401.
318. Braun, M. B.; Traenkle, B.; Koch, P. A.; Emele, F.; Weiss, F.; Poetz, O.; Stehle, T.; Rothbauer, U. Peptides in headlock--a novel high-affinity and versatile peptide-binding nanobody for proteomics and microscopy. *Scientific reports* **2016**, *6*, 19211.
319. Shu, X.; Shaner, N. C.; Yarbrough, C. A.; Tsien, R. Y.; Remington, S. J. Novel chromophores and buried charges control color in mFruits. *Biochemistry* **2006**, *45* (32), 9639–9647.
320. Pédelacq, J.-D.; Cabantous, S.; Tran, T.; Terwilliger, T. C.; Waldo, G. S. Engineering and characterization of a superfolder green fluorescent protein. *Nature biotechnology* **2006**, *24* (1), 79–88.
321. Shaner, N. C.; Campbell, R. E.; Steinbach, P. A.; Giepmans, B. N. G.; Palmer, A. E.; Tsien, R. Y. Improved monomeric red, orange and yellow fluorescent proteins derived from *Discosoma* sp. red fluorescent protein. *Nature biotechnology* **2004**, *22* (12), 1567–1572.
322. Meessen, J. H. Urea. *Ullmann's encyclopedia of industrial chemistry*, Ed. 6; Wiley-Blackwell: Weinheim, **2003**; p. 253.
-

- 
323. SUEX® is registered in the U. S. Patent and Trademark office; Taken from:  
<https://djmicolaminates.com/suex/>.
324. Kukharenka, E.; Farooqui, M. M.; Grigore, L.; Kraft, M.; Hollinshead, N. Electroplating moulds using dry film thick negative photoresist. *J. Micromech. Microeng.* **2003**, *13* (4), S67-S74.
325. Daniels, V. G.; Wheeler, R. R.; Burkitt, H.G. *Functional Histology: A text and colour Atlas*; Edinburgh: Churchill Livingstone, **1979**.
326. Braid, C. Certificate of Analysis: Product Name: Human Serum - from human male AB plasma, USA origin, sterile-filtred. taken from: [https://www.sigmaldrich.com/Graphics/COFAInfo/SigmaSAPQM/COFA/H4/H4522/H4522-100ML\\_\\_\\_\\_\\_SLCF0709\\_.pdf](https://www.sigmaldrich.com/Graphics/COFAInfo/SigmaSAPQM/COFA/H4/H4522/H4522-100ML_____SLCF0709_.pdf).
327. Linder, M. C.; Wooten, L.; Cerveza, P.; Cotton, S.; Shulze, R.; Lomeli, N. Copper Transport. *The American journal of clinical nutrition* **1998**, *67* (5), 965S-971S.
328. Absolom, D. R.; van Oss, C. J.; Zingg, W.; Neumann, A. W. Determination of surface tensions of proteins II. Surface tension of serum albumin, altered at the protein-air interface. *Biochimica et Biophysica Acta (BBA) - Protein Structure* **1981**, *670* (1), 74–78.
329. Dellinger, R. P.; Levy, M. M.; Rhodes, A.; Annane, D.; Gerlach, H.; Opal, S. M.; Sevransky, J. E.; Sprung, C. L.; Douglas, I. S.; Jaeschke, R.; Osborn, T. M.; Nunnally, M. E.; Townsend, S. R.; Reinhart, K.; Kleinpell, R. M.; Angus, D. C.; Deutschman, C. S.; Machado, F. R.; Rubenfeld, G. D.; Webb, S. A.; Beale, R. J.; Vincent, J.-L.; Moreno, R. Surviving sepsis campaign: international guidelines for management of severe sepsis and septic shock: 2012. *Critical care medicine* **2013**, *41* (2), 580–637.
330. Barbosa, S.; Taboada, P.; Mosquera, V. Fibrillation and Polymorphism of Human Serum Albumin. *Bio-nanoimaging*; **2014**; 345–362.

## Appendix

### Supplemental Data of Mass Transport Experiments

#### a. Calibration Data

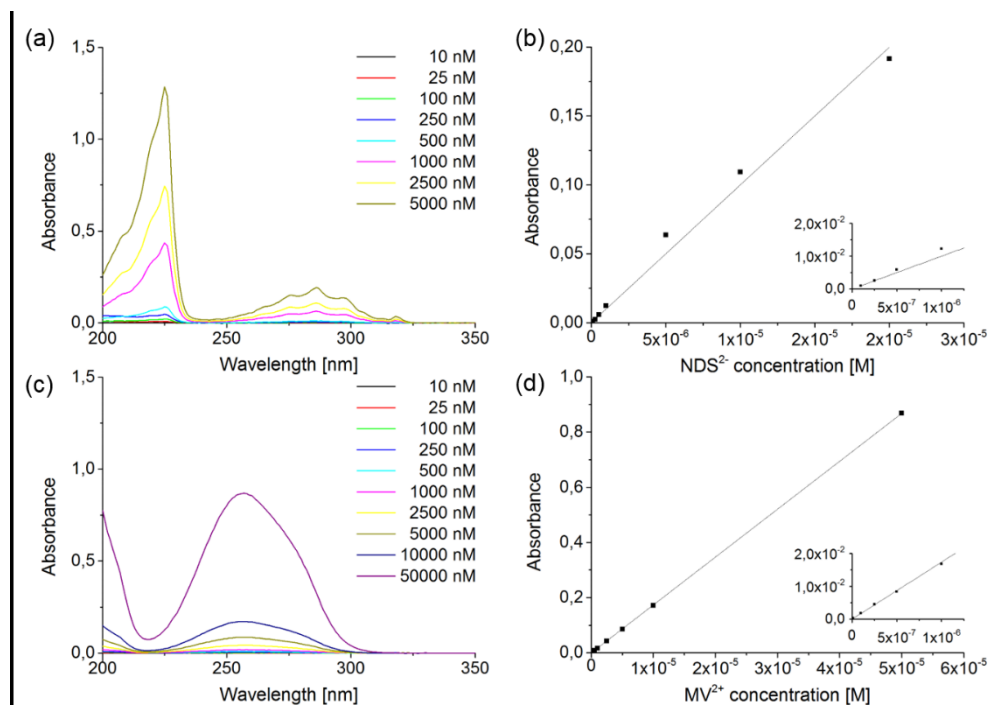


Figure 142: (a) UV/vis-absorbance spectra and (b) calibration curve for NDS-calibration; (c) UV/vis-absorbance spectra and (d) calibration curve for MV-calibration. The calibration experiment performed in a triple measurement. Note that error bars are negligible because they do not protrude beyond the size of the data point. Calibration was performed prior to the mass transport experiments, by measuring the absorbance of the positively charged methylviologen (MV) and the negatively charged 1,5-naphthalene disulfonate (NDS). Here, the maximum absorbance values at a given wavelength 256 nm (for MV) and 286nm (for NDS) is plotted in dependence on the respective analyte concentration. Unknown analyte amounts were calculated using the respective calibration curve according to the BEER-LAMBERT's equation.

#### b. Validation Data

Prior to the investigations on modified membranes, the optimum threshold of diffusion rates using unmodified membranes that were fixed inside the measurement cells. This validation experiment was carried out by Dr. Mathias Diefenbach (RG Biesalski) using multipore membranes having a pore density of  $10^6$ - $10^8$  pores/cm<sup>2</sup> and a pore diameter of 35 nm, 90 nm and 200 nm.

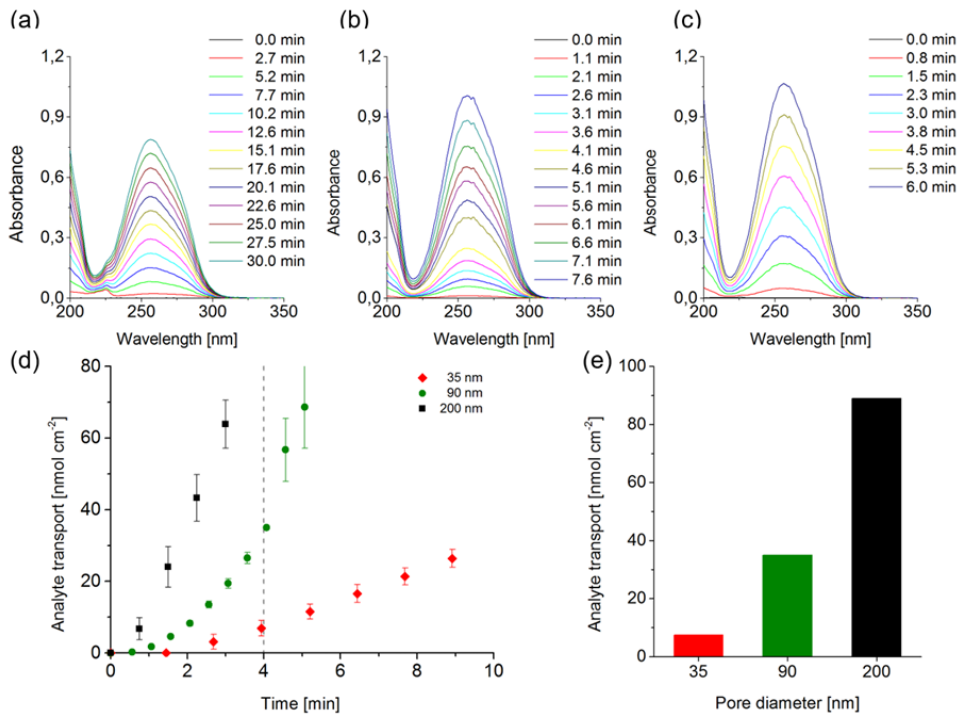


Figure 143: UV/vis-spectra for the time-resolved MV-diffusion across multipore membranes having  $10^7$  pores/cm<sup>2</sup> and a diameter of (a) 35 nm, (b) 90 nm, (c) 200 nm; (d) Time-dependant transport of MV with respect to the pore diameter; (e) transported MV-amount after 4 min of diffusion time according to the respective pore diameter.

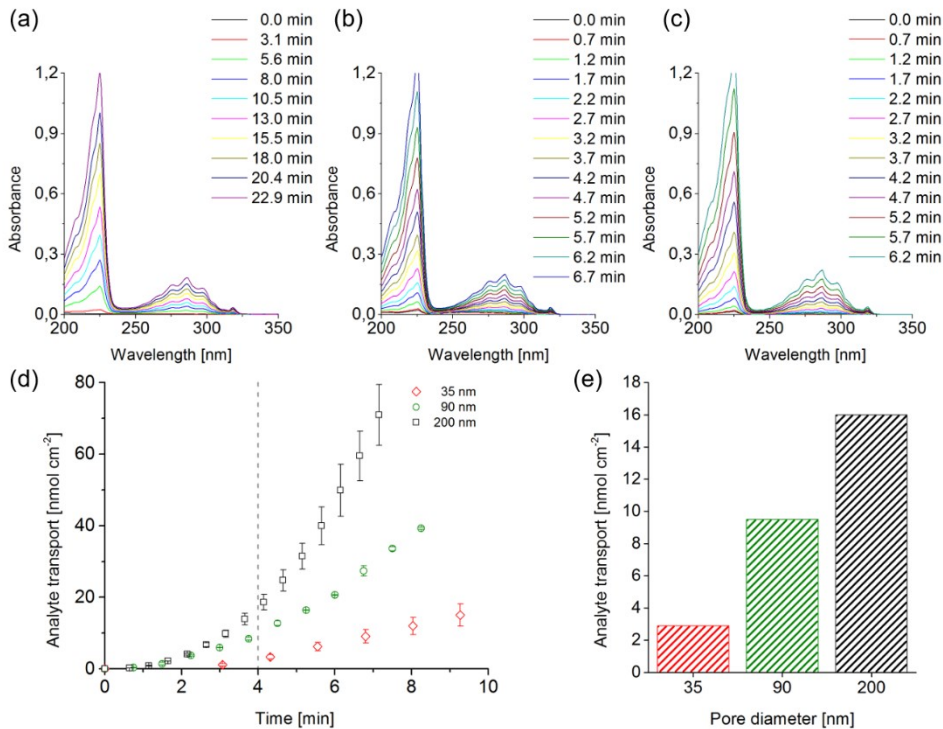


Figure 144: UV/vis-spectra for the time-resolved NDS-diffusion across multipore membranes having  $10^7$  pores/cm<sup>2</sup> and a diameter of (a) 35 nm, (b) 90 nm, (c) 200 nm; (d) Time-dependant transport of NDS with respect to the pore diameter; (e) transported NDS-amount after 4 min of diffusion time according to the respective pore diameter.

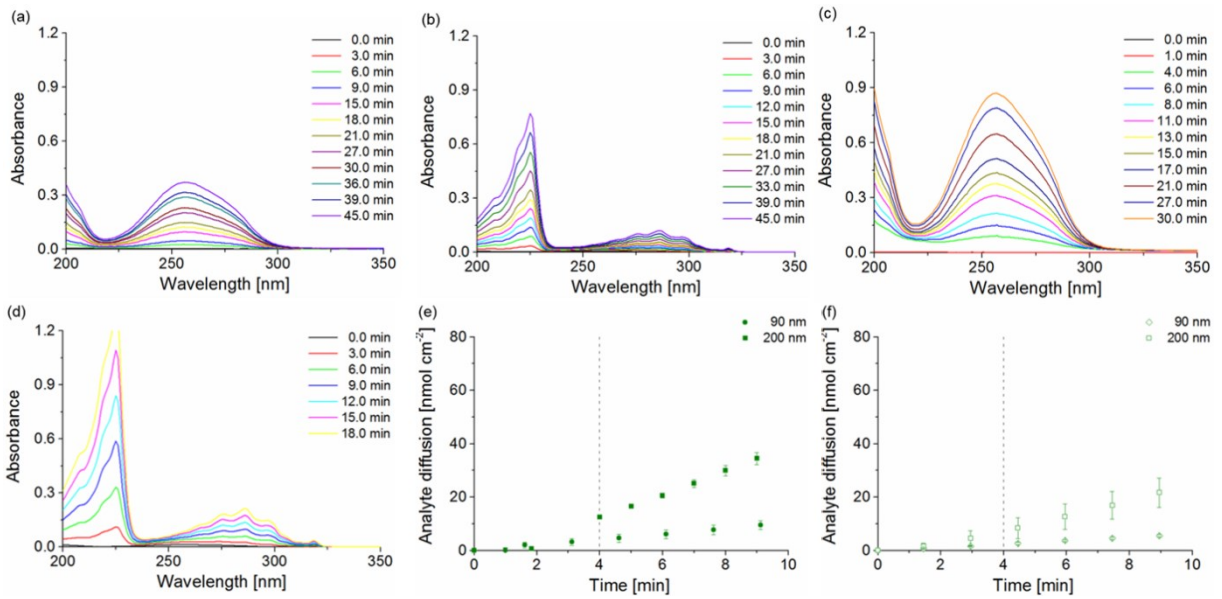


Figure 145: UV/vis-spectra of the analyte diffusion for multipore membranes having  $10^6$  pores/cm<sup>2</sup> and a diameter of 90 nm (a) in case of MV-diffusion and (b) in case of NDS-diffusion. UV/vis-spectra of the analyte diffusion for multipore membranes having  $10^6$  pores/cm<sup>2</sup> and a diameter of 200 nm (c) in case of MV-diffusion and (d) in case of NDS-diffusion; time-dependant diffusion of (e) MV and (f) NDS in dependence to the pore diameter.

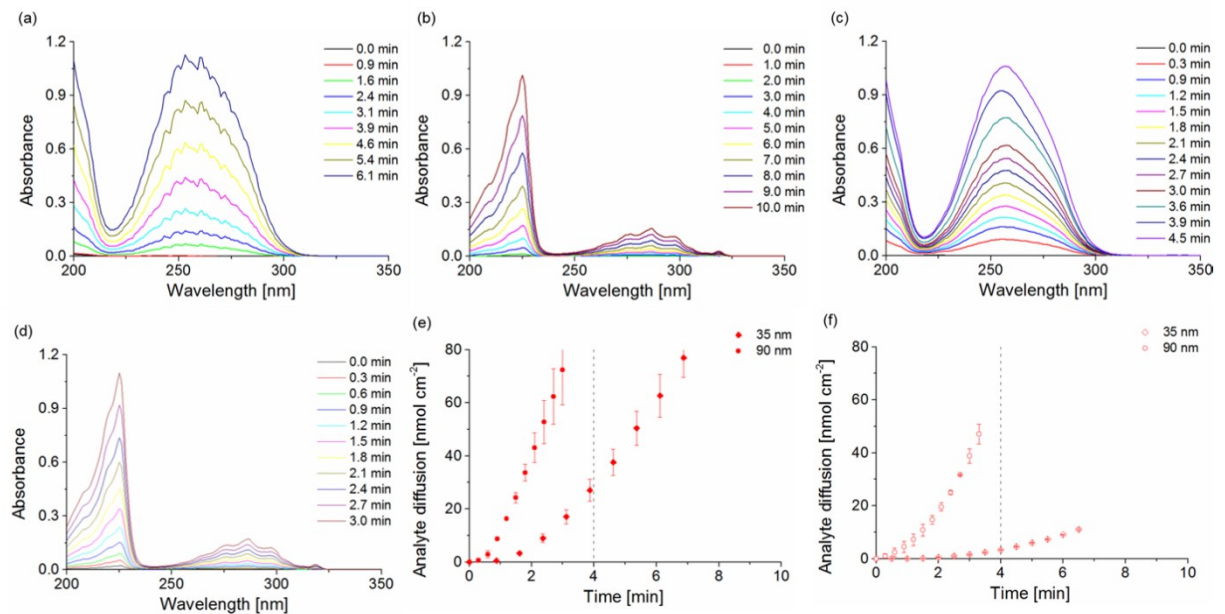


Figure 146: UV/vis-spectra of the analyte diffusion for multipore membranes having  $10^8$  pores/cm<sup>2</sup> and a diameter of 35 nm (a) in case of MV-diffusion and (b) in case of NDS-diffusion. UV/vis-spectra of the analyte diffusion for multipore membranes having  $10^6$  pores/cm<sup>2</sup> and a diameter of 90 nm (c) in case of MV-diffusion and (d) in case of NDS-diffusion; time-dependant diffusion of (e) MV and (f) NDS in dependence to the pore diameter. Note that because of the fast diffusion rate at 90 nm pore diameter, the transport control is not achievable for even larger pore openings.

### c. UV/vis Spectra

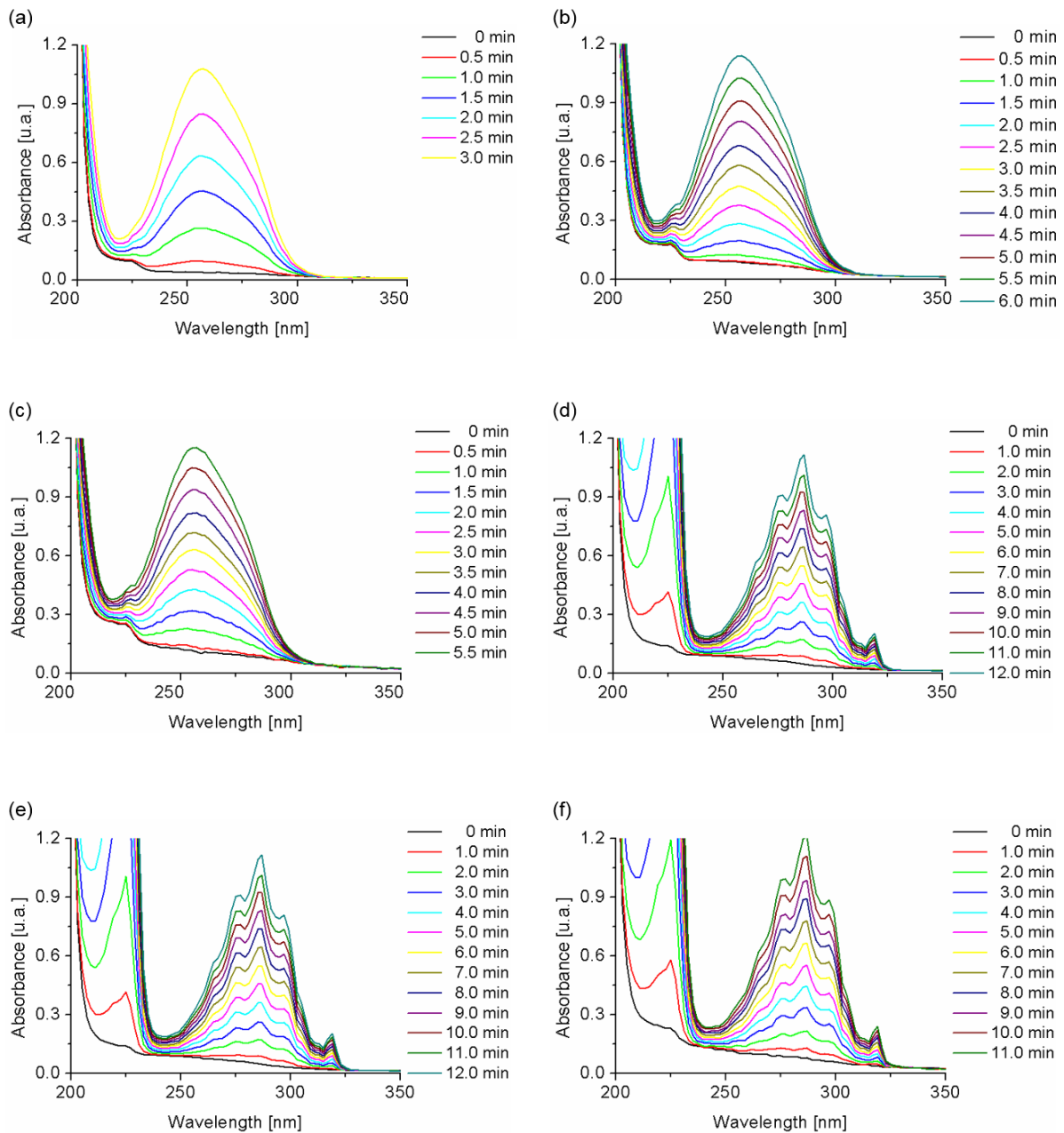


Figure 147: (a) – (c) UV/vis-absorbance of the MV-diffusion with respect to the LBL-modification process; (d) – (f) UV/vis-absorbance of the MV-diffusion with respect to the LBL-modification process; All spectra were recorded using a multipore membrane having a pore density of  $10^7$  pores/cm<sup>2</sup> and pore diameter of 200 nm. The LBL-deposition was performed using a 50:50-blend ratio [PAH|PVP]; ((a) and (d)) blank foil; ((b) and (e)) after deposition of four bilayers; ((c) and (f)) after formation of porous networks.

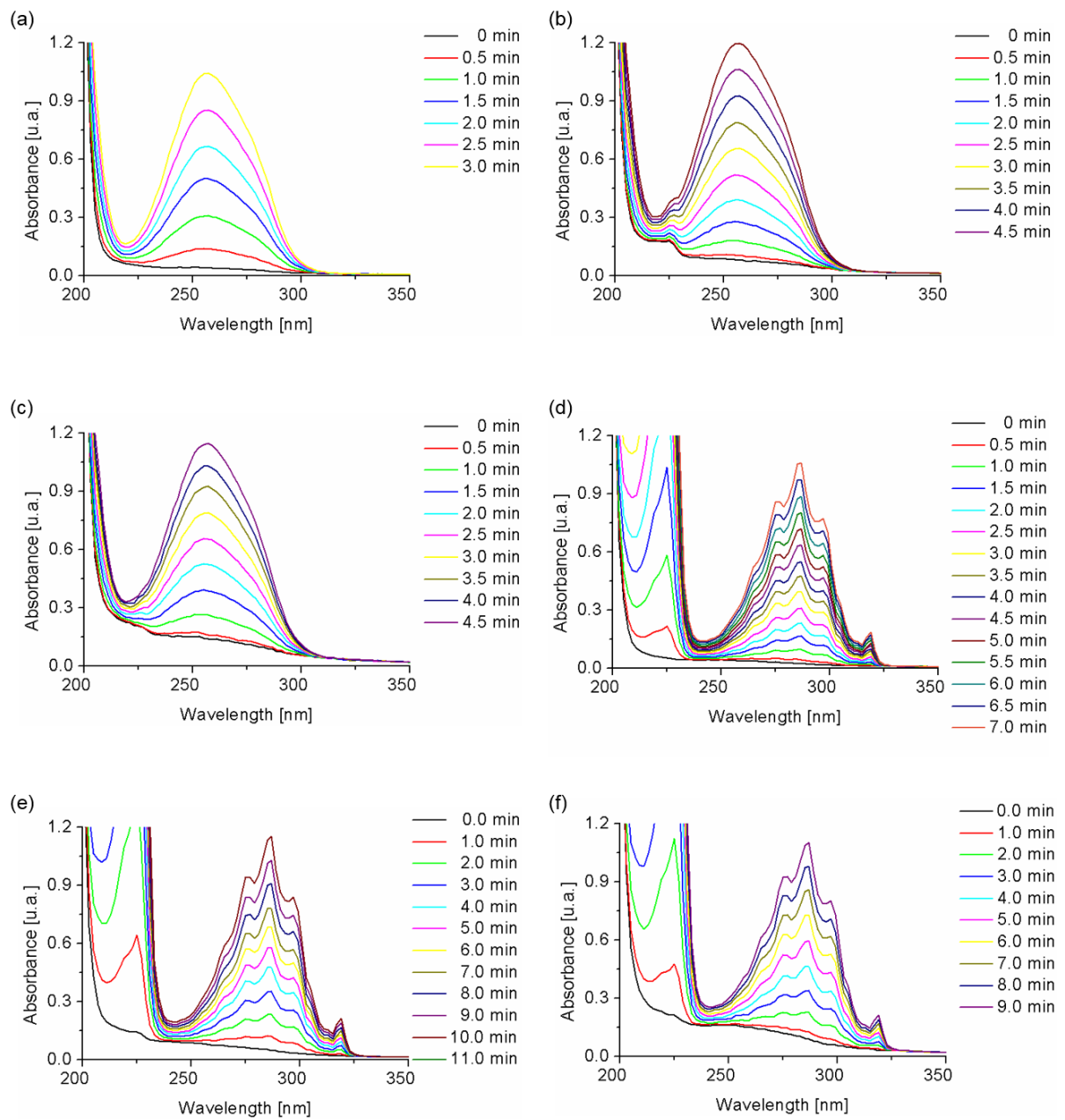


Figure 148: (a) – (c) UV/vis-absorbance of the MV-diffusion with respect to the LBL-modification process; (d) – (f) UV/vis-absorbance of the MV-diffusion with respect to the LBL-modification process; All spectra were recorded using a multipore membrane having a pore density of  $10^7$  pores/cm<sup>2</sup> and pore diameter of 200 nm. The LBL-deposition was performed using a 100:0-blend ratio [PAH|PVP]; ((a) and (d)) blank foil; ((b) and (e)) after deposition of four bilayers; ((c) and (f)) after formation of porous networks.

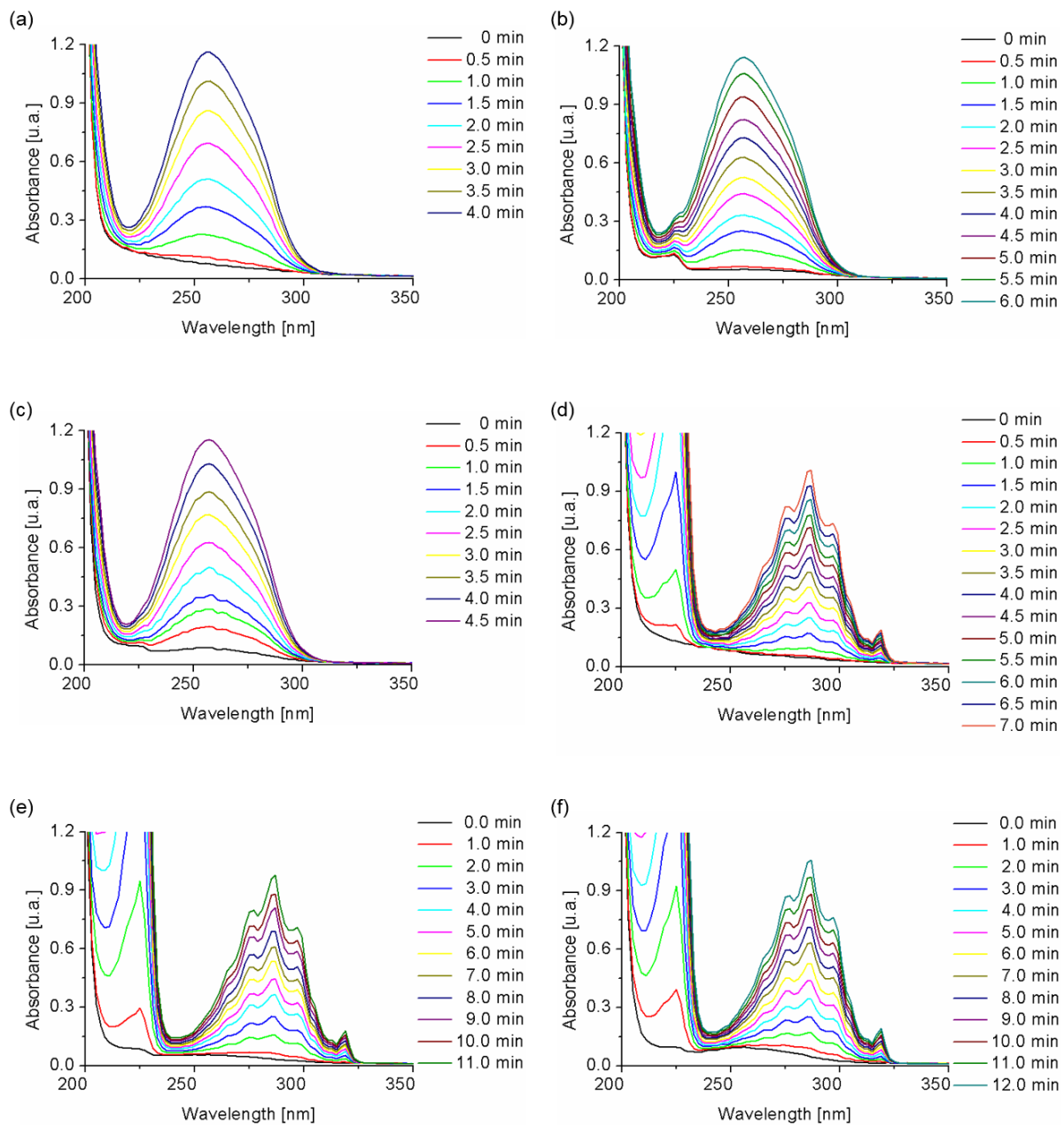


Figure 149: (a) – (c) UV/vis-absorbance of the MV-diffusion with respect to the LBL-modification process; (d) – (f) UV/vis-absorbance of the MV-diffusion with respect to the LBL-modification process; All spectra were recorded using a multipore membrane having a pore density of  $10^7$  pores/cm<sup>2</sup> and pore diameter of 200 nm. The LBL-deposition was performed using a 25:75-blend ratio [PAH|PVP]; ((a) and (d)) blank foil; ((b) and (e)) after deposition of four bilayers; ((c) and (f)) after formation of porous networks.

## Supplemental Data of Nanobody-Experiments

Peptide-sequences for the covalent attachment onto nanopores:

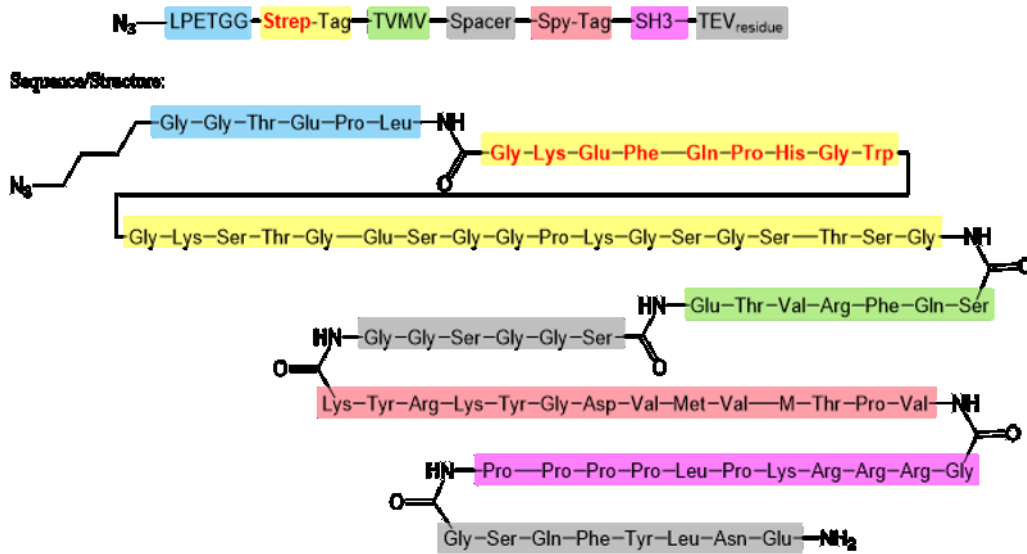


Figure 150: Amino acid sequence of the used peptide-Tag.

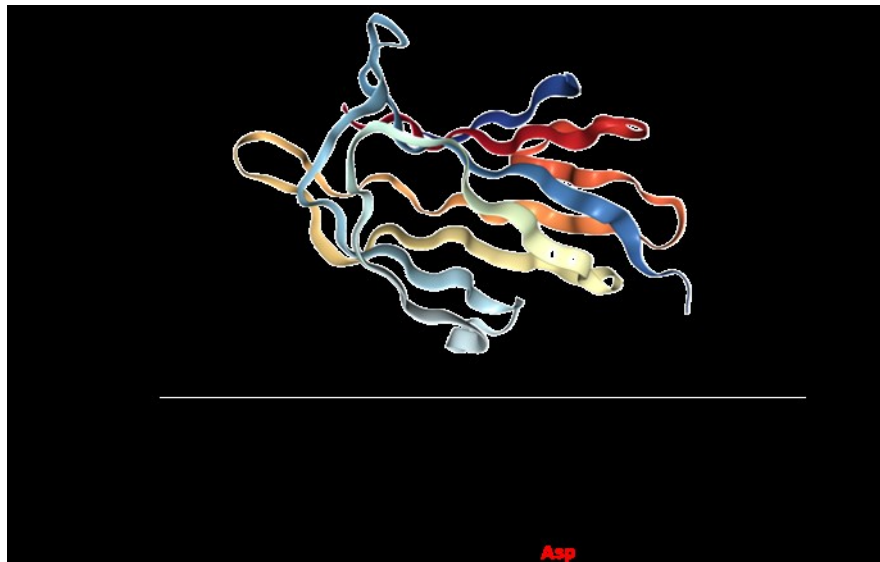


Figure 151: Amino acid sequence of the used SpyCatcher.

## List of Abbreviations

[3+2]	Five-centered cycloaddition	i. e.	id est (lat.); that is (engl.)
↓	precipitated	IHL	inner HELMHOLTZ layer
°C	degree Celsius	<i>I</i> V	Current-Voltage
‡	intermediate product	IVD	<i>in vitro</i> diagnostics
μM	Micromolar (uni); μmol/L	K <sup>+</sup> /KCl	Potassium(I)-ion/ chloride
a. u.	Arbitrary unit	keV/ meV	kilo electronvolt /mega electronvolt
AB	Antibody	L	litre
AD	Alzheimer's disease	<i>L</i>	liquid
ADEX	thin-film epoxy resist	<b>L</b>	lighter antibody chain
AG	Aktiengesellschaft	lat.	latin
Ag/AgCl	Silver/silverchloride	LBL	Layer-by-Layer
Al	aluminium	KIT	Karlsruhe Institute of technology
α, <i>f</i> <sub>rec</sub>	rectification factor	LOC	Lab-on-Chip
aq.	aqueous or solvated	Lys31	Lysine at position 31
ASP117	Asparagine at position 117	M	molar; mol/L
ATCUN	amino terminated copper- and nickel-ion motif	m	free electron mass
Au	Gold	M. Sc.	Master of Science (academic degree)
BMCL	Nα,Nα-bis(carboxymethyl)-L-lysine	MeOH	Methanol (solvent)
Bn.	Billion	MES	2-(N-morpholino)ethanesulfonic acid
C	Carbon	Min	minutes (unit)
c	value for the speed of light	Mol	mole (unit); amount of substance
CA	Contact angle	MoS <sub>2</sub>	molybdenum disulphide
Ca <sup>2+</sup>	Calcium-cation	MP	Multipore
CBA	chlorobenzoic acid	Ms	milli second (unit)
CBD	controlled breakdown	mS	milli Siemens (unit)
C-C	Carbon-carbon single bond	MV	Methylviologen
Cl <sup>-</sup>	Chlorine-anion	N	normal
CLSM	Confocal laser scanning microscopy	N/A	not available
COO <sup>-</sup> /COOH	Carboxylic ion /Carboxylic group	Na <sup>+</sup>	Sodium(I)-ion
Cu/Cu <sup>2+</sup>	Copper (element)/Copper (II)-ion	NaOH	sodium hydroxide
CuAAC	Copper-catalysed azide-alkinyl cycloaddition	Na <sub>2</sub> SO <sub>3</sub>	Sodium sulfite
d, D	tip and bulk diameter	NB	Nanobody
DCM	Dichloromethane	NDS	1,5-Naphatalene disulfate
dE/dx	energy loss	n <sub>e</sub>	electron density of substrate
DMAB	Dimethylamine borane	NH <sub>4</sub> OH	ammonium hydroxide
DMAP	4-N,N-Dimethylaminopyridine	Ni/ Ni <sup>2+</sup>	nichel (elementar)/Nichel(II)-ion
DMF	Dimethylformamide	NiSO <sub>4</sub>	Nickel (II) sulfate
DNA	deoxyribonucleic acid	Nm	nanometer
Dr.	Doktor (academic degree)	NP	nanopore
e	elementary charge	n <sub>t</sub>	number density of target atoms
EDA	ethylene diamine	NTA	Nitrilotriacetic acid
EDC	1-Ethyl-3-(3-dimethylaminopropyl) carbodiimide	O	Oxygen
EDL	electrical double layer	OH	Ohio
EIS	Electrochemical impedance spectroscopy	OH <sup>-</sup>	Hydroxyl ion
engl.	english	OHL	outer HELMHOLTZ layer
<i>et al.</i>	et alii (lat.); and others (engl.)	OP	Oligopore
EtOH	Ethanol	pA	picoampere
GFP	Green fluorescent protein	PAA	Poly(acrylic acid)
Glu77	Glutamic acid at position 77	PAH	Poly(allyl amine hydrochloride)
GmbH	Gesellschaft mit beschränkter Haftung	PC	poly(carbonate)
GSI	Gesellschaft für Schwerionenforschung	PdCl <sub>2</sub>	Palladium dichloride
H	Hydrogen	PET	poly(ethyleneterephthalate)
H <sub>2</sub> O	water	PFP	pentafluorophenol
HATU	1-[Bis(dimethylamino)methylene]-1H-1,2,3-triazolo[4,5-b]pyridinium 3-oxide hexafluorophosphate	pH	potentia hydrogenii (lat.)
HCl	Hydrochloric acid	PI	poly(imide)
HCOH	Formaldehyde	pK <sub>a</sub>	acid dissociation constant
HS	human serum	PLA	Poly(lactid acid)
HSA	human serum albumine	PVP	Poly(4-vinylphdridine)
<i>I</i>	current	RG	Research group
I	ionization energy	RT	Room temperature ( 23°C)
		s	solid
		S/N	signal to noise ratio
		SAM	Self-assembled monolayer
		SDS	sodium dodecylsulfate

---

SEM	Scanning electron microscopy
SHI	swift heavy ions
Si	Silicon
Si <sub>2</sub> N <sub>4</sub>	Silicon nitride
SiC	silicon carbide
SiO <sub>2</sub>	silicon dioxide; silica
SIS-18	name of the ring accelerator at GSI-facility in Darmstadt, Germany
SnCl <sub>2</sub>	Tin dichloride
SP	Single pore
SpAAC	Strain-promoted azide-alkynyl cycloaddition
SUEX	thick-film epoxy resist
<i>sulfo</i> -NHS	N-hydroxysulfosuccinimide
TEA	triethylamine
TM	Transport measurement
<i>u</i>	nucleon
UNILAC	universal linear accelerator
USD	US-Dollar
UV	Ultraviolet
<i>v</i>	velocity of the projectile
<i>v</i>	Vapor
<i>V</i>	Voltage
<i>V</i>	Volume
VHH	variable heavy homodimere
vis	visible
vol.-%	Volume percentage
wt.-%	weight percentage
<i>Z<sub>eff</sub></i>	effective charge of projectile ion
<i>Z<sub>t</sub></i>	atomic number of target atoms
<i>β</i>	ratio of velocity to speed of light

---

## List of Figures

- Figure 1: Classification of membrane transport proteins anchored inside the phospholipid layer: Directed membrane transport of targets: ‘Uniport’, ‘Symport’ and ‘Antiport’ (green-highlighted area); Different classes of membrane proteins according to the transport cargo: selective transport of specific molecules by “Carrier proteins”; water permeation throughout ‘Aquaporins’ and transport of ionic species via ‘Ion Channels’ (blue-highlighted area). Adapted from Hediger *et al.* (17), copyright (2013) Elsevier. ....2
- Figure 2: Schematic illustration of the patch-clamp-technique for the gating characterization of biological pore proteins, i. e. ion channels. Here, the cell membrane containing just a few ion channels is sealed by a glass pipette (a). (adapted from Collingridge *et al.* (29), copyright (2009) Elsevier) In the presence of a corresponding ligand, the channel opens and provides a flux of ions, which is detected as current (mostly in the pA range) (b). (adapted from Unwin *et al.* (30), copyright (1993) Cell Press).....3
- Figure 3: Biomimetic approach towards solid-state nanopores (blue) to overcome the fragility of biological nanopores (green) out of the integral cellular membrane. ....4
- Figure 4: Scheme of step growth polymers with their respective repeating units: a) poly(ethylene terephthalate) (Hostaphan® obtained by Mitsubishi Polyester Films GmbH); (b) poly(carbonate) (Macrofol® obtained by Bayer AG); (c) poly(imide) (Kapton® obtained by Dupont). (77) .....5
- Figure 5: Schematic set-up of the universal linear accelerator (UNILAC) at Wixhausen, Darmstadt. Acceleration pathway is illustrated and divided in three parts: the ion beam source at the beginning (green). The exit-energy amounts to 2.2 keV/u. After the handling in the electrostatic deflector (yellow), the specific energy is increased to 1,4 MeV/u. An additional flight through the high frequency accelerator (purple) speeds up the ion energy to 11.4. MeV/u. (74) (adapted from Toimil-Molares *et al.* (79), copyright (2012) Beilstein-Institute.) .....6
- Figure 6: SHI-irradiation throughout the polymeric sample: First, the sample irradiation generates an energy loss and the kinetic energy of the SHI is transformed into an electrostatic and then a nuclear energy loss. Second, due to the energy transfer, covalent bonds inside the polymeric target are broken along the trajectory of the SHI-pathway. Hence, a latent track formation is observable, including the track core as well as the track halo region. In addition, the process of the SHI provides molecules, such as hydrogen, oxygen, carbon dioxide, as well as particle formation and excitation of neutrons, protons and electrons. (77, 80) .....6
- Figure 7: Penetration depth as a function of specific projectile energy and energy loss  $dE/dx$  in dependence on specific ion energy. Calculated by SRIM 2008. (81) .....7
- Figure 8: Scheme of various pore densities used in this thesis and fabricated by the UNILAC-accelerator. It can be assumed that every track is transformed in to a pore. Consequently, the unit [pore/cm<sup>2</sup>] is used equally to the unit [tracks/cm<sup>2</sup>]. (83, 84) .....9
- Figure 9: Scheme of the etching-profile and the calculation of the etching-rate of the track zone and the bulk region. (adapted from Toimil-Molares *et al.* (79), copyright (2012) Beilstein-Institute).....9
- Figure 10: Underlying ester cleavage mechanism during the etching process. Adapted from Spohr *et al.* (90).....10
- Figure 11: Illustration of symmetrical (a) and asymmetrical (b) shaped nanopores inside polymeric membranes..10
- Figure 12: Schematic composition of the nanopore membrane surface. Here, the molecular surface groups created throughout the track-etching procedure are co-existing in a protonated neutral charged state and a negatively deprotonated stage. The  $pK_a$ -value amounts to 4.5 (a). (96) Formation of the EDL of the electrolyte onto charged surfaces. Rigid IHO = inner HELMHOLTZ-Layer; diffuse OHL= outer HELMHOLTZ-Layer (b).....11
- Figure 13: Scheme of possible surface modifications inside track-etched nanopore membranes based on the conversion of the surface (carboxylic) groups to introduce new functional properties (herein symbolized by the lock-compound): i) covalent coupling chemistry, ii) click-chemistry, iii) electrostatic interaction and iv) metal-surface complexation. Further, the modification using coupling chemistry (i) induces a new molecular bond between the lock-compound and the pore surface. Click-chemistry (ii) is illustrated using the reaction of two puzzle pieces. The electrostatic interaction (iii) is determined using common “plus and minus”
-

symbols and the metal complex (iv) is expressed throughout a complexation between metal ion ( $Me^+$ ) and the surface group. (13, 42, 55, 117) .....	12
Figure 14: Characterisation of the nanopores throughout <i>IV</i> -measurements. The setup consists of two measurement cells separated by the nanopore membrane and filled up with electrolyte solution. A pair of electrodes is inserted into the cells and an Amperemeter/Voltage source (not depicted) (a) Engineered sensing of solid-state nanopores based on a ligand-receptor interaction inside the pore region. Here, the inner surface of the nanopores is covered with receptor-units. In the presence of the respective ligand, the bionconjugation reaction occur causing a blockage of the pore region and leading to a restricted movement of ions. ....	13
Figure 15: Cross-section of a conical shaped nanopore covered by receptor-units across the entire nanopore surface with and without the analyte interaction (a) and their respective current output (b). In absence of the analyte (blank state), the current flow is unimpeded across the pore region (green bar). In contrast, the presence of the respective analyte (red key), the formation of the analyte-receptor conjugate occurs and leads to a blockage of the transmembrane current (red bar). ....	14
Figure 16: The cylindrical pore profile is presented (a) and the underlying current record versus time (green dotted line) caused by the applied triangular voltage versus time (blue line) (b). The plot of the measured current trace against the applied voltage course results in the current-voltage curve (red curve) (c), which explicitly has a linear course and is denoted as OHMIC behaviour. ....	14
Figure 17: The conical pore profile is presented (a) and the underlying current record versus time (green dotted line) caused by the applied triangular voltage versus time (blue line) (b). The plot of the measured current trace against the applied voltage course results in the current-voltage curve (red curve). ....	14
Figure 18: Negatively charged nanopore surface after the immersion of the conical nanopore membrane into the electrolyte (a). For the case of negative bias, the recorded current is mainly caused by the anion movement towards the anode (b). For the case of positive bias, the recorded current is induced by the enlarged cationic movement across the membrane (c). ....	15
Figure 19: Negatively charged nanopore surface upon immersion of the cylindrical nanopore membrane into electrolyte (a). For the case of negative and positive bias, the current flux remains the same leading to a linear shaped <i>IV</i> -curve. Here, no discrimination in the movement of cations and anions take place (b; c).....	15
Figure 20: In acidic surroundings, the carboxylic groups located on the pore surface are protonated and, therefore, the nanopore surface remained uncharged, after the immersion of the nanopore membrane into the electrolyte occurs (a). For the case of negative and positive bias, the current flux remains the same leading to a linear shaped <i>IV</i> -curve. Here, no discrimination of cations and anions take place (b; c). ....	16
Figure 21: Positively charged nanopore surface upon immersion of the conical nanopore membrane into electrolyte. Here, the nanopore surface is already modified with positively charged moieties causing an inverted EDL-arrangement compared to the EDL formed onto negatively charged surfaces (a). For the case of negative bias, the recorded current is mainly caused by the anion movement towards the cathode (b). For the case of positive bias, the recorded current is promoted by the enlarged movement of anions across the membrane (c). ....	16
Figure 22: Scheme of labelled analyte detection. Here, the analyte is interacting directly with the receptor-modified pore. ....	17
Figure 23: Scheme of label-free analyte detection. Here, the analyte is interacting directly with the receptor, which is attached in a preliminary complex to the pore surface having higher affinity to the respective analyte than to the precursor-moiety. ....	17
Figure 24: Sensing concept of a Biosensor: The analyte sample contains a mixture of various Bioligands. After the analyte sample is added to the biosensor, physicochemical signal is generated and transformed into an electrical signal throughout the Transducer. Then, the electrical signal is analysed throughout a data processor (computer). Adapted from (149). ....	20
Figure 25: The parameters that characterises a precise biosensor is illustrated:, sensitivity and selectivity (a) and the stability (b). (Graphical adaption of (150)). ....	20

Figure 26: Top 15 of the top-selling segments of the global medical technology industry in 2017 (blue bars) and forecast for the year 2024 (red bars) in billions of US dollars. (graphical application according to the data of survey "EvaluateMedTech - World Preview 2018, Outlook to 2024" adapted from Statista® on 10 <sup>th</sup> December 2019).	22
Figure 27: Set-up for the symmetrical etching of nanopores to establish cylindrically shaped nanopore within the polymeric membrane.	25
Figure 28: Asymmetrical etching set-up. For conical etching, single pore membranes and multipore membranes are treated simultaneously with the etchant and the identical etching conditions.	26
Figure 29: Scheme of the two-chamber setup filled with modification solution or electrolyte. (a); Picture and geometrical parameters of the half-cells used (b).	26
Figure 30: Scheme of experimental setup for the entire record of the modification procedure. Note that for <i>IV</i> -measurements, the cell is grounded and placed into a FARADAY-cage. Moreover, a pair of Ag/AgCl-electrodes is immersed into half-cells.	27
Figure 31: reprint of Figure 22; Incorporation of the recognition unit (the lock) for the analyte (the key) detection using the covalent modification method.	28
Figure 32: Molecular pathway for the modification of track-etched PET-nanopore membranes using carbodiimide-coupling chemistry. Note that in case $R_3 = \text{PPF}$ , the reaction is carried out in absolute ethanol, whereas in case of $R_3 = \text{sulfo-NHS}$ , an aqueous solution was used instead.	28
Figure 33: Molecular pathway for the modification of track-etched PET-nanopore membranes using carbodiimide-coupling chemistry with 1-[bis(Dimethylamin)methylen]-1H-1,2,3-triazol[4,5-b]pyridinium-3-oxid-hexafluoro-phosphate (HATU). Note, that $R_5$ symbolizes the residual molecular structure of the amine agents used in the HATU-coupling chemistry.	29
Figure 34: Incorporation of the receptor units (the lock) onto the nanopore surface for the later analyte (the key) detection using the modification method based on click-chemistry.	30
Figure 35: Illustrated mechanism of the strain-promoted azide-alkyne cycloaddition (SPAAC) onto the nanopore walls. The detailed sequence of the peptide is presented in the appendix section in Figure 150.	31
Figure 36: SpyTag/Catcher reaction for a successful immobilization of nanobodies onto the nanopore walls.	32
Figure 37: Mechanistic pathway of the covalent formation of the isopeptide bond between the amino acids lysine (Lys 31) of the 'SpyTag'-sequence and aspartic acid (Asp117) of the 'SpyCatcher'-sequence <b>15</b> with glutamic acid acting as proton shuttle <b>16</b> and facilitator of the reaction. Firstly, amino group of Lys31 is nucleophilic attacking the carboxyl-carbon of ASP117 and forms a zwitterionic intermediate <b>17</b> . The proton rearrangement reveals the hydrate structure <b>18</b> of the former Asp117. Finally, the amide group <b>19</b> is generated upon the release of water.	33
Figure 38: Incorporation of the recognition unit (the lock) for the later analyte (the key) detection using the modification method based on electrostatic interactions. For this purpose, the surface carboxylic groups has to be deprotonated (alkaline pH-range) to generate negatively charged surface groups acting as the core for the electrostatic attachment of positively charged molecules bearing a recognition unit for the later analyte detection.	34
Figure 39: Alternating deposition of the cationic Poly(allyl amine hydrochloride) [PAH] <b>20</b> and the anionic Poly(acrylic acid) [PAA] <b>21</b> onto the negatively charged nanopore surface covered with deprotonated carboxylic groups. Note that the deprotonation of carboxylic group occurs above pH 3 according to the $pK_a$ value.	34
Figure 40: Illustration of the alternating deposition of a polycationic blend, made of Poly(allylamine hydrochloride) [PAH] and poly(4-vinylpyridine), and the polyanionic Poly(acrylic acid) [PAA]. Consequently, a bilayer made of three components is formed onto the nanopore surface.	35
Figure 41: Illustrated pathway of metallic surface complexation onto the nanopore walls.	36

Figure 42: Two-step modification pathway for the generation of Ni-NTA-complexes onto the nanopore membrane. Therefore, the carboxylic surface groups are transformed into NTA-moieties throughout the successful EDC/PFP-coupling of BMCL 25. In the presence of Ni <sup>2+</sup> the formation of the stable Ni-NTA-complex 26 occurs. ....	36
Figure 43: Scheme of the metallic deposition onto the nanopore surface throughout a controlled redox-reaction. ....	37
Figure 44: IV-measurement setup for the conductance record across a nanoporous membrane. Here, the exemplary measurement of a single nanopore membrane is presented. The membrane is fixed in-between the two measurement cells filled with electrolyte solution (0.1 M KCl in pure water). A pair of Ag/AgCl-electrodes that is already connected to a grounded voltage source (Keithley 6487), is placed inside each half-cell. By applying a triangular voltage sweep from -1 V to 1 V, the current flux is monitored. ....	40
Figure 45: Mass transport experiment for the evaluation of analyte permeation across multiporous membranes. The membrane is clamped between two chambers, that are filled with feed solution (known amount of analyte) and pure buffer solution inside the permeate cell. Analyte permeation is recorded either using the manual or the automated setup. ....	41
Figure 46: Representative top-view (a) and cross-section (b) image of etched nanopores using scanning-electron microscope at different magnifications (2M NaOH @ 50°C, etching time 37mins). In addition, a thin sputtered gold-layer is covering the scanning samples to avoid charging effects. ....	43
Figure 47: Scheme of bioconjugation reactions inside pore membranes. (a) The ligand terminated nanopore membrane is non fluorescent. The treatment with fluorescent analyte leads to a glowing nanopore region (ON-reaction); (b) The nanopore is functionalized with a fluorescent ligand. The addition of analyte causes a quenching reaction of the former fluorophore (OFF-reaction). ....	44
Figure 48: CLSM holder for the nanopore membranes. ....	44
Figure 49: Scientific approach of track-etched nanopores towards nanopore-based biosensing applications. The investigated parameter is highlighted with the orange colouring. Here, the focus lies on the used pore materials, the successful attachment of (novel) receptors as well as the right choice of the measurement surrounding. ....	46
Figure 50: (a) Beam treatment for the irradiation of polymeric films at: (a) the company <i>it4ip</i> S.A (Adapted from <i>it4ip</i> -webpage (215) , copyright (2020) <i>it4ip-iontracktechnology</i> S. A.) and (b) at the GSI-HELMHOLTZ-Centre for Heavy Ion Research. ....	48
Figure 51: <i>In-situ</i> and <i>ex-situ</i> shape control of nanopores. ....	48
Figure 52: SEM-images of commercial membranes (10 <sup>4</sup> ion tracks/cm <sup>2</sup> ) after immersing the membranes in 2 M NaOH-solution at 50 °C for 20 min (a), 30 min (b) and 60 min (c). ....	49
Figure 53: SEM-images of commercial membranes (10 <sup>7</sup> tracks/cm <sup>2</sup> ) after immersing the membranes in 2 M NaOH-solution at 50 °C for 10 min (a), 30 min (b) and 60 min (c). ....	49
Figure 54: SEM-images of GSI-membranes (10 <sup>7</sup> tracks/cm <sup>2</sup> ) after immersing the membranes in 2 M NaOH-solution at 50 °C for 20 min (a), 30 min (b) and 60 min (c). ....	50
Figure 55: Nanopore opening as a function of etching time (a). IV-measurements of commercial membranes (10 <sup>4</sup> tacks/cm <sup>2</sup> ) after immersing the membranes in 2 M NaOH-solution at 50 °C for certain etching times (b). ....	50
Figure 56: SEM-images of cross-sections of commercial membranes (10 <sup>7</sup> track/cm <sup>2</sup> ) after 30 min (a) and 60 min (b) of etching time. ....	51
Figure 57: Schematic track-etching process and the respective distances <i>d</i> . ....	51
Figure 58: Surface SEM-images of GSI-membranes containing 100 nm pore diameter (a) and commercial membranes containing nanopores with 100 nm diameter (b). In both cases, the specification of the supplier determines pore densities of 10 <sup>7</sup> pores/cm <sup>2</sup> . Red circles simplify the pore localization. ....	53

Figure 59: SEM-images showing the cross-section of nanopores (100 nm) of GSI-membranes (a) and commercial membranes (b). In both cases, the specification of the supplier determines pore densities of $10^7$ pores/cm <sup>2</sup> .	53
Figure 60: SEM-images showing the top-view of GSI-membranes containing 100 nm pore diameter (a) and commercial membranes containing already etched nanopores with 100 nm diameter (b). In both cases, the specification of the supplier determines pore densities of $10^7$ pores/cm <sup>2</sup> .	54
Figure 61: IV-curves of GSI-membranes containing nanopores (100 nm)(a) and commercial membranes containing already etched nanopores of 100 nm diameter (b) before and after DMF-treatment over 12 h, measured at different pH values. In both cases, the specification of the supplier pore densities of $10^4$ pores/cm <sup>2</sup> .	55
Figure 62: IV-curves of GSI-membranes containing 100 nm pore diameter (a) and commercial membranes containing already etched nanopores with 100 nm diameter (b) after EDA-Modification, measured at different pH values. In both cases, the specification of the supplier provides pore densities of $10^4$ pores/cm <sup>2</sup> .	56
Figure 63: pH-dependant surface charge densities inside commercial membranes upon one-sided EDA-modification.	56
Figure 64: shape characterization approach towards PLA-nanopores. First, the irradiated PLA membranes are pre-treated by organic solvents or UV-sensitization. Etched membranes are analysed by SEM-imaging. Additionally, replica were obtained by metal deposition and PLA-removal.	60
Figure 65: IV-curve of three exemplary PLA-membranes prior to the etching step measured in 0.1M KCl solution.	60
Figure 66: Top-view SEM-images of PLA membrane ( $10^7$ tracks/cm <sup>2</sup> ) after 1 h of immersion into aqueous NaOH-solution (50 mM) at 30 °C (a), 40°C (b) and 50°C (c).	61
Figure 67: Top-view SEM-images of PLA membranes ( $10^7$ tracks/cm <sup>2</sup> ) after 1 h of immersion in 50mM NaOH-solution prepared in water-methanol mixture (60:40) at 30°C (a), 40°C (b) and 50°C (c).	62
Figure 68: schematic explanation of the peel-off effect observed on PLA-membranes during the etching process.	62
Figure 69: Top-view SEM-images of PLA membranes ( $10^7$ tracks/cm <sup>2</sup> ) after 1 h of immersion into aqueous 50 mM NH <sub>4</sub> OH-solution at 30 °C (a), 40°C (b) and 50°C (c).	63
Figure 70: Top-view SEM-images of PLA membranes ( $10^7$ tracks/cm <sup>2</sup> ) after 1 h of immersion into 50 mM NH <sub>4</sub> OH-solution prepared in water-methanol mixture (60:40) at 30 °C (a), 40°C (b) and 50°C (c).	63
Figure 71: Top-view SEM-images of PLA membranes ( $10^7$ tracks/cm <sup>2</sup> ) after immersion into 2 M NaOH-solution for different etching times: 60 min (a), 90 min (b) and 120 min (c).	64
Figure 72: Top-view SEM-images of PLA membranes ( $10^7$ tracks/cm <sup>2</sup> ) after immersion into 3 M NaOH-solution for different etching times: 30 min (a), 45 min (b) and 60 min (c).	64
Figure 73: graphical correlation and linear fit of estimated <i>pit</i> diameters with the etching time.	65
Figure 74: Top-view SEM-images of the 3D-replica of PLA membranes ( $10^7$ tracks/cm <sup>2</sup> ) upon nickel film deposition and dissolving of the PLA-membrane. Here, the negative structures are presented after the membrane was exposed to 2M NaOH-solution at 50°C for different etching times: 60 min (a), 90 min (b) and 120 min (c).	65
Figure 75: Top-view SEM-images of the 3D-replica of PLA membranes ( $10^7$ tracks/cm <sup>2</sup> ) after nickel film deposition and dissolution of the PLA-membrane. Here, structures are presented after the membrane was exposed to 3 M NaOH-solution at 50°C for different etching times: 30 min (a), 45 min (b) and 60 min (c).	66
Figure 76: estimation of tip-height <i>H</i> and cone-angle $\alpha$ based on SEM-images.	66
Figure 77: Lateral SEM-images of the 3D-replica of PLA membranes ( $10^7$ tracks/cm <sup>2</sup> ) after nickel film deposition and dissolution of the PLA-membrane. Here, the structures are presented after the membrane was exposed to 2 M NaOH-solution at 50 °C for 45 min (a), 60 min (b), 90 min (c) as well as 120 min (d) and into 3M NaOH-solution for 60 min (e) as well as 90 min (d), respectively.	66

Figure 78: Changes in the IV-characteristics (a) and nanopore conductance (b) on the successful surface modification of COOH groups with BMCL and subsequent formation of Ni-NTA-complexes onto the nanopore surface. ....	70
Figure 79: Detection of histamine (Hm) using NTA-modified conical single nanopore. On exposure to Hm, a stable Ni-Hm-complex is generated, which leads to the regeneration of NTA-moieties onto the nanopore. ....	71
Figure 80: IV-characteristics of the Ni-NTA modified conical single nanopore (tip diameter = 35 nm; base diameter = 700 nm) in presence of different Hm-concentrations including the calculated surface charge density (a). Course of the respective conductance G at 1 V obtained from the corresponding I-V curve (b). ..	72
Figure 81: IV-characteristics (a) and conductance (b) for the selective Hm-measurement within a conical single pore membrane (tip diameter: 35 nm; base diameter: 700 nm). IV-curve of the blank pore (red graph) is presented Ni-NTA complexes onto the pore surface as well as the IV-curves in presence of various neurotransmitters (1mM) in the electrolyte solution: glycine (Gly), 5-hydroxytryptamine (5-HT), $\gamma$ -aminobutyric acid (GABA), dopamine (DA), histamine (Hm).....	73
Figure 82: IV-characteristics (a) and conductance (b) for selective Hm-measurement within a conical single pore (tip diameter: 45 nm; base diameter; 800 nm). IV-curve of blank pore (red graph) is presented indicating Ni-NTA complexes onto the pore surface as well as the IV-curves in presence of various neurotransmitters (1mM) in the electrolyte solution: glycine (Gly), 5-hydroxytryptamine (5-HT), $\gamma$ -aminobutyric acid (GABA), dopamine (DA), histamine (Hm). ....	73
Figure 83: The plots determined the reversibility of the complexation/ decomplexation along the Hm-detection, tested by performing cycles to track the changes obtained in the conductance G(1V). ....	74
Figure 84: sensing concept of specific potassium detection. Here, the track etched nanopore membrane was modified in the presence or absence of potassium ions with bis-podand-NH <sub>2</sub> . ....	76
Figure 85: IV-curves of unmodified-nanopore (a) and bis-podand-modified nanopore (b) upon exposure to various electrolyte solutions having a concentration of 100 mM of the metal chloride (pH 6.5). ....	77
Figure 86: IV-measurement and respective conductance values (at 2 V) showing the sensitivity towards potassium cations using the single pore membrane modified with bis-podand moieties in presence of different KCl concentration in electrolyte solution. ....	78
Figure 87: The 'floppy' vs 'in plane'-scaffold of bis-podand-NH <sub>2</sub> in presence and absence of potassium ions. ....	79
Figure 88: The changes in the ionic transport of the unmodified pore membrane (a) and after the random attachment of bis-podand-moieties in absence (b) of potassium ions.....	80
Figure 89: Experimental setup and procedure for the surface modification using LBL-deposition technique onto nanopore membranes. In this case, the experimental pathway for the deposition of two oppositely charged layers is shown by repeating the LBL-assembly the generation of multi-layered films onto the nanopore surface is achieved. After every polyelectrolyte deposition numerous washing steps are carried out, by removing the polyelectrolyte solution and filling the half-cells with pure buffer-solution. ....	83
Figure 90: LBL-modification performed through the deposition of two compounds (classical system), presented in section 3.2.1 and three compounds (hybrid system), presented in section 3.2.2., separately. ....	84
Figure 91: Schematic modification of track-etched nanopores using LBL-method, to deposit polyelectrolytes onto the entire nanopore surface. Here, the deposition of one bilayer [PAH] <sub>1</sub> [PAA] <sub>1</sub> is presented as well as their transformation into porous networks. Firstly, the unmodified nanopore is coated with a layer of [PAH] followed by a layer of [PAA]. Coulomb attraction between positive amine groups and negative carboxylic groups are demonstrated leading to the generation of the stacked structures. Afterwards, exposition to silver(I)-ion solutions is carried out leading to a generation of pores within the multilayers. ....	85
Figure 92: (a) Characteristic IV- curves before (black line) and after LBL self-assembly of two bilayers of PAH and PAA using a singlepore membrane (D= 307 nm and d= 28 nm). IV-curves are measured in 0.1 M KCl-electrolyte. (b) respective zoomed IV-curves of (a). Illustration of the rectifying factors $f_{rec}$ calculated by the ratio of the current at +1 V to -1 V, respectively (c). ....	86

Figure 93: Characteristic <i>IV</i> -curves before (black line) and after LBL-assembly of two bilayers of PAH and PAA using a multipore membrane ( $10^7$ pores/cm <sup>2</sup> ; $D=107$ nm; $d=28$ nm) measured in 0.1 M KCl-electrolyte. ....	87
Figure 94: (a) Characteristic <i>IV</i> -curves of the single conical nanopore modified with [PAH] <sub>2</sub> [PAA] <sub>2</sub> (black line) upon exposure to aqueous solutions containing different concentrations of silver(I)ions. (b) Cross-section of multipore membrane having 200 nm cylindrical nanopores ( $d=200$ nm) modified with four bilayers of PAA and PAH and (c) the same multipore membrane after exposure to aqueous Ag <sup>+</sup> -solution (100 nM). ....	88
Figure 95: Schematic representation of LBL modification of track-etched nanopores by the deposition of polyelectrolytes onto the entire nanopore surface. Here, the deposition of two bilayers [PAH PVP] <sub>2</sub> [PAA] <sub>2</sub> is presented as well as their transformation into porous networks. Firstly, the unmodified nanopore is coated with a layer of [PAH PVP] followed by a layer of [PAA]. Coulomb attraction between positive amine groups and negative carboxylic groups as well as hydrogen-bridges of PVP and protonated carboxylic groups are demonstrated, leading to the generation of the stacked structure. Afterwards, cross-linking of the multilayers on the channel surface occurred by a layer contraction. Finally, the pH induced wash-out of hydrogen-bonded PVP is carried out leading to the generation of pores within the multilayers. ....	90
Figure 96: <i>IV</i> -measurements using a single pore membrane (a) and an oligopore membrane (b) having a diameter of 200 nm. Note that the measurements were performed using an MES-buffered KCl-electrolyte having a concentration of 100 mM (pH: 3.9). Inlet shows corresponding conductance values at +1 V in dependence on the underlying modification state. Modification state 1 to 4 is referred to one deposited bilayer of polyelectrolytes, e. g. modification state 1 symbolizes [PAH PVP] <sub>1</sub> [PAA] <sub>1</sub> . ....	91
Figure 97: Transport of (a) MV and (b) NDS with respect to the modification state using a 50:50-ratio of [PAH PVP]. (the corresponding UV/vis-data given in Appendix); (c) comparison of transported amounts and corresponding UV/absorbance spectra of MV (left) and NDS (right) for a fixed diffusion time of 4 min in dependence on the modification state. The results contain the average of three measurements. Note that the error bars are negligible because their value does not protrude beyond the size of the data point. ....	94
Figure 98: Transport of (a) MV and (b) NDS with respect to the modification state using a 100:0-ratio of [PAH PVP]. (corresponding UV/vis-data given in Appendix); (c) comparison of transported amounts and corresponding UV/vis-absorbance spectra of MV (left) and NDS (right) for a fixed diffusion time of 4 min in accordance to the modification state. The results contain the average of three measurements. Note that error bars are negligible because their value does not protrude beyond the size of the data point. ....	96
Figure 99: Transport of (a) MV and (b) NDS with respect to the modification state using a 25:75-ratio of [PAH PVP]. (corresponding UV/vis-data given in Appendix section 5.3); (c) comparison of transported amounts and underlying UV/vis-absorbance spectra of MV (left) and NDS (right) for a fixed diffusion time of 4 min in accordance to the modification state. The results contain the average of three measurements. Note that error bars are negligible because their value does not protrude beyond the size of the data point. ....	97
Figure 100: Sensing concept for copper detection using track-etched nanopore membranes modified with fluorophore-marked tripeptide-moieties bearing ATCUN-motif sequence for the specific copper binding. Note that in presence of cupric ions, the formation of the ATCUN-copper-complex occurred, leading to the fluorescent quenching. The addition of EDTA induces the regeneration of the pore surface. ....	100
Figure 101: BOLTZMANN-fit (black and grey line) determines the sigmoidal trend of titration curve. The respective absorption values are based on the UV/vis-spectra using 1 mM solution of Cu(II) (black) and Ni(II) (grey) at different the pH conditions. The experimental results were analysed by Dr. Lena Müller. ....	101
Figure 102: Fluorescence titration curve using the ATCUN-peptide (1 $\mu$ M in 100 mM MES-buffered solution, pH 6.5) at different concentrations of CuSO <sub>4</sub> (a) and NiSO <sub>4</sub> (b). For the case of copper ions, upon increasing the concentration of copper ions (from 0 to 25 $\mu$ M), the significant fluorescence reduction is observed as a function of the molar ratio of copper-(II)-ions to ATCUN-peptide. For the case of nickel ions, upon increasing the concentration of nickel ions (from 0 to 1.3 mM), only marginal fluorescence reduction is observed as a function of the molar ratio of nickel-(II)-ions to ATCUN-peptide. The fluorescence spectra were carried out and analysed by Dr. Lena Müller. ....	101
Figure 103: <i>IV</i> -curves demonstrating the ATCUN-modification onto a blank conical pore membrane having $10^4$ pores/cm <sup>2</sup> . ....	102

Figure 104: <i>IV</i> -curve of the ATCUN-modified nanopore membrane upon exposure to various Cu <sup>2+</sup> -concentrations in the electrolyte solution (100 mM KCl, MES buffer, pH 6.5) (a). The corresponding conductance values are obtained from the respective <i>IV</i> -data at 1 V that result in a sigmoidal response with respect to the tested Cu <sup>2+</sup> -concentrations (b).....	103
Figure 105: <i>IV</i> -curve of the ATCUN-modified pore membrane upon exposure to various divalent metal ions (100pM) in the electrolyte solution (100 mM KCl, MES buffer, pH 6.5) (a) and conductance values at 1 V shows reversible complexation/decomplexation of Cu <sup>2+</sup> -ions (b). Here, the exposure to 1 nM Cu <sup>2+</sup> -amount in the electrolyte solution (100 mM KCl, MES buffer, pH 6.5) leads to the current increase (red dots) due to the enhance surface charge of the pore upon generation of ATCUN-Cu-moieties across the entire pore surface. The on-going treatment with 1 mM EDTA-solution causes the removal of Cu <sup>2+</sup> -ions from the pore surface, inducing a recovery of the pore surface (blue dots). .....	104
Figure 106: AFM-images of nanopore membrane surfaces having a pore density of 10 <sup>7</sup> pores/cm <sup>2</sup> . AFM-images of the blank nanopore membranes are shown in (a) and (b), whereas the ATCUN-modified pores are shown in (c) and (d). Note that the figures (a) and (c) provide the topological images of the respective pore and (b) and (d) shows phase differences. In this case brighter areas show higher interactions between cantilever and pore surfaces. The resulting halo in (d) indicates softer regions and, therefore, the presence of the peptide. The AFM-images were kindly recorded by Dr. Christian Dietz (RG Stark). .....	105
Figure 107: CLSM- images of fluorescently labelled ATCUN-moieties after the covalent attachment onto the multipore membrane (10 <sup>7</sup> pores/cm <sup>2</sup> ). Here, the reflected light as well as the florescent emission images are shown in (a) and (b), respectively. Note that, the dark area indicated the absence of fluorescent groups, i.e., the absence of ATCUN because the etching area is not identical to the modification area. Moreover, the quantification of fluorescence reduction upon exposure to various concentrations of Cu <sup>2+</sup> ion ranging from 0 μM to 60 μM is presented and linearly fitted in (c). .....	106
Figure 108: CLSM-images to evaluate the “on-off”-state of ATCUN-modified nanopore membranes, showing the reversibility of the ACTUN-Cu <sup>2+</sup> -interaction in presence of 100 μM Cu <sup>2+</sup> -solution and 1 mM EDTA-solution. Note that the term ‘+wash’ means in total one washing-step with MES-buffer (pH6.5) followed by three washing steps with pure water. ....	107
Figure 109: Antibodies (AB) composition and respective structural coherency of nanobodies (NB). .....	109
Figure 110: Formation of an intact domain using splitted SpyTag and SpyCatcher-sequences. Peptide and protein structures are adapted from protein data bank (Code: 4MLI). .....	110
Figure 111: Modification pathway for the covalent attachment of NB-moieties onto the nanopore surface. First, the pore surface is modified with DBCO-groups using EDC/PFP-chemistry. Then, the peptide-tag is attached through a [3+2]-cycloaddition between azido-units of the peptide-tag and the DBCO-triple bond. Upon exposing the membrane to SpyCatcher-NB-moieties, the isopeptide bond formation within the Tag/Catcher-system occurs, connecting the NB with the pore surface. ....	111
Figure 112: <i>IV</i> -curves of single pore membranes for different modification steps measured in 0.1 M KCl electrolyte (PBS, pH 7). .....	112
Figure 113: <i>IV</i> -curves for positive voltages (a) and respective conductance values at 1 V (b) of the single pore membrane functionalized with NB <sub>GFP</sub> -moieties, upon exposure to different GFP-concentrations measured in 0.1 M KCl electrolyte (PBS buffer, pH 7). .....	113
Figure 114: side-view and top-view of the crystal structure of GFP (PDB-code: 1EMA).....	113
Figure 115: <i>IV</i> -curves for positive voltages (a) and respective conductance values at 1 V (b) of the single pore membrane functionalized with NB <sub>mCherry</sub> -moieties, upon exposure to different mCherry-concentrations measured in 0.1 M KCl electrolyte (PBS buffer, pH 7). .....	114
Figure 116: Side-view and top-view of the crystal structure of mCherry (PDB-code: 1EMA). .....	114
Figure 117: <i>IV</i> -curves of pore membranes for different modification steps measured in 0.1 M KCl electrolyte (PBS, pH 7). .....	115

Figure 118: <i>IV</i> -curves for positive voltages of the single pore membrane functionalized with NB <sub>GFP</sub> -moieties, upon exposure to different mCherry-concentrations (a) and different GFP-concentrations (b) measured in 0.1 M KCl electrolyte (PBS buffer, pH 7). Conductance values at 1 V with respect to the measured proteins (c)...	115
Figure 119: <i>IV</i> -curves for positive voltages of the single pore membrane functionalized with NB <sub>mCherry</sub> -moieties, upon exposure to different mCherry-concentrations (a) and different GFP-concentrations (b) measured in 0.1 M KCl electrolyte (PBS buffer, pH 7). Conductance values at 1 V with respect to the measured proteins (c). .....	116
Figure 120: Cross-sectional CLSM-images of the NB-modified multipore membranes (10 <sup>7</sup> pores/cm <sup>2</sup> , bulk opening of 510 nm for NB <sub>GFP</sub> -modified membrane; 680 nm for NB <sub>mCherry</sub> -modified membrane) after exposing the membrane to the respective Protein-solutions. The following combinations are displayed: (a) NB <sub>GFP</sub> -membrane interacting with GFP, (b) NB <sub>mCherry</sub> -membrane interacting with mCherry, (c) NB <sub>mCherry</sub> -membrane interacting with GFP, (d) NB <sub>GFP</sub> -membrane interacting with mCherry. ....	117
Figure 121: <i>IV</i> -curves for positive voltages of the single pore membrane functionalized with the peptide-tag, upon exposure to different mCherry-concentrations (a) and different GFP-concentrations (b) measured in 0.1 M KCl electrolyte (PBS buffer, pH 7). Conductance values at 1 V with respect to the measured proteins (c)...	118
Figure 122: <i>IV</i> -curves (a) and respective conductance values (b) measured in 0.1 M KCl electrolyte (PBS buffer, pH 7) of the single pore membrane functionalized with the peptide-tag. The <i>IV</i> -curves were recorded prior to the protein exposure, herein referred to as Peptide <sub>blank</sub> -state (black graph and bar) and after the respective protein series, herein referred to as Peptide <sub>mCherry</sub> -state (red graph and bar) and Peptide <sub>GFP</sub> -state (green graph and bar). Note that after every protein series, the membrane was washed with urea, EtOH and pure buffer in order to remove protein residues. ....	119
Figure 123: <i>IV</i> -curves for positive voltages of the single pore membrane functionalized with the NB-moieties with an affinity towards GFP, upon exposure to different mCherry-concentrations (a) and different GFP-concentrations (b) measured in 0.1 M KCl electrolyte (PBS buffer, pH 7). Conductance at 1 V with respect to the measured proteins (c). ....	120
Figure 124: Comparison and construction of the laboratory set-up for the <i>IV</i> -measurement (a) and the designed nanopore-based LOC-system (b). The LOC-image is adapted with permission of Mario El-Khoury, M. Sc. (RG Schlaak).....	123
Figure 125: 1 <sup>st</sup> and 2 <sup>nd</sup> generation of the LOC-devices. ....	124
Figure 126: pH-dependent <i>IV</i> -characteristics of multipore membranes having a pore density of 10 <sup>7</sup> pores/cm <sup>2</sup> . The LOC is composed of a nanopore membrane area of 5 x 5 mm <sup>2</sup> originated from the same multipore membrane. ....	125
Figure 127: <i>IV</i> -curves monitoring the successful modification and histamine detection inside the 1 <sup>st</sup> generation of LOC-chips. ....	126
Figure 128: Demonstration of the leaking ADEX-material of the upper microfluidic chamber (a) and respective scheme indicating the presence of free adhesive residues that are dissolved upon intensive contact with modification mixtures and electrolyte solutions. ....	126
Figure 129: pH-dependent <i>IV</i> -characteristics of multipore membranes having a pore density of 10 <sup>7</sup> pores/cm <sup>2</sup> . LOC is composed of a nanopore membrane piece of 5 x 5 mm <sup>2</sup> taken from the same multipore membrane already used for the 1 <sup>st</sup> LOC-generation. ....	127
Figure 130: <i>IV</i> -curves of Chip 3 (a) and Chip (4) measured in 0.1 M KCl-electrolyte to monitor the NTA-modification procedure inside the 2 <sup>nd</sup> LOC-generation.....	128
Figure 131: <i>IV</i> -curves of Chip 3 (a) and Chip 4 (b) measured in 0.1 M KCl-electrolyte to monitor the histamine detection inside the 2 <sup>nd</sup> LOC-generation. ....	129
Figure 132: Conductance values of Chip 3 (a) and Chip 4 (b) at 1 V measured in 0.1 M KCl-electrolyte to monitor the histamine detection inside the 2 <sup>nd</sup> LOC-generation. Note that the dashed line is the assumed sigmoidal correlation between conductance and histamine amount.....	129

Figure 133: Classes of possible experimental media. The classical electrolyte used for <i>IV</i> -measurements consists of 100 mM KCl-solution. The electrolyte complexity is stepwise increased from electrolyte based on human serum albumin (HSA)) to human serum (HS) solutions with aiming to perform measurements in blood samples (dotted line).....	131
Figure 134: <i>IV</i> -curve of the unmodified oligopore membrane with respect to various electrolyte solutions: distilled water, 100 mM KCl-electrolyte and human serum-electrolytes at different temperature. ....	132
Figure 135: <i>IV</i> -curves demonstrating the ATCUN-modification onto a blank conical pore membrane having $10^4$ pores/cm <sup>2</sup> .....	133
Figure 136: <i>IV</i> -curve of the ATCUN-modified membrane having $10^4$ pores/cm <sup>2</sup> upon exposure to various Cu <sup>2+</sup> -concentrations in the electrolyte solution (100 mM KCl, MES buffer, pH 6.5) (a). The underlying conductance values are obtained from the corresponding <i>IV</i> -data at 1 V with respect to the tested Cu <sup>2+</sup> -concentrations (b). <i>IV</i> -curve of the ATCUN-modified oligopore upon exposure to various divalent metal ions (100 pM) in the electrolyte solution (100 mM KCl, MES buffer, pH 6.5) (c). Conductance values at 1 V shows the reversible complexation/decomplexation of Cu <sup>2+</sup> -ions. Here, on exposure to 100 pM Cu <sup>2+</sup> -concentration in the electrolyte solution (100 mM KCl, MES buffer, pH 6.5) exhibits the current increase (red dots) due to the enhance surface charge of the pore upon generation of ATCUN-Cu-moieties on the pore surface. Treatment with 1 mM EDTA-solution causes the removal of Cu <sup>2+</sup> -ions from the pore surface, inducing a recovery of pore surface (blue dots).....	134
Figure 137: <i>IV</i> -measurements using the ATCUN-modified oligopore membrane upon exposure to different Cu <sup>2+</sup> -concentrations with respect to the electrolyte composition: 100 mM KCl solved in pure HS-solution (a); 100 mM KCl solved in 1:2 diluted HS-water-solution (b) and 100 mM KCl solved in diluted 1:10 HS-water-solution (c). The underlying conductance values at 1 V are presented with respect to the electrolyte composition and Cu <sup>2+</sup> -amount (d).....	135
Figure 138: <i>IV</i> -curve of the ATCUN-modified oligopore upon exposure to various divalent metal ions (100 pM) in the HS-based electrolyte solution (100mM KCl, 1:2-ratio of HS and water) (a). Conductance values at 1V show the reversible complexation/ decomplexation of Cu <sup>2+</sup> -ions. Here, on exposure to 100 pM Cu <sup>2+</sup> -amount in the HS-based electrolyte solution provides the current reduction (red dots) due to the suggested HSA-interaction upon the generation of ATCUN-Cu-moieties. The on-going treatment with 1mM EDTA-solution leads to the removal of Cu <sup>2+</sup> -ions from the pore surface, inducing a recovery of ATCUN moieties (blue dots). ....	136
Figure 139: Conductance and <i>IV</i> -curves for positive applied voltages using unmodified oligopores with respect to various Cu <sup>2+</sup> -amounts solved in 0.1 M KCl electrolyte solution (1:2-diluted HS-water-mixture). ....	137
Figure 140: <i>IV</i> -curves for positive applied voltages of the ACTUN-modified oligopores with respect to various Cu <sup>2+</sup> -amounts dissolved in HS-based electrolyte solution containing 0.1M KCl in 1:2-diluted HS-water-mixture (a) and dissolved in HSA-based electrolyte consisting of 0.1M KCl in aqueous 150 mM HSA-solution (b). ....	138
Figure 141: Suggested interaction between Cu <sup>2+</sup> -moieties and ATCUN-modified pore surface. For the case of performing the Cu <sup>2+</sup> -series in aqueous electrolyte, the adsorption of Cu <sup>2+</sup> -ions leads to an increased surface net charge. For the use of HS-based electrolytes, the presence of albumin protein provides the formation of ATCUN-Cu <sup>2+</sup> -albumin groups, causing a decrease of current due to the huge spatial expansion. ....	139
Figure 142: (a) UV/vis-absorbance spectra and (b) calibration curve for NDS-calibration; (c) UV/vis-absorbance spectra and (d) calibration curve for MV-calibration. The calibration experiment performed in a triple measurement. Note that error bars are negligible because they do not protrude beyond the size of the data point. Calibration was performed prior to the mass transport experiments, by measuring the absorbance of the positively charged methylviologen (MV) and the negatively charged 1,5-naphthalene disulfonate (NDS). Here, the maximum absorbance values at a given wavelength 256 nm (for MV) and 286nm (for NDS) is plotted in dependence on the respective analyte concentration. Unknown analyte amounts were calculated using the respective calibration curve according to the BEER-LAMBERT's equation. ....	159
Figure 143: UV/vis-spectra for the time-resolved MV-diffusion across multipore membranes having $10^7$ pores/cm <sup>2</sup> and a diameter of (a) 35 nm, (b) 90 nm, (c) 200 nm; (d) Time-dependant transport of MV with respect to the	

pore diameter; (e) transported MV-amount after 4 min of diffusion time according to the respective pore diameter. ....	160
Figure 144: UV/vis-spectra for the time-resolved NDS-diffusion across multipore membranes having $10^7$ pores/cm <sup>2</sup> and a diameter of (a) 35 nm, (b) 90 nm, (c) 200 nm; (d) Time-dependant transport of NDS with respect to the pore diameter; (e) transported MV-amount after 4 min of diffusion time according to the respective pore diameter. ....	160
Figure 145: UV/vis-spectra of the analyte diffusion for multipore membranes having $10^6$ pores/cm <sup>2</sup> and a diameter of 90 nm (a) in case of MV-diffusion and (b) in case of NDS-diffusion. UV/vis-spectra of the analyte diffusion for multipore membranes having $10^6$ pores/cm <sup>2</sup> and a diameter of 200 nm (c) in case of MV-diffusion and (d) in case of NDS-diffusion; time-dependant diffusion of (e) MV and (f) NDS in dependence to the pore diameter. ....	161
Figure 146: UV/vis-spectra of the analyte diffusion for multipore membranes having $10^8$ pores/cm <sup>2</sup> and a diameter of 35 nm (a) in case of MV-diffusion and (b) in case of NDS-diffusion. UV/vis-spectra of the analyte diffusion for multipore membranes having $10^6$ pores/cm <sup>2</sup> and a diameter of 90 nm (c) in case of MV-diffusion and (d) in case of NDS-diffusion; time-dependant diffusion of (e) MV and (f) NDS in dependence to the pore diameter. Note that because of the fast diffusion rate at 90 nm pore diameter, the transport control is not achievable for even larger pore openings. ....	161
Figure 147: (a) – (c) UV/vis-absorbance of the MV-diffusion with respect to the LBL-modification process; (d) – (f) UV/vis-absorbance of the MV-diffusion with respect to the LBL-modification process; All spectra were recorded using a multipore membrane having a pore density of $10^7$ pores/cm <sup>2</sup> and pore diameter of 200 nm. The LBL-deposition was performed using a 50:50-blend ratio [PAH PVP]; ((a) and (d)) blank foil; ((b) and (e)) after deposition of four bilayers; ((c) and (f)) after formation of porous networks. ....	162
Figure 148: (a) – (c) UV/vis-absorbance of the MV-diffusion with respect to the LBL-modification process; (d) – (f) UV/vis-absorbance of the MV-diffusion with respect to the LBL-modification process; All spectra were recorded using a multipore membrane having a pore density of $10^7$ pores/cm <sup>2</sup> and pore diameter of 200 nm. The LBL-deposition was performed using a 100:0-blend ratio [PAH PVP]; ((a) and (d)) blank foil; ((b) and (e)) after deposition of four bilayers; ((c) and (f)) after formation of porous networks. ....	163
Figure 149: (a) – (c) UV/vis-absorbance of the MV-diffusion with respect to the LBL-modification process; (d) – (f) UV/vis-absorbance of the MV-diffusion with respect to the LBL-modification process; All spectra were recorded using a multipore membrane having a pore density of $10^7$ pores/cm <sup>2</sup> and pore diameter of 200 nm. The LBL-deposition was performed using a 25:75-blend ratio [PAH PVP]; ((a) and (d)) blank foil; ((b) and (e)) after deposition of four bilayers; ((c) and (f)) after formation of porous networks. ....	164
Figure 150: Amino acid sequence of the used peptide-Tag. ....	165
Figure 151: Amino acid sequence of the used SpyCatcher. ....	165

---

## List of Tables

Table 1: Overview of the developed methods for the fabrication of nanopores. (CBD = critical break-down).....	4
Table 2: list of the used nanopore membranes including they thickness and track fluences. ....	24
Table 3: Overview and classification of used membrane characterizations. ....	39
Table 4: Parameters and settings for the <i>IV</i> - measurements.....	40
Table 5: Based on the lateral tip-images the listed values were archived for the calculation of the bulk-to-track ratio.....	67
Table 6: Technical data of the laboratory set-up and LOC-system. ....	124
Table 7: List of maximum and minimum current values and respective rectification factors for the <i>IV</i> -measurements of Chip 1 and Chip 2.....	125
Table 8: Maximum and minimum current values and respective rectification factors for the <i>IV</i> -measurements of Chip 3 and Chip 4.....	127